

ARO

The Scientific Journal of Koya University

Topical Powder Mix of Chalcantite, Alum, and Clove as an Effective Feet Odor Treatment

Natural Radioactivity and Radon Exhalation in the Sediment River Used in Sulaymaniyah Governorate, Iraq, Dwellings

Load Balancing Evaluation Tools for a Private Cloud: A Comparative Study

Efficient and Fair Bandwidth Scheduling in Cloud Environments

Membrane Computing for Real Medical Image Segmentation

Factors Controlling the Development of Wine-Glass Forms in the Mountains of the Kurdistan Region, Iraq

Reliability of Trigonometric Transform-based Multi-Carrier Scheme

Phytochemical Constituents of Leaves Essential oils of *Achillea fragrantissima* (Asteraceae) from Iraq

Feasible Time for Extraction of Lead from Spent Paste by Pyrometallurgical Process

Thermal Stability and Reproducibility Enhancement of Organic Solar Cells by Tris(hydroxyquinoline)gallium Dopant Forming a Dual Acceptor Active Layer



ARO-The Scientific Journal of Koya University

The ARO (“Today” in Hewramí Kurdish), is an international scientific journal published by the Koya University with p-ISSN: 2410-9355, e-ISSN: 2307-549X and DOI: 10.14500/2307-549X. ARO is a journal of original scientific research, global news, and commentary. The ARO Scientific Journal is a peer-reviewed, open access journal that publishes original research articles as well as review articles in all areas of Science.



ARO Executive Publisher

Dr. Wali M. Hamad; is the President of Koya University and the Executive Publisher of ARO.

ARO Editorial Board

The Editorial Board of ARO includes an eight-member Senior Executive Editorial Board and a seven-member Associate Editorial Board that help in setting journal policy; a Board of Reviewing Editors consisting of more than 210 leading scientists.

ARO Editorial Group

Senior Executive Editors: Dilan M. Rostam, Salah I. Yahya, Basim M. Fadhil, Fahmi F. Muhammad, Mohammed H. Zangana, Jorge Correia, Fouad Mohammed, Jacek Binda and Nadhir Al-Ansari.

Associate Editors: Hamed M. Jassim, Husein A.H. Shekhabzainy, Ikbal M.G. Tahir, Saddon T. Ahmad, Sahar B. Mahmood, Tara F. Tahir and Yazen A. Khaleel.

This issue reviewers: Ali Ahmed, Asaad H. Ismail, Fahmi F. Muhammad, Ghassan A. Qasmarrogy, Hazeem B. Taher, Ikbal M. Al-Barzinji, Kayhan Zrar, Layth I. Abd Ali, Nadhir Alansari, Naser H. Salman, Saad N. Alsaad, Salah I. Yhaya, Salim Sulaiman, Steven Wright, Yaseen N. Mahmood, Zaynab S. Lazim and Zubair Ahmed.

ARO Editorial Web and New Media: Dilan M. Rostam and Salah I. Yahya

Secretarial Office of the Journal: Haneen H. Falah

Journal Proofreader: Salah I. Yahya

ARO, the International journal of original scientific research and commentary is an online and published twice a year, as well, by Koya University. The published articles are free and online open access distributed under the Creative Commons Attribution License (CC BY-NC-SA 4.0: <https://creativecommons.org/licenses/by-nc-sa/4.0/>). Responsibility of the content rests upon the authors and not upon ARO or Koya University.

ARO the Scientific Journal Office

Koya University, University Park
Danielle Mitterrand Boulevard, Koya KOY45
Kurdistan Region - F.R. Iraq

Tel.: +964 (0) 748 012 7423

Mobile: +964 (0) 750 187 5489

E-mail: aro.journal@koyauniversity.org

url: aro.koyauniversity.org

December 2018 | Befranber – 2718

ARO

The Scientific Journal of Koya University

Vol VI, No 2(2018)

Contents

Aro Editorial Words	iii
Amera G. Baker	01
Topical Powder Mix of Chalcantite, Alum, and Clove as an Effective Feet Odor Treatment	
Adil M. Hussein	07
Natural Radioactivity and Radon Exhalation in the Sediment River Used in Sulaymaniyah Governorate, Iraq, Dwellings	
Sahand Kh. Saeid, Tara Ali Yahiya	13
Load Balancing Evaluation Tools for a Private Cloud: A Comparative Study	
Mustafa Khaleel, Mengxia Zhu	20
Efficient and Fair Bandwidth Scheduling in Cloud Environments	
Rafaa I. Yahya, Siti Mariyam Shamsuddin, Salah I. Yahya, Bisan Alsalibi, Ghada K. Al-Khafaji	27
Membrane Computing for Real Medical Image Segmentation	
Varoujan K. Sissakian, Arsalan A. Othman, Ahmed T. Shihab	39
Factors Controlling the Development of Wine-Glass Forms in the Mountains of the Kurdistan Region, Iraq	
Samah A. Mustafa	49
Reliability of Trigonometric Transform-based Multi-Carrier Scheme	
Karzan O. Qader, Sahar A.A. Malik Al-Saadi, Ibrahim M. Faraj	56
Phytochemical Constituents of Leaves Essential oils of <i>Achillea fragrantissima</i> (Asteraceae) from Iraq	
Fakhri H. Ibraheem	63
Feasible Time for Extraction of Lead from Spent Paste by Pyrometallurgical Process	
Fahmi F. Muhammad, Khaulah Sulaiman	69
Thermal Stability and Reproducibility Enhancement of Organic Solar Cells by Tris(hydroxyquinoline)gallium Dopant Forming a Dual Acceptor Active Layer	
General Information	79
Guide to Author	80
Aro Reviewer/Associate Editor Application Form	82

ARO Editorial Words

Dear readers,

Aro, the Scientific Journal of Koya University, is closing its eleventh issue (Vol VI, No 2, 2018). It has been an exciting and yet dynamic season for our journal. Aro is publishing its 6th issue as an internationally listed Scientific Journal in Kurdistan Region of Iraq. Notably, Aro has been accepted for indexing in the Emerging Sources Citation Index (ESCI), a new edition of Web of Science™ as of Feb 2016. Content in this index is under consideration by Thomson Reuters to be accepted in the Science Citation Index Expanded™ (SCIE). Aro's individual articles are currently listed by Thomson Reuters using articles unique DOI numbers which is a historical achievement for our academic community. Aro is starting its sixth-year journey in leading the quality of regional scientific publications with global impact. The editorial team have been working tirelessly to keep the novel mission and sustain Aro's future publications with greater impacts and citations. It is exciting that Aro has been awarded to DOAJ Seal listing which is an indication of a trusted high standard open access scientific work. The upcoming new season will be an even more exciting period in Aro's life as Thomson Reuters will examine our journal for a full permanent listing.

Aro continues its mission to provide resources, support and advice for researchers in the process of publishing their scientific papers, while at the same time offering free public access to scientific research by open online access. This is a daunting task which we hope to advance in the years to come. Thus, in the sections to follow, we would like to share and elaborate on the core elements that constitute Aro. However, finding reliable and skilled reviewers remain a big challenge for us.

Aro was created with a long-term vision of becoming accessible to all researchers in Kurdistan and beyond, and covering a wide range of scholarly disciplines in sciences. Aro is a peer-reviewed, open access journal that publishes original scientific research, global news, letters and commentary as well as review articles in areas of natural sciences and technology. In this issue, you will have access to original research papers in a variety of areas, such as Physics, Chemistry, Biology, Material Science, Civil Engineering, Architectural Engineering, Software Engineering, Electrical and Electronics Engineering, Petroleum Engineering and Geology.

The great responses from researchers, academics and professionals in the last five years have made us create a wider Editorial Board which serves the wider submitted scientific manuscripts. However, it is clear that having a dedicated and well-organised editorial board for the journal is only one side of the coin. The other is the ability to attract submissions of quality research and scholarly work. We are thankful to all of those who put their trust in Aro and presented their original research work for publication in Vol VI, No 2 (2018) of the journal, as well as, our thanks are extended to the 20 peer-reviewers from the Universities worldwide for their efforts in reviewing and enabling this issue of Aro.

Your support and feedback are invited and appreciated.

Dilan M. Rostam
Editor-in-Chief

Wali M Hamad
Executive Publisher

Dilan M. Rostam, Salah I. Yahya, Basim M. Fadhil, Fahmi F. Muhammad, Mohammed H.S. Zangana, Jorge Correia, Fouad Muhammad and Nadhir Al-Ansari
Executive Editorial Board

Topical Powder Mix of Chalcanthite, Alum, and Clove as an Effective Feet Odor Treatment

Amera G. Baker

Department of Physics, Faculty of Science and Health, Koya University, Danielle Mitterrand Boulevard, Koya KOY45, Kurdistan Region – F.R. Iraq

Abstract—Treating foot odor infected with pathogenic fungus and bacteria has been a major concern for pharmaceutical companies. Finding a right treatment with minimum side effects has been of particular importance. This study configures a homemade topical powder mix in treating foot odor. The homemade topical powder mix is free of any harmful chemical constituents; its main constituents being Chalcanthite, Alum, and Clove. Energy dispersive X-ray fluorescence was used for the determination of the chemical composition component of Chalcanthite, Alum, Clove, and the powder mix of Chalcanthite, Alum, and Clove. X-ray fluoresces techniques was able to measure elements such as oxygen, sulfur, aluminum, potassium, and copper in *ka* line. The antimicrobial activity of the powder mix of Chalcanthite, Alum, and Clove was studied against two pathogenic fungi, which are *Epidermophyton* sp., and *Trichophyton* sp., and two pathogenic bacteria, which are *Brevibacterium* sp., and *Staphylococcus* sp. Screening for antibacterial and antifungal was done using agar disk diffusion. The growth inhibition zone measured ranged from 16 to 28 mm for all the sensitive fungal, and ranged from 14 to 27 mm for the sensitive bacteria.

Index Terms—Alum, Chalcanthite, Clove, Pathogenic fungus, Topical powder, X-ray fluoresces techniques.

I. INTRODUCTION

Foot odor is a type of body odor that affects the feet of humans and is generally considered to be an unpleasant smell. This problem practically is seen among people wearing closed shoes and specifically among sports and army people (Sharquie, et al., 2013). The main cause is foot sweat, sweat itself is odorless, but it creates a beneficial environment for certain bacteria to grow and produce bad-smelling substances. These bacteria are naturally present in our skin as part of the human flora (Ara, et al., 2006). The most common type of bacteria is *Brevibacterium* sp., which is considered a major cause of foot odor because they ingest dead skin on the feet and, in the process, convert amino

acid methionine into methanethiol, which has a sulfuric aroma and cheesy odor (Marshall, et al., 1988). Furthermore, *Propionibacteria* sp., *Staphylococcus* sp., and *Bacilli* sp. that perform fermentation on carbohydrates, proteins, and fatty acids that come from dead skin cells on peoples feet (Kanda, et al., 1990). There are many systemic drugs like topical anti-perspiration agents such as aluminum salts, zinc sulfate solution, and iontophoresis have been used as therapeutic measures (Sharquie, 1996). Furthermore, anticholinergic (glycopyrrolate) and topical antibacterial drugs such as erythromycin, clindamycin, and benzoyl peroxide have been used in the treatment of feet odor (McWilliams, et al., 1987).

Natural products have been used for a long time in treating human disease, and they contain many constituents of therapeutic value, environmentally safer, easily available, and cheap (Oro, et al., 2015).

The present study configures a homemade topical powder mix in treating foot odor. The elements present in the homemade topical powder mix of Chalcanthite, Alum, and Clove can be explored, identified. Concentration calculation of the composites composition has been made using X-ray fluorescence (XRF) techniques. Furthermore, studies were performed on the composites antimicrobial activities against *Epidermophyton* sp., *Trichophyton* sp., *Brevibacterium* sp., and *Staphylococcus* sp. The homemade topical powder mix of chalcanthite, alum, and clove was practically applied for many people, which has been a successful positive product in the treatment of foot odor. Complete healing was achieved within 3 days of use without the presence of any side effects. The homemade topical powder mix has a nice smell; it is soft on the skin and inexpensive.

II. MATERIALS AND METHODS

A. Specimens

Three different materials were purchased from Al Shorja local market, the herbal shop, in Baghdad city, including chalcanthite powder (copper sulfate locally called blue), alum powder (potassium aluminum sulfate), and dried clove (*syzygium aromatic*). Table I shows the symbols assignments for the used materials.

B. Preparation of powder

Chalcanthite powder (Z-1), Alum powder (Z-2), and



TABLE I
SYMBOLS FOR MATERIALS

Material	Symbols
Chalcanthite	Z-1
Alum	Z-2
Cloves	Z-3
Mix of the three materials	Z-123

dried clove (Z-3) were grinding in a Mini-Mill 2 analytical milling device to produce a fine powder for each of them. Then, mixing the fine powder of chalcanthite (Z-1), Alum (Z-2), and Clove (Z-3) was carried out to produce a mix of the three materials (Z-123) at the mixing ratio (1:1:1), and was made ready for XRF test. Furthermore, mixing the fine powder of chalcanthite (Z-1), alum (Z-2), and clove (Z-3) was made to produce a mix of the three materials (Z-123) at the mixing ratio 1:1:1, 1:0.5:0.5, 0.5:1:0.5 and 0.5:0.5:1, of chalcanthite (Z-1), alum (Z-2), and clove (Z-3), respectively, for antimicrobial activity.

C. The XRF

The XRF was performed using Rigaku NEX CG XRF spectrometer. Powder of Z-1, Z-2, and Z-3, was pressed into a pellet of 32 mm diameter under 10 tons/cm² pressures using the hydraulic press. Furthermore, powder of Z-123 was mixed at the ratio (1:1:1), of Z-1, Z-2, and Z-3 and pressed into a pellet of 32 mm diameter under 10 tons/cm² pressures using a hydraulic press. The samples were placed in the chamber and measured by 20 mm diaphragm in a vacuum. X-ray spectra were obtained using RX9, Cu, Mo, and Al conditions. In these analyses, the X-ray tube current was set to approximately 1 mA for RX9 target and into 0.5 mA for other targets. The X-ray tube voltage has been set to 25 kV for RX9 and 50 kV for Cu, Mo, and Al targets. The X-ray measuring time was 200s for Al target and 100s for other targets.

D. Microorganisms

Pure cultures isolated from infected feet are two pathogenic fungi (*Epidermophyton* sp. and *Trichophyton* sp.) and two pathogenic bacteria (*Brevibacterium* sp. and *Staphylococcus* sp.) were obtained from the Al-Kindi General Hospital in Baghdad city, and diagnosed has been examined in the microbiology laboratory, College of Sciences, University of Baghdad.

The fungi and bacteria isolated cultures were incubated for 24 h at 37°C on potato dextrose agar and nutrient agar medium, respectively, isolated cultures were maintained at 4°C (Barbaro and Symonds, 2006; Wayne, 2007). Fungal isolates were grown on potato dextrose agar contained in dilution bottles for approximately 2 weeks. After sufficient incubation, a fungal spore suspension was obtained by aseptically dispensing 10 ml of sterile saline (0.65% NaCl) into the bottles and gently removing spores and hyphal fragments from the surface of the plate using a sterile glass rod. Bacterial cultures were grown in 5 ml nutrient broth for 18–24 h. After the 18–24 h incubation period, 100 ml aliquots of culture were aseptically spread over the surface of

nutrient agar plates using the spread plate technique.

E. Antimicrobial activity

The antimicrobial activity susceptibility profiles of two pathogenic fungi and two pathogenic bacteria were investigated by the agar disk diffusion method (Bauer, et al., 1966; CLSI, 2012). The mix of the three materials Z-123 compressed to be suitable for antimicrobial activity test, the pellet is 50 mg with 8 mm diameter at the mixing ratio (1:1:1, 1:0.5:0.5, 0.5:1:0.5, and 0.5:0.5:1), of Z-1, Z-2, and Z-3, and screened for their antimicrobial activities against *Epidermophyton* sp., *Trichophyton* sp., *Brevibacterium* sp., and *Staphylococcus* sp. The zones of growth inhibition around the disks were measured after 3–5 days of an incubation at 28°C for fungal, and 18–24 h of an incubation at 37°C for bacteria. The sensitivities of the microorganism species of Z-123 were determined by measuring the sizes of inhibitory zones on the agar surface around the disks.

III. RESULTS AND DISCUSSIONS

A. XRF analysis

The XRF is working on the principle of absorbing fluorescence by detectors its proportion conductance is a change in the energy of the fluorescence which is processed by the electronics. The signal of fluorescent was measured in kilo-electron volts on the horizontal axis; the vertical axis was an intensity occurrence per second. The energy of the fluorescent determined the elements while the intensity of the fluorescence was identified as the concentration of the elements in a sample, (Peng, et al., 2013; Jang, 2010).

The chemical compositions of components of Z-1, Z-2, Z-3, and Z-123 have detected by the XRF.

Table II, XRF measurements of major, minor and trace elements of Z-1, Z-2, Z-3, and Z-123 (as percentages), the XRF measurements indicated that all the materials are contained oxygen (O), sulfur (S), aluminum (Al), potassium (K), copper (Cu), iron (Fe), zinc (Zn), calcium (Ca), silicon (Si), and chlorite (Cl). However, all the materials were found to have extra elements, copper (Cu) and silicon (Si), which were missing in the case of Z-2 and zinc (Zn) and nickel (Ni) were missing in the case of Z-3. The concentrations of elements are found to be different for all components. Fig. 1, comparison of mass percentage concentrations of selected elements (Al, Cu, K, O, and S) of Z-1, Z-2, Z-3, and Z-123 determined by XRF. It can be observed, in all cases, that oxygen (O) was found to be the highest concentration. Oxygen (O) does not give XRF peaks because fluorescence photons for oxygen are too low in energy to be transmitted through the air and are not efficiently detected using conventional Si based detectors. Furthermore, the highest concentration of the element is sulfur (S), copper (Cu), aluminum (Al), and potassium (K) which these elements give XRF peaks. When these materials are irradiated with X-rays, the intensity as a function of energy can be calculated over the energy ranges 1–10 keV at the same computing conditions. Fig. 2, intensity versus the energy of Z-1, calculated over the energy range

TABLE II
X-RAY FLUORESCENCE MEASUREMENTS OF MAJOR, MINOR, AND TRACE
ELEMENTS OF Z-1, Z-2, Z-3, AND Z-123 (AS PERCENTAGES)

Element	Z-1%	Z-2%	Z-3%	Z-123%
O	72.1	71.2	93.8	71.8
Cu	16.8	-	0.154	8.43
S	9.08	16.9	0.425	11.3
Al	0.824	9.12	0.208	4.97
K	0.0716	3.31	2.74	2.36
Zn	0.356	0.0012	-	0.200
Ni	0.0984	0.0008	-	0.0545
Si	0.487	-	0.212	0.215
Fe	0.0571	0.0144	0.0511	0.153
Ca	0.0523	-	1.20	0.305
W	0.0329	-	-	0.0092
Cr	0.0120	0.0005	0.0266	0.0032
Sn	0.0053	0.0044	-	0.0064
Ti	0.0046	0.0021	-	0.0038
Pb	0.0036	-	-	0.0017
Cl	-	0.213	0.534	0.177
Ta	-	0.0010	-	--
Ga	-	0.0007	-	-
V	-	0.0007	-	0.0007
Rb	-	0.0006	-	0.0023
Tl	-	-	-	0.0005
Sr	-	0.0004	-	0.0017
Mg	-	-	0.355	-
P	-	-	0.144	-
Mn	-	-	0.112	0.0150
Hf	-	-	0.0387	-
W	-	-	-	0.0092
Ag	-	-	-	0.0003

1–10 keV using XRF with RX9, Mo, Cu, and Al targets. The peaks are shown in the ranges 1.50, 2.31, 2.63, 6.44, 8.058, and 8.95 keV, corresponding to Al- α , S- α , Fe- α , Cu- α , and Zn- α lines. Fig. 3, intensity versus the energy of Z-2, calculated over the energy range 1–10 keV using XRF with RX9, Mo, Cu, and Al targets. The peaks are shown in the ranges 1.50, 2.31, 3.35, and 6.44 keV, corresponding to Al- α , S- α , K- α , and Fe- α lines. Fig. 4, intensity versus the energy of Z-3, calculated over the energy range 1–10 keV using XRF with RX9, Mo, Cu, and Al targets. The peaks are shown in the ranges 1.76, 2.01, 2.31, 3.35, 3.68, 5.46, 5.91, 6.44, 8.058, and 8.95 keV, corresponding to Si- α , P- α , S- α , K- α , Ca- α , Cr- α , Mn- α , Fe- α , Cu- α , and Zn- α lines. Fig. 5, intensity versus the energy of Z-123, calculated over the energy range 1–10 keV using XRF with RX9, Mo, Cu, and Al targets. The peaks are shown in the ranges 1.50, 2.31, 2.63, 6.44, 8.058, and 8.95 keV, corresponding to Al- α , S- α , Fe- α , Cu- α , and Zn- α lines. The most important elements of Z-123 are sulfur (S), copper (Cu), aluminum (Al), potassium (K), iron (Fe), and zinc (Zn).

B. Antimicrobial activity

The antimicrobial activity of Z-123 was studied against two pathogenic fungi (*Epidermophyton* sp., and *Trichophyton* sp.) and two pathogenic bacteria (*Brevibacterium* sp. and *Staphylococcus* sp.), at the mixing ratio (1:1:1, 1:0.5:0.5, 0.5:1:0.5, and 0.5:0.5:1), of Z-1, Z-2, and Z-3. The antifungal and

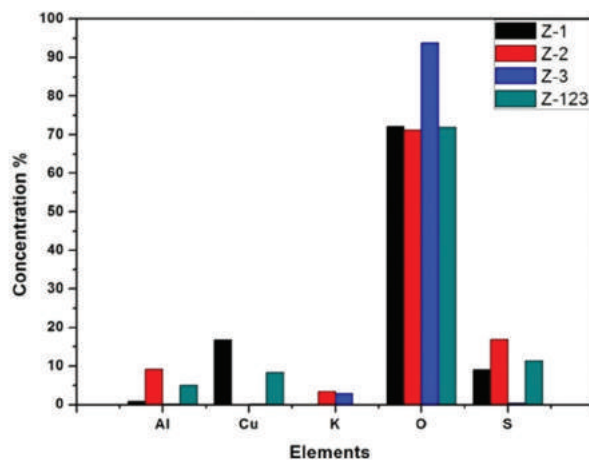


Fig. 1. Comparison of mass percentage concentrations of selected elements (Al, Cu, K, O, and S) of Z-1, Z-2, Z-3, and Z-123, determined by X-ray fluorescence.

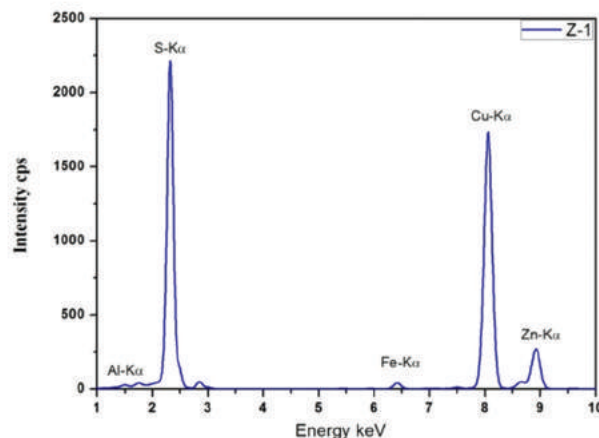


Fig. 2. Intensity versus the energy of Z-1 calculated over the energy range 1–10 keV using XRF with RX9, Mo, Cu, and Al targets.

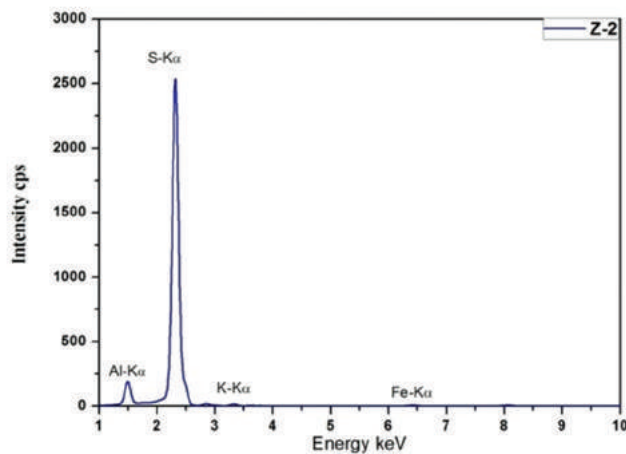


Fig. 3. Intensity versus the energy of Z-2, calculated over the energy range 1–10 keV using X-ray fluorescence with RX9, Mo, Cu, and Al targets.

antibacterial potential of Z-123 was assessed in terms of zone of inhibition of fungal and bacterial growth. The results are presented

in Tables III and IV. The growth inhibition zone was found to be high (28 mm) when mixing Z-1, Z-2, and Z-3 at the same ratio 1:1:1 and the growth inhibition zone was found to be low (14 mm) at the mixing ratio 0.5:0.5:1. The growth inhibition zone measured ranged from 16 to 28 mm for all the sensitive fungal, and ranged from 14 to 27 mm for the sensitive bacteria as shown in Fig. 6.

I have used the topical powder mix of Chalcantite, Alum, and Clove for many people in Iraq country, in Baghdad, Erbil, and Koya cities. A person who has foot odor was instructed to wash his feet without drying and applies it's between the toes and on the soles of the feet 1 time daily for 3 days only. All the persons who used the topical powder mix assured that complete healing within 3 days only without any side effects recalls after treatment externally on the affected areas. Topical powder mix is an effective therapy for feet infected

TABLE III
ANTIFUNGAL ACTIVITY OF Z-123, AGAINST FUNGAL TEST ORGANISM

Microorganisms	Mixing ratio	Zone of inhibition in mm
<i>Epidermophyton</i> sp.	1:1:1	28
	1:0.5:0.5	20
	0.5:1:0.5	17
	0.5:0.5:1	16
<i>Trichophyton</i> sp.	1:1:1	27
	1:0.5:0.5	21
	0.5:1:0.5	18
	0.5:0.5:1	17

TABLE IV
ANTIBACTERIAL ACTIVITY OF Z-123, AGAINST BACTERIAL TEST ORGANISM

Microorganisms	Mixing ratio	Zone of inhibition in mm
<i>Brevibacterium</i> sp.	1:1:1	27
	1:0.5:0.5	23
	0.5:1:0.5	17
	0.5:0.5:1	15
<i>Staphylococcus</i> sp.	1:1:1	26
	1:0.5:0.5	22
	0.5:1:0.5	15
	0.5:0.5:1	14

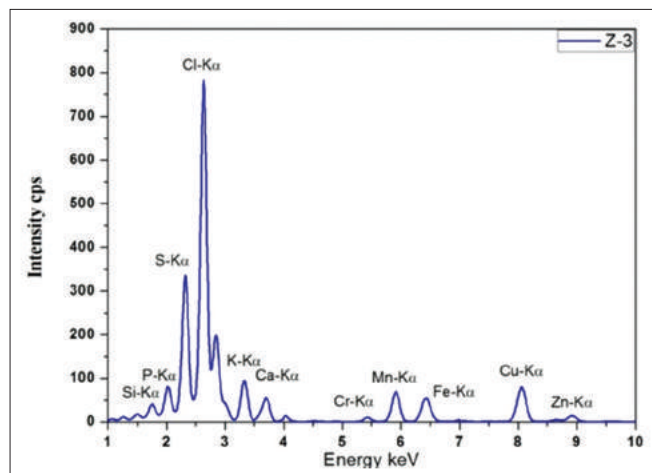


Fig. 4. Intensity versus the energy of Z-3, calculated over the energy range 1–10 KeV using XRF with RX9, Mo, Cu, and Al targets.

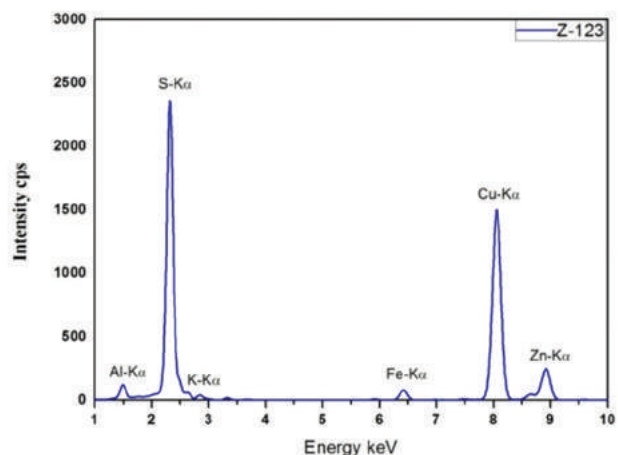


Fig. 5. Intensity versus the energy of Z-123, calculated over the energy range 1–10 KeV using X-ray fluorescence with RX9, Mo, Cu, and Al targets.

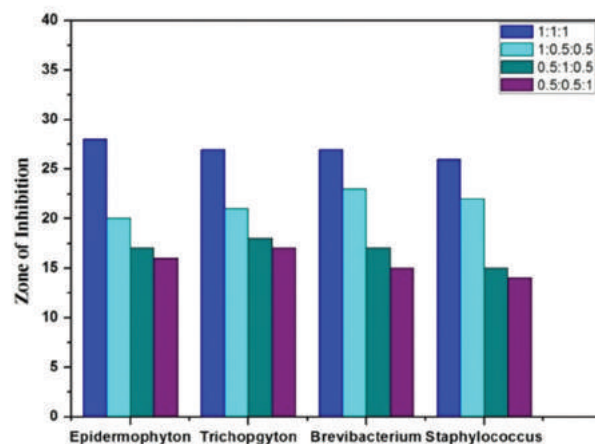


Fig. 6. Zone of inhibition of Z-123 at different mixing ratio versus antifungal and antibacterial activity against *Epidermophyton* sp., *Trichophyton* sp., *Brevibacterium* sp., and *Staphylococcus*.

with pathogenic fungus and bacteria that cause itching, stinging, and burning between the toes and on the soles of the feet, blisters on the feet that itch, cracking and peeling skin on the feet, most commonly between the toes and on the soles, dry skin on the soles or sides of the feet, raw skin on the feet. The topical powder mix has a nice smell, soft on the skin, and inexpensive.

The important elements in the topical powder mix of chalcantite, alum, and clove are sulfur (S), copper (Cu), aluminum (Al), potassium (K), iron (Fe), and zinc (Zn).

The mechanism of action of the topical powder mix of chalcantite, alum, and clove related to its multiple effects such as antibacterial, antifungal, and antiperspirant actions. Sulfur is used in pharmaceutical skin preparations for the treatment of acne and other conditions. It acts as a catalytic agent and also kills bacteria, fungi, scabies mites, and other parasites (Kim, et al., 2006; Suleiman, et al., 2015). Many metallic elements have an ability to inhibit the growth of bacteria and to inactivate enzymes. This antimicrobial effect is shown by metals such as mercury, silver, copper, lead, zinc,

gold, aluminum, and other metals (Peciulyte and Dirginciute-Volodkiene, 2102; Percival, et al., 2005). Copper is an essential mineral in the topical powder mix of chalcantite, alum, and clove that plays a key role in many physiological and metabolic processes, including angiogenesis, skin generation and expression, and stabilization of extracellular skin proteins. Copper has also a potent wide spectrum based properties. The combination of these two distinct properties of copper makes copper a very attractive active material for the improvement of skin well-being (Borkow, 2014). Copper (Cu) and potassium (K) particles were reported to have antimicrobial activity against a wide spectrum of bacteria, including *Micrococcus lutes*, *Klebsiella pneumonia*, *Escherichia coli*, *Pseudomonas aeruginosa*, *Staphylococcus aureus*, and *Bacillus subtilis* (Dawson and Boling, 1987; Yamamoto and Ishihama, 2005). Moreover, Cu particles have been shown to suppress the vegetative growth of some fungal species such as *Aspergillus flavus*, *Aspergillus niger*, *Alternaria alternata*, *Fusarium solani*, *Penicillium chrysogenum*, and *Candida albicans* (Essa and Khallaf, 2016). The mechanism by which antimicrobial copper kills bacteria is a complex by nature, but the effect is simple. Science suggests that copper surfaces affect bacteria in two sequential steps: The first step is a direct interaction between the surface and the bacterial outer membrane, causing the membrane to rupture. The second is related to the holes in the outer membrane, through which the cell loses vital nutrients and water, causing a general weakening of the cell (Hobman and Crossman, 2014). Every cell's outer membrane, including that of a single cell organism like a bacterium, is characterized by a stable electrical microcurrent. This is often called Trans membrane potential, and is, literally, a voltage difference between the inside and the outside of a cell. It is strongly suspected that when a bacterium comes in contact with a copper surface, a short-circuiting of the current in the cell membrane can occur. This weakens the membrane and creates holes (Smaldone and Helmann, 2007). Another way to make a hole in a membrane is by localized oxidation or rusting. This happens when a single copper molecule, or copper ion, is released from the copper surface and hits a building block of the cell membrane (either a protein or a fatty acid). If the hit occurs in the presence of oxygen, the oxidative damage, or rust will occur. An analogy is rust weakening and making holes in a piece of metal. Now that the cell's main defense (its outer envelope) has been breached, there is an unopposed stream of copper ions entering the cell. This puts several vital processes inside the cell in danger. Copper literally overwhelms the inside of the cell and obstructs cell metabolism. These reactions are accomplished and catalyzed by enzymes. When excess copper binds to these enzymes, their activity grinds to a halt. The bacterium can no longer breathe, eat, digest, or create energy. Experts explain the speed with which bacteria perish on copper surfaces by the multi-targeted nature of copper's effects. After membrane perforation, copper can inhibit any given enzyme that "stands in its way," and stop the cell from transporting or digesting nutrients, from repairing its damaged membrane, and from breathing or multiplying. It

is, thus, not surprising that copper and copper compounds have been used by many different civilizations to treat skin diseases, as well as other maladies. The safety of using the copper oxide containing products has been examined in several non-clinical studies and in more than 10 clinical trials. In all the studies, not even one adverse reaction was recorded. The products were found to be non-irritating, non-sensitizing, and safe to use, both when in contact with intact and broken skin (Varkey, 2010).

IV. CONCLUSION

Freedom from foot odor and foot infection will improve a people's health, specifically among sports and army people, both physically and mentally. Furthermore, it will be benefited by reducing the costs of medical treatment and productive days lost for that treatment. For these reasons configures a homemade topical powder mix of chalcantite, alum, and clove in treating foot odor. Moreover, it's free of any harmful chemical constituents. The chemical compositions of components of the topical powder mix of chalcantite, alum, and clove have detected by the XRF, the most important elements in the topical powder mix are Sulfur (S), copper (Cu), aluminum (Al), potassium (K), iron (Fe), and zinc (Zn). The antimicrobial activity of the topical powder mix was found to be effective against *Epidermophyton* sp., *Trichophyton* sp., *Brevibacterium* sp., and *Staphylococcus*. The growth inhibition zone was found to be high (28 mm) when mixing chalcantite, alum, and clove at the same ratio 1:1:1, respectively, and the growth inhibition zone was found to be low (14 mm) when mixing chalcantite, alum, and clove at the mixing ratio 0.5:0.5:1, respectively.

I have used the homemade topical powder mix of chalcantite, alum, and clove for many people, and it's showing a successful positive product in the treatment of foot odor. Complete healing within 3 days only without any side effects.

To the best of our knowledge, this is the first study carried out. There is no previous results were published in this regard.

V. ACKNOWLEDGMENT

The author is grateful to the Department of Biology at Baghdad University for antimicrobial activity test and Department of Physics at Koya University for using their facility of XRF technique.

REFERENCES

- Ara, K., Hama, M., Akiba, S., Koike, K., Okisaka, K., Hagura, T., Kamiya, T. and Tomita, F., 2006. Foot odor due to microbial metabolism and its control. *Canadian Journal of Microbiology*, 52(4), pp.357-364.
- Barbaro, S.E. and Symonds, J.A., 2006. The efficacy of a novel Quaternary ammonium foot spray (NQAFS) against foot odor causing microorganisms. *Rivier College Online Academic Journal*, 2, pp.1.
- Bauer, A.W., Kirby, W.M., Sherris, J.C. and Turck, M., 1966. Antibiotic susceptibility testing by a standardized single disk method. *American Journal of Clinical Pathology*, 45(4), pp.493-496.

- Borkow, G., 2014. Using copper to improve the well-being of the skin. *Current Chemical Biology*, 8(2), pp.89-102.
- CLSI. Clinical and Laboratory Standards Institute., 2012. *Performance Standards for Antimicrobial Susceptibility Testing; Twenty-Second Informational Supplement*. CLSI Document M 100-S22.
- Dawson, K.A. and Boling, J.A., 1987. Effects of potassium ion concentrations on the antimicrobial activities of ionophores against ruminal anaerobes. *Applied and Environmental Microbiology*, 53(10), pp.2363-2367.
- Essa, A.M. and Khallaf, M.K., 2016. Antimicrobial potential of consolidation polymers loaded with biological copper nanoparticles. *BMC Microbiology*, 16(1), pp.144.
- Hobman, J.L. and Crossman, L.C., 2015. Bacterial antimicrobial metal ion resistance. *Journal of Medical Microbiology*, 64(5), pp.471-497.
- Jang, M., 2010. Application of portable X-ray fluorescence (PXRF) for heavy metal analysis of soils in crop fields near abandoned mine sites. *Environmental Geochemistry and Health*, 32(3), pp.207-216.
- Kanda, F., Yagi, E., Fukuda, M., Nakajima, K., Ohta, T. and Nakata, O., 1990. Elucidation of chemical compounds responsible for foot malodour. *British Journal of Dermatology*, 122(6), pp.771-776.
- Kim, S., Kubec, R. and Musah, R.A., 2006. Antibacterial and antifungal activity of sulfur-containing compounds from *Petiveria alliacea* L. *Journal of Ethnopharmacology*, 104(1-2), pp.188-192.
- Marshall, J., Holland, K.T. and Gribbon, E.M., 1988. A comparative study of the cutaneous microflora of normal feet with low and high levels of odour. *Journal of Applied Microbiology*, 65(1), pp.61-68.
- McWilliams, S.A., Montgomery, I., Jenkinson, D.M., Elder, H.Y., Wilson, S.M. and Sutton, A.M., 1987. Effects of topically-applied antiperspirant on sweat gland function. *British Journal of Dermatology*, 117(5), pp.617-626.
- Oro, D., Heissler, A., Rossi, E.M., Scapin, D., da Silva Malheiros, P. and Boff, E., 2015. Antifungal activity of natural compounds against *Candida* species isolated from HIV-positive patients. *Asian Pacific Journal of Tropical Biomedicine*, 5(9), pp.781-784.
- Peciulyte, D. and Dirginciuote-Volodkiene, V., 2012. Effect of zinc and copper on cultivable populations of soil fungi with special reference to entomopathogenic fungi. *Ekologija*, 58(2), pp.65-85.
- Peng, S., Liu, Z., Sun, T., Ma, Y., and Ding, X., 2013. Spatially resolved in situ measurements of the ion distribution near the surface of an electrode in steady-state diffusion in an electrolytic tank with confocal micro X-ray fluorescence. *Analytical Chemistry*, 86(1), pp.362-366.
- Perceval, S.L., Bowler, P.G. and Russell, D., 2005. Bacterial resistance to silver in wound care. *Journal of Hospital Infection*, 60(1), pp.1-7.
- Sharquie, K.E., 1996. Intralesional therapy of cutaneous leishmaniasis with 2% zinc sulfate solution. *Journal Pan Arab League of Dermatologist*, 7, pp.41-46.
- Sharquie, K.E., Noaimi, A.A. and Hameed, S.D., 2013. Topical 15% zinc sulfate solution is an effective therapy for feet odor. *Journal of Cosmetics, Dermatological Sciences and Applications*, 3(03), pp.203-208.
- Smaldone, G.T. and Helmann, J.D., 2007. CsoR regulates the copper efflux operon copZA in *Bacillus subtilis*. *Microbiology*, 153(12), pp.4123-4128.
- Suleiman, M., Al-Masri, M., Al Ali, A., Aref, D., Hussein, A., Saadeddin, I. and Warad, I., 2015. Synthesis of nano-sized sulfur nanoparticles and their antibacterial activities. *Journal of Materials and Environmental Science*, 6(2), pp.513-518.
- Varkey, A.J., 2010. Antibacterial properties of some metals and alloys in combating coliforms in contaminated water. *Scientific Research and Essays*, 5(24), pp.3834-3839.
- Wayne, P.A., 2007. Clinical and laboratory standards institute. *Performance Standards for Antimicrobial Susceptibility Testing*, 2007, 17.
- Yamamoto, K. and Ishihama, A., 2005. Transcriptional response of *Escherichia coli* to external copper. *Molecular Microbiology*, 56(1), pp.215-227.

Natural Radioactivity and Radon Exhalation in the Sediment River Used in Sulaymaniyah Governorate, Iraq, Dwellings

Adil M. Hussein

Department of Physics, Advanced Nuclear Laboratory, Faculty of Science and Science Education, University of Sulaimani, Kurdistan Region - F.R. Iraq

Abstract—The samples, sand and pebble (Sediment River), were collected from their selling places in Sulaymaniyah city, Iraq. Sand and pebble emanate each of ^{238}U , ^{232}Th , ^{40}K , and radon naturally. The radon concentration in the air (C_0) and gamma-specific activity (A_s) of the samples were measured using passive detectors (CR-39) and gamma spectrum analyzer (3×3 NaI (TI) connected to digital spectrum analyzer), respectively. The mean value of the $C_0 \pm$ deviation of the investigated samples was 176.5 ± 6.9 Bq/m³, which is lower than the worldwide value of 300 Bq m⁻³ reported by the IAEA. However, an anomaly in C_0 value was found in Tanjaro (Sand) sample. The mean value radon mass exhalation rate (E_M) was 10.9 ± 0.5 $\mu\text{Bq/kg/h}$. The second part of the measuring is the gamma-specific activities (A_s) of each ^{226}Ra , ^{232}Th , and ^{40}K . The A_s values were ranged (4.3 ± 0.2 – 22.6 ± 0.2), (1.9 ± 0.1 – 4.2 ± 0.1), and (39.8 ± 0.2 – 86.0 ± 0.4) Bq/kg, respectively. The mean calculated value of radium equivalent (Ra_{eq}) was 20.2 ± 0.2 Bq/kg. The annual effective dose rate of gamma (H_{ann}) was 0.13 mSv/y. Fortunately, the H_{ann} value of the samples is lower than the world average value of 0.48 mSv/y.

Index Terms—Building Materials, Gamma-Specific Activity, Gamma/Radon Radiological Parameters, Radon Mass Exhalation, Sediment River (Sand and Pebble).

I. INTRODUCTION

Sediment river provides valuable information about radiological contamination in the environment. Sand and pebble particles depose on the bottom of lakes, but currents continue to move the relict sediment along riverbank or stream. Sediment river (sand and pebble) is the raw materials used mainly in building construction in Iraq. These materials emanate naturally occurring radioactivity, since they contain long-lived radionuclides such as ^{238}U , ^{235}U , ^{232}Th , with their

progenies, and ^{40}K . The precursors of ^{226}Ra in the ^{238}U series are generally ignored because 98.5% of the radiological effects of the ^{238}U series are produced by the ^{226}Ra and its daughter products (Turhan and Varinliog, 2012).

The natural radioactive nuclides such as radon contribute mainly in radiation exposure of the human population. Radon is a decay product of ^{226}Ra from the natural series decay of ^{238}U with half-life of 3.82 days (Gulfink, 2008). In general, unlike the gas radon itself, radon daughters are solids and stick to surfaces of dust particles in the air. If such contaminated dust inhaled, these particles can stick to the airways of the lung and increase the risk of developing lung cancer (Mass, 2011). Previous studies (Poschl, 2007; Turhan, 2008) reported that natural radioactivity and the terrestrial gamma dose depend effectively on geological and geographical conditions, due to this radon and its progenies depend on the geological and geographical condition too (more information about geographical parameters are required). Much information about the radon emanating from the materials has been recorded in academic studies. High levels of radon are associated with granite igneous rocks, shale, dirty quartz sedimentary rocks, phosphate deposits, and some beach sands, which may contain high levels of radon progenitors (Brill, 1994). All types of building materials such as sand, gravel, concrete, brick, and granite contain potassium, uranium, thorium, and their progenies; they generate a direct radiation exposure (Cetin, et al., 2012). Previous studies reported that the radon and other natural radionuclide traces emanate of sand and gravel (raw building materials) (Banman, et al., 1982; Mansoor, et al., 2005).

A major part of concrete and brick consists of sand and pebble. These materials are commonly used for developing buildings in Iraq. This research work is to assess the inhalation and exhalation doses of the sand and pebble samples. These samples were collected from screen factories established near the rivers and streams of different areas of Sulaymaniyah Governorate. The main objective of the current work is to study the natural radionuclide concentrations for 12 samples. Furthermore, radon concentration \pm deviation in the air (C_0) and the specific activity of gamma (A_s) of ^{238}U (^{226}Ra), ^{232}Th , and ^{40}K was measured using two techniques (CR-39 and NaI (TI) detector - digital spectrum analyzer [DSA]) for

ARO-The Scientific Journal of Koya University
Volume VI, No. 2 (2018), Article ID: ARO.10381, 6 pages
DOI: 10.14500/aro.10381

Received 08 March 2018; Accepted: 15 August 2018

Regular research paper: Published 21 September 2018

Corresponding author's, e-mail: adel.hossien@univsul.edu.iq

Copyright © 2018 Adil M. Hussein. This is an open-access article distributed under the Creative Commons Attribution License.



the collected samples. The potential radiological hazards of radon associated with those materials (sand and pebble) were calculated such as annual radon effective dose ($D_{ann(Rn)}$) and radon mass exhalation rate (E_M). In addition, the gamma dose parameters were calculated as such the radium equivalent (Ra_{eq}), the gamma dose rate (H), the annual effective dose rate (H_{ann}), and the gamma hazard index (I). Unfortunately, according to our knowledge, there are no sufficient data in the literature on natural radioactivity levels (specific activity of gamma, radon concentration) in sand and pebble used in building materials in the studied area.

II. EXPERIMENTAL METHOD

The samples (sand and pebble) were collected from their selling places of Sulaymaniyah city, Iraq. The selling places bring sand and pebble from their screening factories, these screening factories are established near the different rivers and streams, covered the area of about 3300 km². The rivers and stream discharge in a two main lakes Dukan and Darbandikhan located in Sulaymaniyah Governorate.

A. Geological description

radon concentration in the sediment river can be predicted by studying the lithology and depositing the weathering part of the sample. The previous study classified the samples (Table I) used in this work as can be seen elsewhere (Kamal, et al., 2011).

B. Radon concentration and exhalation measurement

the passive (SSNTD) detector uses in a wide range of long-term measuring of radon in the worldwide, the previous researchers used it for different purposes as mentioned in Nisha, et al., 2016; Ajay, 2015; and Nguyen, et al., 2005. Eight different types of sediment samples, sand and pebble, were collected from their selling places in Sulaymaniyah city - Iraq to study their radionuclide concentrations. At the laboratory, samples were grinded and sieved with size 1 mm to homogenize their particles and then dried at 110°C temperature in an oven to eliminate the water content. Equal amount of samples (100 g) was placed in the Can – chamber (cylinder chamber), of 7.2 cm diameter by 28.5 cm height as shown in Fig. 1. CR-39 plastic track detector (1 cm × 1.5 cm) was suspended to the selling of Can – chamber, CR-39 made by Track Analysis Systems Ltd - Bristol, United Kingdom. Sufficient pieces of CR-39 detectors were calibrated using standard alpha emitter source (²⁴¹Am) to obtain a linearity response process, fully detail can be seen elsewhere (Kamal, 2013).

The Can_ chambers were sealed tightly with a thick tape to prevent gas escape and then stored for 60 days to obtain radioactive equilibrium between ²²⁶Ra and its decay products of short half-life, and to reduce statistical error while the alpha particles track the detector, can be seen elsewhere (Al-Sharkawy, et al., 2012). The detectors were etched chemically using 6.25 M of NaOH at 70°C for 6 h, to enlarge the alpha tracks. Etched detectors were washed and then dried. The radon

TABLE I
LITHOLOGY DESCRIPTION OF SAND AND PEBBLE SAMPLES (KAMAL, ET AL., 2011)

Samples	Geological composite
Chwarqurna (Pebble)	Dolomite (limestone), some chert (silica)
Darbandikhan (Pebble)	Chert, limestone, igneous
Darbandikhan (Sand)	Chert, limestone, minor igneous
Goptapa (Pebble)	Chert, limestone, some igneous
Goptapa (Sand)	Chert, limestone, minor igneous
Qaladize (Sand)	Igneous, metamorphic, limestone, few chert
Qaladize (Pebble)	Few igneous, chert, limestone
Kani Bee (Sand)	Some igneous, chert, limestone
Said Sadiq (Sand)	Organic-rich limestone, some chert
Sharbazher (Sand)	Chert, limestone, few igneous
Tanjaro (Sand)	Limestone, chert, shale
Tanjaro (Pebble)	Limestone, chert, some shale

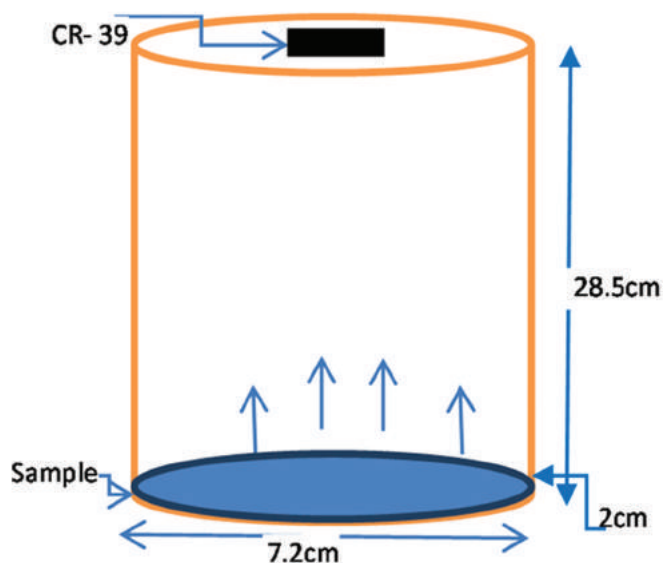


Fig. 1. Schematic diagram of closed cup tube, CR-39 detector was suspended in the upper part of it.

track density (track/cm²) on the CR-39 detectors was counted using an optical microscope (Olympus) with magnification power (×400) that is similar to the work of Kamal, 2013.

The integrated radon concentration in the air was calculated due to the measured track density of the samples of sand and pebble as given in Azam, et al., 1995,

$$\rho = K C_0 T \quad (1)$$

Where, ρ is the track density Tr/cm^2 , K is the calibration factor for cylindrical shape that equals to 0.0577 ($Tr \text{ cm}^{-2}/d/Bq \text{ m}^{-3}$). Calculation of K same as used in Kamal, 2013 and Barillon, et al., 1993. C_0 is integrated radon exposure inside the closed cup tube ($Bq \text{ cm}^{-3} \text{ h}^{-1}$) and T -radiate time (60 days).

C. Gamma emitters' measurement

the samples of sand and pebble were prepared for gamma spectroscopy measurements. The collected samples were crushed and sieved to <1 mm particle size. Each sample was

homogenized and dried for 24 h in an air circulating oven at 110°C to ensure that moisture was completely removed. About 1000 g of each sample was stored in polyethylene containers (Marinelli beaker) and sealed for 3 weeks before analyzing for ⁴⁰K, ²²⁶Ra, and ²³²Th spectrums.

The gamma spectrum analyzer (NaI (Tl) with DSA 1000) has been used as a suitable radiation measuring technique found in Ramasamy, et al., 2011; Ali, et al., 2015; and Laith, et al., 2011. The NaI (Tl) detector specified by model (3 in × 3 in) produced by Canberra industries INC., with an energy resolution of about 7.5% at the 662 keV peak of ¹³⁷Cs, the detector was interfaced to the DSA-1000 made by Canberra industries INC. The detector was surrounded by a cylindrical lead shield (10.0 cm thick and 40 cm height) fixed on steel holder and covered by a thick (5 cm) lead to reduce the background radiation. The energy calibration of the gamma spectrometry systems was carried out using standard radionuclides ¹³⁷Cs and ⁶⁰Co. Furthermore, the counting and signal process has been done for each sample in a 21,000 second period. The spectroscopy information includes count versus channel, peak searching, net peak evaluation, energy/efficiency calibration, nuclide identification, and net count area. The photopeak at 1460 KeV was used for the measurement of ⁴⁰K, whereas those at 1760 KeV peak from ²¹⁴Bi and 2614 KeV from ²⁰⁸Tl were used for the measurement of ²²⁶Ra and ²³²Th, respectively. The activity concentration (*A_s*) in Bq/kg of ²²⁶Ra, ²³²Th, and ⁴⁰K radionuclides is given by (El-Taher, 2012),

$$A_s = N / [\varepsilon_{(E_\gamma)} * P_\gamma * t * M] \quad (2)$$

Where, *N* is the net peak area of γ -ray energy (*E_γ*), $\varepsilon_{(E_\gamma)}$ is the full-energy peak efficiency for γ -rays, *P_γ* is the γ -ray yield per decay, *t* is the counting live time, and *M* is the dried sample mass in terms of kilogram.

D. Radon exhalation and dose assessment

the rectangular chamber is suitable for measuring the surface exhalation rate (*E_A*). The cylindrical chamber is suitable for measuring the radon mass exhalation rate (*E_M*) (Predrag, et al., 2010 and Sharma, et al., 2003), cylindrical chamber was used in this work; therefore, we focused on *E_M* calculation only. The *E_M* is derived from the *E_A* equation, which found in Barillon, et al., 1993, and the modified formula of *E_M* can be found in Imme, et al., 2014; Kovler, 2006; and Khan, et al., 1992 as,

$$E_M = \frac{C_0 V \lambda}{M [T + 1 / \lambda (e^{-\lambda T} - 1)]} \quad (3)$$

Here, *E_M* is the radon exhalation rate in terms of mass (Bq/kg/h), *V* is the effective volume of the Can container in m³, *C₀* is integrated radon exposure, *T* is the exposure time in hours (h), λ is the decay constant for radon (h⁻¹), and *M* is the mass of sand or pebble sample (100 g).

E. Estimation of gamma dose rate

a common radiological index has been introduced to represent the *A_s* level of ²²⁶Ra, ²³²Th, and ⁴⁰K, which is usually known as radium equivalent activity (*Ra_{eq}*) (Beretka and Mathew, 1985).

$$Ra_{eq} = A_{Ra} + 1.43 A_{Th} + 0.077 A_K \quad (4)$$

Where, *A_{Ra}*, *A_{Th}*, and *A_K* are the *A_s* of ²²⁶Ra, ²³²Th, and ⁴⁰K, respectively, in Bq/kg. In the definition of *Ra_{eq}*, it is assumed that 10 Bq/kg of ²²⁶Ra, 7 Bq/kg of ²³²Th, and 130 Bq/kg of ⁴⁰K produce equal γ -ray dose rate. The *A_s* of ²²⁶Ra, ²³²Th, and ⁴⁰K through conversion factor in units (nGy/h per Bq/kg) results *H* for different materials. According to EC-112, 1999 and Baykara, et al., 2011, the *H* is formulated for the sand and sandstone as,

$$H_{nGy/h} = 0.430 A_{Ra} + 0.666 A_{Th} + 0.042 A_K \quad (5)$$

The annual effective dose rate (*H_{ann}*) in unit (mSv/y) is an important radiation risk parameter, can be formulated from the *H* as (UNSCEAR- annexb, 2000; Caridi, et al., 2015),

$$H_{ann} (mSv / y) = H (nGy / h) * \frac{8760h}{yr} * 0.7 Sv / Gy * 10^{-6} = 0.006132 * H (nGy / h) \quad (6)$$

Where, the number 0.7 (Sv/Gy) is a conversion factor.

Radiation hazard was determined by a hazard index (*I_γ*) of gamma, the maximum range of them was 1 mSv/y. *I_γ* is expressed in terms of the specific activities of ²²⁶Ra, ²³²Th, and ⁴⁰K, and their conversion factors were evaluated in EC,1999 and UNSCEAR, 1993,

$$I_g = \frac{A_{Ra}}{300 B_q / k_g} + \frac{A_{Th}}{200 B_q / k_g} + \frac{A_K}{3000 B_q / k} \quad (7)$$

TABLE II
RADON CONCENTRATIONS IN AIR (C0) IN UNIT , RADON MASS EXHALATION (EM) IN UNIT (BQ/Kg/h), THE RADON EFFECTIVE DOSE (D_{EFF (RS)}) IN UNIT nGY/H, AND ANNUAL EFFECTIVE DOSE (D_{EFF (RS)}) OF RADON IN UNIT MSV/Y OF THE SAND AND PEBBLE SAMPLES WERE CALCULATED

Samples	ρ (Track/cm ²)	C ₀ (Bq/m ³)	E _M (μBq/kg/h)
Chwarqurma (Pebble)	503.04	138.27±6.16	8.6±0.4
Darbandikhan (Pebble)	503.04	138.27±6.16	8.6±0.4
Darbandikhan (Sand)	786	216.06±7.70	13.5±0.5
Goptapa (Pebble)	848.88	233.34±8.00	14.5±0.5
Goptapa (Sand)	345.84	95.06±5.11	5.9±0.3
Qaladize (Sand)	786	216.06±7.70	13.5±0.5
Qaladize (Pebble)	314.4	86.42±4.87	5.4±0.3
Kani Bee (Sand)	848.88	233.34±8.01	14.5±0.5
Said Sadiq (Sand)	534.48	146.92±6.35	9.2±0.4
Sharbazheer (Sand)	597.36	164.20±6.71	10.2±0.4
Tanjaro (Sand)	943.2	259.27±8.44	16.2±0.5
Tanjaro (Pebble)	691.68	190.13±7.23	11.9±0.5
Mean value	641.9	176.45±6.87	10.9±0.46

III. RESULTS AND DISCUSSION

A. Radon measurements

The integrated radon concentration in the air (C_0) \pm deviation can be calculated via Eq. 1, and radon mass exhalation rate (E_M) from Eq. 3. The C_0 value was ranged between 86.4 ± 4.9 and 259.3 ± 8.4 Bq/m³ as shown in Table II. The mean value of C_0 is lower than the worldwide value of 300 Bq/m³, which is given in IAEA, 2018. Furthermore, the C_0 value of the sand samples from the locations Tanjaro, Kani Bee, Qaladize, and Darbandikhan with Goptapa (pebble) was close to the worldwide value. However, the mentioned samples are widely used in construction materials of our governorate (area). The maximum exhaled value of radon (E_M) was 16.2 ± 0.5 (μ Bq/k_g/h) recorded in the Tanjaro (Sand) sample, and the minimum was 5.4 ± 0.3 (μ Bq/k_g/h) returned to Qaladize (Pebble), whereas the E_M mean value was 10.9 ± 0.5 (μ Bq/k_g/h). The high radon dose rate is a result of discharging sewage of Sulaymaniyah city into the Tanjaro stream, which causes to sediment the sand near the Tanjaro factory of screening sand (Rebwar, et al., 2016). This result differs from the E_M value of Tanjaro (pebble), which was much less than Tanjaro (sand) sample. The reason is that the Tanjaro screening factory (sand and pebble) established in a position of collecting most sewage of the Sulaymaniyah city. The sewage containing organic materials, these materials labeled sand particle more than the pebble one. In addition, the heavy metals Cr, Mn, Cu, and Pb were detected in the wastewater of Qalyasan stream (Salih, et al., 2014). These materials are the main sources in increasing radon concentration (Andrew, 2014 and Lookman and Ayser, 2016) because the surface area of the sand covered totally by the organic material, the ratio (surface area/mass) of the sand particle is more than the pebble one.

The mentioned radiology parameters are lower than the values recorded in most previous studies (Zakariya, et al., 2013; Mansour, 2005; and Zakariya, 2017).

B. Γ -ray measurements

Table III shows that the A_s value of ²²⁶Ra, ²³²Th, and ⁴⁰K ranged (4.3 ± 0.2 – 22.6 ± 0.2) B_q/K_g, (1.9 ± 0.1 – 4.2 ± 0.1)

B_q/k_g, and (39.8 ± 0.2 – 86.0 ± 0.4) B_q/k_g, respectively. These comparisons based on the specific activities of ²²⁶Ra, ²³²Th, and ⁴⁰K values of 50, 50, and 500 B_q/k_g, respectively, reported by the UNSCEAR, 2008.

The important radiological parameters of gamma were derived from the measured A_s such as the radium equivalent (Ra_{eq}), the gamma dose rate (H), the annual effective dose rate (H_{ann}), and the gamma hazard index (I) were tabulated in Table III. Equations (2, 4-7) were used for calculating the mentioned parameters, respectively. The mean Ra_{eq} value was 20.2 ± 0.2 B_q/k_g, which was lower than the worldwide one 200 B_q/k_g (UNSCEAR, 2008). Fortunately, the minimum value of Ra_{eq} was 7.4 ± 0.2 B_q/k_g recorded in Darbandikhan (pebble); furthermore, these raw materials are widely used in construction building in Sulaymaniyah Governorate. In addition, the mean value of I was 0.17 which is less than the unity (EC, 1999). The I value of Darbandikhan (pebble) was 0.08, whereas in Darbandikhan (sand) was 0.19, which is greater than the calculated mean value. The reason is that the heavy metals (⁴⁰K, Ti, Mn, Fe, Mg, Si, P, and Ca) were detected in the Darbandikhan dam as reported in Adeeb, et al., 2017, another fact is that the fine particles (sand) deposit faster than the coarse one (Rebwar, et al., 2016).

In addition, the mean values of the H and the H_{ann} were 21.9 nGy/h and 0.13 mS_v/y, respectively. The H_{ann} values of the samples are low than the worldwide average value of 0.48 mS_v/y (UNSCEAR, 2000 and Darwish, et al., 2015). The measured specific activity of the ²²⁶Ra value is close to the ²²⁶Ra value found in Zakariya, 2017; Kamal, et al., 2014; and Imme, et al., 2014. The measured H and H_{ann} values are lower than the values of the previous studies (Ramasamy, et al., 2011 and Ramasamy, et al., 2014). The reason is that the measured natural radionuclides dose with NaI (3X3) detector is always less than the actual value, because only three energy peaks (1460 KeV ⁴⁰K, 1760 KeV ²¹⁴Bi, and 2614 KeV ²⁰⁸Tl) of the sample spectra were calculated based on the method that allows to calculate just three energy peak of the measured spectra of the sample.

TABLE III

THE RADIUM EQUIVALENT (Ra_{eq}) ACTIVITIES IN BQ/K_g AND THE GAMMA DOSE RATE (H) IN nGy/h, THE ANNUAL EFFECTIVE DOSE RATE (HANN) IN mS_v/y AND THE HAZARD INDEX (I) OF GAMMA-RAY WERE CALCULATED BASED ON THE SPECIFIC ACTIVITIES (A_s) OF ²²⁶RA, ²³²TH, AND ⁴⁰K, FOR THE SAND AND PEBBLE SAMPLES

Sample	Specific activities (A) in B _q / k _g			²²⁶ Ra Equivalent B _q /k _g	Hazard index (I)	H (nGy/h)	H _{ann} (mSv/y)
	⁴⁰ K	²³² Th	²²⁶ Ra				
Chwarqurna (Pebble)	41.95±0.25	2.41±0.04	22.59±0.2	26.37±0.26	0.20	26.80	0.16
Darbandikhan (Pebble)	49.47±0.27	1.85±0.05	4.34±0.16	7.36±0.23	0.08	9.98	0.06
Darbandikhan (Sand)	72.62±0.31	3.57±0.05	16.33±0.17	22.00±0.25	0.19	24.76	0.15
Goptapa (Pebble)	48.74±0.27	3.02±0.05	14.61±0.16	19.31±0.23	0.16	20.67	0.13
Goptapa (Sand)	62.37±0.30	3.56±0.05	15.03±0.16	20.61±0.24	0.18	22.74	0.14
Qaladize (Sand)	85.99±0.36	4.18±0.06	17.57±0.17	24.22±0.25	0.22	27.65	0.17
Qaladize (Pebble)	52.24±0.28	3.07±0.05	14.17±0.15	18.96±0.22	0.16	20.59	0.13
Kani Bee (Sand)	67.32±0.32	3.72±0.05	16.04±0.16	21.88±0.24	0.19	24.23	0.15
Said Sadiq (Sand)	41.59±0.25	2.44±0.04	15.94±0.17	19.75±0.23	0.16	20.68	0.13
Sharbazheer (Sand)	53.88±0.28	2.99±0.05	14.63±0.16	19.31±0.24	0.16	21.05	0.13
Tanjaro (Sand)	41.15±0.25	2.62±0.04	19.48±0.19	23.55±0.25	0.18	24.10	0.15
Tanjaro (Pebble)	39.83±0.24	2.51±0.04	14.84±0.16	18.73±0.23	0.15	19.60	0.12
Mean value	54.76±0.28	2.99±0.05	15.47±0.17	20.17±0.24	0.17	21.90	0.13

IV. CONCLUSIONS

The radium isotope contributed mainly in specific activity of gamma (A_γ) in comparison with the thorium isotope. The C_o values of half of the samples were close to the worldwide value. These samples specified by high count rate are commonly used in construction materials for building in the Sulaymaniyah Governorate, Dwelling (Alsaedi, et al., 2013).

Most dwelling areas of the northern region of Iraq (Kurdistan region) are bounded by mountains. Usually, high gamma (radon) dose emanates from the houses floor of the mentioned area. Therefore, the building should contract with raw materials containing a low radon/gamma dose. Fortunately, the lowest value of H_{ann} was clarified in Table III that encourages the author to suggest that the best locations for establishing the construction material factory including Goptapa, Qaladize, and Darbandikhan areas. An anomaly in C_o value was found in Tanjaro (Sand) sample, this means that the sand sample of this Tanjaro sand screening factory is not appropriate for buildings. Therefore, the author suggests that the authorities should prevent to establish the (sand and pebble) screening factory near a stream draining of a city.

V. ACKNOWLEDGMENT

The author gratefully appreciates the support of the University of Sulaimani - Ministry of Higher Education and Scientific Research.

REFERENCES

- Adeeb, O.J., Ali, H.A., and Wan, M.S., 2017. Assessment of natural radionuclide's in sediments of Darbandikhan Lake water resources at Kurdistan Region-Northeastern of Iraq. *ZANCO Journal of Pure and Applied Sciences*, 29 (2), pp.43-52.
- Ajay, M.K., 2015. Measurement of radon exhalation rate in sand samples from Gopalpur and Rushikulya beach Orissa, Eastern India. *Physics Procedia*, 80, pp.140-143.
- Ali, A.A., Lubna, A.A., Ahmed, R.S., Faeq, A.A., and Afnan, A.H., 2015. Assessment of annual effective dose for natural radioactivity of gamma emitters in biscuit samples in Iraq. *Journal of Food Protection*, 78(9), pp.1766-1769.
- Alsaedi, A.K., Almayahi, B.A., and Alasadi, A.H., 2013. Cement ^{222}Rn and ^{226}Ra concentration measurements in selected samples from different companies. *Asian Journal of Natural and Applied Sciences*, 2(4), pp.95-100.
- Al-Sharkawy, A., Hiekal, M.T., Sherif, M.I., Badran, H.M., 2012. Environmental assessment of gamma-radiation levels in stream sediments around Sharm El-Sheikh, South Sinai, Egypt. *Journal of Environmental Radioactivity*, 112, pp.76-82.
- Andrew, J.K., Nathaniel, R.W., Ori, L., and Avner, V., 2014. Radium and barium removal through blending hydraulic fracturing fluids with acid mine drainage. *Environmental Science and Technology*, 48(2), pp.1334-1342.
- Azam, A., Naqvi, A.H., and Srivastava, D.S., 1995. Radium concentration and radon exhalation measurements using LR-115 Type II plastic track detectors. *Nuclear Geophysics*, 9(6), pp.653-657.
- Banman, A., Hervat, D.J., Lokobauer, N., 1982. *Natural Radiation Environment*. Willy R. Ltd, New Delhi.
- Barillon, R., Klein, D., and Chambandet, A.D.C., 1993. Comparison of the effectiveness of three radon detectors (LR-115, CR-39 and Si. Diode pin) placed in cylindrical device, theory and experimental techniques, nuclear track.

Radiation Measurement, 22(4), pp.281-282.

- Baykara, O., Sule, K., and Mahmut, D., 2011. Assessments of natural radioactivity and radiological hazards in construction materials used in Elazig, Turkey. *Radiation Measurements*, 46, pp.153-158.
- Beretka, J., and Mathew, P.J., 1985. Natural radioactivity of Australian building materials, industrial wastes and by-products. *Health Physics*, 48, pp.87-95.
- Brill, A.B., David, V.B., Kevin, D., Stanley, J.G., Bennett, G., Ken, K., H, R., Edward, B.S., and Edward, W.W., 1994. Concerning environmental radon (levels, mitigation, strategies, dosimetry, effects, guidelines). *Nuclear Medicine*, 35(2), pp.85-94.
- Caridi, F., Marguccio, S., Belvedere, A., and Belmusto, G., 2015. Measurements of gamma radioactivity in river sediment samples of the Mediterranean, Central Basin. *American Journal of Condensed Matter Physics*, 5(3), pp.61-68.
- Cetin, E., Yuksel, O., and Altinsoy N., 2012. Natural radioactivity levels of granites used in Turkey. *Radiation Protection Dosimetry*, 151(2), pp.299-305.
- Darwish, D.A.E., Abul-Nasr, K.T.M., and El-Khayatt, A.M., 2015. The assessment of natural radioactivity and its associated radiological hazards and dose parameters in granite samples from South Sinai, Egypt. *Journal of Radiation Research and Applied Sciences*, 8, pp.17-25.
- El-Taher, A., 2012. Assessment of natural radioactivity levels and radiation hazards for building materials used in Qassim area, Saudi Arabia. *Romanian Journal of Physics*, 57(3-4), pp.726-735.
- European Commission (EC), 1999. *Radiological Protection Principles Concerning the Natural Radioactivity of Building Materials*. Radiation Protection Report (112), Directorate General Environment, Nuclear Safety and Civil Protection, European Commission.
- Gulfink, O.M., 2008. Principal decay scheme of the uranium series. Hazards for building materials used in Qassim area. *Romanian Journal of Physics*, 57(3-4), pp.726-735.
- Imme, G.R., Catalano, G., and Mangano, D.M., 2014. Radon exhalation measurements for environmental and geophysics study. *Radiation Physics and Chemistry*, 95, pp.349-351.
- Kamal, H.K., Hemin, K., Mushir, M.B., and Khaled, H., 2011. Significance of angular unconformities between Cretaceous and tertiary strata in the northwestern segment of the Zagros fold-thrust belt, Kurdistan Region, NE Iraq. *Geological Magazine*, 148(5-6), pp.925-939.
- Kamal, K.A., Salih, M.A., and Muhanned, R.A., 2014. Assessment natural radioactivity of marl as raw material at Kufa cement quarry in Najaf Governorate. *Iraqi Journal of Science*, 55(2A), pp.454-462.
- Kamal, O., 2013. *Natural Radioactivity Measurements of Soil and Water in Sulaimani Governorates*. Doctoral dissertation, PhD Dissertation, University of Sulaimani, Iraq.
- Khan, A.J., Rajendra, P., and Tyagi, R.K., 1992. Measurement radon exhalation rate from some building materials. *International Journal of Radiation Applications and Instrumentation Part D*, 20(4), pp.609-610.
- Kovler, K., 2006. Radon exhalation of hardening concrete: Monitoring cement hydration and prediction of radon concentration in construction site. *Journal of Environmental Radioactivity*, 86, pp.354-366.
- Laith, A.N., Firas, M.A., and Enas, M.A., 2011. Natural radioactivity levels of limestone rocks in northern Iraq using gamma spectroscopy and nuclear track detector. *Journal of Radioanalytical and Nuclear Chemistry*, 289, pp.709-715.
- Lookman, M.M.G., Ayser, M.A., 2016. Suspended Sediment concentration and stream discharge relationship during storm events in tributaries of smaqli stream, Erbil, Iraq. *Iraqi Journal of Science*, 57(3A), pp.1748-1758.
- Mansoor, H.H., Khdar, S.P., Abdulla, H.Y., Muhamad, N.Q., Othman, M.M., and Qader, S., 2005. Measurement of indoor radon levels in Arbil by using solid state nuclear track detectors. *Radiation Measurement*, 40, pp.544-547.
- Public Health Fact Sheet on Radon-Health and Human Services*, 2011.

Available from: http://www.massgroupholding.com/English/unit_real.aspx?cor=3&title=Cement

Nguyen, D.C., Edward, C., and Lukasz, P., 2005. Factors controlling measurements of the radon mass exhalation rate. *Journal of Environmental Radioactivity*, 82, pp.363-369.

Nisha, M., Amit, K., Sushil, K., and Chauhan, R.P., 2016. Measurement of indoor radon - Thoron in air and exhalation from soil in the environment of western Haryana, India. *Radiation Protection Dosimetry*, 171(2), pp.248-253.

Poschl, M., 2007. *Radionuclides Concentration in Food and the Environment*. Taylor and Francis Group, USA.

Predrag, U., Igor, C., Aleksandar, K., Ivana, V., Mirjana, U.S., Du, D., and Zora, S.Z., 2010. Internal exposure of building materials exhaling ^{222}Rn and ^{220}Rn as compared to external exposure due to their natural radioactivity content. *Applied Radiation and Isotopes*, 68, pp.201-206.

Ramasamy, V., Paramasivam, K., Suresh, G., and Jose, M.T., 2014. Role of sediment characteristics on natural radiation level of the Vaigai river sediment, Tamilnadu, India. *Journal of Environmental Radioactivity*, 127, pp.64-74.

Ramasamy, V., Suresh, G., Meenakshisundaram, V., and Ponnusamy, V., 2011. Horizontal and vertical characterization of radionuclides and minerals in river sediments. *Applied Radiation and Isotopes*, 69, pp.184-195.

Rebwar, H., Nadhir, A., Salahalddin, S.A., Ammar, A.A., Twana, A., and Sven, K., 2016. Dukan dam reservoir bed sediment, Kurdistan Region, Iraq. *Engineering*, 8, pp.582-596.

Salih, N.M., Ahmed, I.K., Ghafour, A.M.R., and Zana, H.A., 2014. Bioaccumulation, enrichment and translocation factors of some heavy metals in *Typha angustifolia* and *Phragmites australis* Species growing ALONG Qalyasan stream in Sulaimani City/IKR. *Journal of Zankoy Sulaimani- Part A*, 16(4), pp.93-109.

Sharma, D.K., Ajay, K., Mukesh, K., and Surinder, S., (2003) Study of uranium, radium and radon exhalation rate in soil samples from some areas of Kangra district, Himachal Pradesh, India is using solid-state nuclear track detectors. *Radiation Measurements*, 36, pp.363-366.

Turhan, S., 2008. Assessment of the natural radioactivity and radiological hazards in Turkish cement and its raw materials. *Journal of Environmental Radioactivity*, 99(2), pp.404-441.

Turhan, S., and Varinliog, I.A., 2012. Radioactivity measurement of primordial radionuclides in and dose evaluation from the marble and glazed tiles used as covering building materials in Turkey. *Radiation Protection Dosimetry*, 151 (3), pp.546-555.

United Nations Scientific Committee on the Effects of Atomic Radiation (UNSCEAR), 1993. *Sources and Effects of Ionizing Radiation*. Report to the General Assembly, Scientific Committee on the Effects of Atomic Radiation, United Nations, New York.

UNSCEAR., 2008. *Sources and Effects of Ionizing Radiation*, Scientific Committee on the Effects of Atomic Radiation, Session, 63 (46), United Nations, New York.

UNSCEAR-annexb., 2000. *Sources and Effects of Ionizing Radiation*. Report to the General Assembly, with Scientific Annexes, Vol. 2, United Nations, New York.

Zakariya, A.H., 2017. Measurement of radon exhalation rate and radium activity from building material samples used in Erbil, Iraqi Kurdistan. *ZANCO Journal of Pure and Applied Sciences*, 29(4), pp.154-160.

Zakariya, A.H., Mohamad, S.J., Asaad, H.I., and Ammar, A.B., 2013. Radon exhalation rate from building materials using passive technique nuclear track detectors. *International Journal of Scientific and Engineering Research*, 4(7), pp.1276-1281.

Load Balancing Evaluation Tools for a Private Cloud: A Comparative Study

Sahand Kh. Saeid and Tara Ali Yahiya

Department of Computer Science and Engineering, School of Sciences and Engineering,
University of Kurdistan Hewler, 30 Meter Avenue, Erbil, Kurdistan Region - F.R. Iraq

Abstract - Cloud computing turns out to be an emerging technology that revolutionized the world of IT infrastructure. However, since the number of users is increasing daily, the demand for cloud services is increasing too. Thus, congestion occurs on the servers that provide services in the cloud. To avoid congestion, we used load balancer tools such as HAProxy and Nginx to intercept the requests of users and distribute them evenly to the servers. Jmeter is used to measure the performance metrics of least connection algorithm in terms of CPU utilization, response time, and concurrency level. Results showed high performance of HAProxy compared to Nginx in terms of response time and treating requests. Furthermore, we examined the characteristic of availability of the load balancer through deploying redundant load balancers, and we studied the effect of the failure of the load balancer on the quality of service of the end users. Keepalived is used to ensure a smooth transition between the two load balancers. According to the concurrency level, results proved that the number of unsuccessful requests during the failure of the master load balancer is proportionally minuscule compared to the total number of requests sent in a normal situation.

Index Terms—Cloud computing, Least connection algorithm, Load balancing.

I. INTRODUCTION

Recently, cloud computing became one of the hottest topics in the technology field. It has a powerful impact on the industry and its business. The difference between cloud computing and traditional computing is that cloud computing reduces expenses by eliminating hardware, consuming less power, and minimizing the space of utilization (Kashyap and Viradiya, 2014). One of the major problems of cloud computing is the loss of control where users do not know where and how their data are stored and processed, for a normal user this may not be a big problem, but for an organization, it is very critical and can have a huge impact on it if the data are not in the right

hands. This problem will definitely not occur in a private cloud environment, which is one of the models of cloud computing where a specific user can work in a virtual environment, bearing in mind that a private cloud is used for internal use just like the case of a small company or an enterprise (Luís, 2016). In the past few years, more than 60% of the IT industries have implemented a private cloud as their own paradigm for storage and computation (Luís, 2016). Private cloud provides computing resources such as servers, storage, and applications as services in a virtualized environment from a pool of computing resources. When the number of users who accesses these resources increases, congestion may occur, this would cause the servers to be overloaded, and then in the worst case, this can cause a failure of the servers. The load here can be represented by the number of connections, though the need of balancing loads among the nodes of cloud computing is emerging. That is why in many organizations they use a load balancer in their environment to distribute the requests among the servers so they will not be overloaded and the resources will be used efficiently (Gupta and Beri, 2016). The aim of this article is to first implement a private cloud environment using Linux based operating system (OS) and other open source tools that are used in every organization without much cost. Within the private cloud, two types of load balancing tools are installed to distribute the traffic among three servers, in our case; we selected the case of web servers. The performance of these tools was tested and evaluated by some load tester tools. The performance parameters that are used to evaluate and compare both load balancers tools are CPU utilization, number of requests, response time, and number of failed requests. Furthermore, high availability of two load balancers is also tested and investigated through the article.

This article is organized as follows: Section 2 presents the state of the art of load balancing tools and their implementation, section 3 presents the implementation environment and the numerical results obtained from the load balancer tools and performance metrics, and section 4 concludes the article.

II. STATE OF THE ART

Load balancer is one of the main components of cloud computing, and it is responsible for keeping the system stable and working efficiently when the load is increasing along with providing high available service in ubiquitous way.



To implement a load balancer in the cloud, it is essential to install tools that act as a load balancer, and it may provide some options for algorithms of load balancing. In general, in such kind of context, there is almost only one method to test the performance of a load balancer algorithm (as depicted in Fig. 1). The method starts with generating loads in terms of requests to some servers in the cloud, that is, web server and database server. The load generation can be done through a tool for generating requests. Then, the requests will travel through the internet to the cloud (Qasmi, et al. 2018). These requests will be intercepted by the load balancer (after for sure some security control) where all the algorithms are implemented. According to the design of the algorithm, the requests will be forwarded to the proper servers (Madani and Jamali, 2018). The main problem is how to test the performance of a load balancer through some tools to decide whether or not the load balancer is meeting the requirements of stability and high availability.

Faizal, 2017, used an algorithm called least time first-byte algorithm (LFB) and combined it with multi-agent system in distributed load balancing, the agent is responsible for collecting information about resources on the backend servers, this information is then combined with the LFB algorithm, they called it LFB with multi-agent system (LFB-MAS). The results showed that this load balancing algorithm provides better performance for all the servers. The LFB-MAS received 100% of the 1,800 requests, where other algorithms like weighted least connection are only capable of receiving 74,50% from the 1,800 requests and LFB without agent could only receive 75,61% of the 1,800 requests. They could prove that this algorithm is reliable and can handle a high number of requests.

Pi'orkowski, 2010, reviewed some of the load balancing algorithms such as Round Robin (RR), weighted RR, least connection, request counting, and many others. They used some load balancing tools such as Apache web server, Nginx, HAProxy, Inlab, and Lighttpd. Once results are obtained, it was proven that the use of load balancers increase the system throughput effectively. The best results for load balancing tools are Inlab and Lighttpd with the Shortest Queue First algorithm and Apache web server with Pending Request Counting algorithm. As for the other tools such as HAProxy and Nginx with RR, the throughput was slightly lower; the worst results were achieved by load balancers with Source Hashing and Destination Hashing algorithms. Authors proved that the combination between the tool and the algorithm play an important role to reach the highest performance level of web server clustering.

In Kovari, 2012, the authors compared two virtualization platforms, the first one is OpenNode which is an open source CentOS based server virtualization and management solution, and the other one is Proxmox VE that is a tweaked Debian distribution with a custom optimized kernel. According to their results, Proxmox proved to be better than OpenNode ten times regarding the speed of treating the requests. As well, some technical aspect of both platform were investigated. For example, Proxmox uses unique virtualization API, but on the other hand, OpenNode is based on libvirt which supports

several types of virtualization solutions. Proxmox can use a web interface to manage the virtual machines (VMs) as a cluster, but it has also some drawbacks such as outdated or non-existing templates. If in the future OpenNode gets important features such as PXE, high availability clustering, and network management support then it would be a good choice over Proxmox, but for now, Proxmox is a better option.

Sharma and Iyer, 2016, focused on comparing four load testing tools, WebLOAD, Apache Jmeter, HP Load Runner, and the Grinder. The primary objective of their paper is to study these load testing tools and select the best tool among them. They used some parameters to evaluate the tools such as unlimited load generation, server monitoring, ease of use, and cost. It is concluded that Load Runner has many great and strong features, but to use this features, the license should be purchased with a high cost. As for grinder, and according to the test performed by the author, it showed that it cannot deal with the large request and it is vulnerable to failure. While in WebLOAD, the users can simulate many different systems and connection configurations to create a single test script with many IP protocols, and it supports JavaScript. In Jmeter less technical skills are required, and it has availability of startup scripts and availability in the user interface, but in the UI it has limited feedback, and it also has some memory problems when downloading files that have a very large size. At the end of their comparison, the authors selected Jmeter as the better tool among the other tools since it is free has good load generation and its UI is easy to use.

Widianto, 2016, implemented a system with HAProxy load balancer and used heartbeat as a tool to ensure high availability of the HAProxy load balancers. They installed three web servers and two HAProxy servers for testing the failover. Httperftool is used for load testing, two scenarios with and without load balancer were created and tested. Through the implementation, it is observed that it took around 10 ms to activate the backup load balancer during the failure of the main load balancer, and during that time a number of requests will fail, and this number varies among different algorithms. For example, the least connection algorithm outperformed the RR and source algorithm in terms of response time, throughput, connection rate, and failed connections.

In our work, we implement first the environment of a private cloud with its two parts, the physical and the virtual

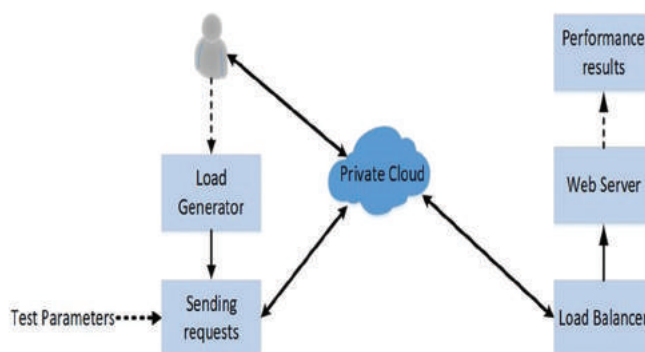


Fig. 1. Load generating architecture.

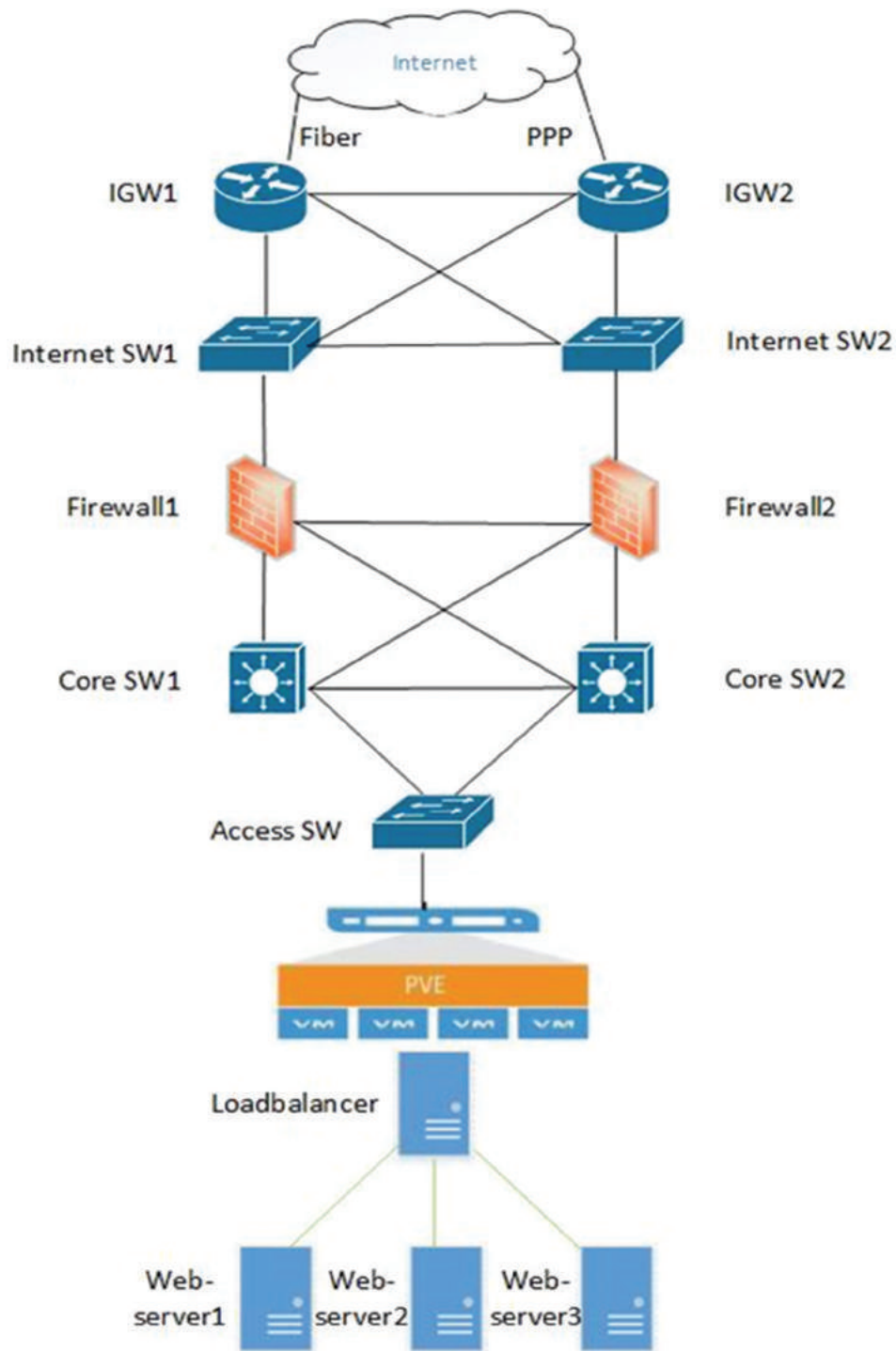


Fig. 2. Cloud computing architecture.

one. The main difference between our work and the other literature work is that the architecture used to evaluate the load balancer is a real one used for a medium size company. As well, according to the conclusion of the other work, we used HAProxy and compared it with Nginx to investigate the performance of both of them within the physical architecture. The main objective of this paper is to prove that we can build a private cloud with an open source system including the OS, the virtualized platform, and the software tools used to simulate the load balancer algorithms with less cost, more

efficiency, and more stable system.

III. IMPLEMENTATION ENVIRONMENT AND RESULTS

A. The physical part of the private cloud

The architecture that we have implemented for cloud computing is composed of Internet Gateway to connect the network of the company to the exterior world; they are connected to two Internet Switches which are connected in their turn to the firewalls in which all security rules

are implemented. The firewalls are connected to the Core Switches to create the core network of the company. Note that all the devices are redundant to ensure the connectivity and availability of the whole architecture.

B. The virtual part of the private cloud

Our private cloud consists of one physical server where Proxmox is installed, Proxmox is a platform of virtualization that can simulate a private cloud with less physical resources (Proxmox, 2018). 6 VMs are created in this platform each VM is dedicated to a different purpose as shown in Table 1.

The first three VMs have Apache installed onto work as web servers, they have the same hardware specifications, but the only difference is that two of them have the Ubuntu desktop OS and the third one has Ubuntu server OS. The purpose of having different OSs is to study the performance comparison between the desktop and the server version of Ubuntu (Apache, 2018). The fourth and fifth VMs in the table have HAProxy installed on, each acts as a separate load balancer but the reason of having two HAProxy servers is because Keepalived (Keepalived is a routing software that can be used for high availability by assigning a virtual IP to two or more servers and monitoring the servers, when one server fails it will automatically change to the other active server) (Keepalived, 2018) is installed between them, hence they have high availability in case of a failure of one of them. The virtual IP that Keepalived assigned to them is 192.168.100.50, this will be further discussed in the coming sections of the scenarios. The sixth and the last VM has Nginx installed on; it is the second load balancer; thus, we can have a comparison between Nginx and HAProxy in one of the following scenarios. Fig. 3 shows the scheme of the whole work.

Performance metrics

In load testing, performance metrics are a significant measure of the degree to which a process, system, or component obtains a given attribute. In other words, metrics can help to estimate the progress and health of a system. Each resource that can be monitored for availability, performance, reliability or any other attribute has many metrics which data can be collected from. The data of the following metrics are collected in our environment (Mustafa, 2017):

- Number of completed requests: It is the number of requests that are sent and received without failure in a given amount of time.
- Requests per second: It is the number of requests sent and received during a second, the higher the handled number of

requests the better the performance of the server, that is, the server is faster than a server with a lower number of requests per second.

- Response time (ms): It is also known by latency, it is the total amount of time it takes a request to travel across a network path from the sender to the receiver, it is the sum of waiting time and the replying time.
- Time per request: Is the amount of time each request is served, for a very efficient server the time per request should be very short, most of the time it should be less than seconds.
- CPU usage: It is the amount of load handled by the CPU, the CPU usage differs from the types of the tasks that are

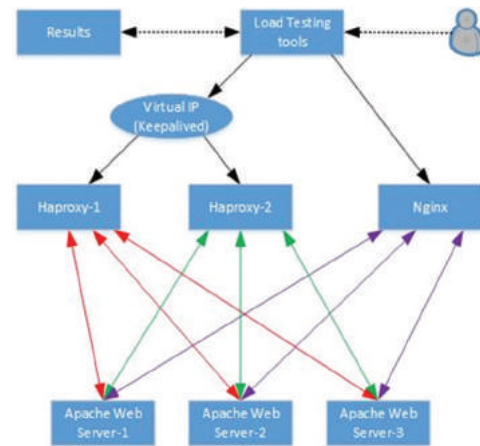


Fig. 3. Working scheme.

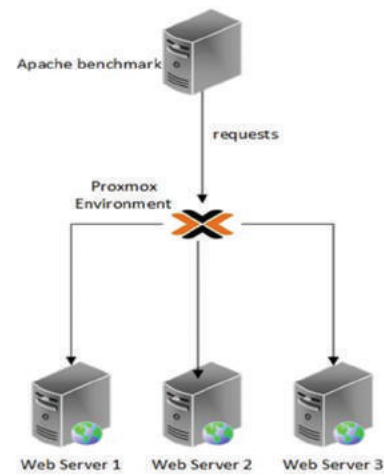


Fig. 4. No load balancer scenario.

TABLE I
VM'S IN THE PRIVATE CLOUD

No.	Name	IP address	OS	RAM	CPU in Core	Hard drive	Type of server
1	Proxmox pve	192.168.100.100	Proxmox ISO	24GB	8	8.7TB	Physical
2	Apache-webserver-1	192.168.100.31	Ubuntu desktop	2-4GB	8	50GB	Virtual
3	Apache-webserver-2	192.168.100.34	Ubuntu desktop	2-4GB	8	50GB	Virtual
4	Apache-webserver-3	192.168.100.35	Ubuntu server	2-4GB	8	50GB	Virtual
5	HAProxy-1	192.168.100.33	Ubuntu desktop	16GB	8	100GB	Virtual
6	HAProxy-2	192.168.100.32	Ubuntu desktop	16GB	8	100GB	Virtual
7	Nginx	192.168.100.40	Ubuntu desktop	16GB	8	100GB	Virtual

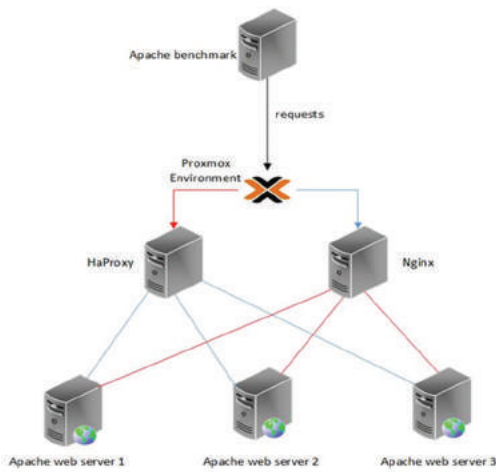


Fig. 5. Load balancer scenario.

```

Server Software: Apache/2.4.18
Server Hostname: 192.168.100.33
Server Port: 80

Document Path: /
Document Length: 11295 bytes

Concurrency Level: 100
Time taken for tests: 3.124 seconds
Complete requests: 10000
Failed requests: 0
Total transferred: 115481896 bytes
HTML transferred: 112950000 bytes
Requests per second: 3201.01 [#/sec] (mean)
Time per request: 31.240 [ms] (mean)
    
```

Fig. 6. HAProxy results.

```

Server Software: nginx/1.10.3
Server Hostname: 192.168.100.40
Server Port: 80

Document Path: /
Document Length: 11295 bytes

Concurrency Level: 100
Time taken for tests: 3.297 seconds
Complete requests: 10000
Failed requests: 0
Total transferred: 115471652 bytes
HTML transferred: 112950000 bytes
Requests per second: 3032.79 [#/sec] (mean)
Time per request: 32.973 [ms] (mean)
    
```

Fig. 7. Nginx results.

performed by the processor, most of the time the usage is very low as most of the applications do not use much of the CPU, however, for a web server which many users have access to it, the load can increase and the CPU usage will increase to a very high amount.

- Number of failed requests: It is the number of requests that failed to reach the destination or failed to get back to the sender due to various reasons, for example, the destination server was down, so the request was lost.
- Concurrency level: It is the number of concurrent users involved in the test (Apache, 2018).

Performance analysis for the studied scenarios

In this section, three scenarios will be discussed which were tested in the environment.

- The first scenario where the Apache web servers without any load balancers is implemented.
- The second scenario includes load balancers deploying least connection algorithm within the load balancer, both first and

second scenario is compared.

- The third scenario is about testing the high availability of HAProxy to see how it performs and its effects on the environment during a failure of the master node.

No load balancer scenario

In this scenario, there are no load balancers installed there are only three separated Apache web servers with the same specifications except the OS type. The diagram of this scenario is shown in Fig. 4.

The tests are done with Apache Benchmark with 100,000 requests and a concurrency of 300 and 700 the results are shown in Table 2.

The two Apache web servers that are installed on Ubuntu desktop VMs have almost the same output, they finished almost at the same time, and the server requests per second is almost the same, however, the Apache web server that is installed on Ubuntu Server VM performs almost half of the other two as it can be seen from the results. The CPU usage of all three servers is very high especially the third one, but this is normal because without a load balancer there is a high number of requests on each server and that puts a lot of pressure on them that is why having a load balancer is recommended.

Comparative scenarios

In this scenario two separated load balancers are installed, the first one is HAProxy and the second one is Nginx as shown in Fig. 5, on both of them the least connection algorithm is used because, it is a semi-static algorithm, besides there are a lot of work done on the other algorithms such as RR and source that is why least connection is selected in this article. We will generate load on each of them with Apache benchmark through six different tests to get the most accurate data from both. The first three tests will be based on the concurrency level which will start with 100, 300, and 500 with a request number of 10,000 for each. The past three tests will be based on a specific time starting from 60 to 120 and 200 s to see how many requests the load balancers can handle in a given time and how much the response time will be.

Low load scenario

The first test starts with a request number of 10,000 with a concurrency level of 100. The output of the test is shown for HAProxy in Fig. 6 and Nginx in Fig. 7.

As it can be seen from the results that HAProxy finished the test in 3.124 s which is slightly faster than Nginx, the reason behind that for each request it took HAProxy 31.240 ms compared to the 32.973 ms of Nginx and in each second HAProxy served 3201 requests where Nginx only served 3032 requests in a second. However, the CPU utilization of Nginx is around 20% which is much lower than the CPU utilization of HAProxy where it is around 50%, but the CPU utilization for the Apache web servers is almost the same in both load balancers. The same test was done again, but this time the concurrency is increased to 300, and again HAProxy was faster in serving the requests and finishing the test, and Nginx CPU utilization is 40% that is lower than HAProxy which

used 82%. In the third test, the concurrency was increased to 500, but this time Nginx could not even handle this high number of requests see the error message received in Fig. 8.

The reason is due to that Nginx has limited capacity in handling a high number of requests; however, it can be fine-tuned to make it possible to handle this number of requests or Nginx plus can be used which is another version of Nginx that has much more features, but it is not free and needs to be purchased.

High load scenario

The first test takes 60 s as it can be shown in Fig. 9.

HAProxy serves more requests and the response time is less than Nginx, from the beginning the response time on both load balancer is almost the same but during the final seconds of the test, the response time in Nginx is increasing to a high number. The same can be seen in the next two tests; the only difference is that the longer the test it takes the gap between the served requests becomes larger as shown in Figs. 10 and 11.

High availability scenario

In this scenario, two HAProxy load balancers are installed for high availability through the Keepalived tool which assigned a virtual IP to them and assigned master role to the first load balancer and backup role to the second load balancer as can be shown in Fig. 12.

There are three tests done with Jmeter tool in each of them the number of samples is increased to see whether there will be a loss of packets or not and if there are a loss how many packets will be lost and how long it takes until the backup server becomes the master. The first test is done using 1,000 samples, the second is done with 10,000 samples, and the last one is done with 100,000 samples. Whereas Fig. 13 depicts in each test a number of samples failed during the time, the master server was down until the backup took its place (Jmeter, 2018).

In the first test from 1,000 samples, 300 samples failed that is 30% from all the samples, it took only 2 s until the second server becomes the master. In the second test from 10,000 samples, 4,000 samples failed which is equivalent to 40%, and it also took around 2 s. In the last test 11,000 samples failed in 2 s from the 100,000 samples that are a percentage of 11%. As the results show a high number of samples fail in each test, of course, this is a high risk for organizations to loss this amount of requests if one of their load balancers is down, but during all the three tests, it took

only around 2 s until the backup server took over and in real life this amount of time is not much and won't affect the users experience as they almost won't notice it.

CONCLUSION

This work investigates the performance of some load balancing tools in the environment of cloud computing where the congestion is one of its main problems. The implemented algorithm by these tools was the least connection algorithm. This algorithm was tested through the use of HAProxy and Nginx tools to examine its behavior and to study the feasibility of both tools to provide a stable system even when it receives a high number of requests.

We tested the environment through implementing two scenarios; with and without load balancer to show the effect of the absence of load balancing in a system that changes the status from low load to high load in terms of the number of requests. This article proved that installing a load balancer is mandatory so that the servers in the private cloud will not be overloaded and the resources will be used very efficiently. Furthermore, it is concluded during the implementation and the test that HAProxy is faster than Nginx in serving the requests, but on the other hand, Nginx has less CPU utilization. It is also observed that during a failure of the master server, the load balancer loses some requests but the time during which the backup server becomes the master one is too short in a way that it can

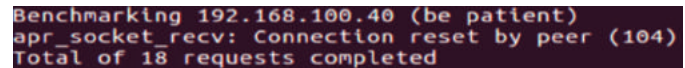


Fig. 8. Nginx error.

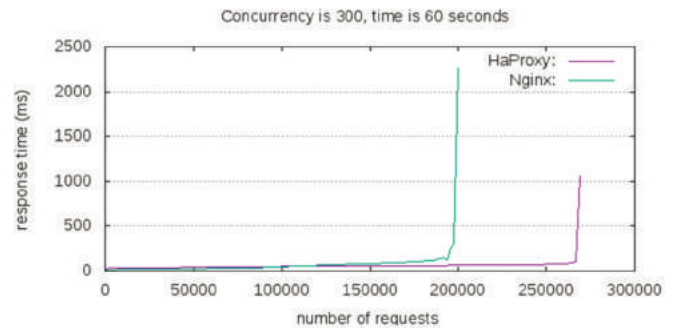


Fig. 9. Concurrency 300, time 60 s.

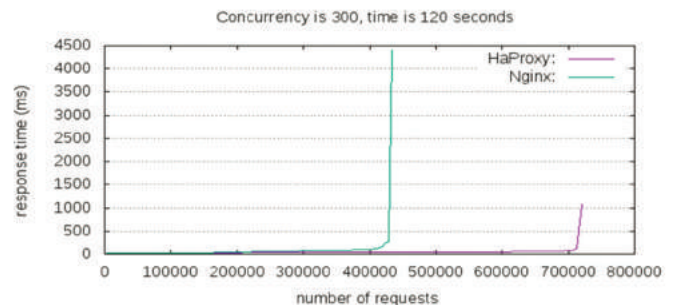


Fig. 10. Concurrency 300, time 120 s.

TABLE II
TEST RESULTS

1-100,000 requests with a concurrency of 300				
Apache servers	OS installed	Requests per second	Time taken	CPU usage %
Webserver-1	Ubuntu desktop	7270.82	13.754	94
Webserver-2	Ubuntu desktop	7710.43	12.965	93
Webserver-3	Ubuntu server	4298.58	23.285	233
2-100,000 requests with a concurrency of 700				
Webserver-1	Ubuntu desktop	7025.11	14.235	96
Webserver-2	Ubuntu desktop	7198.24	13.516	96
Webserver-3	Ubuntu server	3296.34	31.216	250

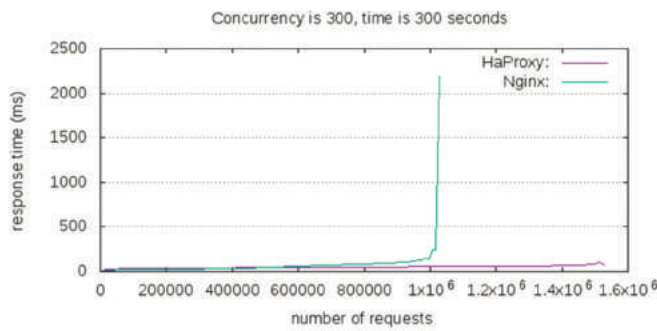


Fig. 11. Concurrency 300, time 300 s.

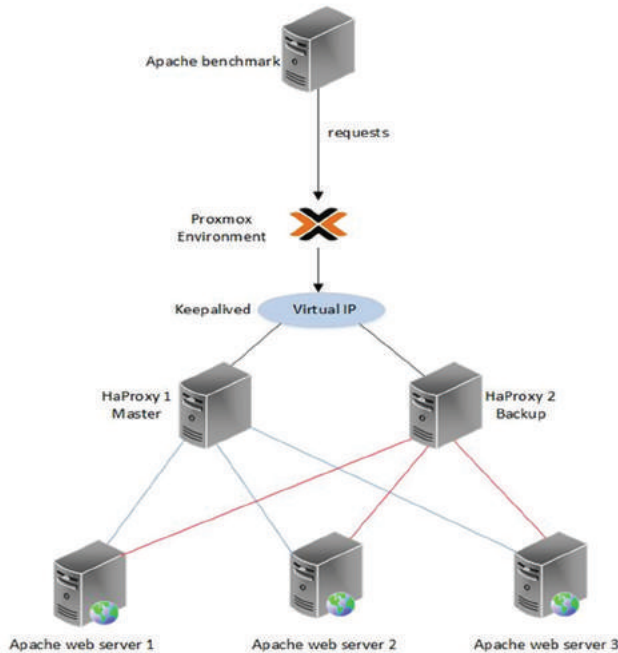


Fig. 12. HAProxy high availability scenario.

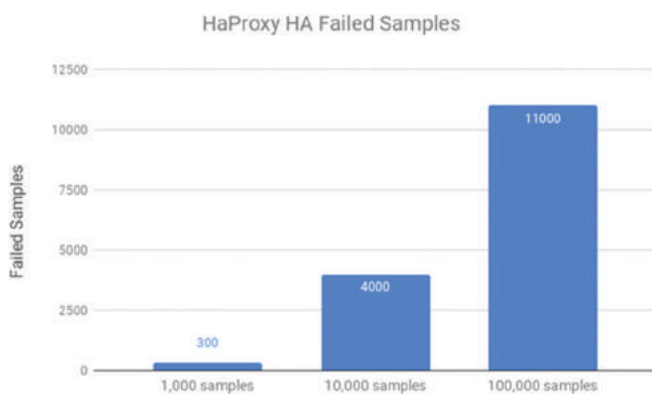


Fig. 13. Number of failed samples.

be considered as transparent for the users who are making requests, as they do not feel it especially that non real-time application is considered in such scenario. As a conclusion, the disruption time is not violating the QoS requirements of the users involved in the test.

For our future work, many other aspects should be investigated, for example, implementing a dynamic load

balancing algorithm to study its performance compared to the static one indifference system conditions.

REFERENCES

Afriansyah, M.F., Somantri, M. and Riyadi, M.A., 2017. Sistem Load Balancing Menggunakan Least Time First Byte dan Multi Agent System. Available from: <http://www.ejnteti.jteti.ugm.ac.id/index.php/JNTETI/article/view/331>. [Last accessed on 2018 May 03].

Luis, B.A., 2016. Implementation of a Private Cloud. Faculdade Ciencias Tecnologia Universidade Nova Lisboa, Master thesis. Available from: https://www.run.unl.pt/bitstream/10362/20248/1/Alves_2016.pdf.

Apache., 2018. The Apache HTTP Server Project. Available from: <https://www.httpd.apache.org/download.cgi>. [Last accessed on 2018 Mar 03].

Gupta, K. and Beri, R., 2016. Cloud Computing: A Survey on Cloud Simulation Tools. Available from: <http://www.ijirst.org/articles/IJIRSTV2I11180.pdf>. [Last accessed on 2018 May 09].

Jmeter., 2018. Apache Jmeter. Available from: <https://www.jmeter.apache.org>. [Last accessed on 2018 Mar 10].

Kashyap, D. and Viradiya, J., 2014. A Survey of Various Load Balancing Algorithms in Cloud Computing. Available from: <https://www.pdf.semanticscholar.org/370a/4ee7ea3e85cac3565ef44485393d27c63075.pdf>. [Last accessed on 2018 May 04].

Keepalived., 2018. Keepalived for Linux. Available from: <http://www.keepalived.org/index.html>. [Last accessed on 2018 Mar 5].

Kovari, A., 2012. KVM and OpenVZ Virtualization based IaaS Open Source Cloud Virtualization Platforms: Open Node, Proxmox VE. Available from: https://www.researchgate.net/profile/Eko_Didik_Widianto/publication/315861457_Performance_comparisons_of_web_server_load_balancing_algorithms_on_HAProxy_and_Heartbeat/links/59d5b88ba6fdcc8746969fe9/Performance-comparisons-of-web-server-load-balancing-algorithms-on-HAProxy-and-Heartbeat.pdf?origin=publication_detail. [Last accessed on 2018 May 04].

Madani, S. and Jamali, S., 2018. A comparative study of fault tolerance techniques in cloud computing. *International Journal of Research in Computer Applications and Robotics*, 6(3), pp.7-15. Available from: https://www.ijrcar.com/Volume_6_Issue_3/v6i302.pdf. [Last accessed on 2018 Sep 10].

Mustafa, M.E., 2017. Load Balancing Algorithms Round Robin (RR), Least Connection, and Least Loaded Efficiency. Available from: <http://www.gesj.internet-academy.org.ge/download.php?id=2886.pdf&t=1>. [Last accessed on 2018 May 05].

Pi'orkowski, A., Kempny, A., Hajduk, A. and Strzelczyk, J., 2010. Load Balancing for Heterogeneous Web Servers. Available from: https://www.link.springer.com/chapter/10.1007/978-3-642-13861-4_19. [Last accessed on 2018 May 04].

Proxmox., 2018. Download and Documentation Files-Important Downloads. Available from: <https://www.proxmox.com/en/downloads>. [Last accessed on 2018 Mar 02].

Qasmi, W., Siddiqui, T. and Shehzad, M., 2018. A Comparative Study of Failover Schemes for IaaS Recovery. *International Conference on Information Networking (ICOIN)*, Thailand.

Sharma, M., and Iyer, V.S., 2016. Sugandhi Subramanian and Abhinandhan Shetty A Comparative Study on Load Testing Tools. Available from: http://www.academia.edu/download/46336846/201_A_Comparative.pdf. [Last accessed on 2018 May 05].

Widianto, E.D., 2016. Performance Comparisons of Web Server Load Balancing Algorithms on HAProxy and Heartbeat. Available from: https://www.researchgate.net/profile/Eko_Didik_Widianto/publication/315861457_Performance_comparisons_of_web_server_load_balancing_algorithms_on_HAProxy_and_Heartbeat/links/59d5b88ba6fdcc8746969fe9/Performance-comparisons-of-web-server-load-balancing-algorithms-on-HAProxy-and-Heartbeat.pdf?origin=publication_detail. [Last accessed on 2018 May 04].

Efficient and Fair Bandwidth Scheduling in Cloud Environments

Mustafa Khaleel¹ and Mengxia Zhu²

¹Department of Computer, College of Science, University of Sulaimani, Kurdistan Region - F.R. Iraq

²Department of Computer Science, College of Science, Montclair State University, New Jersey, USA

Abstract—Hundreds of thousands of servers from data centers are operated to provide users with pay-as-you-go infrastructure as a service, platform as a service, and software as a service. Many different types of virtual machine (VM) instances hosted on these servers oftentimes need to efficiently communicate with data movement under current bandwidth capacity. This motivates providers to seek for a bandwidth scheduler to satisfy objectives, namely assuring the minimum bandwidth per VM for the guaranteed deadline and eliminating network congestion as much as possible. Based on some rigorous mathematical models, we formulated a cloud-based bandwidth scheduling algorithm which enables dynamic and fair bandwidth management by categorizing the total bandwidth into several categories and adjusting the allocated bandwidth limit per VM for both upstream and downstream traffics in real time. The simulation showed that paradigm was able to utilize the total assigned bandwidth more efficiently compared to algorithms such as bandwidth efficiency persistence proportional sharing (BEPPS), PPS, and PS at the network level.

Index Terms—Cloud infrastructure, Cloud scheduler, Pay-as-you-go, Makespan.

I. INTRODUCTION

The increasingly growing demands from a large number of active cloud users have put forward many performance challenges for both processing and bandwidth orchestration in a cloud architecture. As a result, maintaining and troubleshooting the connection among various virtual

machines (VMs) along many communication paths calls for a performance-guaranteed bandwidth scheduling strategy. Many modern datacenters (DCs) that support large-scale processing workflows require hundreds of thousands cloud-based VMs to be established and these VMs need to exchange data frequently (Saurabh, et al., 2011). According to the reported by Environmental Protection Agency (EPA) in 2007, these high-performance computing DCs consumed approximately 7.2 billion US dollars within 1 year (Jonathan, 2007 and Massoud and Inkwon, 2010). In 2013, every 60 s, 204 million emails were sent; 5 million searches were made on Google engine; 1.8 million “Likes” were posted on Facebook; 35,000 tweets were sent on Twitter; \$272 thousands of commodities were sold on Amazon; and finally for sound marketing, 15,000 tracks were downloaded through iTunes according to Natural Resources Defense Council (Pierre and Josh, 2014) and the U.S. EPA (Richard, et al., 2008). The high volume of incoming and outgoing traffics requires cloud providers to dedicate an efficient network bandwidth scheduler that considers both the network proportional fairness and low risk of bandwidth congestion. As Garg stated that if cloud providers do not strive to improve resource utilization to meet the ever-increasing demands under limited resources, they might increase the cost for cloud users to maintain their profits which eventually pricing themselves out of existence (Saurabh, et al., 2009). Idle servers are usually shut down to save the power and allocated bandwidth (Giorgio, et al., 2013). Statistics shows that the average resources utilization rate in modern DCs can be as low as 20% with many idle servers. We propose a bandwidth scheduler to enhance the bandwidth utilization rate per (VMs) through dynamic classification of the total allocated bandwidth into percentage classes and providing the minimum assurance best effort bandwidth per VM for both up streaming and down streaming traffics to guaranteed deadline. Then, readjusting the limited assigned bandwidth per VM based on the necessity of available workloads. The submitted user jobs are formulated as general directed acyclic graph (DAG)-structured workflows with module dependency. The simulation results based on CloudSim (Tarun, et al., 2012) showed that our approach significantly enhanced the rates of bandwidth utilization per VM compared with other algorithms such as bandwidth efficiency persistence proportional sharing (BEPPS), PPS, and PS at the network level (Xiang and Nirwan, 2013).

ARO-The Scientific Journal of Koya University
Volume VI, No.2 (2018), Article ID: ARO.10441, 7 pages
DOI: 10.14500/aro.10441

Received 29 July 2018; Accepted 8 November 2018

Regular research paper; Published 29 November 2018

Corresponding author's, e-mail: mustafa.khaleel@univsul.edu.iq

Copyright © 2018 Mustafa Khaleel and Mengxia Zhu. This is an open access article distributed under the Creative Commons Attribution License.



II. RELATED WORK

Many performance metrics including job makespan, energy cost, and bandwidth fairness have been considered in many cloud computing research. Researchers are trying to find an equilibrium point between high bandwidth utilization and high-resource utilization for cloud resources. For instance, a concept of providing bandwidth control as a service was proposed by classifying the network connections into groups and adjusting the weights over the links connecting different VMs (Anthony, 2016). However, BEPPS at network level was presented to increase the provider's profits through disbanding the unfair bandwidth utilization (Xiang and Nirwan, 2013). The bandwidth allocated for the communicating VM pairs which utilizes the bottleneck link will be increased. Furthermore, the downlink spectrum efficiency was enhanced by incorporating coalitions of remote radio head (RRH) (Zhuofu, et al., 2016). Each RRH can be attached or dispatched per coalition for better utilization. A prototype system was proposed with a single joint optimization function considering both efficiency of energy and spectral efficiency. Orthogonal frequency division multiplexing-based networks were used to improve the functionality of RE (Dingzhu, et al., 2017). Data replication

was used to reduce the network delays while achieving the quality of service (QoS) (Dejene, et al., 2015).

III. CLOUD CONCEPTUAL FRAMEWORK

Cloud tenants submit their job requests either as a single independent task or as a DAG-structured workflow to the cloud meta-scheduler. The cloud scheduler applies four main duties after applying topological sorting for the DAG: First, detecting any anomalous behaviors via cloud snooping module; second, pricing the providers in case of deadline violation; third, initiating the minimum assurance best effort per VM for the guaranteed deadline and monitoring the allocated bandwidth through sending and receiving status requests to and from the cloud bandwidth controller; and finally, based on bandwidth and computing capacities, the scheduler maps the workflow tasks to the appropriate VMs. Cloud bandwidth controller readjusts the inner allocated bandwidth per VM when the level of workloads increases. Based on the bandwidth availability, the cloud bandwidth controller will assign new percentage values to the current bandwidth allocated to enhance the system utilization rates. Fig. 1 demonstrates our prototype architecture.

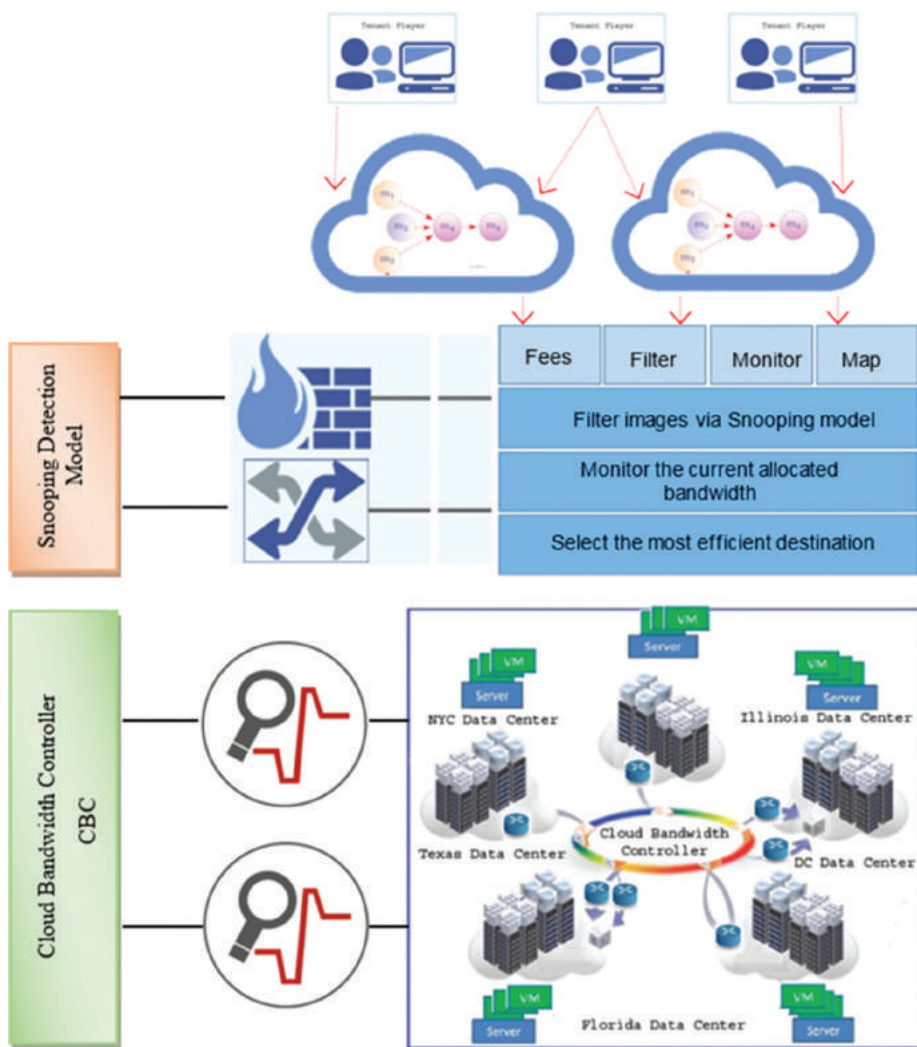


Fig. 1. The proposed cloud framework.

IV. MATHEMATICAL MODEL

For decades, researches have considered the efficiency as one of the major parameters when it comes to establishing a fair data transporter. Nowadays, increasing cloud provider's interests through bargaining both the overhead of cloud-based bandwidth and workflow's execution time become researcher's primary concern. According to Dara, et al., 2009 and Anshul, et al., 2009, the cost consumed by idle resources is about 70% of the total aggregate cost exhausted by fully operated resources. As these servers are fully interconnected through high dedicated bandwidth, the idle resources will make those high dedicated bandwidths unproductive (Yogesh, et al., 2016 and Dinh-Mao, et al., 2017). These challenges motivated us to formulate a conceptual framework with the aim of achieving bandwidth proportionality fairness among fully interconnected VMs. This heuristic is based on two main ideas; first, the total bandwidth allocated is categorized to classes with different bandwidth capabilities. Second, a minimum assurance bandwidth is assigned per VM and will be adjusted by cloud bandwidth controller depending on the workloads. Mathematically, we have provided the model for executing a single module m_i over a VM Vm_j from time 0 to time n in equation (1) and the running time for executing a batch of modules mapped onto node V_j in equation (2). Where, $\mathcal{G}(u_i)$ is the total aggregate data input for the module u_i and $\zeta_i(\cdot)$ is the complexity of the same assigned module. $C_{-}(vm-mk \in v_j)$ is the normalized computing power of virtual Vm_k to execute module u_i .

$$T_{exe}(m_i, vm_j) = \sum (\alpha(T) \times \delta_i(T) / P(v_j) \tau_0, \tau_n) \quad (1)$$

$$\mathcal{R}_{\hat{a}_i, \hat{a}_n}^{M_m, V_j} = \sum_{u_i \in M_m, V_j} \mathcal{J}(\hat{u}_i) \times \zeta_i(\cdot) / (C_{vm, mk \in v_j})_{\tau_0, \tau_n} \quad (2)$$

Subject to: $u_i \in CP(W_i)$

Where, $\mathcal{R}_{\tau_0, \tau_n}^{M_m, V_j}$ is the running time of a batch of modules M_m mapped over server j 's V_j th VM starts at time τ_0 and ends at time τ_n . $CP(W_i)$ is the critical path that exists in workflow i . $C(DC_d[\tau_0, \tau_n])$ is the normalized computing power of datacenter DC_d during time τ_0 to τ_1 .

V. DAG - SCIENTIFIC WORKFLOW

DAG as defined in Maria and Rajkumar, 2017 includes dual major parameters, namely vertices $|v_a|$ and the edges $|E_a|$, among these modules. The first parameter consists of an array of the batch of module applications $\{a_1, a_2, a_3, \dots, a_q\}$ which initiates with a_1 and terminates with a_q . The second parameter represents the weights from a module to others. There are various types of scientific workflows where researchers conduct them to improve the QoS specified in service level agreement. A tremendous advantage of scheduling cloud images as workflows is the dependency and parallelism which embedded in the structure of workflows. Some required conditions are as follows: First, the modules should be dispatched collectively as a group which increases the execution efficiency. Second, none of prepared modules can start its execution unless it receives the total aggregated input from its preceding modules. Third, the complexity function of each module will be added to its total input

data size. Finally, when a specific module executed through specific computing resource, the outcome result will be transferred to the module's succeeding module. However, the running time for executing a workflow W_i over cloud server v_j from time 0 to time n is given in equation (3) and the total cost of running the entire workflows mapped onto cloud DCs is given in equation (4). Table 1 illustrates the sample workflows with their sizes and edges that have been conducted in our paradigm's simulation.

$$\mathcal{R}(W_i) = \sum_{v_j \in DC_d} \mathcal{P}(V_j)_{\tau_0, \tau_n} (t_{st} + \mathcal{R}_{\tau_0, \tau_n}^{M_m, V_j} + Idle(V_j) + t_{sh}) \quad (3)$$

$$\mathcal{T}_5 = \sum_{i=1}^W \mathcal{R}(W_i) / \sum_{d=1}^D C(DC_d[\tau_0, \tau_n]) \quad (4)$$

Where, t_{st} is the initial startup times, $Idle(v_j)$ is the idle time for node v_j , and t_{sh} is the shutdown times. $C(DC_d[\tau_0, \tau_n])$ is the normalized computing power of datacenter d during times τ_0, τ_n .

VI. Cloud Bandwidth Controller

One of the major cloud bandwidth controller (CBC) duties is to map the allocated total aggregated bandwidth into group of percentage classes for dynamic bandwidth management. Each class has specific characteristics in terms of inner VM connections. At the first glance, when the scheduling of DAG - scientific workflows initiates to be processed over cloud-based VM infrastructure, CBC assigns the minimum assurance best effort bandwidth per VM where each connection is fully utilized within limited incoming and outgoing traffics. Right after the network becomes oversubscribed, the CBC will adjust the preassigned allocated bandwidth per VM. Equations 5 and 6 formulate the cloud bandwidth controller and efficiency, respectively.

$$CBC = T_5 / \min(ass(\beta v_i, v_j, \tau_0, \tau_n)) \quad (5)$$

$$EFF = \text{Total Bandwidth Allocated} / \min(\text{assurance Best Effort Bandwidth Per VM}) \quad (6)$$

Where, $(\beta v_i, v_j, \tau_0, \tau_n)$ is the allocated bandwidth from v_i to v_j from time 0 to time n . Illustration (2) explains how the cloud bandwidth controller works during the module execution time. As the process launches at period 1–10, the available bandwidth would be free and the VMs will be assigned fixed bandwidth limits. At time 15 s, when the network's load becomes heavier, the CBC will readjust those channels that

TABLE I
SCIENTIFIC WORKFLOW CONFIGURATION

Workflow ID	Workflow size $ V_q $	Workflow edge $ E_q $
1-r C	15	32
2-C	25	43
3-C	34	55
4-C	57	90
5-C	78	113
6-C	84	126
7-T	108	144
8-T	125	157
9-T	160	232
10-T	230	303

would otherwise enter congestion status. The system becomes oversubscribed at time 25 s and the CBC will assign new bandwidth values per VM to accommodate the current need.

VII. PROBLEM FORMULATION

As many tenants share the same underlying cloud infrastructure, the problem arises when the network bandwidth may not be allocated efficiently and results in low performance. This results in unpredictable bandwidth utilization and needs to be addressed through allocating more bandwidth to big jobs and allocates less bandwidth to small jobs while assuring the bandwidth availability and eliminating network congestion.

Definition 1: Given a DAG-structured workflow $G_t=(V_r,E_t)$ and underlying heterogeneous cloud hardware $G_m=(V_m,E_m)$, where each computing server is allocated with a minimum bandwidth for the guaranteed deadline, we concentrate on finding a workflow mapping schedule that the fairness is increased under the certain *MEED* constraint and avoid congestion.

$$\begin{aligned} & \underset{\text{possible mapping}}{\text{increase}} \left(\mathcal{F}_{v_s, v_d} (T) \right) \\ & \text{Subject to} \left\{ \begin{array}{l} T < MEED \\ \mathcal{K}_{Conn, v_s, v_d} \notin \text{congestion} \end{array} \right. \end{aligned} \quad (7)$$

Where, F_{v_s, v_d} with source and destination server as v_s, v_d is the fairness for all allocated bandwidth. K_{Conn, v_s, v_d} is the entire connections between the source and destination servers. *MEED* is the minimum end-to-end delay that cannot be violated.

VIII. PERFORMANCE EVALUATION

A. Experimental Setup

For this testbed evaluation, several workflows with different workloads have been estimated using the well-known open source Java-based CloudSim toolkit (Tarun, et al., 2012). However, these workflows are scheduled over heterogeneous cloud-based data centers where each one includes 100 computing servers. The CPU frequencies are ranged from 0.8 GHz to 2.5 GHz with the random access memory. Furthermore, various VMs with different instance types have been assigned to each computing server to serve the

user’s needs on different cost types. For the cloud provider’s interest, we set the unit price for each module execution as \$0.6/h and the VM’s initiating time and eliminating time to 100 and 8 s, respectively. To evaluate network bandwidth efficiency, we have compared our paradigm with algorithms, namely BEPPS, PS, and PPS, at network level (Xiang and Nirwan, 2013).

B. Experimental Results

To visualize the full coverage of bandwidth efficiency persistence propositional at network layer, five performance metrics have been used in this experiment. They include bandwidth utilization rate, incoming bandwidth limits, outgoing bandwidth limits, and provider’s interest. Since we have evaluated 10 different workflows scheduled over 10 heterogeneous cloud data centers, it is not feasible to plot all 20 workflows under all different data centers. Selected experiments have been presented as shown in Figs. 3-12. Based on server’s capabilities in terms of workflow module execution, we have selected six DCs from the total of 10 DCs to evaluate bandwidth utilization rate in Fig. 3. According to Fig. 3, our paradigm achieved the highest utilization rates, especially in DCs 4, 5, and 6 compared to the other algorithms BEPPS, PS, and PPS. Our lowest difference rate in datacenter 1 is 0.22 compared to PPS, 0.35 compared to PS, and 0.16 compared to BEPPS, whereas the highest difference rate can be observed in datacenter 6 which is 0.15 compared to PPS, 0.18 compared to PS, and 0.11 compared to BEPPS. We have repeated the same scenario for assigned workflows in Fig. 4. Among the six workflows, the highest utilization rates achieved in both workflows 3 and 4 are 0.99. The lowest bandwidth utilization rates are seen in workflows 5 and 6. The diversity in both workflows 3 and 4 is exaggerated compared to workflows such as 1, 5, and 6. The worst case can be observed compared with algorithm PS. The highest rates are 0.7 and 0.72, whereas the lowest rates are 0.12 and 0.15. We also have evaluated the cloud interest over six workflows and DCs as demonstrated in Figs. 5 and 6. First, we have calculated the interest per DCs in diagram (5) and our heuristic gains the highest payoff compared to methods BEPPS, PS, and PPS. In datacenter 2, our algorithm is supreme to earn approximately \$563, whereas the minimum revenue is achieved in datacenter 4 which is \$294. The test scenario is repeated for algorithm PS which accomplished the worst case, especially in datacenter 1 with profit of \$230.

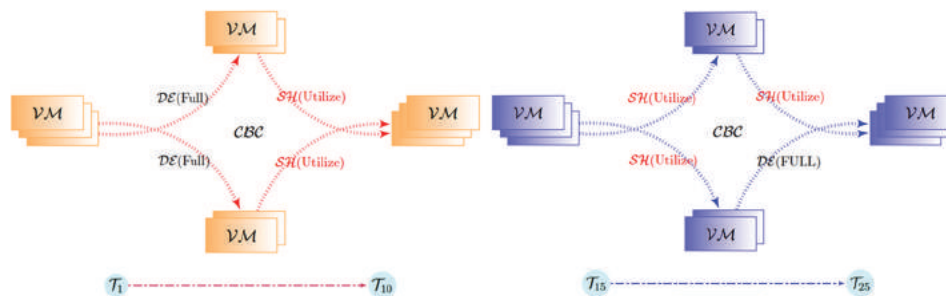


Fig. 2. Allocated bandwidth during different times.

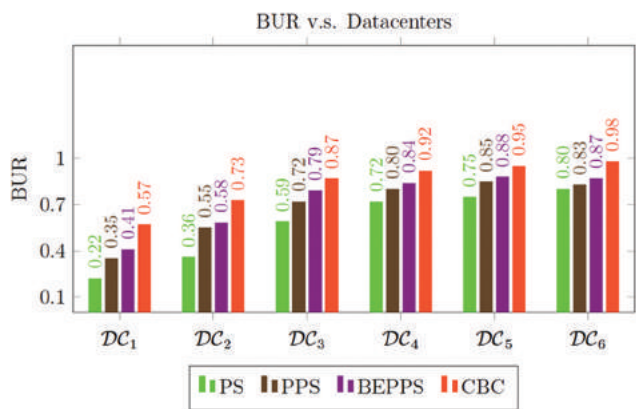


Fig. 3. Bandwidth utilization versus datacenters.

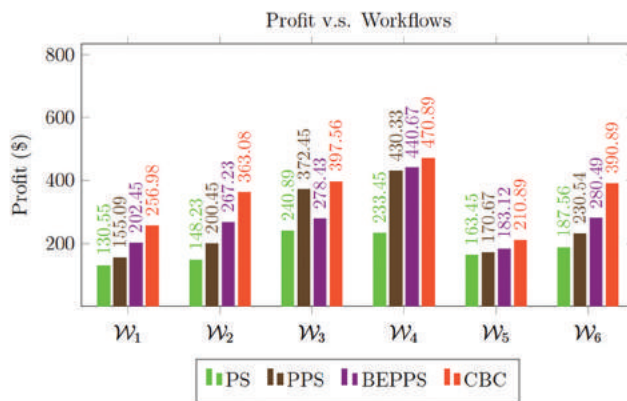


Fig. 6. Cloud provider profit versus workflows scheduling.

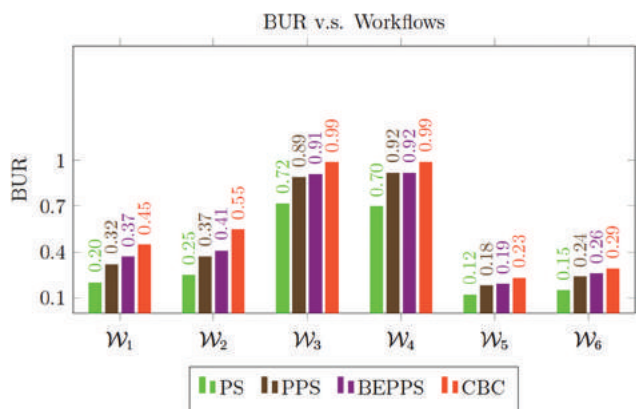


Fig. 4. Bandwidth utilization versus workflows scheduling.

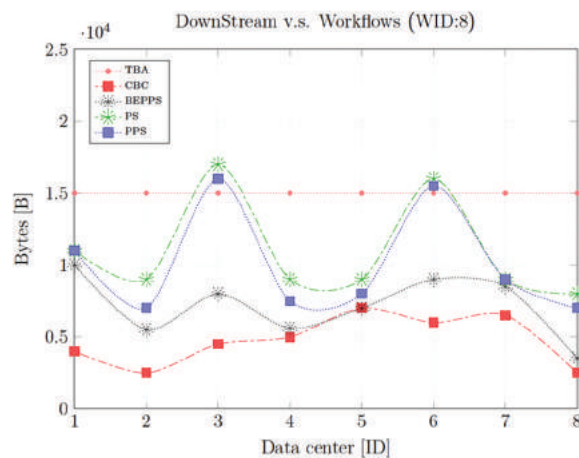


Fig. 7. Downstream traffics versus datacenters.

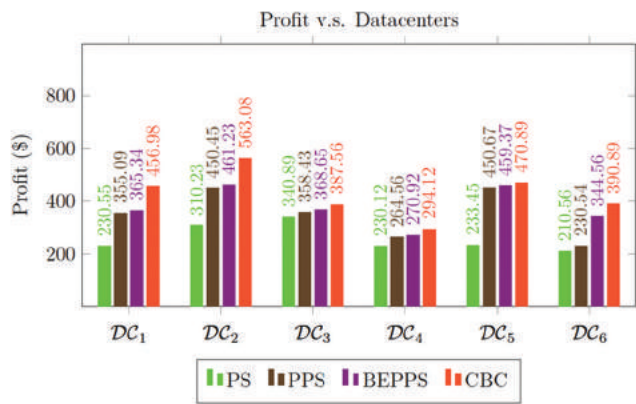


Fig. 5. Cloud provider profit versus datacenters.

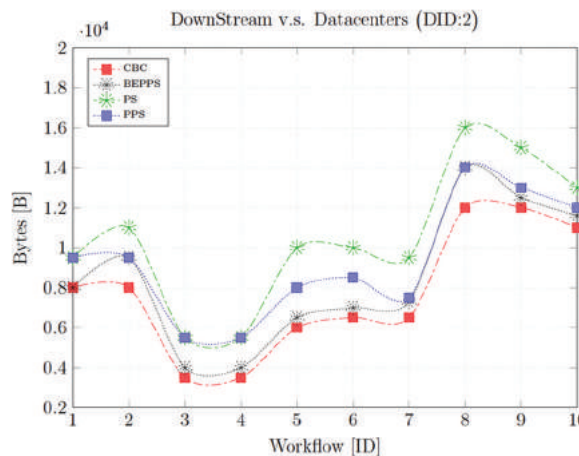


Fig. 8. Downstream traffics versus workflow scheduling.

Our technique has achieved the highest output in workflows 3 and 4 which are \$397 and \$470, respectively. For both metrics incoming and outgoing bandwidth limits, we have evaluated a total of 10 workflows under one datacenter as well as 10 DCs for a single scheduled workflow as illustrated in Figs. 7-10. For incoming and outgoing bandwidth limits versus DCs, the total bandwidth allocated is used as baseline for the comparison as shown in Figs. 7 and 9, respectively. It can be seen that the other two algorithms, namely PS and PPS, violated the baseline bandwidth, whereas our paradigm maintained the workload under deadline as shown in Fig. 7.

The main reason is that our heuristic allocated bandwidth fairly per VM. In terms of assigned workflows metric, the best fairness case can be observed within our pattern, whereas the BEPPS is achieved better fairness compared to the other two algorithms PS and PPS. However, for outgoing bandwidth limit metric, the values of our algorithm have changed over each datacenter consecutively as in Fig. 9. PS algorithm is inferior to others, especially under DCs ID

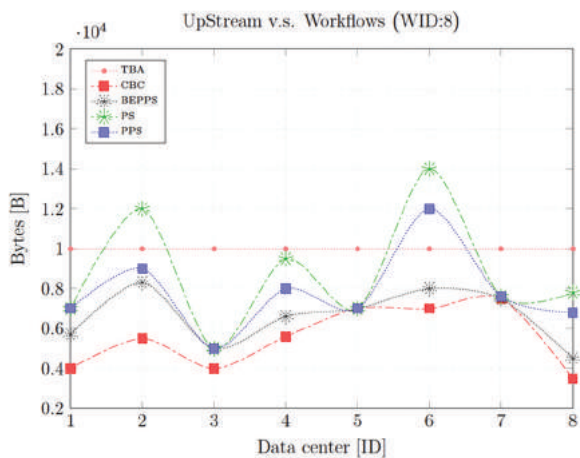


Fig. 9. Upstream traffic versus datacenters.

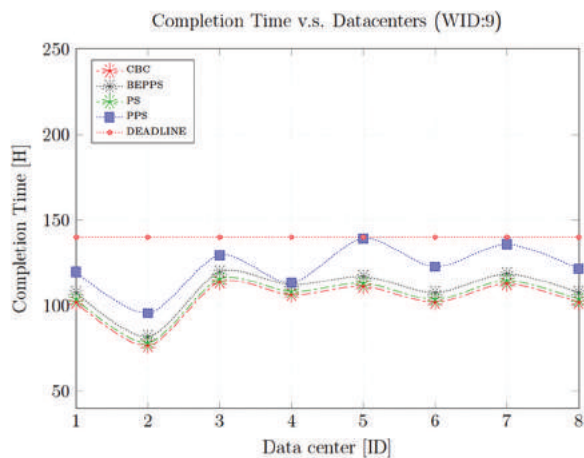


Fig. 11. Execution time versus datacenters.

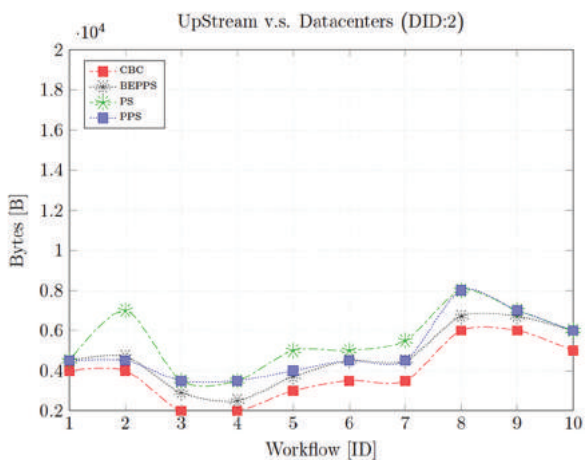


Fig. 10. Upstream traffic versus workflow scheduling.

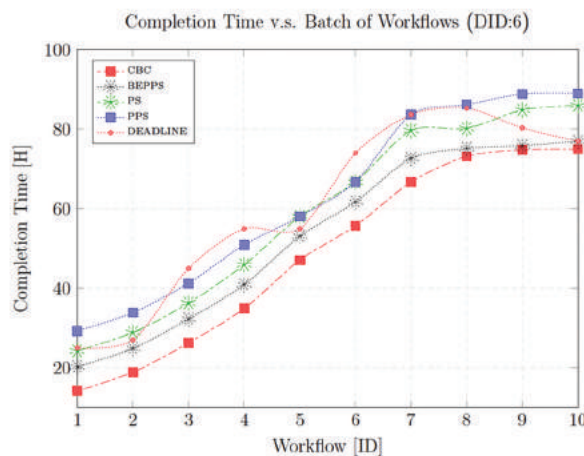


Fig. 12. Execution time versus workflow scheduling.

= 2 and 6. Furthermore, CBC heuristic attains steady rates when the workflows are scheduled over datacenter ID = 2. The other two algorithms PS and PPS have the same rates over most workflows. Moreover, we also have integrated the evaluation for the module application completion time (Makespan) against batch of workflows and eight different DCs. In Fig. 11, our paradigm executed the scheduled workflows in less time compared to BEPPS, PS, and PPS. We can observe that the other three algorithms either have violated the tenant’s deadline or close to violate them. Our objective’s bandwidth fairness technique is based on utilizing cloud resources more efficient while executing modules applications within tenant’s deadline. However, in Fig. 12, CBC heuristic achieved better completion time, especially in datacenter 2, 4, and 6. The worst case can be seen for PS algorithm in both figures. It required more times to complete the execution process.

IX. CONCLUSION

Cloud providers would like to execute as many tasks as possible from multiple tenants for high system throughput and resource utilization. Efficiently allocating and utilizing

bandwidth resources among communicating VMs are a critical task to achieve the throughput and efficiency. A bandwidth scheduler was proposed in this paper to meet objectives of assuring the minimum bandwidth per VM for the guaranteed deadline and reducing network congestion as much as possible. Our approach exploited the idea of dynamic bandwidth utilization by categorizing the total allocated bandwidth into percentage values and regulating the bandwidth per VM based on upstream and downstream traffics. The simulation results have shown that our heuristic preserved a considerable amount of bandwidth through utilizing the allocated bandwidth more efficiently compared to algorithms such as BEPPS, PS, and PPS at network level (Xiang and Nirwan, 2013).

REFERENCES

Anshul, G., Mor H.B., Rajarshi, D., and Charles, L., 2009. Optimal power allocation in server farms. *Proceedings of the eleventh international joint conference on Measurement and modeling of computer systems.* (SIGMETRICS '09). ACM, New York, USA, pp.157-168.

Anthony, A. Jr., 2016. *Improving Bandwidth Allocation in cloud Computing Environments via Bandwidth as A Service Partitioning.* Available from: <https://www.digital.library.txstate.edu/handle/10877/6315>. [Last accessed on 2018 Aug 01].

- Dara, K., Jeffery, O.K., James, E.H., Nagarajan, K., and Guofei J., 2009. Power and performance management of virtualized computing environments via look ahead control. *Cluster Computing*, 12(1), pp.1-15.
- Dejene, B., Dzmitry, K., Fabrizio, G., Pascal B., and Albert. Y.Z., 2015. Energy-efficient data replication in cloud computing datacenters. *Cluster Computing*, 18(1), pp.385-402.
- Dingzhu, W., Guanding, Y., Rongpeng, L., Yan, C., and Geoffrey, Y.L., 2017. Results on energy-and spectral-efficiency tradeoff in cellular networks with full-duplex enabled base stations. *IEEE Transactions on Wireless Communications*, 16(3), pp.1494-1507.
- Dinh-Mao, B., YongIk, Y., Eui-Nam, H., SungIk, J., and Sungyoung, L., 2017. Energy efficiency for cloud computing system based on predictive optimization. *Journal of Parallel and Distributed Computing*, 102, pp.103-114.
- Giorgio, L.V., Samee. K., and Pascal B., 2013. Energy-efficient resource utilization in cloud computing. *Large Scale Network-Centric Distributed Systems*, 45, pp.377-408.
- Jonathan, G.K., 2007. Estimating Total Power Consumption Report by Servers in the US and the World. Available from: <http://www-sop.inria.fr/mascotte/Contrats/DIMAGREEN/wiki/uploads/Main/svrpwrusecompletefinal.pdf>. [Last accessed on 2016 Jul19].
- Maria, A.R., and Rajkumar, B., 2017. Budget-driven scheduling of scientific workflows in IaaS clouds with fine-grained billing periods. *ACM Transactions on Autonomous and Adaptive Systems*, 12(2), DOI: <https://doi.org/10.1145/3041036>.
- Massoud, P., and Inkwon, H., 2010. *Power and Performance Modeling in a Virtualized Server System*. 39th International Conference on Parallel Processing Workshops (ICPPW), San Diego, CA, USA: September 13-16.
- Pierre, D., and Josh, W., 2014. Scaling Up Energy Efficiency Across the Data Center Industry: Evaluating Key Drivers and Barriers. Available from: <https://www.nrdc.org/sites/default/files/data-center-efficiency-assessment-IP.pdf>. [Last accessed on 2014 Aug 29].
- Richard, B., Eric, M., Bruce, N., Bill, T., Arman, S., John, S., Jonathan, K., Dale, S., and Peter, C., 2008. *Report to Congress on Server and Data Center Energy Efficiency: Public Law 109-431*. Lawrence Berkeley National Laboratory.
- Saurabh, K.G., Chee, S.Y., Arun A., and Rajkumar, B., 2011. Environment-conscious scheduling of HPC applications on distributed cloud-oriented data centers. *Journal of Parallel and Distributed Computing*, 71(6), pp.732-749.
- Saurabh, K.G., Chee, S.Y., Arun, A., and Rajkumar, B., 2009. *Energy-Efficient Scheduling of HPC Applications in Cloud Computing Environments*. Ithaca, New York, CoRR, abs/0909.1146.
- Tarun, G., Ajit, S., and Aakanksha, A., 2012. Cloudsim: Simulator for cloud computing infrastructure and modeling. *Procedia Engineering*, (38), pp.3566-3572.
- Xiang, S., and Nirwan, A., 2013. *Improving Bandwidth Efficiency and fairness in cloud computing*. IEEE Global Communications Conference (GLOBECOM). Atlanta, GA, USA: December 9-13.
- Yogesh, S., Bahman, J., Weisheng, S., and Daniel, S., 2016. Reliability and energy efficiency in cloud computing systems: Survey and taxonomy. *Journal of Network and Computer Applications*, 74, pp.66-85.
- Zhuofu, Z., Jun, P., Xiaoyong, Z., Kaiyang, L., and Fu, J., 2016. A game-theoretical approach for spectrum efficiency improvement in cloud-RAN. *Mobile Information Systems*, 2014, 11.

Membrane Computing for Real Medical Image Segmentation

Rafaa I. Yahya^{1,2}, Siti Mariyam Shamsuddin^{2,3}, Salah I. Yahya^{4,5}, Bisan Alsalibi^{2,6},
Ghada Al-Khafaji^{2,7}

¹Department of Computer, College of Science, University of Al-Mustansiriyah, Baghdad, Iraq

²UTM Big Data Center, Ibnu Sina Institute for Scientific and Industrial Research, Universiti Teknologi Malaysia, UTM Skudai, 81310 Johor, Malaysia

³Faculty of Computing, Universiti Teknologi Malaysia, UTM Skudai, 81310 Johor, Malaysia

⁴Department of Software Engineering, Faculty of Engineering, Koya University, University Park, Danielle Mitterrand Boulevard, Koya KOY45, Kurdistan Region, Iraq

⁵Department of Computer Science and Engineering, School of Science and Engineering, University of Kurdistan Hewler, Kurdistan region, Iraq

⁶School of Computer Science, Universiti Sains Malaysia, Malaysia

⁷Department of Computer Science, College of Science, University of Baghdad, Iraq

Abstract—In this paper, membrane-based computing image segmentation, both region based and edge based, is proposed for medical images that involve two types of neighborhood relations between pixels. These neighborhood relations - namely 4-adjacency and 8-adjacency of a membrane computing approach - construct a family of tissue-like P systems for segmenting actual two-dimensional (2D) medical images in a constant number of steps; the two types of adjacency were compared using different hardware platforms. The process involves the generation of membrane-based segmentation rules for 2D medical images. The rules are written in the P-Lingua format and appended to the input image for visualization. The findings show that the neighborhood relations between pixels of 8-adjacency give better results compared with the 4-adjacency neighborhood relations because the 8-adjacency considers the eight pixels around the center pixel, which reduces the required communication rules to obtain the final segmentation results. The experimental results proved that the proposed approach has superior results in terms of the number of computational steps and processing time. To the best of our knowledge, this is the 1st time an evaluation procedure is conducted to evaluate the efficiency of real image segmentations using membrane computing.

Index Terms—Edge-based segmentation, Medical images, membrane computing, P-Lingua, Region-based segmentation, tissue-like P system.

ARO-The Scientific Journal of Koya University
Volume VI, No.2 (2018), Article ID: ARO.10442, 12 pages
DOI: 10.14500/aro.10442

Received 16 August 2018; Accepted: 05 December 2018
Regular research paper: Published 10 December 2018

Corresponding author's, e-mail: salah.ismaeel@koyauniversity.org
Copyright © 2018 Yahya RI, Shamsuddin SM, Yahya SI, Alsalibi B, Al-Khafaji G. This is an open-access article distributed under the Creative Commons Attribution License.



I. INTRODUCTION

Membrane computing (MC) is a fascinating and fast-growing area of research that takes its inspiration from the subdivisions of biological cells into compartments delimited by membranes. The computational models in MC, which are a new class of distributed and parallel systems, are known as P systems in honor of their initiator Paun (2000, 2002). The distinguishing hallmarks of P systems are the intrinsic parallelism, the locality of interactions, and the capacity of generating new cells in linear time. The basic ingredients of a membrane system consist of (1) the membrane structure and delimiting compartments, which either correspond to a tree-like hierarchical arrangement of membranes as in a cell or a net of membranes represented by a directed graph as in a tissue. In each membrane, (2) multisets of objects are placed in the compartments, which evolve according to specific and (3) evolution rules. Typically, the external membrane is called the skin membrane, which contains several internal membranes, of which the elementary membrane is the one without any other membranes inside it (Paun and Rozenberg, 2000). Several variants of P systems have been proposed: Cell-like P systems (inspired from the structure of the cell) (Paun, 2000), tissue-like P systems (inspired from the organization of cells in tissue) (Martí, et al., 2003), and spiking neural-like membrane systems (inspired from the way neurons are linked in neural nets) (Ionescu, et al., 2006). The tissue-like P system, one of the most widely investigated P systems, is inspired by the intercellular communication and cooperation between neurons. Its mathematical model is basically a network of processors working with objects and communicating these objects through communication channels specified in advance. From the computational point of view, the essential feature of this P system is that

membranes do not have electrical charges as in cell-like P systems (Paun, 2000). Most recently, it has been proved that MC has strong potential to be applied to different problems related to biology as well as to linguistics, computer graphics, cryptography, and image processing, to name a few.

Image segmentation is one of the common tools in the image processing spectrum. It partitions the digital image into several regions (sets of pixels) and assigns a specific label to every pixel such that pixels with the same labels typically share similar visual characteristics. Interestingly, segmentation of medical images is a significant step before computer-aided diagnosis, because it is essential for further medical image processing, such as cancer detection. The image segmentation process has different approaches and mechanisms such as thresholding, boundary tracking, clustering, and region-based mechanisms. The result of image segmentation is a set of segments that collectively cover the entire image or a set of contours extracted from the image. Each of the pixels in a region is similar with respect to a certain characteristic or computed property, such as color, intensity, or texture (Shapiro and Stockman, 2001). In recent years, substantial effort has been invested into the problem of medical image segmentation, and several approaches have been proposed: For instance, the probability density-based segmentation approach, histogram-based approaches, the region-based method, and fuzzy clustering.

This paper proposes membrane-based computing image segmentations, both region based and edge based, for medical images that involve two types of neighborhood relations between pixels. Superior results in terms of the number of computational steps and processing time have been achieved using real medical images of different formats.

The paper is organized as follows: Section 2 investigates the related works. Section 3 presents the formal framework of tissue-like P systems. Section 4 explains the proposed segmentation methods for real medical images. Section 5 evaluates the proposed approach. Section 6 analyzes the experiment results. Section 7 concludes the paper.

II. RELATED WORKS

MC possesses several interesting features including the encapsulation of data, a trivial way of representing information as well as achieving maximal parallelism, all of which are most proper when handling digital images. A new research line has been recently launched in which MC has been adapted to solve several problems related to digital imagery. For example, image segmentation was investigated in Christinal, et al. (2009; 2010; 2011). However, in Christinal et al's. work, they used artificial images rather than real images for testing. Furthermore, other problems related to digital images, such as homology (Díaz-Pernil, et al., 2010; Alsalibi, et al., 2014; and Christinal, et al., 2010) and smoothing (Pena-Cantillana, et al., 2011), have been proposed within the framework of MC. With regard to segmentation, the authors in Christinal, et al. (2009) have proposed a family of tissue-like P systems using communication and evolution rules to perform edge-based segmentation of a two-

dimensional (2D) image by employing 4-adjacency. Their results have been achieved in a constant number of steps in which the system was tested by the tissue simulator to check its validity. Christinal, et al. (2010) designed an MC approach to solve the thresholding problem using cell-like P system rules in which the massive parallelism feature of MC helps reach the solution in linear time according to the size of the input image. Carnero, et al. (2010) designed a new hardware tool - namely a field-programmable gate array unit (FPGA) - to conduct segmentation of digital images to address the problems of edge-based detection and noise removal. From a different angle, Reina-Molina, et al. (2010) proposed a new version of the tissue-like P system by replacing the concept of one cell with the use of multiple auxiliary cells to address segmentation problem and exploit all potential parallelization. Similarly, the authors in Díaz-Pernil, et al. (2010) proposed a new software tool for segmenting 2D digital images based on the tissue-like P system, wherein the object-oriented C++ programming language was used in the implementation part. However, they did not provide a clear explanation regarding the technical aspects of developing the proposed tool. Christinal, et al. (2011) introduced a tissue-like P system (using communication rules) to the problem of region-based segmentation. In their work, a 4-adjacency relationship between pixels was adapted to segment 2D digital images, whereas 6-adjacency was used for 3D digital images. The researchers in Peña-Cantillana, et al. (2011) proposed bioinspired MC software program to solve the thresholding problem, and it has been developed by an innovative device architecture called the Compute Unified Device Architecture (CUDA). The researchers of Carnero, et al. (2011) proposed FPGAs to implement tissue-like P system rules and solve segmentation problems. In the work of Sheeba, et al. (2011), the authors constructed a family of tissue-like P system to segment medical images (nuclei of white blood cells) of the peripheral blood smear images in a morphology segmentation technique, and their algorithm was implemented using MATLAB software.

The authors in Díaz-Pernil, et al. (2012) designed a new software tool to segment images, in which a tissue-like P system was used to solve the problem in constant time due to the intrinsic parallelism of MC computational models. In Zhang and Peng (2012), a novel infrared object segmentation based on a thresholding method was proposed using the cell-like P system to obtain the best set of parameters quickly. In Christinal, et al. (2012), a variant of the P system (tissue-like P system) was constructed using the rules to perform a parallel color segmentation of 2D images based on a thresholding method. The authors in Peng, et al. (2012) proposed a thresholding segmentation method based on cell-like-based membrane algorithm to improve the performance of the threshold segmentation. In the same manner, the authors of Yang, et al. (2013) proposed an image segmentation technique by the use of a tissue-like P system to perform conventional region-based image segmentation. In the work of Díaz-Pernil, et al. (2013), a novel device architecture called CUDA was proposed to implement tissue-like P system rules for segmenting images by the use of gradient-based edge

detection to enhance the classical methods of segmentation. In Peng, et al. (2014), the authors proposed novel segmentation by enhancing the conventional region-based color image segmentation method using tissue-like P systems. In the work of Isawasan, et al. (2014), tissue-like P system rules were used to perform region-based segmentation of 2D hexagonal images in which the segmentation was performed in seven steps. However, they did not illustrate how they used P-Lingua to perform the segmentation. In the work of Peng, et al. (2015), the authors presented a new method using a cell-like P system (membrane algorithm) to solve the optimal multilevel thresholding problem. Yahya, et al. (2015) proposed a classical region-based segmentation with tissue-like P system rules. In their proposed work, a simple artificial image was used to provide a detailed illustration of the basic idea of how the P system works. Furthermore, various color relations have been investigated to illustrate the effect of colors on the segmentation results. Yahya, et al. (2016) proposed a tissue-like P system, where variant of MC was used to segment 2D hexagonal artificial images by employing edge-based segmentation and region-based segmentation. P-Lingua programming language was used to implement and validate the proposed P system Yahya, et al. (2017).

III. DEFINITION OF TISSUE-LIKE P SYSTEMS

Tissue-like P systems were first introduced in Marti, et al. (2003) and Martin-Vide, et al. (2002). In tissue-like P systems, the membrane structure is a general directed graph. The edges of such graphs are not given explicitly, but they are deduced from the set of rules. The biological inspiration behind this model is 2-fold: Intercellular communication and cooperation between neurons. From the computational perspective, the essential feature of this P system is that membranes do not have electrical charges as in the cell-like P systems (Diaz-Pernil, et al., 2010).

Basically, a tissue-like P system is a tuple of degree $q \geq 1$:

$$\Pi = (\Gamma, \Sigma, \varepsilon, w_1, \dots, w_q, R, i_\pi, o_\pi)$$

Where,

- Γ is the finite alphabet of objects, including two distinguished objects yes and no, occurring in at least one copy in some initial multisets M_i but not in ε ;
- $\Sigma(\subseteq \Gamma)$ is the input alphabet;
- $\varepsilon \subseteq \Gamma$ is the list of objects in the environment, each one of arbitrarily infinite copies;
- w_1, \dots, w_q are strings over Γ representing the multisets of objects associated with the cells at the initial configuration;
- R is a finite set of rules of the form.
 - Communication rule: $(i, u/v, j)$, for $i, j \in \{0, 1, 2, \dots, q\}$, $i \neq j$, $u, v \in \Gamma$;
 - Division rules: $[a]_i \rightarrow [b]_i [c]_p$, where $i \in \{1, 2, \dots, q\}$ and $a, b, c \in \Gamma$;
- $i_\pi \in \{1, 2, \dots, q\}$ is the input membrane;
- $o_\pi \in \{0, 1, 2, \dots, q\}$ is the output membrane.

In the typical framework of MC, each cell is viewed as a computing unit working in a maximally parallel and non-deterministic manner. The configuration is an instantaneous

description of the P system at a particular time, in which a sequence of computation steps can be applied in a parallel way to obtain a new configuration. A computation is said to be successful if it halts, reaching a specific configuration in which no more rules can be further applied to the current objects. With a halting computation, the associated output can be codified by the content of the output membrane. A more detailed description of tissue-like P systems can be found in Diaz-Pernil, et al. (2010) and Martin-Vide, et al. (2002).

IV. METHODS

A. Tissue-like P system for real medical image segmentation

We define a family of tissue-like P systems as follows:

$$\Pi(n, m) = (\Gamma(n, m), \Sigma, \varepsilon(n), \mu, M_1, M_2, M_3, R, i_\pi, o_\pi)$$

Where,

- The working alphabet $\Gamma(n, m)$ is the set $\{B_{ij}, W_{ij}, Wx_{ij} : 1 \leq i \leq n, 1 \leq j \leq m\} \cup \{Z_i : 1 \leq i \leq 9\}$;
- The initial membrane structure is $\mu = [[[]]1 [[]]2]0$;
- The input alphabet $\Sigma = \{B_{ij}, W_{ij} : 1 \leq i \leq n, 1 \leq j \leq m\}$;
- The environment $\varepsilon = \Pi(n, m) - \Sigma$;
- Initial multisets: $M_1 = M_2 = \emptyset$;
- i_π, o_π are the input and the output membranes, respectively;
- R is the set of communication rules as follows:

$$\begin{aligned} & [z\{i\}]^1 \leftarrow [z\{i+1\} * 2]^0 : 1 \leq i \leq 8; \\ & [W\{i, j\}, B\{i, j+1\}]^1 \leftarrow [Wx\{i, j\}, B\{i, j+1\}]^0 : 1 \leq i \leq n, 1 \leq j \leq m; \\ & [W\{i, j\}, B\{i, j-1\}]^1 \leftarrow [Wx\{i, j\}, B\{i, j-1\}]^0 : 1 \leq i \leq n, 1 \leq j \leq m; \\ & [W\{i, j\}, B\{i+1, j\}]^1 \leftarrow [Wx\{i, j\}, B\{i+1, j\}]^0 : 1 \leq i \leq n, 1 \leq j \leq m; \\ & [W\{i, j\}, B\{i-1, j\}]^1 \leftarrow [Wx\{i, j\}, B\{i-1, j\}]^0 : 1 \leq i \leq n, 1 \leq j \leq m; \end{aligned}$$

The previously mentioned communication rules are used when the image has edge pixels (two adjacent pixels with different associated colors). In this case, the pixel with less associated color (white pixel) will be marked, and the system brings from the environment an object representing this marked edge pixel (Wx). However, the next set of rules will be used to mark with a bar all pixels that are adjacent to two pixels of the same color which were marked before, but with the condition that the marked objects are adjacent to another pixel with a different associated color. Those rules are as follows:

$$\begin{aligned} & [Wx\{i, j\}, W\{i, j+1\}, Wx\{i+1, j+1\}, B\{i+1, j\}]^1 \leftarrow [Wx\{i, j\}, Wx\{i, j+1\}, Wx\{i+1, j+1\}, B\{i+1, j\}]^0; \\ & [Wx\{i, j\}, W\{i-1, j\}, Wx\{i-1, j+1\}, B\{i, j+1\}]^1 \leftarrow [Wx\{i, j\}, Wx\{i-1, j\}, Wx\{i-1, j+1\}, B\{i, j+1\}]^0; \\ & [Wx\{i, j\}, W\{i, j+1\}, Wx\{i-1, j+1\}, B\{i-1, j\}]^1 \leftarrow [Wx\{i, j\}, Wx\{i, j+1\}, Wx\{i-1, j+1\}, B\{i-1, j\}]^0; \\ & [Wx\{i, j\}, W\{i+1, j\}, Wx\{i+1, j+1\}, B\{i, j+1\}]^1 \leftarrow [Wx\{i, j\}, Wx\{i+1, j\}, Wx\{i+1, j+1\}, B\{i, j+1\}]^0; \\ & [z\{9\}, Wx\{i, j\}]^1 \leftarrow [\#]^2 : 1 \leq i \leq n, 1 \leq j \leq m; \end{aligned}$$

B. Segmentation with a Tissue-Like P System

To work with real medical images, the P-Lingua programming language, including PLinguaCore4, is used in this work. The P-Lingua programming language pioneered the standardization of P systems by providing an open source,

plugin-based software architecture meant for its extension by interested developers. P-Lingua is a software tool that provides a specification language in which designers can define and describe P systems. Furthermore, it provides a set of Java simulators such that users can select the simulator from those included that best suits their requirements. P-Lingua consists of Java standalone software, an application program interface (API) - namely PLinguaCore4 - which performs two operations:

1. Simulate a P system and display the results and
2. Translate a P system between two (presumably different) formats.

On a PLinguaCore4 simulation, the user specifies the location of the input, the format in which this input is encoded and the simulation algorithm. The API then reads through these files looking for the implementation of both the format parser and the simulation algorithm. First, it identifies the P system type defined in the input and checks the existence of the definition in its XML files for this type. If the definition does not exist, PLinguaCore outputs a failure message and halts. Otherwise, the API reads the input file. If this file contains any errors or does not comply with the restrictions defined for its type, the execution halts, and error messages are output.

This information is intended to serve as a guide for debugging the P system. On the other hand, if the file specification correctly describes a P system, then PLinguaCore4 simulates its P system according to the parameters above. The workflow of PLinguaCore4 is shown in Fig. 1.

More precisely, based on Fig. 1, the P-LinguaCore4 API reads the input file to check for syntax errors using the compiler. If there are no errors, a binary file will be generated, which, in turn, will be simulated to produce the final output file. The methodology of the proposed approach is shown in Fig. 2 in which P-Lingua is linked to C# to perform automatic segmentation of real images according to the detail process of each step described in the next subsection. Fig. 3 presents the algorithm of image segmentation.

Loading image

In the first step of the proposed approach, the input image will be loaded into the system using the load button.

The system accepts different image formats, so the image extension can be any of the most common raster image formats (.jpg,.png,.gif, etc.). Once the image is loaded into the system, it will be resized to a specific size for scalable computation. As shown in this work, real medical images were used to test the system; a skin cancer bmp-type image (1280 px × 1024 px), bones jpg-type image (890 px × 694 px), and lung jpg-type image (248 px × 189 px) (Fig. 4a-c), respectively.

Binarization

To work with color images in P-Lingua, many rules will be required to test all possibilities of color relationships between pixels, which, in turn, will impose high computational overhead. To address this drawback, the color images will be converted into binary (black and white) images. The binarization will reduce not only the number of required rules but also the computational time.

Therefore, the input image will be converted to binary with only black and white pixels to simplify the segmentation rules and speed up the execution. Binarization refers to the process in which each pixel in an image is converted into one bit with the value of one or zero depending on the specified threshold value of all pixels. If the pixel value is greater than the particular threshold value, then the pixel will be converted to one; otherwise, it will be zero. A binary image is a digital image with only two possible values for each pixel (black or white). In the proposed approach, the average RGB value of each pixel is computed and then compared with the threshold value (128). If it is greater than the threshold, then the pixel will be converted to white; otherwise, it will be black.

Converting an image to P-Lingua syntax format

Typically, in the standard P-Lingua syntax format, the pixels should have color and coordinates. Basically, the color and coordinates of each pixel will be read and converted to P-Lingua syntax. The standard syntax is to indicate the color of the pixel followed by curly brackets that contain the coordinate of the associated pixel, which, in turn, will be written into the.txt file. For example, in $B\{x,y\}$, x and y are the coordinates of the black pixel in the image as shown in Fig. 5. In this paper, all pixels are converted to the syntax of P-Lingua automatically in the system (Fig. 5).

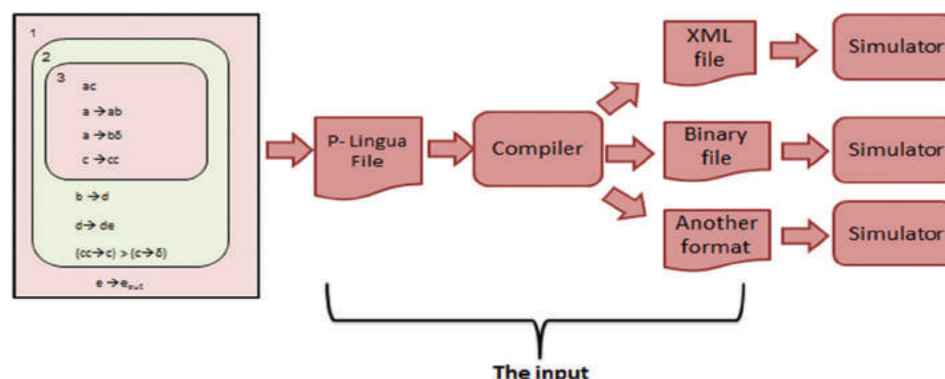


Fig. 1. Workflow of the PLinguaCore Java simulator (Garcia-Quismondo, et al., 2009).

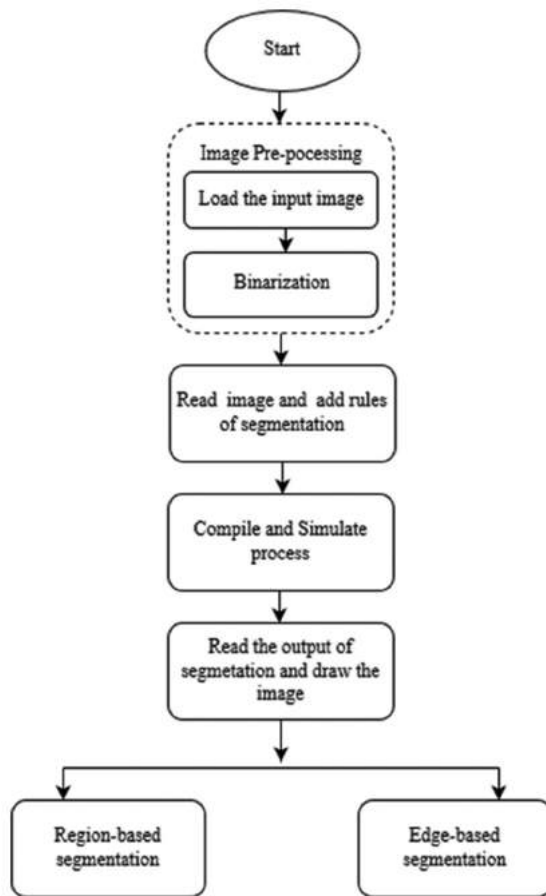


Fig. 2. Methodology of automatic segmentation of real image.

Writing the rules of segmentation in the P-Lingua format

In this paper, the segmentation rules follow the rules of MC for the 2D image segmentation method proposed in the work of Christinal, et al. (2011). The rules are written in the P-Lingua format, appended to the input image, and then saved in a text file, but with a (.pli) extension. This file is now ready to be executed.

Technically speaking, a 2D digital image can be encoded by a matrix in which each pixel in the image is an element of the matrix. Basically, this paper considers two types of neighborhoods surrounding a pixel - namely 4-adjacency and 8-adjacency. In 4-adjacency, four neighborhoods $\{(x-1,y), (x,y+1), (x+1,y), \text{ and } (x,y-1)\}$ contain only the pixels above, below, to the left, and to the right of the central pixel (x,y) as shown in Fig. 6. In 8-adjacency, eight neighborhoods include the four previous neighborhoods plus the four diagonal neighbors, which are $\{(x-1,y-1), (x-1,y), (x-1,y+1), (x,y+1), (x+1,y+1), (x+1,y), (x+1,y-1), \text{ and } (x,y-1)\}$ as illustrated in Fig. 6.

For instance, if the image contains two colors, which are green and blue, if 4-adjacency is considered, the segmentation rules will be as follows:

$$\begin{aligned}
 [G\{i,j\}, B\{i,j+1\}]^1 &\leftrightarrow [Gx\{i,j\}, B\{i,j+1\}]^0; \\
 [G\{i,j\}, B\{i,j-1\}]^1 &\leftrightarrow [Gx\{i,j\}, B\{i,j-1\}]^0; \\
 [G\{i,j\}, B\{i+1,j\}]^1 &\leftrightarrow [Gx\{i,j\}, B\{i+1,j\}]^0; \\
 [G\{i,j\}, B\{i-1,j\}]^1 &\leftrightarrow [Gx\{i,j\}, B\{i-1,j\}]^0;
 \end{aligned}$$

Algorithm 1: Segmentation using P-Lingua

```

input : A real medical image with size n × m
output : The segmented image
1 begin
2   Load the input image
3   Show the original image in PictureBox
4   for (i=0; i < image.Height; i++) do
5     for (j=0; j < image.Width; j++) do
6       Start image binarization process
7       get the RGB values of Pixel (i,j)
8       Compute the average RGB(RGB) value of pixel (i, j)
9       If (RGB) > 128 then
10        RGB(pixel(i,j)) = (255,255,255);
11      else RGB(pixel(i,j)) = (0,0,0);
12      Convert pixel(i,j) to syntax of P-lingua
13      Show the binary image in PictureBox
14      Create a P-lingua file (test.pli)
15      Append the model and parameters to test.pli
16      Append the input image to test.pli
17      for (i=0; i < image.Height; i++) do
18        for (j=0; j < image.Width; j++) do
19          get the RGB values of Pixel (i, j)
20          if (i == image.Height - 1 and j == image.Width - 1)
21            then
22              Add the last pixel of the input image to test.pli
23            else Add the pixel of the input image to test.pli
24              followed by ","
25          Add the rules to test.pli
26          Execute test.pli using PlinguaCore
27          Read and analyze the result from the output cell
28          Draw the image after segmentation
  
```

Fig. 3. Algorithm of image segmentation.

Along the same formulation, if 8-adjacency is considered, then four more rules will be added to cover the diagonal pixels as described in the following:

$$\begin{aligned}
 [G\{i,j\}, B\{i,j+1\}]^1 &\leftrightarrow [Gx\{i,j\}, B\{i,j+1\}]^0; \\
 [G\{i,j\}, B\{i,j-1\}]^1 &\leftrightarrow [Gx\{i,j\}, B\{i,j-1\}]^0; \\
 [G\{i,j\}, B\{i+1,j\}]^1 &\leftrightarrow [Gx\{i,j\}, B\{i+1,j\}]^0; \\
 [G\{i,j\}, B\{i-1,j\}]^1 &\leftrightarrow [Gx\{i,j\}, B\{i-1,j\}]^0; \\
 [G\{i,j\}, B\{i-1,j+1\}]^1 &\leftrightarrow [Gx\{i,j\}, B\{i-1,j+1\}]^0; \\
 [G\{i,j\}, B\{i-1,j-1\}]^1 &\leftrightarrow [Gx\{i,j\}, B\{i-1,j-1\}]^0; \\
 [G\{i,j\}, B\{i+1,j-1\}]^1 &\leftrightarrow [Gx\{i,j\}, B\{i+1,j-1\}]^0; \\
 [G\{i,j\}, B\{i+1,j+1\}]^1 &\leftrightarrow [Gx\{i,j\}, B\{i+1,j+1\}]^0;
 \end{aligned}$$

Linking Java with C# and P-Lingua

As mentioned previously, P-Lingua is an official language for membrane computing. The P-Lingua program can encode a family of P systems (with the help of some parameters) in a flexible manner, whereas the object code generated by the compilation tool specifies only a single P system of the family. In this way, the applications which accept that object code is not required to process parametric systems, so their implementation is much easier.

Once the P-Lingua file with extension.pli is ready, it will be compiled and executed through PLinguaCore4. Recalling

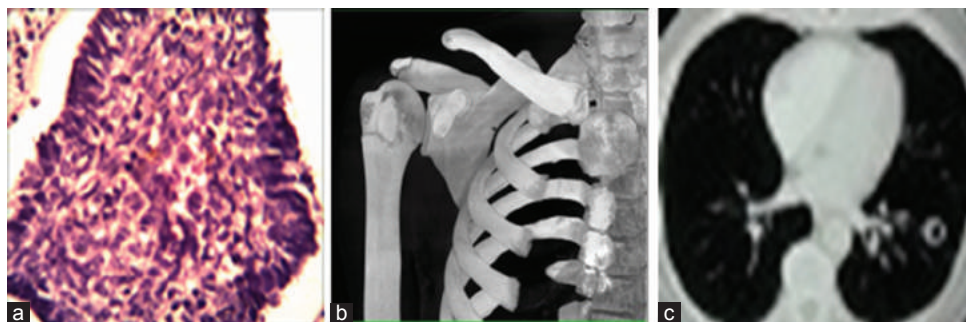


Fig. 4. Input images example; (a) skin cancer, (b) bones, and (c) lungs.

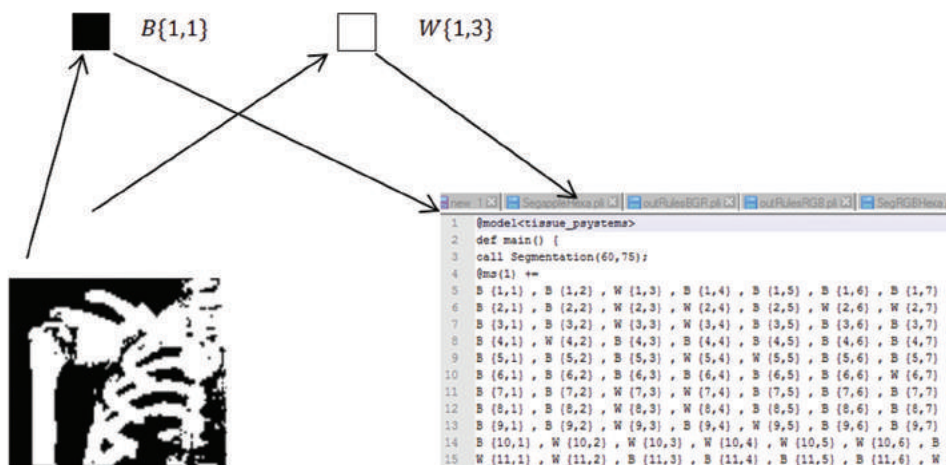


Fig. 5. Illustration of the binary image in P-Lingua.

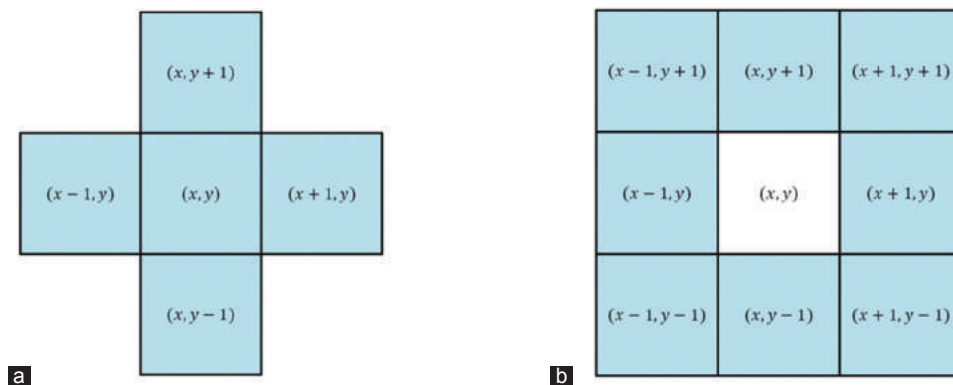


Fig. 6. 4 and 8-adjacency; (a) 4-neighborhood and (b) 8-neighborhood.

that C# should be linked to Java to perform this operation, a Java process (java.exe) will be invoked from the C# environment.

Reading output and visualization

The final result of the segmentation process is written to the file that is generated after segmentation (.txt). This file contains the details of every step of segmentation as well as information such as the configuration, input of the cell, output of the cell, environment, time of every step, memory usage, and final time of execution as shown in Table I.

Once the image has been segmented using MC, recalling that our model contains two different cells, the output can be read from any of these cells as needed. In the first case, if the

output is read from cell two, then edge-based segmentation will be obtained and visualized. It is worth mentioning that cell two contains the border and edge pixels, which is why edge-based segmentation can be obtained from this particular cell. Otherwise, in the second case, if the output is being read from cell one, then region-based segmentation will be obtained. More specifically, two types of segmentation strategies can be obtained regarding the philosophy of reading the output from the chosen cell.

Reading output and visualization from cell one

To draw the image according to the region-based criteria, the outputs of cell one and cell two must be read. To

Algorithm 2: Drawing of the segmented image according to Region-Based Segmentation

```

input : The generated output file in text
output : The segmented image based on region -based segmentation
1 begin
2   While outfile contain lines do
3     Read the generated output file line by line
4     Create a string Output to store the edge from cell two
5     Create a string outputcellone to store the white pixels from
      cellone
6   Create a string outputcellone1 to store the black pixels from
      Cell one
7   Read the final execution time and print it
8   Read the memory and print it
9   if Output is not empty then
10    prepare the string output to store only the coordinates of the border pixels
11   if Outputcellone is not empty then
12    prepare the string outputcellone to store only the coordinates of the
      white pixels
13   if Outputcellone1 is not empty then
14    prepare the string outputcellone1 to store only the coordinates of the
      black pixels
15   Create a bitmap image (outputting) to visualize the pixels
16   for (i=0; i<outputting.Height; i++) do
17     for (j=0; j<outputting.Width; j++) do
18       if (output(i,j) == 1) then
19         Draw this pixel as blue
20         color=Color.FromArgb(0,0,255);
21         outputting.SetPixel(j,i,color);
22       if (outputcellone(i,j) == 1) then
23         Draw this pixel as blue
24         color=Color.FromArgb(255,255,255);
25         outputting.SetPixel(j,i,color);
26       else (outputcellone1(i,j) == 1) then
27         Draw this pixel as black
28         color=Color.FromArgb(0,0,0);
29         outputting.SetPixel(j,i,color);
30   preview the outputting in the picture box

```

Fig. 7. Algorithm of drawing the output image from cell one.

formulate this idea, three strings will be created to keep track of the output from the two cells. To be specific, the first string called the output will store the output of cell two. Similarly, the second and third string - namely outputCellone and outputCellone1 - will be used to store the contents of cell one. Technically speaking, outputCellone will be used to keep track of the white-colored pixels from input cell one. In the same context, outputCellone1 will be utilized to keep track of the black-colored pixels from input cell one. To obtain the output of cell two from Jout.txt, the algorithm will search for the last index of the word "Multiset" and take a substring starting from this index until the last index of "ENVIRONMENT;" this will return the multiset of cell two only. Fig. 7 explains the algorithm to perform region-based segmentation.

Reading output and visualization from cell two

Once the image has been segmented using MC rules in the P-Lingua environment, we must visualize the image after edge-based segmentation. To accomplish this, we must read the output P-Lingua file that contains the result of edge-based segmentation. As commonly known in MC, P-Lingua

Algorithm 3: Drawing of the segmented image according to Edge-Based Segmentation

```

input : The generated output file in text
output : The segmented image based on edge -based segmentation
1 begin
2   While outfile contain lines do
3     Read the generated output file line by line
4     Create a string Output to store the edge from cell two
5     Read the final execution time and print it
6     Read the memory and print it
7     prepare the string output to store only the coordinates of the border pixels
8     if Output is not empty then
9       Replace all the ";" with ",";
10      Get a substring starting from the first occurrence of ","
11      Replace all the "WX" with " "
12      Replace all the "}" with ""
13      Split string output based on ; and store in temp
14      for (i=0; i<temp.length; i++) do
15        Index=temp[i].Split(',');
16        outArray[int.Parse(index[0])-1,int.Parse(index[1])-1]=1;
17      Create a bitmap image (outputting) to visualize the pixels
18      for (i=0; i<outputting.Height; i++) do
19        for (j=0; j<outputting.Width; j++) do
20          if (outArray(i,j) == 1) then
21            Draw this pixel as black
22            color=Color.FromArgb(0,0,0);
23            outputting.SetPixel(j,i,color);
24          else (outArray(i,j) == 0)
25            Draw this pixel as white
26            color=Color.FromArgb(255,255,255);
27            outputting.SetPixel(j,i,color);
28      Preview the outputting in the picture box

```

Fig. 8. Algorithm of drawing the output image from cell two.

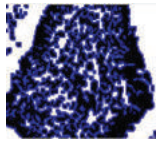
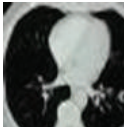
generates an output file that stores the result of the input and the output cell as long as the configuration continues.

To draw the image according to the edge-based segmentation strategy, the output of only cell two must be read. In contrast, it is notable that in the region-based segmentation technique, the outputs of both cell one and cell two are read synchronously. To establish this idea technically, an output string will be created to keep track of the output from cell two. To be specific, this string, called "output," will store the output of cell two, which contains the coordinates of the edge pixels (borders). Specifically, to obtain the output of cell two from the generated output file "Jout.txt," the algorithm will search for the last index of the word "Multiset" and take a substring starting from this index until the last index of "ENVIRONMENT;" this will return the multiset of only cell two. Fig. 8 explains the algorithm to perform edge-based segmentation (Table II).

V. EFFICIENCY OF THE PROPOSED TISSUE-LIKE P SYSTEM SEGMENTATION COMPARED TO GROUND TRUTH IMAGE

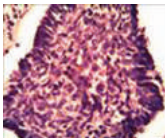
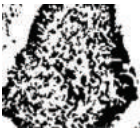
In this section, a thorough evaluation procedure is carried out to demonstrate the robustness of the proposed method on real image segmentation. To illustrate the effectiveness of the proposed segmentation approach, the segmentation results obtained from four adjacencies are compared with eight adjacencies. The algorithm is evaluated in terms of accuracy and efficiency, in which accuracy corresponds to the degree

TABLE I
COMPARING THE PERFORMANCE OF 4-ADJACENCY AND 8-ADJACENCY USING TWO DIFFERENT PLATFORMS BASED ON REGION-BASED SEGMENTATION IN TERMS OF TIME AND MEMORY SPACE

Images	Binarization	Segmentation	Intel Core i5		Intel Core i7			
			4-adjacency	8-adjacency	4-adjacency	8-adjacency		
 100×126 (bmp)			T	4852.885 s	4466.74 s	T	1689.833 s	1646.49 s
			M	423613 kb	645781 kb	M	825744 kb	654328 kb
 100×77 (jpg)			T	1212.017 s	1180.237 s	T	610.749 s	608.125 s
			M	647924 kb	594864 kb	M	714432 kb	805258 kb
 64×47 (jpg)			T	129.433 s	123.891 s	T	94.584 s	87.834 s
			M	891580 kb	568198 kb	M	607691 kb	695966 kb

T: Time used for segmenting the image. M: Memory space used for segmenting the image

TABLE II
COMPARING THE PERFORMANCE OF 4-ADJACENCY AND 8-ADJACENCY USING TWO DIFFERENT PLATFORMS BASED ON EDGE-BASED SEGMENTATION IN TERMS OF TIME AND MEMORY SPACE.

Images	Binarization	Segmentation	Intel Core i5		Intel Core i7			
			4-adjacency	8-adjacency	4-adjacency	4-adjacency		
 100×126 (bmp)			T	4708.789s	4641.864s	T	3024.055 s	2568.154 s
			M	469123 Kb	652117kb	M	684737 kb	616432 kb
 100×77 (jpg)			T	1659.376 s	1334.951 s	T	517.114 s	515.771 s
			M	802063 kb	581857 kb	M	713158 kb	858164 kb
 64×47 (jpg)			T	137.026 s	125.355 s	T	82.119 s	70.67 s
			M	632686 kb	750024 kb	M	570762 kb	711489 kb

T: Time used for segmenting the image. M: Memory space used for segmenting the image

with which the delineation of the object corresponds to the truth. Efficiency corresponds to the amount of time required to perform the segmentation. The Jaccard index method (Shi, et al., 2014) is used to measure the accuracy of the segmentation for both region-based metrics and boundary-

based metrics. Typical region-based evaluation metrics correspond to the ratio of the number of matching pixels to the total number of both matching pixels and mismatching pixels. Boundary-based metrics focus on the evaluation of the distorted segment result's boundary compared to the ground

truth image. To evaluate the segmentation quality, the Jaccard index method measures the similarity between the ground truth of the original image and that of the segmented image. The segmentation result and its corresponding ground truth are typically denoted by S and G, respectively. The Jaccard index is defined as follows:

$$\text{Jaccard Index} = \frac{A(G \cap S)}{A(G \cup S)} \quad (1)$$

Where, A(.) is the operation of counting the amount. In Equation (1), the numerator corresponds to the number of matching pixels (true positives), whereas the denominator counts the total number of matching and mismatching pixels. Basically, it is an absolute “0” or “1,” and the closer the value to one, the better the segmentation.

In the first experiment, we compare the performance of 4-adjacency and 8-adjacency relations for both region-based and edge-based real image segmentation, and the results are

presented in Tables III and Table IV, respectively. From the obtained results, it is evident that 4-adjacency outperforms 8-adjacency for region-based segmentation. However, for edge-based segmentation, 8-adjacency achieves better results than 4-adjacency in the skin cancer image and lung image, whereas for the bone image, the performance is similar, as shown in Fig. 9.

As can be depicted from the results in Fig. 9, changing the value of the threshold dramatically affects the accuracy of segmentation. For instance, considering the edge-based segmentation of the bone image, when the value of the threshold is set to 0.9, the accuracy is very low, whereas when setting the value of the threshold to 0.5, the best results are obtained.

In the next experiment, ground truth benchmark data are used to compare the performance between 4-adjacency and 8-adjacency in terms of accuracy. The benefit of using benchmark data is that one is able to compare results with those of other approaches in a significant way. Therefore, using ground truth data, the same experimental procedure is repeated for edge-based and region-based segmentation as

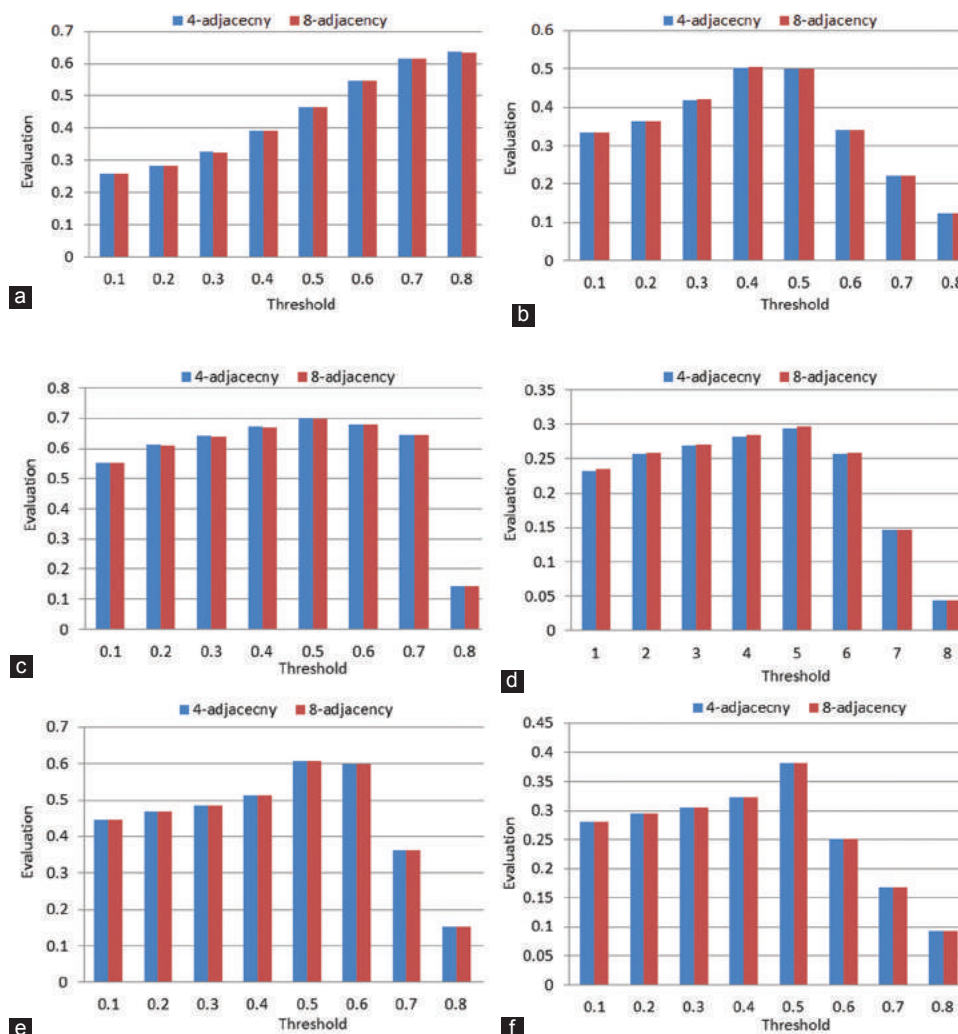


Fig. 9. Effect of the value of threshold parameter on region- and edge-based segmentation performance; (a) and (b) skin cancer image, (c) and (d) lung image, and (e) and (f) bone image.

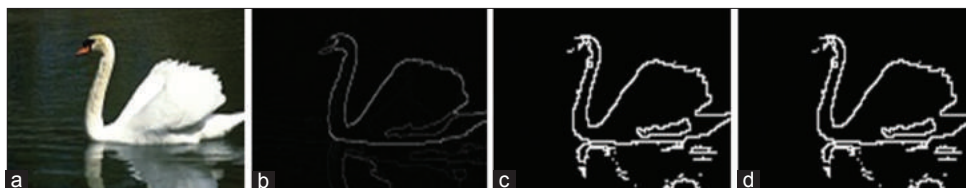


Fig. 10. Original image, ground truth, and results of the proposed edge-based segmentation.

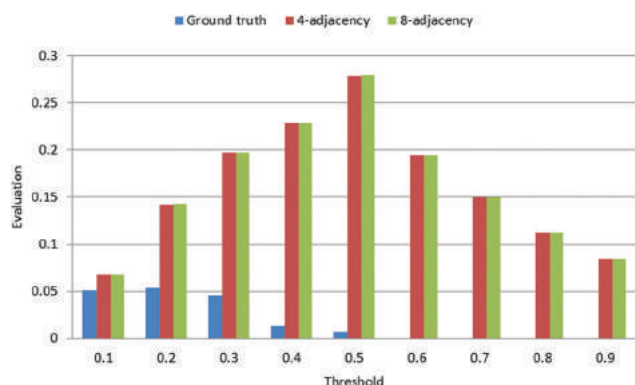


Fig. 11. Comparison between the ground truth benchmark with the proposed 4-adjacency and 8-adjacency edge-based segmentation in terms of evaluation against the threshold.

TABLE III
JACCARD INDEX ACCURACY FOR 4-ADJACENCY AND 8-ADJACENCY OF REGION-BASED SEGMENTATION

Results	Skin cancer	Bone	Lung
4-adjacency	0.6344	0.6071	0.7011
8-adjacency	0.6336	0.6071	0.6987

TABLE IV
JACCARD INDEX ACCURACY FOR 4-ADJACENCY AND 8-ADJACENCY OF EDGE-BASED SEGMENTATION

Results	Skin cancer	Bone	Lung
4-adjacency	0.5028	0.3815	0.2941
8-adjacency	0.5032	0.3815	0.2965

TABLE V
JACCARD INDEX VALUES OF THE GROUND TRUTH IMAGE, 4-ADJACENCY, AND 8-ADJACENCY (EDGE-BASED SEGMENTATION)

Type of image	Ground truth	4-adjacency	8-adjacency
Swan	0.0507	0.2791	0.2795

presented in the following.

Edge-based segmentation

In this experiment, the dataset used for evaluating the proposed system is a swan image of size 481×321 with its ground truth, as shown in Fig. 10. Note that this dataset has been taken from the Berkeley segmentation dataset (BSDS500) benchmark (Computer Vision Group, 2013).

The image of the ground truth data is compared to the original image of swan using the Jaccard index. The original image is segmented using the proposed tissue-like P system segmentation of two adjacency relationships - that

is, 4-adjacency and 8-adjacency. The Jaccard index method is used to compare the result of the ground truth with 4-adjacency and 8-adjacency, as seen in Fig. 10. The results in Table V show that the segmentation using the 8-adjacency relationship outperforms the 4-adjacency counterparts for the swan image, and both 4- and 8-adjacency segmentations outperform the ground truth. In Fig. 11, the larger the threshold values, the better the segmentation accuracy of the proposed approach. However, with larger threshold values, the ground truth accuracy deteriorates, and the proposed tissue-like P system segmentation becomes better for deep visualization of the image including the shadow and the lake.

Region-based segmentation

In this experiment, the benchmark dataset used for evaluating the proposed system is a duck image (Rahtu, et al., 2010) with size of 400×300 pixels from the ground truth dataset was used for evaluation and the results as shown in Fig. 12. Region-based segmentation using 4-adjacency and 8-adjacency relationships was conducted using the proposed method.

As can be seen from the results in Table VI and Fig. 12, both types of relationship adjacencies achieved similar results. Fig. 12 reveals that the segmentation using ground truth is slightly better accurate than the proposed method, but visually in the ground truth image, the eye and peak of duck and the lines of sea were not accurately detected. For the proposed approach, the eye and peak of duck and the lines of sea were detected.

In Fig. 13, the effect of using different threshold values was evaluated and compared. The results show that, with a threshold value of 0.6–0.8, the best segmentation results were obtained.

VI. CONCLUSION

The effectiveness and robustness of the proposed work have been presented. Two different platforms were used in this experiment: A PC with an Intel Core i5-M430 processor running at 2.27 GHz and 4 GB of memory, and a PC with an Intel Core i7-M430 processor running at 2.27 GHz and 4 GB of memory.

In the first experiment, a region-based segmentation approach was evaluated, and the results showed that 8-adjacency relationships gave better performance in terms of computational time and memory usage. This was due to the capability of 8-adjacency with eight pixels around the center, which reduces the communication rules for obtaining the final segmentation output.

In the second experiment, an edge-based segmentation

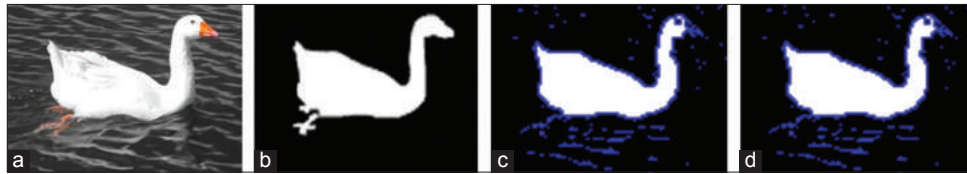


Fig. 12: Region-based segmentation results between original image, ground truth, and proposed method.

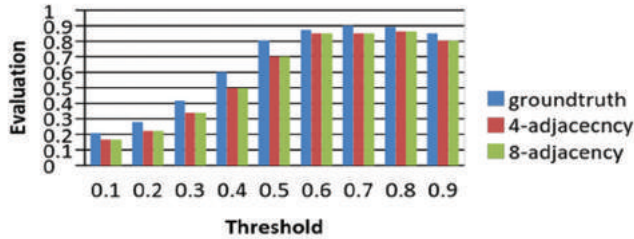


Fig. 13. Comparison between the ground truth benchmark and the proposed 4-adjacency and 8-adjacency region-based segmentation in terms of evaluation against thresholding.

TABLE VI

JACCARD INDEX VALUES OF THE GROUND TRUTH IMAGE, 4-ADJACENCY, AND 8-ADJACENCY (REGION-BASED SEGMENTATION)

Type of image	Ground truth	4-adjacency	8-adjacency
Duck.png	0.9004	0.8642	0.8642

approach was evaluated, and once again the results of 8-adjacency are better, with significant time reduced using the Intel Core i7 platform.

The contributions of the paper are summarized as follows: First, the input image was codified automatically by linking P-Lingua with the C# platform. Second, two types of adjacency relationships were investigated and compared in terms of performance and speed on two different hardware platforms. The proposed methods were tested using real medical images from different image formats. Furthermore, two types of neighborhood adjacency were used to test the performance. It is worth mentioning that, to the best of our knowledge, no study has been performed on the efficiency of automatic real image segmentations using membrane computing. Our experimental results showed that the use of 8-adjacency achieved faster computational time due to the reduced number of rules needed to complete the segmentation process.

The limitation of our approach is on sequential architecture simulation for the experiments, which, in turn, does not exploit the massive parallelism inherent in P systems. In our future work, to make full use of the MC parallelism, a parallel architecture such as CUDA™ will be used to gain higher performance speedups over the typical serial implantation.

VII. ACKNOWLEDGMENT

This work is partially supported by The Malaysian Ministry of Higher Education under the Fundamental Research Grant Scheme (4F802 and 4F786). The authors would like to

thank the Research Management Centre (RMC), Universiti Teknologi Malaysia (UTM), for the support in R and D.

REFERENCES

Alslibi, B., Venkat, I., Subramanian, K. and Christinal, H., 2014. *A Bio-Inspired Software for Homology Groups of 2D Digital Images*. Asian Conference on Membrane Computing ACMC 2014, Coimbatore, pp.1-4.

Carnero, J., Díaz-Pernil, D. and Gutiérrez-Naranjo, M.A., 2011. Designing tissue-like P systems for image segmentation on parallel architectures. *Ninth Brainstorming Week on Membrane Computing*, 2011, pp.43-62.

Carnero, J., Díaz-Pernil, D., Molina-Abril, H. and Real, P., 2010. Image segmentation inspired by cellular models using hardware programming. *3rd International Workshop on Computational Topology in Image Context*, 1(3), pp.143-150.

Christinal, H.A., Díaz-Pernil, D. and Jurado, P.R., 2009. Segmentation in 2D and 3D image using tissue-like P system. *Progress in Pattern Recognition, Image Analysis, Computer Vision, and Applications*. Springer, Switzerland, pp.169-176.

Christinal, H.A., Díaz-Pernil, D. and Real, P., 2010. P systems and computational algebraic topology. *Mathematical and Computer Modelling*, 52(11), pp.1982-1996.

Christinal, H.A., Díaz-Pernil, D. and Real, P., 2011. Region-based segmentation of 2D and 3D images with tissue-like P systems. *Pattern Recognition Letters*, 32(16), pp.2206-2212.

Christinal, H.A., Díaz-Pernil, D., Gutiérrez-Naranjo, M.A. and Pérez-Jiménez, M.J., 2010. Thresholding of 2D images with cell-like P systems. *Romanian Journal of Information Science and Technology (ROMJIST)*, 13(2), pp.131-140.

Christinal, H.A., Díaz-Pernil, D., Jurado, P.R. and Selvan, S.E., 2012. Color segmentation of 2D images with thresholding. *Eco-friendly Computing and Communication Systems*, 305, pp.162-169.

Computer Vision Group. 2013. *Contour Detection and Image Segmentation Resources*. University of California, Berkely. Available from: <http://www.eecs.berkeley.edu/Research/Projects/CS/vision/grouping/resources.html>. [Last accessed on 2016 Jan 10].

Díaz-Pernil, D., Berciano, A., Peña-Cantillana, F. and Gutiérrez-Naranjo, M.A., 2013. Segmenting images with gradient-based edge detection using membrane computing. *Pattern Recognition Letters*, 34(8), pp.846-855.

Díaz-Pernil, D., Gutiérrez-Naranjo, M.A., Molina-Abril, H. and Real, P., 2012. Designing a new software tool for digital imagery based on P systems. *Natural Computing*, 11(3), pp.381-386.

Díaz-Pernil, D., Gutiérrez-Naranjo, M.A., Real, P. and Sánchez-Canales, V., 2010. Computing homology groups in binary 2D imagery by tissue-like P systems. *Romanian Journal of Information Science and Technology*, 13(2), pp.141-152.

Díaz-Pernil, D., Molina-Abril, H., Real, P. and Gutiérrez-Naranjo, M., 2010. A bio-inspired software for segmenting digital images. Proceeding of the 2010 IEEE fifth international conference on Bio-inspired computing theories and applications BIC_TA, computer. *Society*, 2, pp.1377-1381.

García-Quismondo, M., Gutiérrez-Escudero, R., Pérez-Hurtado, I. and Pérez-Jiménez, M.J., 2009. P-lingua 2.0: New features and first applications. *Proceedings of the Seventh Brainstorming Week on Membrane Computing, Sevilla, Spain*, 1, pp.141-167.

- Ionescu, M., Paun, G. and Yokomori, T., 2006. Spiking neural P systems. *Fundamenta Informaticae*, 71(2), pp.279-308.
- Isawasan, P., Venkat, I., Subramanian, K., Khader, A., Osman, O. and Christinal, H., 2014. Region-based segmentation of Hexagonal digital images using membrane computing. *Asian Conference on Membrane Computing (ACMC)*, pp.1-4.
- Marti, C., Păun, G. and Pazos, J., 2003. Tissue P systems. *Theoretical Computer Science*, 296(2), pp.295-326.
- Martin-Vide, C., Pazos, J., Păun, G. and Rodríguez-Patón, A., 2002. A new class of symbolic abstract neural nets: Tissue P systems. *Computing and Combinatorics*, 2327, pp.290-299.
- Păun, G. and Rozenberg, G., 2002. A guide to membrane computing. *Theoretical Computer Science, Elsevier*, 287(1), pp.73-100.
- Păun, G., 2000. Computing with membranes. *Journal of Computer and System Sciences*, 61(1), pp.108-143.
- Păun, G., 2002. Introduction: Membrane computing—what it is and what it is not. *Membrane Computing*. Springer, London, pp.1-6.
- Peña-Cantillana, F., Díaz-Pernil, D., Berciano, A. and Gutiérrez-Naranjo, M.A., 2011. A parallel implementation of the thresholding problem by using tissue-like P systems. *International Conference on Computer Analysis of Images and Patterns*, 29, pp.277-284.
- Pena-Cantillana, F., Diaz-Pernil, D., Christinal, H.A. and Gutiérrez-Naranjo, M.A., 2011. Smoothing problem in 2D images with tissue-like P systems and parallel implementation. *Proceedings of the Ninth Brainstorming Week on Membrane Computing*. Fénix Editora, pp.317-328.
- Peng, H., Shao, J., Li, B., Wang, J., Pérez-Jiménez, M.J., Jiang, Y. and Yang, Y. 2012. Image thresholding with cell-like P systems. *Proceedings of the Tenth Brainstorming Week on Membrane Computing*, 2, p.3.
- Peng, H., Wang, J. and Pérez-Jiménez, M.J., 2015. Optimal multi-level thresholding with membrane computing. *Digital Signal Processing*, 37, pp.53-64.
- Peng, H., Yang, Y., Zhang, J., Huang, X. and Wang, J., 2014. A region-based color image segmentation method based on P systems. *Science and Technology*, 17(1), pp.63-75.
- Rahtu, E., Kannala, J., Salo, M. and Heikkila, J., 2010. Segmenting salient objects from images and videos. *ECCV*, pp.366-379. Available from: <http://www.cg.cs.tsinghua.edu.cn/people/~cmm/saliency2/>.
- Reina-Molina, R., Carnero, J. and Diaz-Pernil, D., 2010. Image segmentation using tissue-like P systems with multiple auxiliary cells. *Image-A*, 1(3), pp.143-150.
- Shapiro, L. and Stockman, G.C., 2001. *Computer Vision*. 2001 ed. Prentice Hall, Englewood. Cliffs, NJ.
- Sheeba, F., Thamburaj, R., Nagar, A.K. and Mammen, J.J., 2011. *Segmentation of Peripheral Blood Smear Images using Tissue-Like P Systems*. Bio-Inspired Computing: Theories and Applications (BIC-TA), 2011 Sixth International Conference on, IEEE, pp.257-261.
- Shi, R., Ngan, K.N. and Li, S., 2014. Jaccard index compensation for object segmentation evaluation. *IEEE International Conference on Image Processing*, 71, pp.4457-4461.
- Yahya, R.I., Hasan, S., George, L.E. and Alsalibi, B., 2015. Membrane computing for 2D image segmentation. *International Journal of Advances in Soft Computing and its Applications*, 7(1), 1-15.
- Yahya, R.I., Shamsuddinirst, S.M. Hasan, S., Yahyam, S.I., Hasan, S., Salibi B. and Al-Khafajiani, G., 2017. Image segmentation using membrane computing: A literature survey. Chapter: Bio-inspired computing – Theories and applications. *Communications in Computer and Information Science*, 368, pp.314-335.
- Yahya, R.I., Shamsuddinirst, S.M., Hasan, S. and Yahya, S.I., 2016. Tissue-like P system for Segmentation of 2D hexagonal images. *ARO-The Scientific Journal of Koya University*, 4(1), pp.35-42. doi: <http://dx.doi.org/10.14500/aro.10135>
- Yang, Y., Peng, H., Jiang, Y., Huang, X. and Zhang, J., 2013. A region-based image segmentation method under P systems. *Journal Information Computer Sciences*, 10(10), pp.2943-2950.
- Zhang, Z. and Peng, H., 2012. Object segmentation with membrane computing. *Journal of Information and Computational Science*, 9(17), pp.5417-5424.

Factors Controlling the Development of Wine-Glass Forms in the Mountains of the Kurdistan Region, Iraq

Varoujan K. Sissakian^{1,2}, Arsalan A. Othman³ and Ahmed T. Shihab⁴

¹Department of Natural Resources Engineering and Management, School of Science and Engineering, University of Kurdistan Hewler, Erbil, Kurdistan Region - F.R. Iraq

²Private Consultant Geologist Ainkawa, Erbil 44001, Kurdistan Region - F.R. Iraq

³Iraq Geological Survey, Sulaymaniyah Office, Sulaymaniyah, Kurdistan Region - F.R. Iraq

⁴Iraq Geological Survey, Al-Andalus Square, Baghdad 10068, F.R. Iraq

Abstract – The northern and northeastern parts of Iraq are mountainous areas and rugged topography with different erosional and morphological forms; among them are the wine-glass (erosional cirques) forms. They are developed in different shapes, sizes, and depths. In the outlets of the wine-glass forms; usually, alluvial fans are formed. The studied area is characterized by the presence of long and narrow anticlines with NW–SE trend that changes westward to E–W trend. The Cretaceous carbonate rocks form the main carapace of the majority of the mountains; however, locally Paleogene and/or Jurassic rocks form the carapace. In the core, rocks down to Devonian are exposed. In those anticlines where only Cretaceous rocks are exposed, no or very rarely wine-glass forms are developed. This is attributed to the Cretaceous carbonate rocks, which exist in huge thicknesses in many formations, with thickly bedded to massive nature and very hard erosion resisting rocks. Tens of the existing wineglass forms are studied to indicate the factors that control their development, which are the type of exposed rocks, their thicknesses, and hardness. To perform the aim of this study, different satellite imagery with different resolutions was used; besides using GIS technique and field check to improve the acquired data.

Index Terms — Wine-glass form, Erosional-cirque, Alluvial-fan, Cretaceous rocks, Kurdistan Region.

I. INTRODUCTION

The northern and northeastern parts of the Iraqi Kurdistan region are located in the Extremely Rugged Mountainous and High Amplitude Mountainous Provinces and form physiographically mountainous areas with very rugged

topography (Othman and Gloaguen, 2014, 2013a and b; Sissakian and Fouad, 2012). The relief differences are highly variable in different parts of the studied area, attaining up to 2500 m, and exceptionally more. This rugged topography is attributed to the presence of long and narrow anticlines with the effect of the climatic factors that have contributed to increasing the intensity of the erosion, the water being the main agent. Consequently, the anticlines are deeply dissected by tens of erosional forms, among them are the erosional cirques; they will be called in this study as “wine-glass forms” because many publications dealing with geomorphology in the same area have used the same term.

A cirque is an amphitheater-like valley head, formed at the head of a valley glacier by erosion (Mitchel and Humphries, 2014). However, Gornitz (2009) defined the cirque as “although a less common usage, the term cirque is also used for amphitheater-shaped, fluvial-erosion features.” Alternative names for this landform are “corrie” (from Scottish Gaelic coire meaning a pot or cauldron) and “cwm” (Welsh for “valley”). A cirque may also be a similarly shaped landform arising from fluvial erosion (Upton and Wadsworth, 1969); also mentioned by Evans and Cox (1974), Huggett (2007), Gornitz (2009), and Bahrami (2012).

Alden (2014) also defined the cirque or wine-glass form as “A bowl-shaped rock valley on the side of a mountain, often with a glacier or permanent snowfield in it.” Moreover, Al-Jaf and Kadhim (2010), Al-Ma’amar et al. (2011), Yacoub et al. (2012), and Sissakian et al. (2014) also have adopted and used the term of wine-glass form in the Iraqi mountainous areas during describing geomorphological features of the northern and northeastern parts of Iraqi Kurdistan region.

Makhtesh is another form of wine-glass, found in karst landscapes it is formed by intermittent river flow cutting through layers of limestone and chalk leaving sheer cliffs (Wikipedia, 2014). This term, however, is not concerned in this study.

The main aims of this study are to discuss the origin and development of wine-glass forms within certain parts of the studied area; their absence in many others and to elucidate the role of the lithology, tectonics, and erosion in their development.

The location of this study extends in the northern and northeastern parts of Iraq, especially, north of latitude 36° N;

ARO-The Scientific Journal of Koya University
Volume VI, No 2(2018), Article ID: ARO.10415, 10 pages
DOI: 10.14500/aro.10415

Received 30 April 2018; Accepted 05 December 2018

Regular research paper: Published 20 December 2018

Corresponding author’s e-mail: f.khajeek@ukh.edu.krd

Copyright © 2018 Varoujan K. Sissakian, Arsalan A. Othman and Ahmed T. Shihab. This is an open access article distributed under the Creative Commons Attribution License.



at the western part and north of latitude 35° N; at the eastern part (Fig. 1, north of the oblique red line). The coverage area of the studied area is about 59325 km². The studied area is located, tectonically, in the Outer Platform of the Arabian Plate (Fouad, 2012a). Rocks of different ages are exposed in the studied area; ranging from Triassic to Tertiary (Sissakian and Fouad, 2012); however, the majority of the exposed rocks in which wine-glass forms are exposed belong to the Cretaceous period.

II. MATERIALS USED AND METHODOLOGY

Many materials were used to achieve the aim of this study, represented by geological maps, at a scale of 1: 100,000 and 1: 250,000, topographical maps, at scale of 1: 100,000, digital elevation model (DEM) and satellite images; such as Landsat and QuickBird data, and relevant published articles and reports. These materials were used to recognize the anticlines, which exhibit wine-glass forms, in the studied area.

Geological maps and reports of the studied area are compiled by Sissakian (1995, 1993), Fouad (2007), Al-Mousawi et al. (2008), Sissakian and Fouad (2014a, 2014b, 2014c). Moreover, some geological hazard maps and related publications were used too; to indicate extensive erosional areas where wine-glass forms may be developed in the studied area (Sissakian and Al-Jibouri, 2014a; Sissakian and Ibrahim, 2005, 2004a, 2004b; Sissakian, 2013, 2010; Sissakian et al., 2008a, 2008b, 2008c).

Fieldwork was carried out for the period 2006–2012, Sissakian and Fouad (2012) during updating the existing geological maps at different scales in the Iraqi Kurdistan region. The fieldwork was utilized to acquire interesting data, such as type of the exposed rocks in and around the wine-glass forms. Some structural data such as the asymmetry of the limbs, size of the folds, and the distance between the folds were also reviewed to elucidate the relationship between the wine-glass forms and the present structural features.

For performing the current work, 20 QuickBird scenes were used. They were obtained through the Ministry of Planning (Iraq) and were acquired from August 18, 2002, to August 29, 2006. These scenes are 8-bit, orthorectified, and radiometrically corrected, with 0.6 m spatial resolution. Only the three-visible spectral (i.e., blue [450–520 nm], green [520–600 nm], and red [630–690 nm]) bands were processed. These three visible spectral bands data were pan-sharpened using the UNB algorithm (DigitalGlobe, 2006). ArcGIS 10

was used to digitize the wine-glass boundaries, calculate the wine-glass area and prepare base map. The wine-glass form's boundaries were identified from the satellite data based on morphological characteristics such as tone, texture, and the scarps.

III. PREVIOUS STUDIES

Although many publications and reports are available for the studied area, none of the existing works have mentioned about the details of the wine-glass forms. Some of these works have dealt with different geomorphological aspects in the studies area such as Hamza (1997). Although he compiled the geomorphological map of Iraq at a scale of 1:1,000,000 but he did not represent and/or mention the wine glass forms in the compiled map and/ or the enclosed report. Al-Jaf and Kadhim (2010), Al-Ma'amar et al. (2011) investigated parts of the studied area, too. They compiled the geomorphological map with a scale of 1: 250,000 for Kirkuk Quadrangle, and Erbil and Mahabad Quadrangles, respectively, and mentioned about the presence of the wine-glass forms. Yacoub et al. (2012) and Sissakian et al. (2014) compiled the geomorphological map of the low folded zone and the high folded zone in Iraq, respectively, and reported about the presence of many wine-glass forms.

IV. WINE-GLASS FORMS

A. General

Wine-glass forms are forms of erosional cirques; they may be formed due to fluvial erosion. Their shape is described as “concave amphitheater shape is open on the downhill side corresponding to the flatter area of the stage, whereas the cupped seating section is generally steep, cliff-like slopes down, which slope debris combine and converge from the three or more higher sides” (Ward et al., 2000).

B. Enlargements of Wine-glasses Forms

The floor of each wine-glass form ends up bowl-shaped; as it is the complex convergence zone of combining water flows from multiple directions and their accompanying rock burdens, hence, experiences somewhat greater erosion

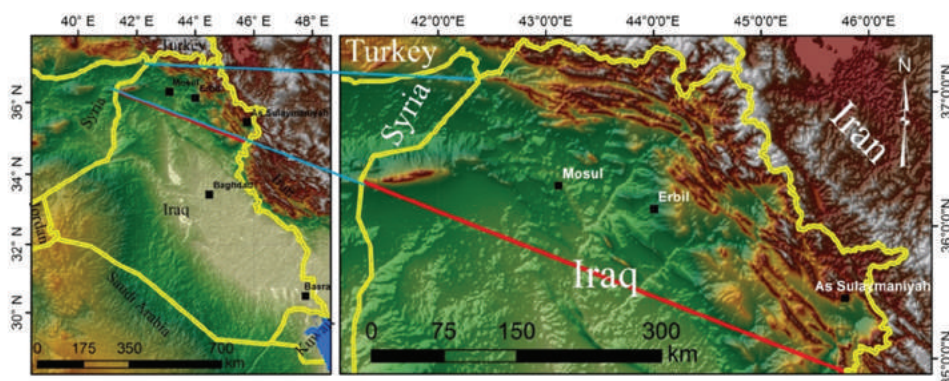


Fig. 1. Digital elevation model GMTED2010 (resolution 30 Arc) overlapping hillshade showing the location of the studied area.

forces. It is most often over-widened backward (backstage) and sideward of the wine-glass form to conjugate with a neighboring one forming a large wine glass form, and very rarely, many wine-glass forms conjugate each other to occupy the whole core of an anticline; forming one large wine-glass form, usually, with many outlets; representing their original outlet forms.

A good example of enlarged wine-glasses is Gara anticline (Fig. 2). Such large wine-glass forms are formed in the studied area only when soft rocks are exposed in the core of the anticline. The Triassic rocks, represented by Baluti Formation (Late Triassic), which consists of soft shale (Sissakian and Saeed, 2012) are highly weathered and eroded; therefore, all formed wine-glass forms are conjugated together to form one very large wine-glass form that almost occupies the whole core of the Gara anticline (Fig. 2). However, when the core and limbs of an anticline consist of hard rocks and in between them are soft rocks, which are easily eroded forming slopes and/or undulated landscape; then the core is remained, and a large wine-glass form is formed around the core with many outlets (Fig. 3).

The development of large wine-glass forms is attributed to: (1) The presence of hard rocks in the cores of anticlines, (2) the hardcore is dissected by steep valleys that drain the

rainwater toward the soft rocks, (3) the soft rocks (Shiranish, Tanjero, Kolosh, and Gercus formations) are easily weathered and eroded forming gentle slopes and longitudinal valleys, (4) the hard rocks of the Qamchuqa, Bekhme, and Pila Spi formations in the outer parts of the anticlinal limbs also play the same role in accelerating the erosion of the soft rocks, (5) the accumulated water finds the easiest discharge area from the outer part of the limb to discharge the water with the sediments out of the anticline because it will represent the weakest and lowest part topographically, and (6) continuously repeated actions have formed many wine-glass forms, which are enlarged with time to conjugate each other and form a very big wine-glass form with special geomorphological form (Fig. 3).

The hard rocks in the core of Bani Bawi anticline belong to the Bekhme Formation (Fig. 3), it consists of very hard dolomite, dolomitic limestone, and limestone, the fairly hard rocks belong to the Shiranish Formation (thinly well bedded marly limestone and papery blue marl), whereas the soft and highly weathered rocks belong to the Tanjero, Kolosh, and Gercus formations (soft clastics). The outer part of the limb is represented by the Pila Spi Formation (well bedded very hard dolomitic limestone) (Sissakian and Fouad, 2012; Sissakian and Saeed, 2012).

C. Alluvial Fans Related to Wine-Glasses

A common feature for fluvial-erosion cirques (wine-glass forms) is a terrain, which includes erosion resistant upper structures overlying materials, which are more easily eroded, and often associated with alluvial fans in the outlet of the wine-glass form. The size of the fans depends on the size of the wine-glass forms and the type and the thickness of the exposed rocks that are eroded during forming of the wine-glass form. Tens of wine-glass forms are associated with alluvial fans in the studied area; a good example is Pera Magroon anticline with very large developed alluvial fan; called Zewe alluvial fan (Fig. 4; Sissakian et al., 2014). However, some wine-glass forms, although they are large have not developed alluvial fans in their outlets. This is attributed to: (1) The draining valley of the wine-glass form

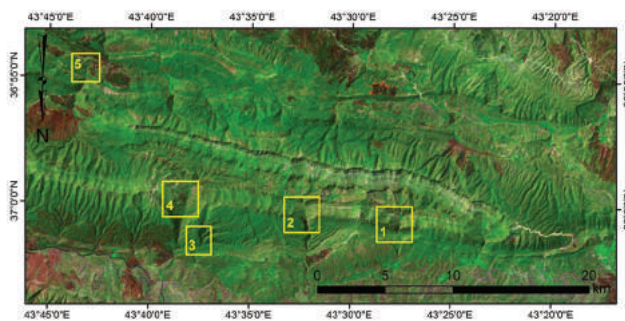


Fig. 2. Landsat image of Gara anticline, facing south. Note, the whole anticline exhibits one extremely large wine-glass form, with three outlets (Nos. 1, 2, and 3, whereas No. 4 is not fully developed) toward the north, and one outlet (No. 5) toward the south.

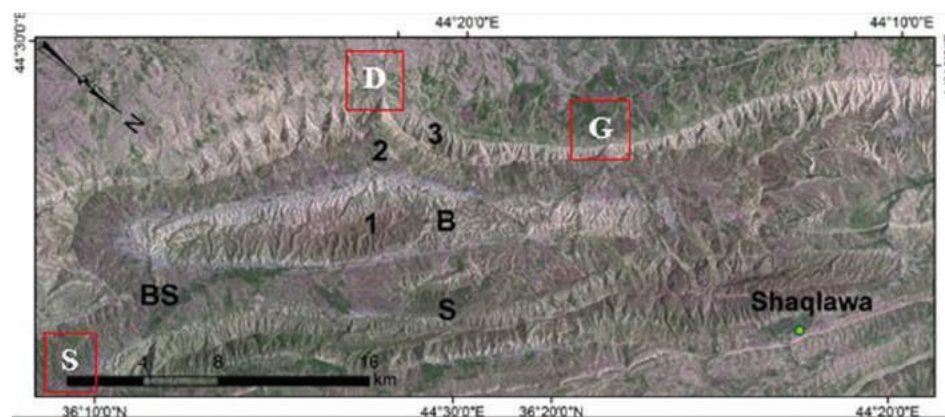


Fig. 3. Landsat image facing N 135° E showing: (B) Bana Bawi anticline exhibiting extremely large wine-glass form, with three outlets, S) Safeen anticline. Formations: (1) Bekhme, (2) Shiranish, Tanjero, Kolosh, and Gercus, and (3) Pila Spi. (BS) In this location, there is no available space for the development of alluvial fan because it is located between two anticlines. The three outlets are: G = Gome Ispan, D = Degala, and S = Sma Qualley.

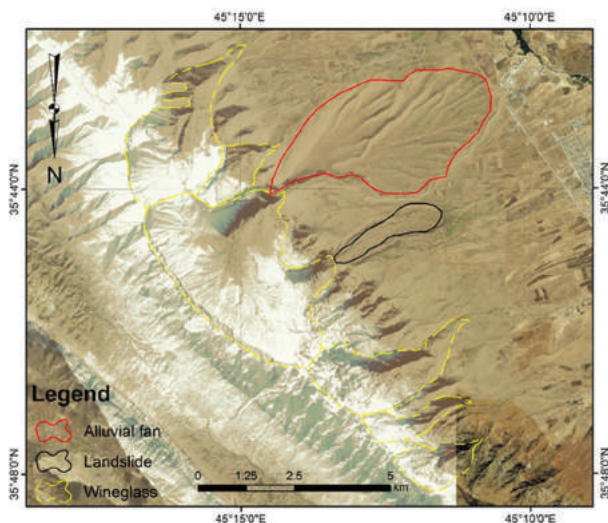


Fig. 4. QuickBird image, facing south of Pera Magroon anticline. Note the large-wine glass form (in yellow); the developed Zewe alluvial fan (in red) and Qara Chatan landslide (in black).

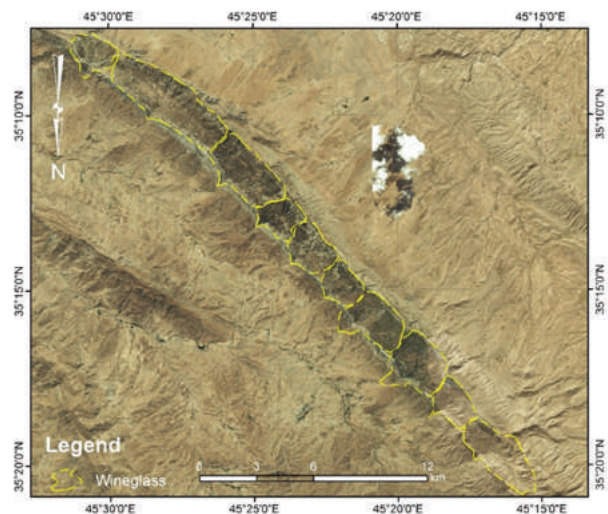


Fig. 5. QuickBird imagery of Qara Dagah anticline, note the developed wine-glasses (limited by yellow lines), most of the whole core of the anticline is occupied by wine-glass forms.

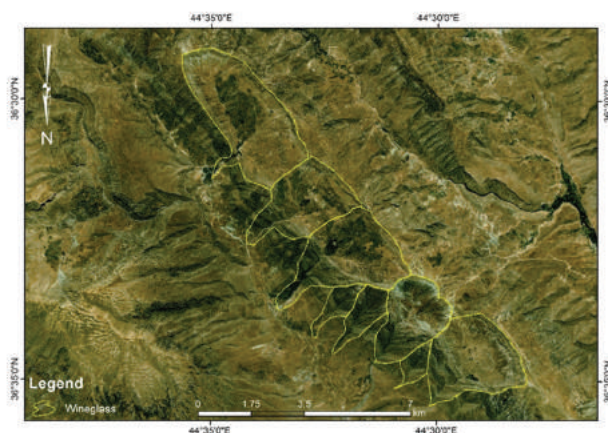


Fig. 6. QuickBird imagery of Korak anticline, note the developed wine-glass forms.

is large and deep with low gradient; hence, the difference on both sides of the outlet is not adequate to develop alluvial fan, (2) presence of another anticline or high ridge just after the outlet; hence no available area occurs for development of alluvial fan (Fig. 3, Point BS, between Bana Bawi and Safeen anticlines), and (3) presence of high anticlinal ridges in the form of cuestas and hogbacks in the outlet.

V. DISCUSSION

A. Development of Wine-glass Forms

In the studied area, the authors have recognized that wine-glass forms are developed in many anticlines, such as Qara Dagah (Fig. 5), Korak (Fig. 6), and Gara (Fig. 7) in which rocks older and/or younger than Cretaceous Period are exposed; more than those in which only Cretaceous rocks are exposed; like Hareer anticline (Fig. 8). Moreover, when only Cretaceous rocks are exposed in anticlines; then the majority of them exhibit whale back-shape structures (Fig. 8). This is attributed to the exposed very hard Cretaceous rocks. Some deeply cut valleys, however, occur in those anticlines, which will change; by time to wine-glass forms by continuous erosion.

The assumption of whale back-shape anticlines is based on the fact that the anticlines in which rocks older than Cretaceous Period are exposed wide anticlines, such as Gara (Figs. 2 and 7) and Pera Magroon (Fig. 4) anticlines. Moreover, the early Cretaceous succession, especially qamchuqa formation and late cretaceous bekhme formation include very thick and hard rocks, which are not easily eroded to exhibit wine-glass forms. On contrary, the Jurassic and even the Triassic successions include soft rocks in their upper parts (Sissakian and Fouad, 2012; Sissakian and Saeed, 2012), which were easily eroded and have developed tens of wine-glass forms. This process had exposed younger erosional surfaces (on Triassic and older rocks); in contrast to hard rocks, which show older erosional surfaces of Cretaceous and younger rocks without the presence of wine-glass forms. A good example is Gara anticline (Figs. 2 and 7) in which Triassic rocks are exposed; the anticline exhibits 20 wine-glass forms; forming one extremely large wine-glass form with many outlets, at opposite directions (Figs. 2 and 7).

In those anticlines where only the Cretaceous hard rocks are exposed and deeply eroded by galley shape valleys (Fig. 9) without wine-glass form development, they may exhibit wine-glass forms in some parts due to either fault escarpments or when the older Qamchuqa Formation is exposed (Fig. 10). This is attributed to the presence of a 30–65 m thick soft succession between the Qamchuqa and Bekhme formations (Sissakian and Al-Jibouri, 2014; Sissakian and Youkhanna, 1979; Youkhanna and Sissakian, 1986).

To the contrary of the aforementioned cases, in some anticlines like Hareer (Figs. 8-10), for example, almost no wine-glass form is developed. This is attributed to: (1) The presence of the Bekhme Formation with very hard and thickly bedded carbonate rocks, (2) the Bekhme Formation forms the carapace of the mountain, with comparatively

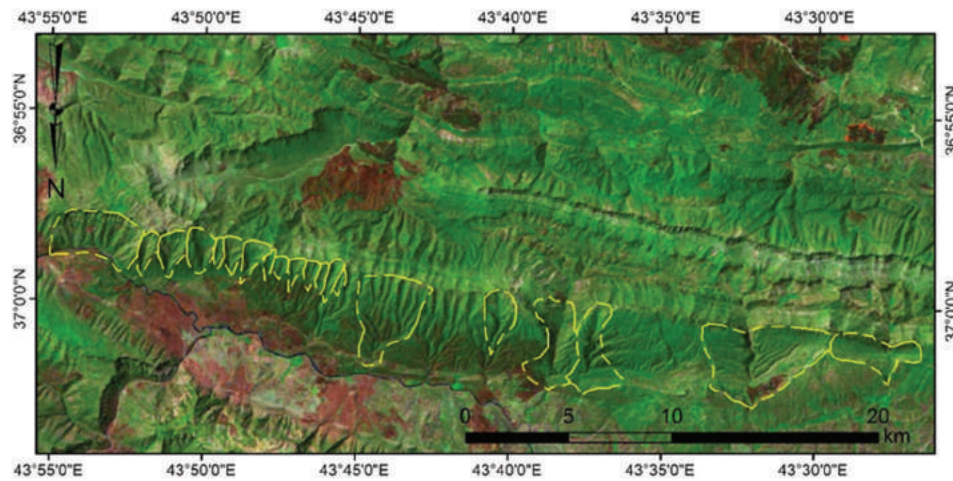


Fig. 7. Landsat image of Gara anticline, note the wine-glass forms (in yellow lines).

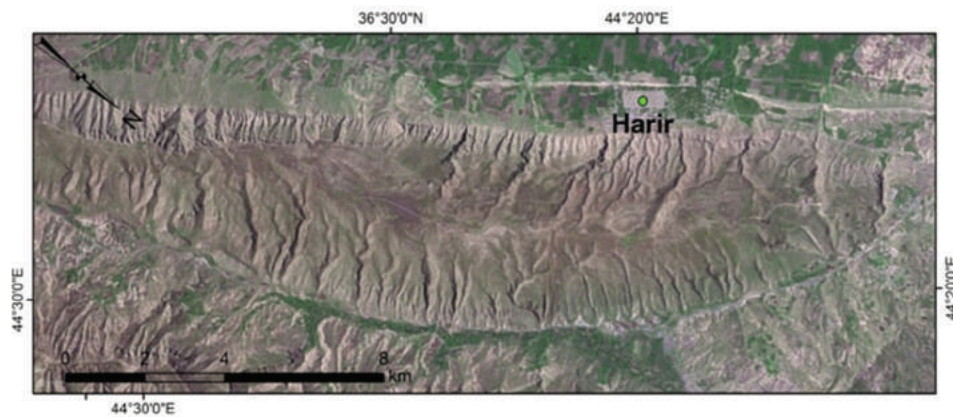


Fig. 8. Landsat image of Hareer anticline; facing N 135° E. Note, the absence of wine-glass form, the presence of deeply cut valleys on both limbs and also note the whale back-shape of the anticline.

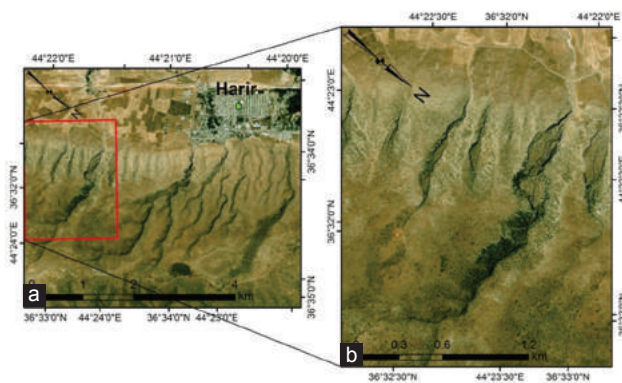


Fig. 9. (a) QuickBird imagery facing NE of Hareer anticline, note the deeply incised valleys without wine-glass form and (b) enlarged part of a deeply incised valley.

wide hinge zone, which decreases the distances between the tension and shear joints that consequently decreases the ability of weathering and erosion due to less disintegrated rocks, and (3) the wide hinge zone, which forms a wide plateau that behaves as retarder to the flowing rainwater on the top of the anticline; consequently, decreases the erosion

ability, especially in the uppermost parts of the anticline. The steep limbs of Hareer anticline, however, exhibit severe gully erosion in majority of the valleys (Figs. 8 and 9) forming deeply eroded valleys with the absence of wine-glass forms. This is attributed to: (1) Box fold shape of the anticline that makes the limbs become steep suddenly after the wide hinge zone, and (2) the steep limbs causes the exposure of the upper beds of the Bekhme Formation (Fig. 9), which are very hard without reaching the lower parts of the formation which includes softer rocks (Fig. 10). These are the main reason for the development of wine-glass forms in other anticlines which are not of box fold type.

Another example is Bana Bawi anticline (Fig. 3). It has very large wine-glass form and three outlets through gorges. In this anticline, the presence of thick and hard rocks of the Bekhme Formation in the core of the anticline and soft late Cretaceous and early tertiary rocks; Shiranish, Tanjero, Kolosh, and Gercus formations, which are overlain by hard rocks of the Pila Spi Formation (Fig. 3) is the reason of forming the extremely large wine-glass form. It is worth mentioning that the presence of large wine-glass forms is a result of conjugation of tens of small wine-glass forms that are widened continuously through the time by eroding the

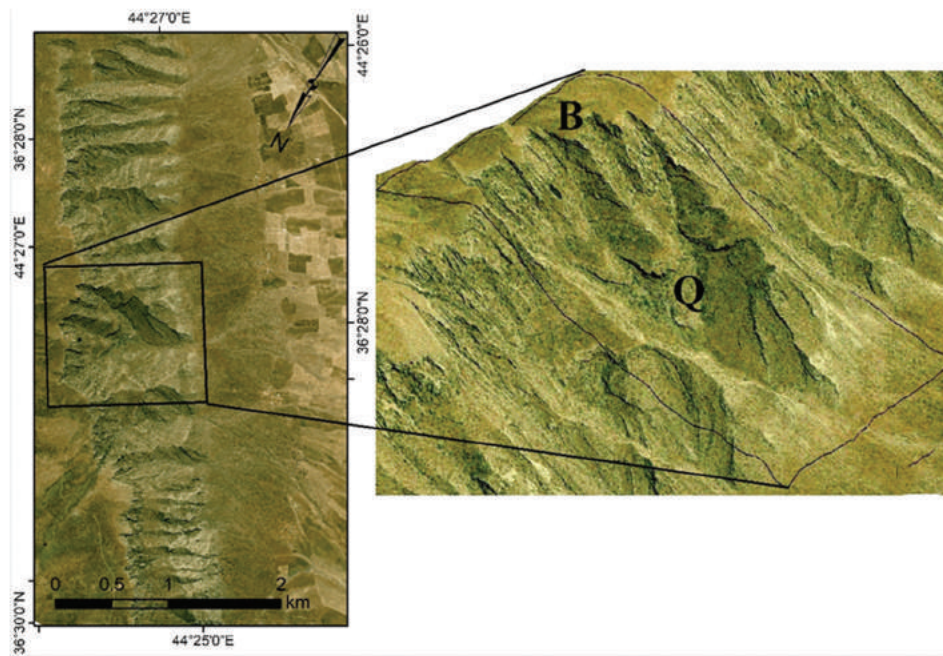


Fig. 10. QuickBird imagery of the eastern part of Hareer anticline (facing west). (a) Development of shallow wine-glass forms; due to continuous erosion and exposure of the Qamchuqa Formation, (b) 3D view enlarged image of a wine-glass form, includes Qamchuqa Formation (Q), and Bekhme Formation (B).

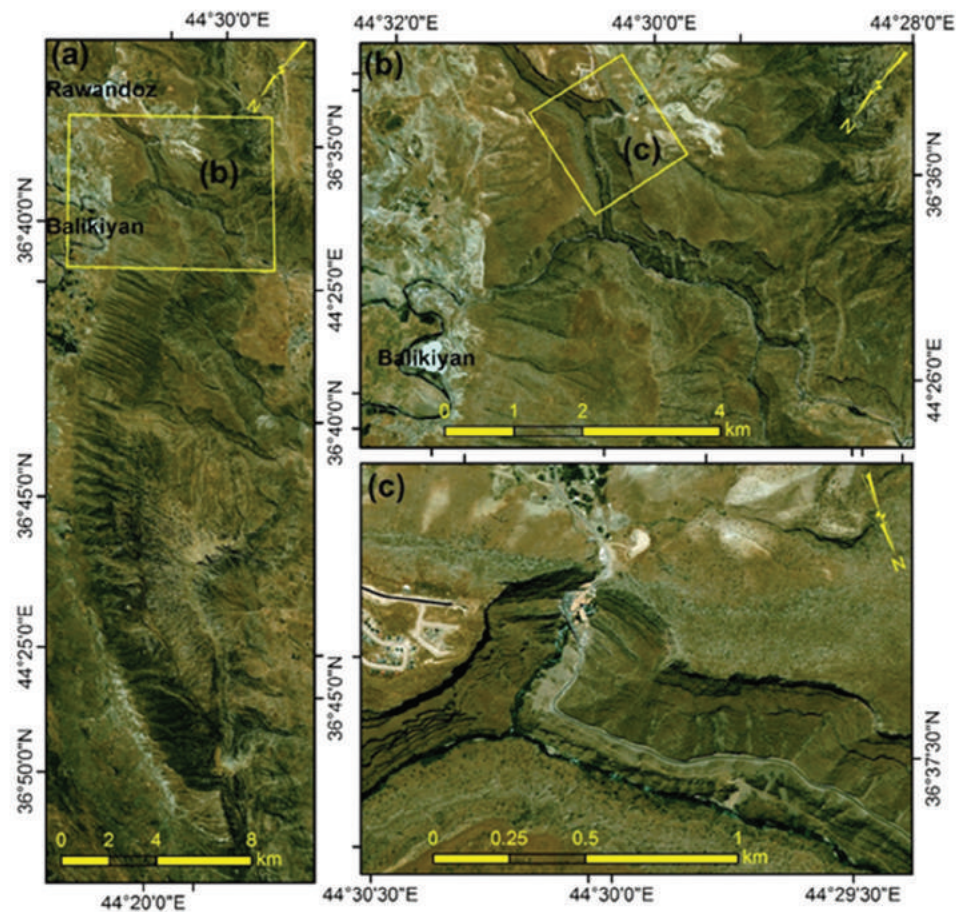


Fig. 11. (a) QuickBird imagery of Bradost anticline, (b) note the blocked inlet of a water gap, which forms a large and longitudinal wine-glass form, and (c) enlarged part of the blocked valley.

divide walls in between two conjugate wine-glass forms, consequently, the formation of the existing extremely large wine-glass form.

B. Development of Wine-glass Forms

In the studied area, water and wind gaps are very common phenomena, Gara anticline exhibit both types of these gaps. If a fold starts to propagate laterally and the incision rate of the river is higher than the uplift rate of the fold, then a gorge called water gap (WG),” will be developed. If the incision rate of the river becomes lower than the uplift rate of the folds during further growth of the anticline, the river gets defeated and diverted leaving behind a dry valley called

“wind gap” (Burbank et al., 1999; Burbank and Pinter, 1999 and Burbank and Anderson, 2000). Moreover, many geomorphological processes may contribute, accelerate or even form WG and change them to wind gaps; such as large landslides and development of alluvial fans (Sissakian and Abdul-Jabbar, 2010).

The developed water and wind gaps may contribute to the development of wine-glass forms or just the reverse. A WG may form a wine-glass form if one side of the WG is blocked by any reason. Good examples are blockage by mass movement phenomena and/or alluvial fans (Sissakian and Abdul-Jabbar, 2010). Such example is observed within Bradost anticline (Fig. 11a), where the northern inlet of a

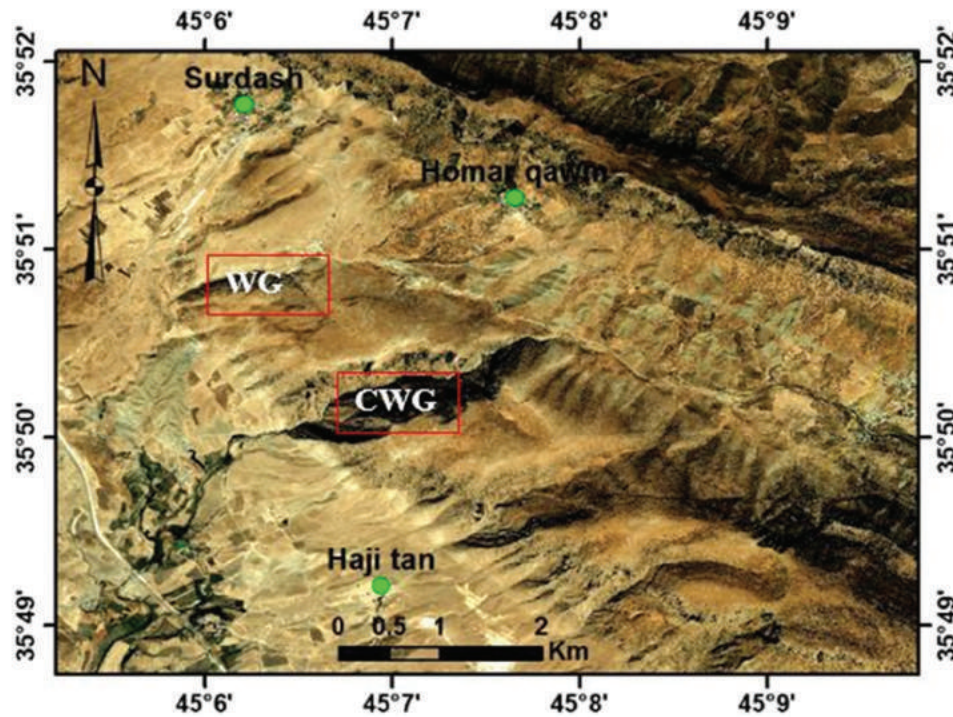


Fig. 12. QuickBird imagery showing the developed CWG and water gap in the northwestern part of Pera Magroon anticline.

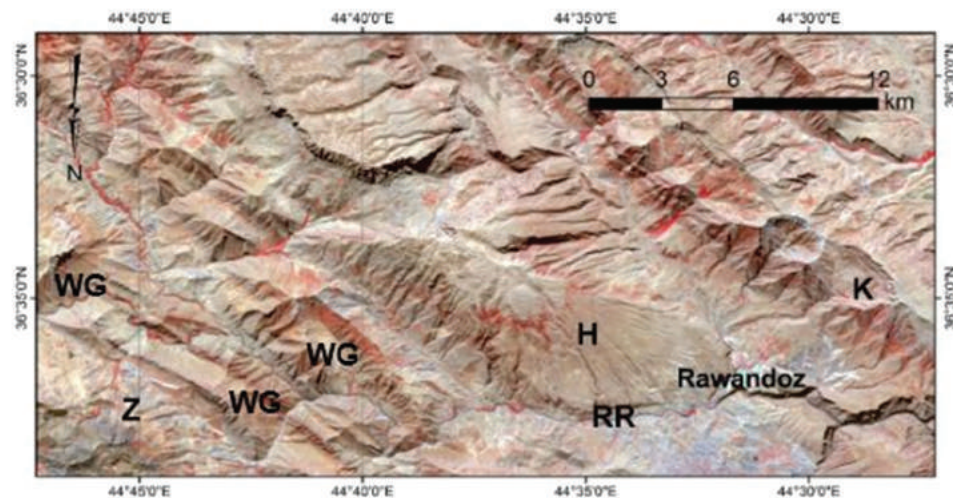


Fig. 13. ASTER image facing south. Note the Rawandoz River (RR); crossing Zozik (Z) and Handreen (H) anticlines. Note the developed wind gaps that are changed to wine-glass forms (WG), and the developed wine-glass forms in Korak anticline (K).

WG is blocked by landslides (Fig. 11b); consequently, the WG is changed to wind gap, which represents a big wine-glass form (Fig. 11c).

A special form of wind gaps, called “curved wind gaps (CWG)” occurs locally. These forms of wind gaps are developed in areas having high tectonic uplift and propagation rates with simultaneous low incision rates, due to very fast propagation and high tectonic uplift ratios of a fold growing in length (Ramsey et al., 2008). A good example is the developed curved water and wind gaps in the northwestern plunge of Pera Magroon anticline (Fig. 12).

It is worth to mention that there are tens of such curved water and wind gaps in different anticlines in the studied area (Sissakian and Abdul-Jab’bar, 2010). Those, CWG and/or curved WG are more favorable areas for development of wine-glass forms, this is attributed to: (1) The curved valleys are usually more dissected on both sides by small rills; consequently, more widening occur to the valley, and (2) the curved valleys exhibit undercut erosion on their concave sides; consequently, more side erosion occurs that accelerates the development of wine-glass forms.

Drainage parallel to a fold axis will likely be diverted in the direction of propagation, as diversions develop, tributary streams are captured and the size of the upstream drainage basin increases until there is sufficient stream power to maintain a channel temporarily at the nose of the fold where propagation has not yet occurred (Keller and Pinter, 2002). This area becomes a WG and eventually defeated by uplift and/or stream capture, if defeat occurs, the channel may be

diverted again in the direction of the lateral propagation, and in the course of a fold development, the channel may make several passes around the fold as the drainage develops. For some folds, there may be several wind gaps produced in this manner, and the drainage will be repeatedly diverted around the nose of the fold, consequently, many wine-glass forms will be developed. Good examples are Zozik and Handreen anticlines (Fig. 13).

C. Development of wine-glass forms in cretaceous rocks

as mentioned before, the authors have noticed that in the studied area, wine-glass forms are not developed in most of the anticlines where the Cretaceous rocks form the bulk of the anticline (carapace of the mountain); apart from the uppermost late Cretaceous rocks (Shiranish and Tanjero formations), which are mainly soft rocks with low resistance to weathering and erosion. However, some exceptions occur for this phenomenon in the southern part of the studied area, which belongs; tectonically to the Low Folded Zone (Fouad, 2012a) and “especially” in those areas where subsurface grabens were inverted to form anticlines after the Cretaceous Period (Fouad and Nasir, 2009); and partly Cretaceous rocks are exposed in their cores.

A good example is Qara Chough anticline (Fig. 14), it is a double plunging anticline; NW – SE trending, mainly Oligocene rocks are exposed in the core; forming the bulk of the anticline. In its northwestern part, a wine-glass form is developed; the exposed rocks belong to the Shiranish and Jaddala formations of uppermost late Cretaceous and Eocene age, respectively (Sissakian, 1993). The wine-glass form was called as “Azkand Cirque” by van Bellen et al. (1959), referring to the nearest village called Azkand.

The authors attribute the development of the wine-glass form in Qara Chough anticline to: (1) Highly fractured Oligocene rocks, (2) the presence of many diagonal faults (Sissakian, 1993); nearby to the wine-glass form, which had increased the fracture system of the rocks; consequently, decreased the weathering resistance, and (3) the anticline, as many others westward, was originally grabens and was inverted to anticlines after Cretaceous period (Fouad, 2012b; Fouad and Nasir, 2009); therefore, the involved area may have suffered from maximum upward forces, as compared to the remaining area, consequently the wine-glass form is developed in which the Shiranish Formation is exposed

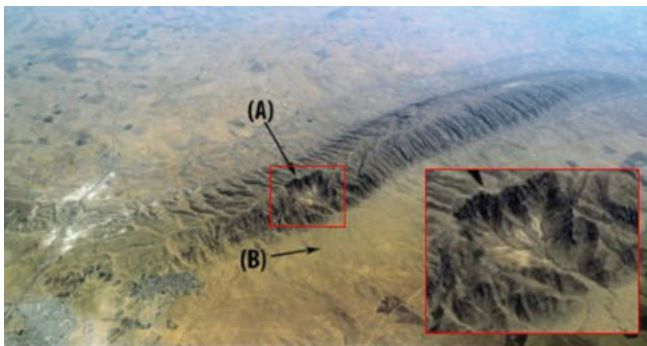


Fig. 14. Landsat image of Qara Chough anticline. Note the developed wine-glass form (a) and the alluvial fan in the outlet (b) and note the absence of the wine-glass forms in other parts of the whole anticline.

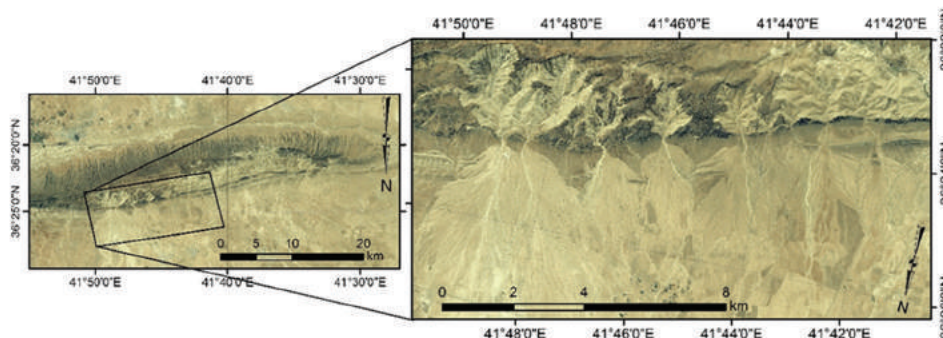


Fig. 15. Landsat image facing south of Sinjar anticline. Note the densely developed wine-glass forms and the related developed alluvial fans.

with Sinjar and Aaliji formations, both of Paleocene age, and the later consists of soft shale and marl (Sissakian and Saeed, 2012).

Another good example for the development of wine glass forms in exposed Cretaceous rocks is Sinjar anticline (Fig. 15) in the northwestern part of Iraq; it is a double plunging and E – W trending anticline. The Sinjar Formation of Paleocene age forms the carapace of the mountain, the formation consists of hard and thick limestone, it is underlain by the Shiranish Formation; it consists of thinly well-bedded limestone and papery marl (Sissakian and Fouad, 2012; Sissakian and Saeed, 2012), both rocks are weakly resistant to weathering and erosion.

The authors attributed the development of wine-glass forms in Sinjar anticline to: (1) The presence of a long fault parallel to the axis of the anticline (Sissakian et al., 1995), (2) the exposure of the Shiranish Formation with its weak rocks, (3) the anticline, as many others in the Jazira Plain, was originally grabens and was inverted to anticlines after Cretaceous period (Fouad, 2012b; Fouad and Nasir, 2009); therefore, the involved area had suffered from upward forces; consequently, the Shiranish Formation is exposed with the Sinjar and Aaliji formations, both of Paleocene age, and the later consists of soft shale and marl (Sissakian and Saeed, 2012), which are the main source for the sediments of the alluvial fans.

VI. CONCLUSIONS

This study demonstrates the erosional forms called cirque or wine-glass forms, which are developed intensely in several anticlines located in the Kurdistan region, north and northeast of Iraq. Many materials were used to perform this study and achieve these conclusions, such as geological and topographical maps, DEM, and satellite images such as Landsat, and QuickBird data, and relevant published articles and reports. The current work has concluded that the wine-glass forms are well developed in the majority of the existing anticlines in the studied area. Anticlines in which the Cretaceous rocks form the carapace, very rarely or no wine glass-forms are developed. When rocks older or younger than Cretaceous period are exposed in the core of an anticline, then wine-glass forms are densely formed there. Moreover, the core of some anticlines exhibits many wine-glass forms; therefore, the whole core resembles one very large wine-glass form. The development and enlargement of wine-glass forms are a continuous process; still ongoing. Many wine-glass forms will merge to neighboring forms, as indicated from the thin divide cliff in between two conjugate forms, thus forming a large-wine glass form.

REFERENCES

- Alden, A., 2014. *Erosional Landforms*. In: GEO ExPro Magazine.
- Al-Jaf, A.A. and Kadhim, T.H., 2010. The Geomorphological Map of Kirkuk Quadrangle, Sheet No. N1-38-2, Scale 1:250000. *Iraq Geological Survey Library, Report No. 3297*, Baghdad, Iraq.
- Al-Ma'amar, A.F., Al-Saady, Y.I. and Al-Saati, R.M., 2011. Series of Geomorphological Maps of Iraq, scale 1: 250000, Erbil and Mahabad Quadrangles, Sheets No. NJ-38-14 and NJ-38-15. *Iraq Geological Survey Library, Report No. 3358*.
- Al-Mousawi, H.A., Sissakian, V.K. and Fouad, S.F., 2008. *The Geology of Zakho Quadrangle, Scale 1:250000*. Iraq Geological Survey Publications, Baghdad, Iraq.
- Bahrami, S., 2012. Morphotectonic evolution of triangular facets and wine-glass valleys in the Noakoh anticline, Zagros, Iran: Implications for active tectonics. *Geomorphology*, 159-160, pp.37-49.
- Burbank, D.W. and Anderson, R.S., 2000. *Tectonic Geomorphology*. Wiley, New York.
- Burbank, D.W. and Pinter, N., 1999. Landscape evolution: The interactions of tectonics and surface processes. *Basin Research*, 11(1), pp.1-6.
- Burbank, D.W., McLean, J.K., Bullen, M.Y. and Miller, M.M., 1999. Partitioning of intermontane basins by thrust-related folding. TienShan, Kyrgyzstan. *Basin Research*, 11(1), pp.75-92.
- DigitalGlobe, 2006. *Quickbird Imagery Products: Product Guide, 4.7.1 ed.* DigitalGlobe, Inc., Longmont, CO., USA.
- Evans, I.S. and Cox, N., 1974. Geomorphometry and the operational definition of cirques. *The Royal Geographical Society*, 6(2), pp.150-153.
- Fouad, S.F., 2007. *The Geology of Kani Rash Quadrangle, Scale 1:250000*. Iraq Geological Survey Publications, Baghdad, Iraq.
- Fouad, S.F., 2012a. *Tectonic Map of Iraq, Scale 1:1000 000*. 3rd ed. Iraq Geological Survey Publications, Baghdad, Iraq.
- Fouad, S.F., 2012b. Western zagros thrust-fold belt. Part 1: The low folded zone. In: *Geology of the low folded zone. Iraqi Bulletin of Geology and Mining*, 5, pp.39-62.
- Fouad, S.F.A. and Nasir, W.A.A., 2009. Tectonic and structural evolution. In: *Geology of Al-Jazira area. Iraqi Bulletin of Geology and Mining*, 3, pp.33-48.
- Gornitz, V., 2009. *Encyclopedia of Paleoclimatology and Ancient Environments*. 1st ed. Springer, Netherlands.
- Hamza, N.M., 1997. *Geomorphological Map of Iraq, Scale 1:1000 000*. Iraq Geological Survey Publications, Baghdad, Iraq.
- Huggett, R., 2007. *Routledge Fundamentals of Physical Geography*. In: *Fundamentals of Geomorphology*. 2nd ed. Taylor and Francis, London.
- Keller, E.A. and Pinter, N., 2002. Hall earth science series. In: *Active Tectonics: Earthquakes, Uplift, and Landscape*. Prentice Hall, New Jersey.
- Mitchell, S.G. and Humphries, E.E., 2014. Glacial cirques and the relationship between equilibrium line altitudes and mountain range height. *Geology*, 43(1), pp.35-38.
- Othman, A.A. and Gloaguen, R., 2013a. River courses affected by landslides and implications for hazard assessment: A high resolution remote sensing case study in NE Iraq-W Iran. *Remote Sensing*, 5(3), pp.1024-1044.
- Othman, A.A. and Gloaguen, R., 2013b. Automatic extraction and size distribution of landslides in Kurdistan region, NE Iraq. *Remote Sensing*, 5(5), pp.2389-2410.
- Othman, A.A. and Gloaguen, R., 2014. Improving lithological mapping by SVM classification of spectral and morphological features: The discovery of a new chromite body in the mawat ophiolite complex (Kurdistan, NE Iraq). *Remote Sensing*, 6(8), pp.6867-6896.
- Ramsey, L.A., Walker, R.T. and Jackson, J., 2008. Fold evolution and drainage development in the Zagros mountains of Fars province, SE Iran. *Basin Research*, 20(1), pp.23-48.
- Sissakian, V.K. and Abdul-Jab'bar, M.F., 2010. Morphometry and genesis of the main transversal gorges in North and Northeast Iraq. *Iraqi Bulletin of Geology and Mining*, 6(1), pp.95-120.

- Sissakian, V.K. and Al-Jibouri, B.S., 2014. Stratigraphy, In: *Geology of the high folded zone. Iraqi Bulletin of Geology and Mining*, 6, pp.73-16.
- Sissakian, V.K. and Fouad, S.F., 2012. *Geological Map of Iraq, Scale 1:1000 000*. 4th ed. Iraq Geological Survey Publications, Baghdad-Iraq. Available from: <http://www.iasj.net/iasj?func=fulltext&aId=99666>. [Last accessed on 2017 Nov 12].
- Sissakian, V.K. and Fouad, S.F., 2014a. *The Geology of Sulaimaniyah Quadrangles, Scale 1:250 000, Sheet No. NI-38-03*. 2nd ed. Iraq Geological Survey Publications, Baghdad, Iraq.
- Sissakian, V.K. and Fouad, S.F., 2014b. *The Geology of Erbil and Mahabad Quadrangles, Scale 1:250 000, Sheets No. NJ-38-14 and NJ-38-15*. 2nd ed. Iraq Geological Survey Publications, Baghdad, Iraq.
- Sissakian, V.K. and Fouad, S.F., 2014c. *The Geology of Kirkuk Quadrangle, Scale 1:250 000, Sheet No. NI-38-2*. 2nd ed. Iraq Geological Survey Publications, Baghdad, Iraq.
- Sissakian, V.K. and Ibrahim, F.A., 2004a. Geological Hazards Map of Mosul Quadrangle, Scale 1:250 000, Sheet No. NJ-38-03. In: *Iraq Geological Survey Library*, Report No. 2860.
- Sissakian, V.K. and Ibrahim, F.A., 2004b. Geological Hazards Map of Erbil and Mahabad Quadrangles, Scale 1: 250 000, Sheets No. NJ-38-14 and NJ-38-15. In: *Iraq Geological Survey Library*, Report No. 2878.
- Sissakian, V.K. and Ibrahim, F.A., 2005. *Geological Hazards Map of Iraq, Scale 1:1000 000*. Iraq Geological Survey Publications, Baghdad, Iraq.
- Sissakian, V.K. and Saeed, Z.B., 2012. Lithological map of Iraq, compiled using GIS techniques. *Iraqi Bulletin of Geology and Mining*, 8(3), pp.1-13.
- Sissakian, V.K. and Youkhanna, R.Y., 1979. Report on Regional Geological Mapping of Erbil-Shaqlawa-Koi Sanjaq-Raidar Area. In: *Iraq Geological Survey Library*, Report No. 975.
- Sissakian, V.K., 1993. *Geological Report on Kirkuk Quadrangle*, Sheet No. NI-38-02, Scale 1:250 000. Iraq Geological Survey Publications, Baghdad, Iraq.
- Sissakian, V.K., 1995. *Geological Report on Al-Mosul Quadrangle*, Sheet No. NJ-38-03, Scale 1:250 000. Iraq Geological Survey Publications, Baghdad, Iraq.
- Sissakian, V.K., 2010. Neotectonic movements in Darbandi Bazian area, Southwest of Sulaimaniyah city, NE Iraq. *Iraqi Bulletin of Geology and Mining*, 6(2), pp.57-69.
- Sissakian, V.K., 2013. Geomorphology and morphometry of the greater Zab river basin, North of Iraq. *Iraqi Bulletin of Geology and Mining*, 9(3), pp.21-49.
- Sissakian, V.K., Kadhum, T.H. and Jab'bar, M.A., 2014. Geomorphology. In: *Geology of the high folded zone. Iraqi Bulletin of Geology and Mining*, 6, pp.7-56.
- Sissakian, V.K., Qambar, A.S. and Ahad, A.D.A., 2008a. Geological Hazards Map of Zahko Quadrangle, Scale 1:250 000, Sheet No. NJ-38-9. *Iraq Geological Survey Library*, Report No. 3129.
- Sissakian, V.K., Qambar, A.S. and Ahad, A.D.A., 2008b. Geological Hazards Map of Sulaimaniyah Quadrangle, Scale 1:250 000, Sheet No. NI-38-03. *Iraq Geological Survey Library*, Report No. 3075.
- Sissakian, V.K., Qambar, A.S. and Ahad, A.D.A., 2008c. Geological Hazards Map of Kani Rash Quadrangle, Scale 1:250 000, Sheet No. NJ-38-10. *Iraq Geological Survey Library*, Report No. 3112.
- Upton, B.G.J. and Wadsworth, W.J., 1969. Early volcanic rocks of réunion and their tectonic significance. *Bulletin Volcanologique*, 33(4), pp.1246-1268.
- van Bellen, R.C., Dunnington, H.V., Wetzel, R. and Morton, D., 1959. *Lexique Stratigraphic International*. Asie, Fasc, Iraq, Paris.
- Ward, D., Saltz, D. and Olsvig-Whittaker, L., 2000. Distinguishing signal from noise: Long-term studies of vegetation in Makhtesh Ramon erosion cirque, Negev desert, Israel. *Plant Ecology*, 150(1-2), pp.27-36.
- Wikipedia, 2014. *Fluvial-Erosion Cirque Formation*. Available from: <https://www.en.wikipedia.org/wiki/Cirque>. [Last accessed on 2017 Aug 18].
- Yacoub, S.Y., Othman, A.A. and Kadhum, T.H., 2012. Geomorphology. In: *Geology of the low folded zone. Iraqi Bulletin of Geology and Mining*, 5, pp.7-38.
- Youkhanna, R.Y. and Sissakian, V.K., 1986. The Stratigraphy of the Shaqlawa-Koisanjaq Area. In: *Proceedings of the 7th Iraqi Geological Congress*, 12 – 15/4/1986, Baghdad, Iraq.

Reliability of Trigonometric Transform-based Multi-Carrier Scheme

Samah A. Mustafa

Department of Electrical Engineering, College of Engineering, Salahaddin University-Erbil, Erbil, Kurdistan Region - F.R. Iraq

Abstract– This work is looking for a new physical layer of a multicarrier wireless communication system to be implemented in low complexity way, resorting to a suitable fast transform. The work presents and assesses a scheme based on Discrete Trigonometric Transform with an appending symmetric redundancy either in each or multiple consecutive transformed blocks. A receiver front-end filter is proposed to enforce a whole symmetry in the channel impulse response. Further, a bank of one tap filter per sub-carrier is applied as an equalizer in the transform domain. The behavior of the transceiver is studied in the context of the practical impairments such as fading channel, carrier frequency offset (CFO), and narrowband interference. Moreover, the performance is evaluated in contrast with the state-of-the-art method by means of computer simulations. It has been found that the new scheme improves the robustness and the reliability of the communication signal, and records lower peak to average power ratio. The study demonstrates that the front-end matched filter effectively performs frequency synchronization to compensate the CFO frequency offset in the received signal.

Index Terms - Discrete cosine transform, Discrete fourier transform, Discrete trigonometric transform, Multicarrier modulation, Orthogonal frequency-division multiplexing.

I. INTRODUCTION

Multicarrier (MC) modulation has been applied widely in wireless communication systems due to its high bandwidth efficiency and robustness to multipath distortion. However, its applications have been restricted to scenarios characterized by sufficiently presence of efficient power amplifier and/or slow

time variations channel impulse response (CIR). However, the presence of a rapidly time-varying CIR where the time selectivity stems, for example, from the Doppler effect or the oscillators' phase noise, destroys the orthogonality between the sub-carriers and causes Inter-Carrier Interference (ICI) (Ren et al., 2016; Shin et al., 2014). Complex equalization techniques must be employed to cope with the latter effect (Mustafa, 2011).

As the conventional discrete Fourier transform (DFT)-based MC system suffers some performance restrictions and high peak to average power ratio (PAPR), the research community has investigated the use of alternative discrete transforms in MC scheme. Wavelet transform in orthogonal frequency-division multiplexing (OFDM) system is studied by Lee and Ryu, 2017, Sirvi and Tharani, 2016, and Suma and Narasimhan, 2018, to replace the DFT in the modulator/demodulator implementation. Another method using the discrete cosine transform (DCT) for MC communication schemes has been studied by Al-Dhahir and Minn, 2006; Cruz-Roldan et al., 2012; Chafii et al. 2016; Feifei et al., 2008; and He et al., 2018). DCT-based scheme has been found as less sensitive to carrier offset. Furthermore, it is a real transform, which can avoid the in-phase/quadrature phase imbalance when the data mapping is real (Feifei et al., 2008).

Many techniques have been investigated to reduce the PAPR in OFDM signal. Wang et al. (2010) proposed a joint companding transform and Hadamard transform method that would introduce high adjacent channel interference with spectrum regrowth. Two different approaches are pointed out in Barsanti and Larue, 2011, active constellation extension method and the reserve carrier algorithm. A precoding method is applied by Hasan (2014) using the decorrelation property of complex Vandermonde matrix. Combination of higher order partitioned partial transmitted sequence along with Bose Chaudhuri-Hocquenghem Code has been proposed by Gupta and Jain (2015). However, these techniques add complexity and consume more resources.

In this paper, two new MC schemes are presented that retain the advantage of the DFT-OFDM of the one-tap filter in the transform domain and reduce the PAPR and the sensitivity to carrier offset substantially. The DFT is replaced by DCT and the well-known discrete trigonometric transform (DTT), namely the DCT and discrete sine transform (DST)

ARO-The Scientific Journal of Koya University
Volume VI, No.2 (2018), Article ID: ARO.10312, 7 pages
DOI: 10.14500/aro.10312

Received 07 October 2017; Accepted: 18 October 2018

Regular research paper: Published 22 December 2018

Corresponding author's e-mail: samah.mustafa@su.edu.krd

Copyright © 2018 Samah A. Mustafa. This is an open access article distributed under the Creative Commons Attribution License.



in this work. DCT and DST are linear Fourier-related transformation similar to the DFT, but using a purely real matrix. DCT/DST is equivalent to the real/imaginary parts of a DFT of roughly twice the length, operating on real data with even/odd symmetry. In DTT-based MC scheme, the DTTs are interspersed in the modulator stage: The DCT coefficients are transmitted on the even subcarriers and the DST coefficients are transmitted on the odd subcarriers.

Pseudo-noise (PN) sequence is used to append symmetric redundancy either in each or multiple consecutive transformed blocks. Many simulations have been carried to outline and assess the schemes in the presence of various channel impairments. The receiver employs the channel estimation based on a matched filter approach: It is used to estimate the random attenuation and phase shift of the fading channel and train the decision to adjust the received signal with amplitude and phase recover.

In Section II, discrete-time transmitter and receiver models based on DCT and DTT schemes are proposed. Section III represents the processing to reconstruct the original data through one-tap per sub-carrier. Simulation results and some further discussions of the error performance over different channel parameters are presented in section IV. Finally, Section V concludes the results.

II. DTT IN MC SCHEME

DCT and DST are orthogonal linear trigonometric transform (Strang, 1999) and each can be implemented by a fast transform that does not require an extensive increase of system complexity. Moreover, they are well-known to have excellent spectral compaction and energy concentration properties which prevent excessive leakage into the adjacent bands (Bouzegzi et al., 2008). They are robust in the presence of ICI.

A. Transmitter Scheme

A linear modulation scheme is presented in Fig. 1. The transmitted signal is obtained by modulating a set of filters $\psi^i(t)$. The filters are chosen as length T rectangular pulse with a suitable multiplexing in the frequency domain as in the uniform filter-bank approach, and based on the discrete transform of interest. We resort to a discrete-time model where $n \triangleq nT_s \triangleq nT/\nu$ (T_s is the sampling interval and ν is the oversampling factor). The transmitted signal is given by:

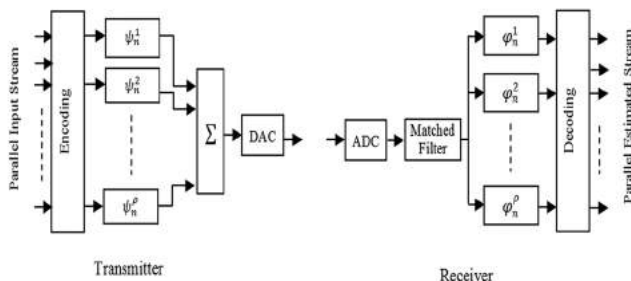


Fig. 1. Discrete time filter bank transceiver.

$$x(t) = \sum_k \sum_{i=1}^{\rho} \xi_k^i \sum_n \psi_n^i \text{rect}\left(\frac{t - kT - nT_s}{T_s}\right) \quad (1)$$

A sequence of complex serial information symbols is given by a generic user at a rate ρ/T and is converted into group of low rate parallel streams; each modulates a mutually orthogonal sub-carrier individually. ρ being an integer design parameter and T is transmitted block time period. The symbols are zero-mean independent random variables (r.v.s) belonging to a given complex constellation. i denotes subcarrier index or symbol position inside a block which is identified by an index k . ψ_n^i denotes the set of oversampled version of the filters. The rectangular function plays the role of digital-to-analog converters. However, slow decay of rectangular pulse in the frequency domain leads to experience strong interference.

In a transmitter scheme employing DCT as an alternative to DFT, transmitter filters are obtained by modulating the rectangular pulse by cosine functions. The orthogonal DCT is classified into many different types with slightly different even/odd boundary conditions at the two ends of the matrix. In this work, the filters are given by

$$\psi_n^i = \frac{1}{\sqrt{\rho}} \sum_{i=1}^{\rho} \alpha_i \cos\left(\frac{\pi(2n+1)(i-1)T_s \Delta f}{\rho}\right) \quad (2)$$

$$\alpha_i = \begin{cases} 1 & i=1 \\ \sqrt{2} & 2 \leq i \leq \rho \end{cases}$$

$1/\sqrt{\rho}$ is a normalization term and Δf is the frequency separation between the adjacent subcarriers. For each transmitted block, the transmitter and receiver carry out a ρ -IDCT and ρ -DCT, respectively. DCT transform operators map a ρ -size real sequence into another ρ -size real sequence, and hence parsed in-phase, and quadrature components of complex data word must be used in each sub-channel individually. Unlike it, the complex information block is forced to be conjugated symmetric to ensure a real-valued inverse DFT output at the transmitter. When real-valued modulation formats, for instance, BPSK or PAM are used, DCT-based scheme doubles the spectral efficiency compared to that in the DFT-based scheme.

This work also studies another transmitter scheme based on both DCT and DST to build DTT-based MC scheme. The rectangular pulse is modulated by a cosine function for the even index subcarriers and by sine function for the odd index subcarriers.

$$\psi_n^i = \begin{cases} \frac{1}{\sqrt{\rho}} \sum_{i=1}^{\rho} \alpha_i \cos\left(\frac{\pi(2n+1)(i-1)T_s \Delta f}{\rho}\right) & \text{if } i \text{ even} \\ \frac{1}{\sqrt{\rho}} \sum_{i=1}^{\rho} \beta_i \sin\left(\frac{\pi(2n+1)iT_s \Delta f}{\rho}\right) & \text{if } i \text{ odd} \end{cases} \quad (3)$$

Where α_i as given before $\alpha_i = \begin{cases} 1 & i=1 \\ \sqrt{2} & 2 \leq i \leq \rho \end{cases}$

and $\beta_i = \begin{cases} 1 & i=\rho \\ \sqrt{2} & 1 \leq i \leq \rho-1 \end{cases}$

Γ output blocks in either DCT or DTT scheme are serialized and encapsulated in a frame to get a vector X of $(\Gamma\nu p)$ elements. νp represents number of samples in each block. To leverage the performance and afford the delay spread over wireless channel, symmetric redundancy (prefix and suffix) each of length β is successively arranged to form the first block in each frame. In this work, PN is inserted as the redundancy in the transmitted sequence. The redundancy sequence strengthens the transmission especially over a channel of long impulse response and restricts the transmission spectral efficiency. The spectral efficiency is the amount of pre-code bits that can be loaded on a time-frequency region characterized by a unitary bandwidth and time slot.

It is well known; there is a tradeoff between the spectral efficiency and the error performance, such that lower number of encapsulated blocks Γ in a frame enhances the performance but with sacrificing in the transmission rate and the spectral efficiency. Compared to the conventional scheme based on DFT, DCT or DTT-based scheme records a gain of 1.19 bps/Hz in the spectral efficiency if the transmitter is considered to transmit a frame of four independent output blocks. A gain of 2.38 bps/Hz is obtained using real signaling to encode the subcarriers.

B. Receiver Scheme

After transmission over a noisy fading channel, the discrete time received signal is given by the convolution of the transmit signal $x(t)$ and the time-varying CIR $\lambda(t)$ as:

$$Y(t) = \int_{-\infty}^{+\infty} \lambda(\tau)x(t-\tau)d\tau + \eta(t) \quad (4)$$

$\lambda(t)$ is zero-mean Gaussian random process, and η is a complex white Gaussian process. At the reception side, a front end pre-matched filter is present to use a fraction signal of each frame to estimate the frame timing and carrier frequency offset (CFO). The estimated information symbol $\hat{\xi}_m^i$ at a subcarrier, i in a processed block m can be found as:

$$\hat{\xi}_m^i = \sum_n \varphi_n^i \int_{-\infty}^{+\infty} (Y(t) * \mathcal{G}(t)) \text{rect}\left(\frac{t - mT - nT_s}{T_s}\right) dt \quad (5)$$

The received signal is processed by a bank of ρ filters φ_n^i . DCT and DST are orthogonal linear transform and hereby $\varphi_n^i = \psi_n^i$. $\mathcal{G}(t)$ denotes the impulse response of the pre-matched filter. The rectangular function here plays the role of analog-to-digital conversion.

In traditional synchronization approaches, one estimate suffers from a performance degradation caused by estimation error of the other. In this work, a matched filter is used to exploit the received training signal for joint coarse time and frequency synchronization too: To estimate the symbol timing and CFO. Fig. 2 shows a block diagram of the matched filter. The matched filter coefficients are $\zeta_1 \zeta_2 \dots \zeta_p$, and ζ_k is the chip value of the redundancy in the transmitted sequence. The symbol timing and carrier offset can be achieved by searching for the correlation peak in the matched filter output.

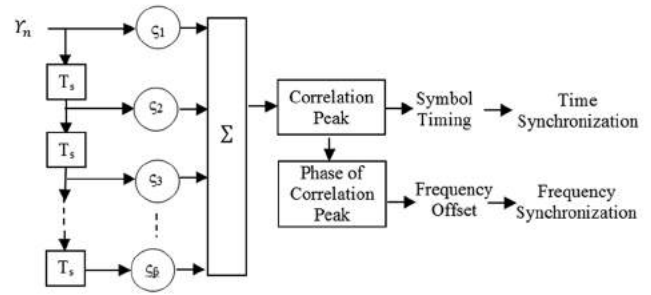


Fig. 2. Block diagram of the pre-matched filter.

The coherent detection of PN synchronization sequence consists of a coherent accumulation of cross-correlations sub-channels by means of the matched filter. It improves frequency acquisition and reduces the miss on a channel with a sufficiently wide coherence bandwidth. The method is proposed in the DFT-based system and presented with detailed derivation in Lin, 2008.

The next section addresses the processing in DCT and DTT-based schemes under which the original data can be reconstructed through one-tap per sub-carrier transform domain equalizer at the receiver. However, the main drawback of DCT or DTT-based system with respect to the conventional DFT-based scheme is the need for a pre-filter at the receiver to make the CIR symmetric.

III. CHANNEL EQUALIZATION IN TRIGONOMETRIC TRANSFORM-BASED SCHEME

This section portrays matrix representation of signal processing in the scheme. The processing is demanded to robust the transmission performance and mitigate the intersymbol interference ISI. Let us consider a CIR given as β filter taps.

$$\underline{\lambda} = [\lambda_o, \lambda_1, \dots, \lambda_p]^T \quad (6)$$

$(.)^T$ is the transposition operator. The front-end filter at the reception side as in Al-Dhahir and Minn, 2006, is used to present symmetry in the channel filter as:

$$\underline{\lambda} = [\lambda_p, \dots, \lambda_1, \lambda_o, \lambda_1, \dots, \lambda_p]^T \quad (7)$$

If a transformed block is given as:

$$\underline{x} = [x_o, x_1, \dots, x_{p-1}] \quad (8)$$

To minimize the probability of interblock interference, each can be extended with \underline{x} appending symmetric redundancy each of length β .

$$\underline{\dot{x}} = [x_p, x_{p-1}, \dots, x_1, x_o, x_1, \dots, x_p, x_{p-1}, x_{p-2}, \dots, x_{p-p-1}] \quad (9)$$

$$\underline{\dot{x}} = \begin{bmatrix} 0_{(p+2p) \times 1} & G_{\beta \lambda \beta} & 0_{(p+2p) \times (p-1)} \end{bmatrix} \underline{x}^T + \begin{bmatrix} 0_{1 \times \beta} & \underline{x} & 0_{1 \times \beta} \end{bmatrix}^T + \begin{bmatrix} 0_{(p+2p) \times (p-1)} & G_{\beta \lambda \beta} & 0_{(p+2p) \times 1} \end{bmatrix} \underline{x}^T \quad (10)$$

0_{MAXN} denotes a matrix of zero elements. The sub-matrix $G_{\beta \times \beta}$ is composed of a single zero column and a Henkel matrix where each ascending skew-diagonal from left to right is constant. In this work, all elements are zeros except, $g_{i, \beta+i} = 1$ and is used to find the prefix and suffix for a transformed block.

$$G = \begin{bmatrix} 0 & \dots & \dots & \dots & 1 \\ \vdots & \ddots & 0 & 1 & 0 \\ \vdots & \ddots & 1 & 0 & 0 \\ \vdots & \ddots & \ddots & \ddots & \vdots \\ 1 & 0 & \dots & \dots & 0 \end{bmatrix} \quad (11)$$

$\frac{G_{\beta \times \beta}}{0_{(\rho+\beta) \times \beta}}$ extends the G matrix by inserting $\rho + \beta$ rows of zero elements. Matrix representation of Eq. (4) using \ddot{H} is a Toeplitz matrix in which each descending diagonal from left to right is constant, and is given as:

$$\underline{y} = \ddot{H} \underline{x}^T + n \quad (12)$$

Based on (2), the delivered signal block can be rewritten as:

$$\underline{y} = \ddot{H} \begin{bmatrix} G_l \\ I_{\rho \times \rho} \\ G_r \end{bmatrix} \underline{x}^T + \eta \quad (13)$$

$$\ddot{H} = \begin{bmatrix} \lambda_\beta & \dots & \lambda_1 & \lambda_0 & \dots & \lambda_\beta & 0 & \dots & 0 & \dots & 0 \\ 0 & \lambda_\beta & \ddots & \lambda_1 & \lambda_0 & \ddots & \ddots & \ddots & \ddots & \ddots & \vdots \\ \vdots & \ddots & 0 & \ddots & 0 \\ 0 & \ddots & 0 & \lambda_\beta & 0 & \ddots & \ddots & 0 & \lambda_\beta & \dots & 0 \\ \vdots & \ddots & \vdots \\ 0 & \dots & 0 & 0 & \dots & \lambda_\beta & \dots & \lambda_0 & \lambda_1 & \dots & \lambda_\beta \end{bmatrix} \quad (14)$$

$$\begin{bmatrix} 0_{\beta \times 1} & G_{\beta \times \beta} & 0_{\beta \times (\rho-\beta-1)} \\ & I_{\rho \times \rho} & \\ 0_{\beta \times (\rho-\beta-1)} & G_{\beta \times \beta} & 0_{\rho \times 1} \end{bmatrix}$$

$\ddot{H}_{\rho \times \rho}$ is a symmetric circular matrix where $\lambda_{ij} = \lambda_{\rho+1-i, \rho+1-j}$. If $\beta=3$ & $\rho=5$, \ddot{H} is given as:

$$\ddot{H} = \begin{bmatrix} \lambda_0 & 2\lambda_1 & 2\lambda_2 & 2\lambda_3 & 0 \\ \lambda_1 & \lambda_0 + \lambda_2 & \lambda_1 + \lambda_3 & \lambda_2 & \lambda_3 \\ \lambda_2 & \lambda_1 + \lambda_3 & \lambda_0 & \lambda_1 + \lambda_3 & \lambda_2 \\ \lambda_3 & \lambda_2 & \lambda_1 + \lambda_3 & \lambda_0 + \lambda_2 & \lambda_1 \\ 0 & 2\lambda_3 & 2\lambda_2 & 2\lambda_1 & \lambda_0 \end{bmatrix} \quad (15)$$

\ddot{H} can be diagonalized by applying inverse and forward DTT: C^{-1} and C respectively. DTT is given in Eq (2).

$$\begin{aligned} \underline{y} &= C^{-1} C \ddot{H} C^{-1} C \underline{x}^T + \eta \\ &= C^{-1} \mathcal{D} C \underline{x}^T + \eta \end{aligned} \quad (16)$$

\mathcal{D} contains the eigenvalues of \ddot{H} which are DTT of $\tilde{\lambda}$.

By sending pilot block \underline{x}_p , the channel state information

CSI presented in $\tilde{\lambda}$ can be estimated by the scalar division of diagonal matrix elements by $C \underline{x}_p$ followed by inverse DTT. A bank of one tap filter per sub-carrier is applied as an equalizer in the transform domain. The efficacy of the filter rises up when the noise in the delivered signal is alleviated.

IV. SIMULATION STUDY

The behavior of the proposed approach is studied in the context of practical impairments such as non-linear distortion, fading channel, and CFO, and in the presence of narrowband interference. Further, the performance of the proposed approach is evaluated in contrast with the state-of-the-art system by means of computer simulations.

Information bits are grouped and mapped using either differential phase shift keying (DPSK) or quadrature amplitude modulation (QAM) with a constellation size of 16 states. With Fourier transformation, the conjugate symmetry condition is imposed in the system under the same transformation size of 256 to provide a fairest comparison possible. The results are averaged over a number of independent iterations of the process.

A. Fading Channel

The received samples at time intervals nT_s can be expressed as:

$$Y_n = \hat{\partial}_n e^{j2\pi\Omega_n n T_s} x_{n-1} + \eta_n \quad (17)$$

t is the unknown delay time in the transmitted sample x . Ω_n denotes the CFO in a sub-carrier spacing centered at a normalized subcarrier frequency is i/ρ . $\hat{\partial}_i$ is the time varying i^{th} sub-channel fade which has Rayleigh distributed envelope and uniformly distributed phase. ε represents the CFO and causes phase ambiguity. It can be expressed as a complex Gaussian random process with the autocorrelation function as given by:

$$E[\hat{\partial}_{i_1} \hat{\partial}_{i_2}^*] = J_0(2\pi f_D |i_1 - i_2| \frac{T}{\rho}) \quad (18)$$

$E[\cdot]$ denotes the statistical expectation operation, and $J_0(\cdot)$ is the zeroth-order Bessel function of the first kind. f_D is the maximum Doppler frequency caused directly by relative motion.

Flat fading channel

The coherence bandwidth measures the separation in frequency after which two signals will experience uncorrelated fading. In flat fading, the coherence bandwidth of the channel is larger than the bandwidth of the signal. Therefore, all frequency components of the signal will experience the same magnitude of fading $\hat{\partial}$. The channel can be expressed as a single complex filter tap. The channel gain is random with a significant probability that the channel is in a deep fade, that is, $|\lambda|^2 < N_o/E$. The probability of this event is roughly defined in Tse and Viswanath, 2005, as:

$$P(|\lambda|^2 < \frac{N_o}{E}) \approx \frac{N_o}{E} \quad (19)$$

E/N_o is the average received signal energy-to-noise energy ratio per complex symbol time. To assess the performance of

DCT and DTT-based MC schemes over fading channel, the error curves are examined as a function of signal energy-to-noise E/N_0 . The results are compared with the corresponding performance of DFT-based scheme. Non-coherent communication is considered here where the receivers have no prior knowledge of the channel. Fig. 3 shows the performance of different encoded sub-carriers where the new proposed schemes approach the linear transmission. The distortion arose from a fading channel can be compensated by increasing E/N_0 . As depicted, DPSK signals in all the investigated MC systems perform well depending on the phase tracking of the decoder: DPSK modulated sub-carriers track and predict the channel response by itself. It is clearly observed that QAM modulated sub-carriers behave better in DCT and DTT-based schemes, while in the conventional scheme based on DFT they result in higher error rates.

Slow fading channel

By the assumption of transmission over a slow fading channel, the coherence time of the channel is large relative to the delay constraint of the channel. The amplitude and phase change imposed by the channel can be considered roughly constant over the period of a frame. Slow fading can be caused by events such as shadowing, where a large obstruction such as a hill or large building obscures the signal path. In this regime, the number of encapsulated symbols in a frame gets higher and subsequently increases the bandwidth efficiency.

Extra simulations have been carried out to investigate the performance of coherent detection in the new schemes over a slow fading channel. For a coherent communication, the receiver estimates the channel state information CSI and adaptively equalizes the delivered symbols to compensate the fade impairments. The CSI in each coherence time is estimated, and the weight of each tap in the equalizer is trained by pilot PN sequence in DCT and DTT-based frames.

Previous works have addressed the problem of obtaining a condition under which the original data can be reconstructed through one-tap per sub-carrier equalizer in DCT-based MC scheme. Following the same approach in Dominguez-Jimenez et al., 2011, to correct the fade impairments, a suffix and a prefix are inserted in the transmitted DCT-symbol. Moreover, a front-end pre-filter is employed in the receiver to force symmetry in the CIR.

Fig. 4 graphs the simulated error rates as a function of in E/N_0 the received signal. The blind detection process with no channel state information results in an irreducible error. A bank of scalars as a channel equalizer at the receiver results in better performance. DTT scheme records an improvement in the error performance over both DFT and DCT schemes, where a slight difference in the error rates has been found between the latter two schemes.

B. CFO and narrowband interference

The DFT-based scheme offers reliable, effective transmission; however, it is far more vulnerable to CFO that can cause a high bit error rate and performance degradation due to ICI. In DCT and DTT-based schemes, one extension interval is used for

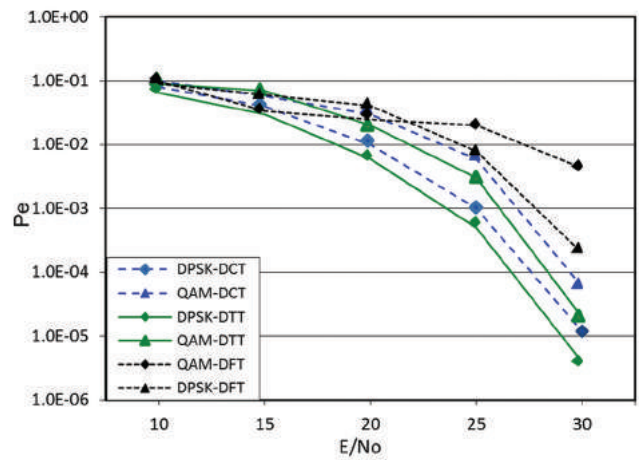


Fig. 3. Error performance of different multicarrier schemes over flat fading channel.

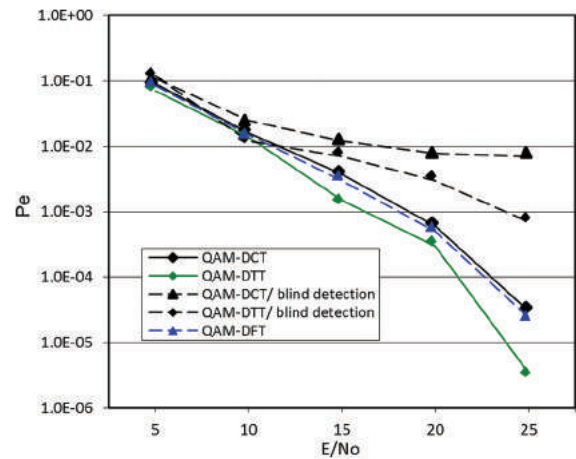


Fig. 4. Error performance of different multicarrier schemes over a slow fading channel. The receiver is either based on blind detection or the estimated CSI.

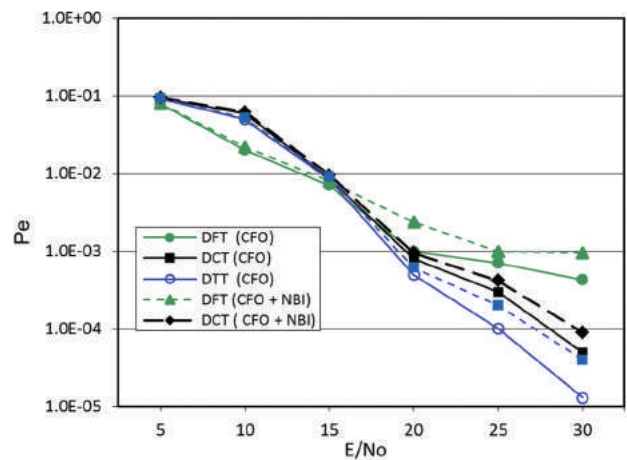


Fig. 5. Error performance of multicarrier schemes in the presence of CFO and a narrowband interference.

each frame of a number of consecutive output blocks. Common estimates of the symbol timing and the frequency offset can be

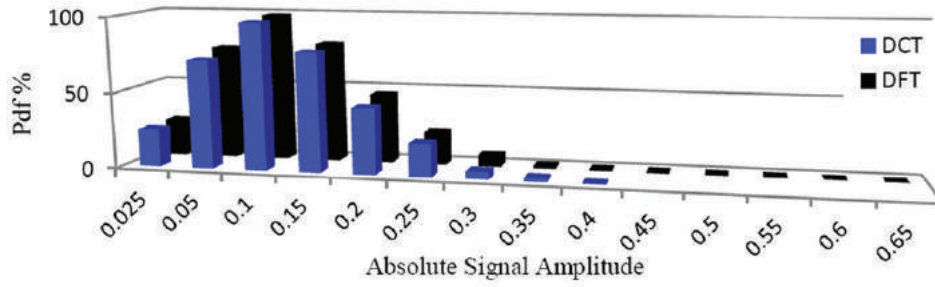


Fig. 6. Probability distributions function of the absolute amplitude of DCT - and DFT-based transformed blocks.

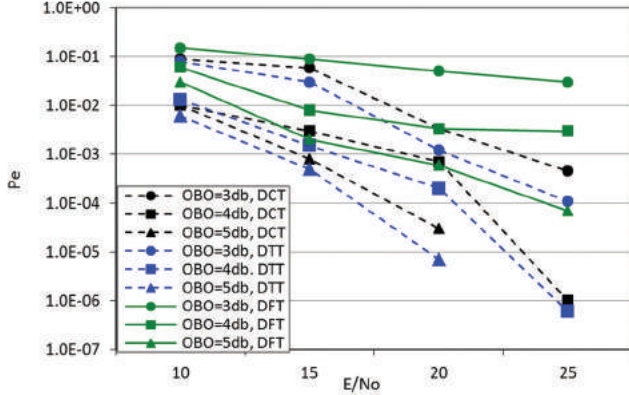


Fig. 7. Error performance of multicarrier schemes with the presence of non-linear distortion.

evaluated jointly when a peak is found in the correlator output. It is proved that DCT and DTT schemes are more robust in the presence of CFO and a narrowband interference NBI. Fig. 5 graphs the error rates in the presence of CFO of 0.13 in the delivered signal over an additive white Gaussian noise channel, and interference as a continuous wave signal.

C. Non-linear distortion

In this section, the time domain transformed amplitude in the conventional OFDM and the proposed systems are analyzed as depicted in Fig. 6. The probability density function (PDF) depends on the probability of occurrence of each discrete sample level. The distribution of MC signal with 512 sub-carriers and 16-QAM is founded where the amplitude ε has Rayleigh distribution with PDF given by:

$$(\varepsilon; \sigma) = \begin{cases} -e^{-\varepsilon^2/(2\sigma^2)} & \text{if } \varepsilon \geq 0 \\ 0 & \text{elsewhere} \end{cases} \quad (20)$$

σ is the scaling parameter. For Rayleigh distribution, as seen the signal levels around the mean value have higher probability than other levels, whereas the occurrence of higher signal levels has smaller probability. It is reasonable to cast a way to change the statistic of the amplitude for the benefit of PAPR reduction. Notice that PAPR is a r.v. for each transmitted block, and,

generally, is given as the ratio of the maximum instantaneous power in the block to the average block power $E[x_i^2]$.

$$PAPR\{x_i^k\} = \frac{\max_{1 \leq i \leq p} |x_i|^2}{E[|x_i|^2]} \quad (21)$$

High PAPR in OFDM signal has a detrimental effect on the performance: The power amplifier clips the transmitted signal and results in non-linear distortion. Based on number of independent runs for the schemes, the proposed system is found to preserve the average power and a reduction of about 4.5 db in the peak power and 1.6 db in the PAPR compared to the conventional OFDM scheme.

The BER performance when the system encompasses power amplifier within its structure is presented in this section. Non-linear power amplifier is applied with AM/AM response of clipping scheme at the saturation point at three different output back off (OBO); 3, 4, and 5 dB. OBO is defined as the ratio of the maximum possible amplifier output power to the average output power. The error performance of the new MC scheme based on DCT and DTT has been compared with the corresponding performance of the traditional Fourier-based MC scheme (Fig.7) over a noisy channel. The complex-valued noise is assumed to be independent and identically distributed, zero-mean white Gaussian noise. Its variance is equal to N_o per real dimension.

In the traditional MC scheme, low OBO generates an almost flattened error curve indicating saturation of the power amplifier. These results can be directly compared with the results of the new schemes. It is found that the simulated performance approaches the linear transmission due to the overall net improvement in the PAPR. However, lower OBO causes non-linear distortion that diverge the performance from the linear case. The PAPR in DTT blocks and the performance of DTT-based scheme with existence of OBO is quite similar to that presented for the DCT-based scheme.

V. CONCLUSION

In this work, two MC schemes based on trigonometric transform are introduced. In the first scheme, the subcarriers are DCT transformed whereas the subcarriers are either DCT or DST transformed based on their index in the second scheme. Extensive simulations have been carried out to study the

performance of DCT and DTT schemes compared to that of the traditional DFT-based scheme. The performance is investigated over flat fading and slow fading channels, where DCT and DTT schemes show better error performance at high E/N_0 .

In the proposed scheme appending symmetric redundancy (as prefix and suffix) in the transmit block and symmetric equivalent CIR, implies the use of a bank of scalars in the corresponding trigonometric transform domain to equalize the channel response. The study is carried by several simulations in wireless communication scenarios, considering the presence of CFO and multipath channel. The results indicate that trigonometric-based systems outperform the conventional scheme based on the Fourier transform.

Our simulation results showed a reduction in the PAPR and leverage in bandwidth efficiency. Performance improvement in the presence of non-linear distortion for the case of the proposed system has been achieved in comparison with that for the conventional OFDM systems.

REFERENCES

- Al-Dhahir, N., and Minn, H., 2006. Optimum CDT-based multicarrier transceivers for frequency-selective channels. *IEEE Transaction on Communications*, 54(5), pp.911-921.
- Barsanti, R.J., and Larue, J., 2011. Peak to average power ratio reduction for digital video broadcast T2. *Southeastcon IEEE*, 2011, pp.117-121.
- Bouzegzi, A., Ciblat, P., and Jallon, P., 2008. *Matched Filter Based Algorithm for Blind Recognition of OFDM Systems*. 68th IEEE Vehicular Technology Conference, pp.1-5.
- Chafii, M., Palicot, J., Gribonval, R., and Bader, F., 2016. A necessary condition for waveforms with better papr than OFDM. *IEEE Transaction on Communication*, 64(8), pp.3395-3405.
- Cruz-Roldan, F., Dominguez-Jimenez, M.E., Vidal, G.S., Amo-Lopez, P., Blanco-Velasco, M., and Bravo-Santos, A., 2012. On the use of discrete cosine transforms for multicarrier communications. *IEEE Transaction on Signal Processing*, 60, pp.6085-6090.
- Dominguez-Jimenez, M., Sansigre, G., Amo-Lopez, P., and Cruz-Roldan, F., 2011. *DCT Type-III for Multicarrier Modulation*. In: Proceeding 19th European Signal Processing Conference (EUSIPCO 2011). Barcelona, Spain: pp.1593-1597, August- September, 2011.
- Feifei, G., Tao, C., Nallanathan, A., and Tellambura, A., 2008. Maximum likelihood based estimation of frequency and phase offset in DCT OFDM systems under non-circular transmissions: Algorithms, analysis and comparisons. *IEEE Transaction on Communication*, 56(9), pp.1425-1429.
- Gupta, P., and Jain, S., 2015. *Peak to Average Power Ratio Reduction in OFDM Using Higher Order Partitioned PTS Sequence and Bose Chaudhuri Hocquenghem Codes*. In: Proceeding International Conference on Signal Processing and Communication Engineering SPACES; 2015.
- Hasan, M., 2014. A novel CVM precoding scheme for PAPR reduction in OFDM transmissions. *Wireless Networks*, 20(6), pp.1573-1581.
- He, C., Zhang, L., Mao, J., Cao, A., Xiao, P., and Imran, M., 2018. Performance analysis and optimization of dct-based multicarrier system on frequency-selective fading channels. *IEEE Access*, 6, pp.13075-13089.
- Lee, J., and Ryu, H.G., 2017. *Performance comparison between wavelet-based OFDM system and iFFT-based OFDM system*. In: Proceeding International Conference on Information and Communication Technology Convergence ICTC; 2017.
- Lin, J.C., 2006. Coarse frequency-offset acquisition via subcarrier differential detection for OFDM communications. *IEEE Transactions on Communications*, 54(8), pp.1415-1426.
- Mustafa, S., Hikmat, V., Shekha, S. 2011. *Wavelet Filter Bank-Based Non Uniform Multi-tone Transceiver for Digital Subscriber Line*. In: Proceeding IEEE 11th International Conference on Computer and Information Technology, pp.197-203.
- Ren, X., Tao, M., Chen, W. 2016. Compressed channel estimation with position-based ICI elimination for high-mobility SIMO-OFDM systems. *IEEE Transactions on Vehicular Technology*, 65(8), pp.6204-6216.
- Shin, W.J., Lee, S., You, Y.H., 2014. A robust joint frequency offset estimation for the OFDM system using cyclic delay diversity. *Wireless Personal Communications*, 77(4), pp.2483-2496.
- Sirvi, S., Tharani, L. *Wavelet based OFDM system over flat fading channel using NLMS equalization*. In: Proceeding International Conference on Computing, Communication and Automation (ICCCA), 2016.
- Strang, G., 1999. The discrete cosine transform. *SIAM Review*, 41(1), pp.135-147.
- Suma, M.N., and Narasimhan, S.V., 2018. Efficient analytic discrete cosine harmonic wavelet transform OFDM with denoising. *International Journal of Wireless and Mobile Computing*, 14(8), pp.223-228.
- Tse, D., Viswanath, P., 2005. *Fundamentals of Wireless Communications*. New York: Cambridge University Press, 2005.
- Wang, Z., Zhang, S., Qiu, B., 2010. PAPR Reduction of OFDM Signal by Using Hadamard Transform in Companding Techniques. 12th IEEE International Conference on Communication Technology, pp. 320-323.

Phytochemical Constituents of Leaves Essential oils of *Achillea fragrantissima* (Asteraceae) from Iraq

Karzan O. Qader¹, Sahar A.A. Malik Al-Saadi², Ibrahim M. Faraj³

¹Department of Biology, College of Science, University of Sulaimani, Kurdistan Region - F.R. Iraq

²Department of Biology, College of Science, Basrah University, Basrah, F.R. Iraq

³Department of Protected Agriculture, Bakrajo Technical Institute, Sulaimani Polytechnic University, Kurdistan Region -F.R. Iraq

Abstract – Essential oils of *Achillea fragrantissima* extract were prepared and analyzed by gas chromatography–mass spectrometry (GC-MS). A total of 57 phytochemical constituents of chemical compounds were identified in leaves of *A. fragrantissima*. The major constituents of the essential oil were camphor (34.50%), 1, 8-cineole (14.60%), artemisia ketone (10.25%), and 3-thujanone (7.82%). In addition, 43 components were present at <1%. From the 57 identified compounds, four of them was sesquiterpenes (7.01%), whereas 35 compounds were monoterpenes (61.40%).

Index Terms—*Achillea fragrantissima*, camphor, essential oils, gas chromatography–mass spectrometry.

I. INTRODUCTION

Achillea fragrantissima (Forssk.) Sch. Bip. is a wild herbaceous shrub medicinal plant belonging to the *Asteraceae* family. *Achillea* contains around 130–140 perennial species worldwide, it is a white-woolly plant, with erect stems and is widespread in Europe and temperate areas of Asia, North America, and in North Africa, it is easily found growing in fields and on roadsides (Nemeth, 2010).

A. fragrantissima known as yarrow, in Arabic called Qaysoom. Most parts (leaves, flowers, and seeds) of *A. fragrantissima* contain high percentage of volatile oils, flavonoids, tannins, sterols and triterpenes monoterpene ketones, and sesquiterpene lactones (Batanouny, et al., 1999; Bakr, et al., 2014) fatty acids: Lauric, myristic, palmitic, stearic, linoleic, linolenic, and oleic (Al-Mustafa and Al-Thunibat, 2008). So that different parts of *A. fragrantissima* including fruits, leaves and branches have been used as a folk medicine for the treatment of various diseases. It is used as anti-inflammatory, antioxidant, antiproliferative capacities, antimicrobial, antifungal, antiviral,

and anticancer activity (Shalaby and Richler, 1964; Ageel, et al., 1989; Barel, et al., 1991; Al-Mustafa and Al-Thunibat, 2008; Soltan and Zaki, 2009; Elmann, et al., 2011; Hazem, et al., 2012; Vitalini, et al., 2013; Alenad, et al., 2013; Hammad, et al., 2014; and Choucry, 2017). Comparison between the essential oils of *A. fragrantissima* (Forssk.) Sch. Bip. and *A. santolina* L. (*Asteraceae*) studying their antimicrobial activity was reported by El-Shazly, et al., 2004.

The main constituents of *A. fragrantissima* are essential oil santolina alcohol, artemisia ketone, cis-thujone, and trans-thujone (El-Shazly, et al., 2004), whereas Hazem, et al. (2012) shown that 48 components were identified in the oils, and main compounds of oils were 4-terpineol (15.65%), linalool (11%), carvone (9.42%), β -phellandrene (6.2%), γ -terpinene (5.6%), β -pinene (4.55%), verbenone (4.42%), cedrol (3.0%), and *p*-cymene (2.95%). Choucry (2017) reported that 28 compounds were identified in the *A. fragrantissima*, caryophyllene oxide (23.50%), terpinen-4-ol (11.15%), *p*-cymen-3-ol, viridiflorol, and guaiacol (9.84%). In all these studies, chemical compositions were identified and the amount of the yields of essential oils was varied. The aim of this study, *A. fragrantissima* of leaves collected from Choman region, Erbil city, Iraq to extract essential oil and its compositions were analyzed using Gas chromatography and Mass spectrometry (GC-MS).

II. MATERIALS AND METHODS

A. Plant Material

The leaves of *A. fragrantissima* were collected from plants in flowering growth stage from Choman region, 160 km northeast Erbil city, Iraq, in September 2016 at Latitude 36.636310 N, Longitude 44.886767 E, and Altitude 3607 m. The plant was identified at the Basrah University. A voucher specimen was deposited at the herbarium of the Basrah Science, Faculty of Science, Basrah University, Iraq.

The meteorology of the study location for September 2016 was as follows: 26–28°C, 56%, 28 mm, and 2.3 m/s for temperature, relative humidity, rains, and wind speed, respectively, whereas the soil texture was sandy loam.

The samples were air-dried in the shade at room



temperature until dried (2 weeks). To obtain the leaves essential oil, 150 g of dried leaves were crushed, and the method of hydrodistillation for 5 h using the Clevenger-type apparatus was used. The obtained essential oils were dried over anhydrous sodium sulfate and stored in the refrigerator (-18°C) until used (Massada, 1976).

B. GC-MS Analysis

GC-MS analysis was carried out in the University of Basrah, College of Agriculture, Iraq using Shimadzu GC-QP 2010 ultra gas chromatograph. The GC oven temperature was programmed from 40°C to 280°C at a rate of $15^{\circ}\text{C}/\text{min}$. Helium was used as carrier gas; inlet pressure was 96.1 kPa; and linear velocity was 36.1 cm/s. Column flow was 1.00 mL/min, injector temperature: 280°C ; injection mode: split. MS scan conditions was carried using a ion source temperature of 200°C , interface temperature, 280°C with detector gain 0.70 kV+0.10 kV. Scan speed was 1666, start 50 m/z, and then raised to end 800 m/z (Vandendoo and Kratz, 1963). The components of the *A. fragrantissima* were identified by comparing the spectra with those of known compounds stored in the NIST library (2005). The identification of the phytochemical compounds was confirmed based on the molecular formula, peak area, and retention time (Fig. 1-6).

III. RESULTS AND DISCUSSION

The GC-MS chromatogram of *A. fragrantissima* leaves extract (Fig. 7 and Table-1) showed 57 peaks indicate the

presence of 57 compounds (phytochemical constituents).

Most of the chemical components from *A. fragrantissima* leaves are essential oil components including camphor (34.50%), 1, 8-cineole (14.60%), artemisia (10.25%), and 3-thujanone (7.82%). In addition, 43 components were present at $<1\%$ (Table 1 and Fig. 7), from all this component, the number and percentage of sesquiterpenes component were four compounds; methyl 3,4-tetradecadienoate, beta-cubebene, beta-selinene, and benzofuran, 7-cyclohexyl-2,3-dihydro-2-methyl- which represented 7.01% from all compounds in essential oil, and monoterpenes were 35 compounds (61.40%). Our results agree with other literatures, monoterpenes are the principal components of *Achillea* essential oils (Zeedan, et al., 2014; Mottaghi, et al., 2016). Furthermore, 1, 8-cineole (20.1%), camphor (15.6%), and viridiflorol (11.8%) the three most abundant monoterpene components (Toker, et al., 2003).

Most researchers reported that santolina alcohol, artemisia ketone, cis-thujone, and trans-thujone were the major constituents in *A. fragrantissima* (Shalaby and Richter, 1964; El-Deeb, 1985; Hifnawy, et al., 2001; El-Shazly, et al., 2004; Abaas, et al., 2013; and Alshaili and Al-fawwaz, 2014). In addition, borneol and 1,8-cineole (Gohari, et al., 2011; Mazandarani, et al., 2013; Zeedan, et al., 2014). However, our results vary in the chemical composition of essential oils of *A. fragrantissima*, as well as the number and ratio of chemical components. These differences might be due to the diversity of the plant sources, different essential oil hydrodistillation procedures or growth conditions. In Egypt, the essential oil

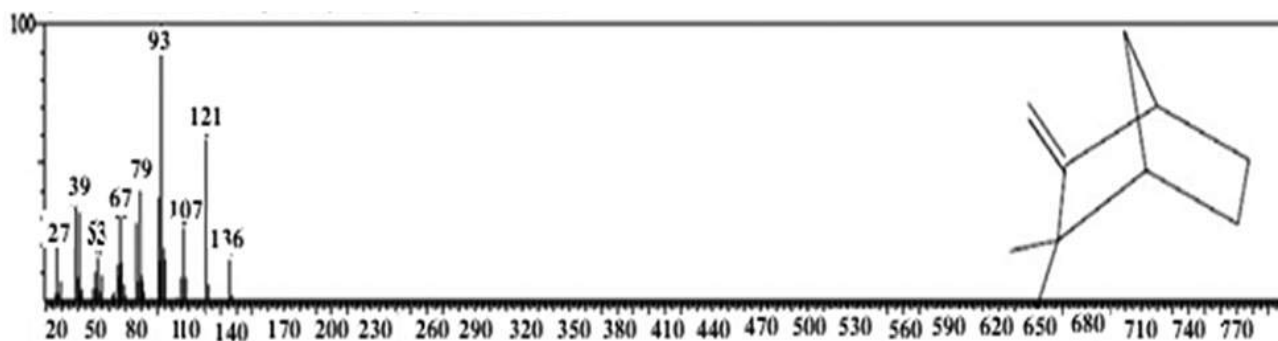


Fig. 1. A typical gas chromatogram of the camphene.

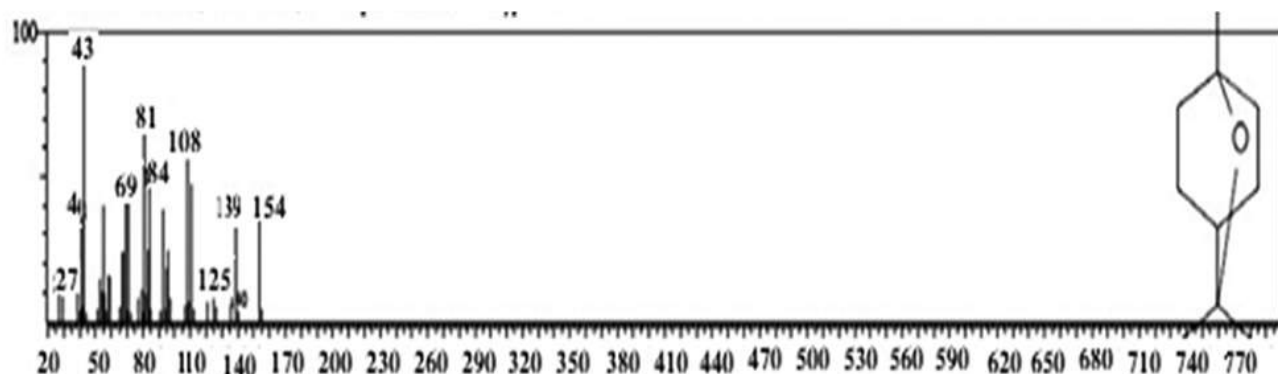


Fig. 2. A typical gas chromatogram of the 1, 8-cineole.

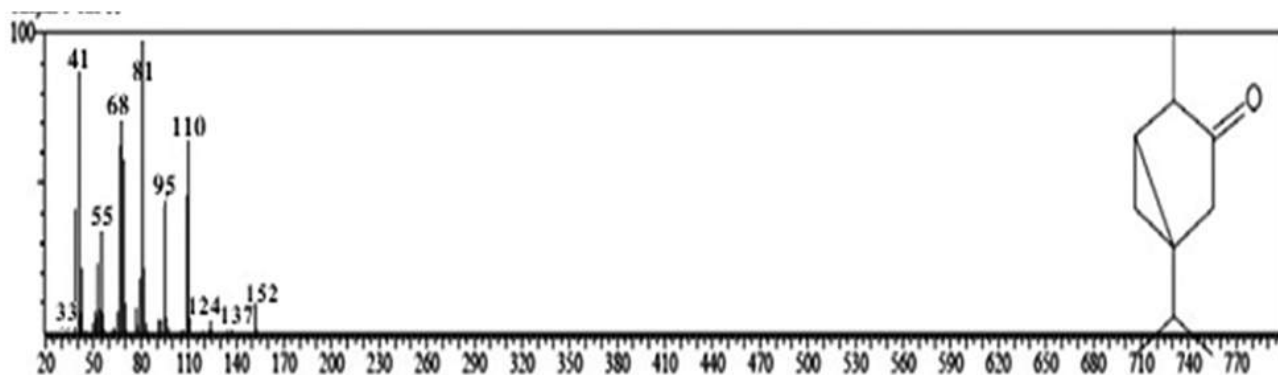


Fig. 3. A typical gas chromatogram of the 3-thujanone.

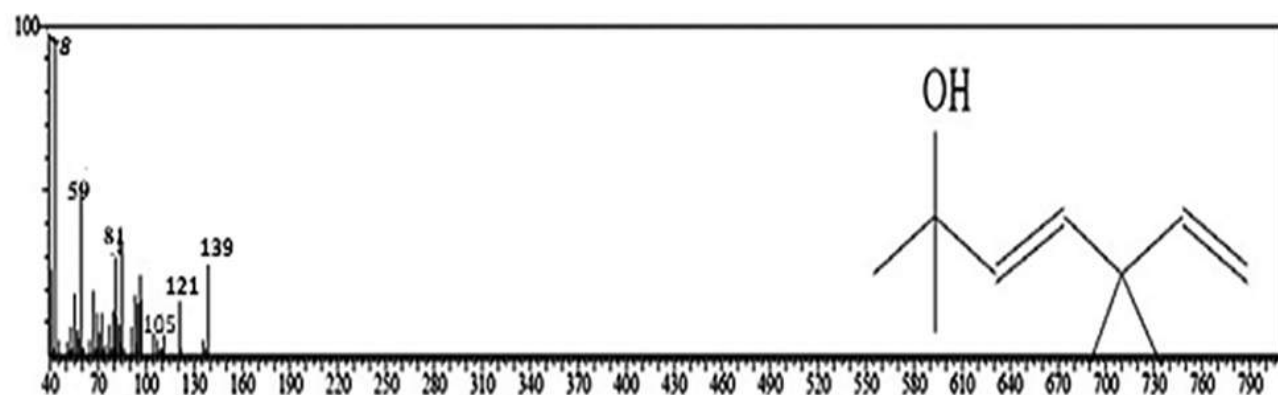


Fig. 4. A typical gas chromatogram of the yomogi alcohol.

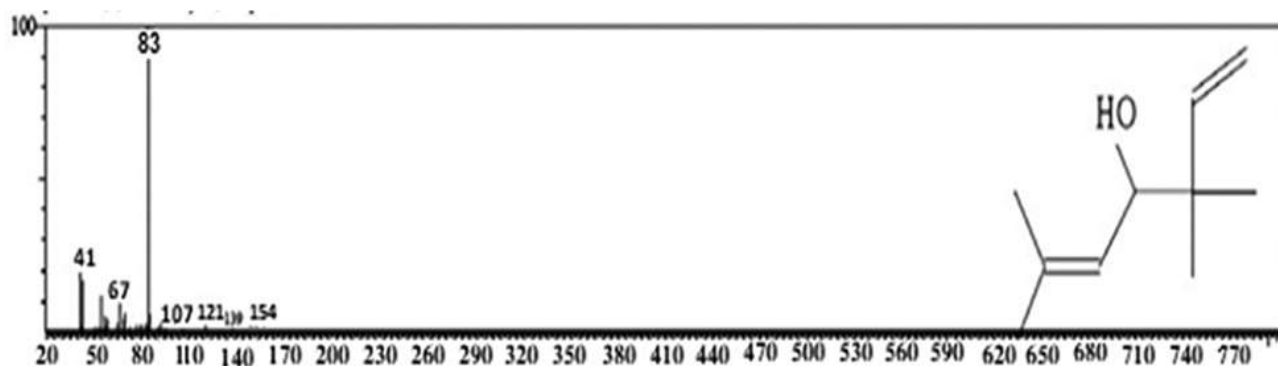


Fig. 5. A typical gas chromatogram of the artemisia alcohol.

obtained by hydrodistillation analyzed using GC-MS was found that the major components of *A. fragrantissima* were thujone (33.97%), eucalyptol 8.17, artemisia alcohol (3.49%), santolina triene (1.97%), and terpineol (0.05%) (Zeedan, et al., 2014). Alshaili (2018) revealed that the chemical composition of essential oil of *A. fragrantissima* contains trans-sabinyl acetate (0.75–10.20%), α -terpineol (3.53–9.39%), trans-menth-2-en-1-ol (6.5–13.34%), and β -thujone (11.34–22.11) using GC-MS, whereas Choucry (2017) reported that the major components were caryophyllene oxide (23.50%) and 1-terpinen-4-ol (11.15). As well as in Jordan

15 compounds were identified of *A. fragrantissima* essential oil, artemisia ketone, β -sesquiphellandrene, and carvacrol are the major observed compounds with ratios 19.87, 14.57, and 13.44%, respectively, (Alshaili, and Al-fawwaz, 2014).

Although β -phellandrene, linalool, verbenone, and cedrol were found in other studies, they could not be detected in the plants from the present study. These variations may be due to the influence of geographical differences, physiological differences, and genetic factors (Adams, 2007). Environmental factors such as climate, soil, harvest season, method of drying, storage conditions, and even the part of the plant tissue

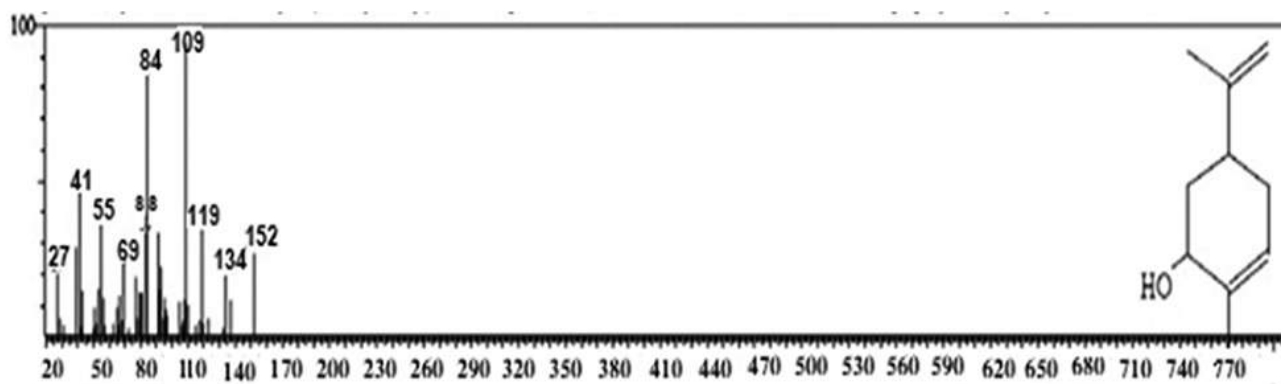


Fig. 6. A typical gas chromatogram of the trans-carveol.

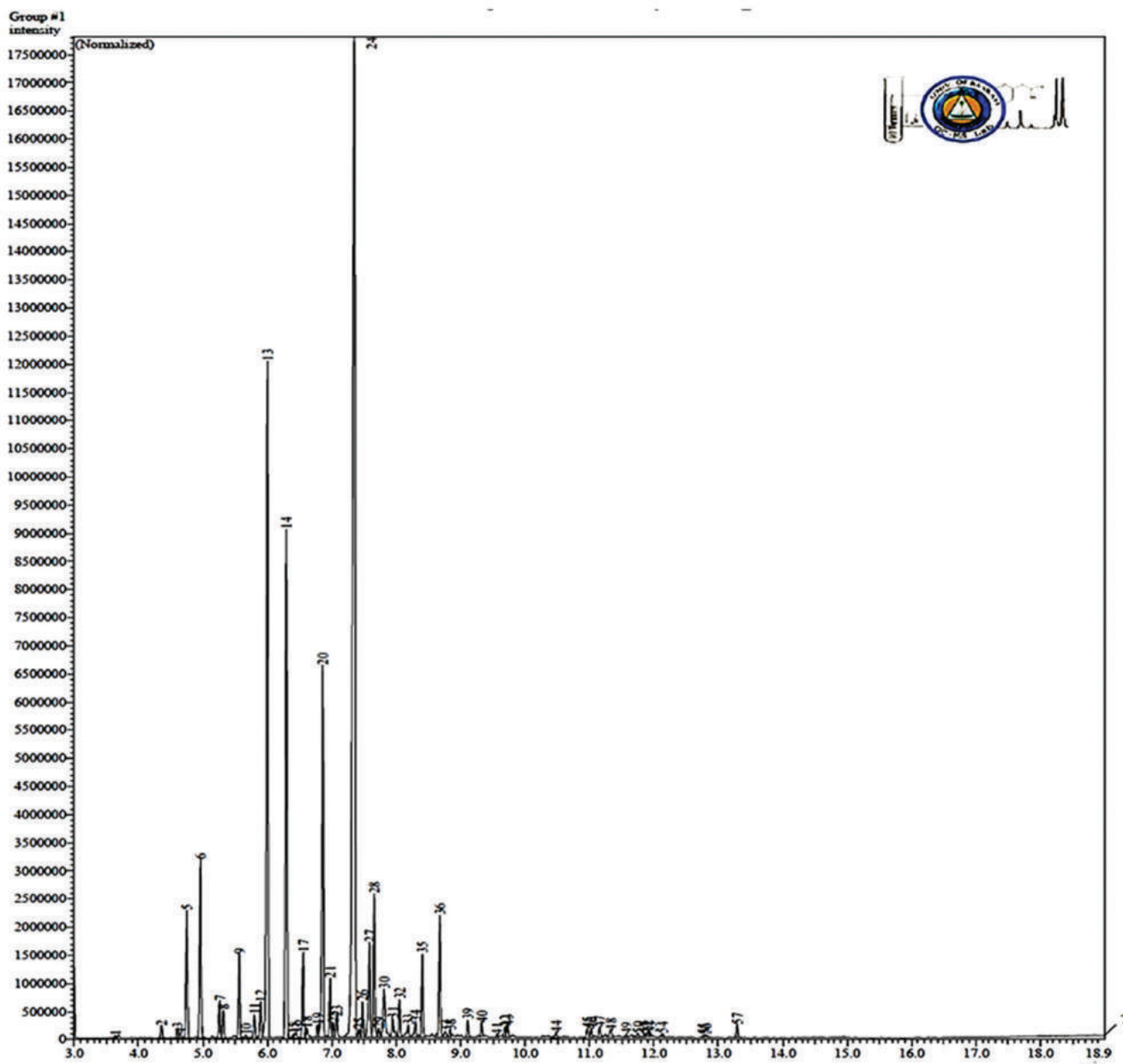


Fig. 7. Chromatogram of essential oil of *Achillea fragrantissima* leaves.

TABLE I
COMPOUNDS IDENTIFIED IN THE ESSENTIAL OIL OF *A. FRAGRANTISSIMA* LEAVES USING GC-MS

Peak number	Formula	Retention time	Retention indices	Content (%)	Components
1	C15H42P6Pd2	3.633	87409	0.06	Dipalladium (0), tris [mu bis(dimethylphosphino) methane]
2	C10H16	4.353	375108	0.26	Santolina
3	C10H16	4.598	295483	0.20	Tricyclo[2.2.1.0 (2,6)]heptane, 1,7,7-trimethyl-(Tricyclene)
4	C41H39NO9	4.642	194053	0.13	1-O-p-Nitrobenzoyl-2,3,4,6-tetra-O-benzyl-beta-d-galactose
5	C10H16	4.749	36731873	2.54	Alpha-Pinene
6	C10H16	4.959	5219456	3.61	Camphene
7	C10H16	5.255	1085767	0.75	Sabinene or Thujene
8	C10H16	5.313	835579	0.58	Beta-pinene
9	C10H18O	5.559	2320358	1.60	Yomogi alcohol
10	C10H16	5.664	96064	0.07	Alpha-Phellandrene
11	C10H16	5.798	674863	0.47	(+)-4-Carene
12	C10H14	5.896	1154110	0.80	m-Cymene
13	C10H18O	5.997	21131715	14.60	1,8-Cineole
14	C10H16O	6.292	14835852	10.25	Artemisia ketone
15	C38H36N2O4	6.402	123812	0.09	Estradiol 17-benzoate-3-phenylazobenzoate
16	C10H18O2	6.440	179688	0.12	alpha-Methyl-alpha- [4-methyl-3-pentenyl] oxiranemethanol
17	C10H18O	6.550	2429384	1.68	Artemisia alcohol
18	C10H16	6.609	378420	0.26	Bicyclo[4.1.0]hept-3-ene, 3,7,7-trimethyl-
19	C9H14	6.779	442115	0.31	Bicyclo (3.3.1)non-2-ene
20	C10H16O	6.859	11322487	7.82	3-Thujanone
21	C10H16O	6.973	1669169	1.15	Thujone
22	C10H14O	7.020	438939	0.30	Chrysanthene
23	C10H18O	7.074	714612	0.49	p-Menth-1(7)-en-9-ol
24	C10H16O	7.346	49947783	34.50	Camphor
25	C9H14O	7.419	277954	0.19	Sabina ketone
26	C10H14O	7.472	1066587	0.74	Pinocarvone
27	C10H18O	7.582	3249579	2.24	Borneol
28	C10H18O	7.658	4070212	2.81	4-Terpeneol
29	C10H14O	7.730	323081	0.22	3,9-Epoxy-p-mentha-1,8(10)-diene
30	C10H18O	7.810	2218854	1.53	alpha-Terpeneol
31	C15H26O2	7.944	780403	0.54	Methyl 3,4-tetradecadienoate
32	C10H16O	8.050	1038638	0.71	trans-carveol
33	C11H22	8.184	560224	0.39	2-Heptene, 5-ethyl-2,4-dimethyl-
34	C10H14O	8.294	561007	0.39	Carvone
35	C10H16O	8.402	2400410	1.66	Piperitone or carvomenthenone
36	C12H20O2	8.676	3450467	2.38	Acetic acid, 1,7,7-trimethyl-bicyclo [2.2.1] hept-2-yl ester
37	C10H14O	8.765	240528	0.17	P-Cymene
38	C10H14O	8.835	208656	0.14	Carvacrol
39	C12H18O2	9.109	459884	0.32	Carvyl acetate
40	C10H12O2	9.323	386113	0.27	3-Allyl-6-methoxyphenol
41	C13H18O	9.559	74539	0.05	Damascenone
42	C10H14O	9.689	401345	0.28	2H-Inden-2-one, 1,4,5,6,7,7a-hexahydro - 7a-methyl-, (S)-
43	C11H14O2	9.727	321481	0.22	Methyl eugenol
44	C15H24	10.479	234465	0.16	beta-Cubebene
45	C19H32O	10.967	351364	0.24	1,9,12,15-octadecatetraene, 1 methoxy-
46	C10H16O	11.025	274199	0.19	beta-Pinene oxide
47	C18H30O5	11.155	393228	0.27	2-Butyloxycarbonyloxy-1,1,10-trimethyl-6,9-epidioxydecalin
48	C10H16O	11.327	376046	0.26	Pinane
49	C21H30O2	11.571	134997	0.09	3-Phenylpropanoic acid, dodec-9-ynyl ester
50	C13H20O3	11.751	200159	0.14	Cyclopentaneacetic acid, 3-oxo-2-(2-pentenyl)-, methyl ester, [1 alpha, 2. Alpha (Z)]-
51	C10H18O	11.850	145938	0.10	Cyclohexanol, 2-methyl-3-(1-methylethenyl)-, (1-alpha.,2-alpha.,3-alpha.)-
52	C15H26O	11.903	155051	0.11	Eudesm-4 or beta-eudesmol) or beta-selinene
53	C15H20O	11.948	86696	0.06	Benzofuran, 7-cyclohexyl-2,3-dihydro-2methyl-
54	C16H24	12.129	118661	0.08	1,3-Di (propen-1-yl) adamantane
55	C11H16O2	12.768	80578	0.06	Jasmololone
56	C11H18N2	12.808	136055	0.09	(+)-1-Cyano-d-camphidine
57	C16H30O2	13.290	373362	0.26	Z-7-Hexadecenoic acid
			144776160	100.00	

GC-MS: Gas chromatography-mass spectrometry, *A. fragrantissima: Achillea fragrantissima*

evaluated are all parameters that should be considered (Skotti, et al., 2014; Bouaziz, et al., 2015). Moreover, Farhat, et al. (2001) showed major seasonal changes in the composition of the oil. Therefore, the concentration and composition of the oil in our tests may result from seasonal and year differences during the collection of plants essential oil content of *Achillea* species changed according to the region therewith medicinal characters of the plants are also changed (Toncer, et al., 2010).

IV. CONCLUSION

Results from this study have shown that the essential oil contains compounds with useful in pharmacological purposes. GC-MS analysis revealed that 57 different chemical components were identified in the *A. fragrantissima* leaves. The camphor compound recorded the highest amounts of 34.50%. We also showed that leaves of *A. fragrantissima* contain different amounts of monoterpenes and sesquiterpenes. All the detected compounds can inter in making different medicinal drugs.

REFERENCES

- Abaas, I.S., Majeed, M.J. and Majeed, A.H., 2013. Analysis with evaluation of drying temperature on essential oil content of *Achillea fragrantissima* and *Artemisia herb-alba*. *International Journal of Pharmacy Pharmaceutical Science*, 5(3), pp.913-914.
- Abdel-Rahman, R.F., Alqasoumi, S.I., El-Desoky, A.H., Solimand, G.A., Paré, P.W. and Hegazy, M.E., 2015. Evaluation of the anti-inflammatory, analgesic and anti-ulcerogenic potentials of *Achillea fragrantissima* (Forssk.). *South African Journal of Botany*, 98, pp.122-127.
- Adams, R.P., 2007. *Identification of Essential Oil Components by Gas Chromatography Mass Spectrometry*. 4th ed. Allured Publishing, Carol Stream, Illinois, p.120.
- Ageel, A.M., Mossa, J.S., Al-Yahya, M.A., Al-Said, M.S. and Tariq, M., 1989. Experimental studies on antirheumatic crude drugs used in Saudi traditional medicine. *Drugs under Experimental and Clinical Research*, 15, pp.369-372.
- Alenad, A.M., Al-Jaber, N.A., Krishnaswamy, S., Yakout, S.M., Al-Daghri, N.M. and Alokail, M.S., 2013. *Achillea fragrantissima* extract exerts its anticancer effect via in-duction of differentiation, cell cycle arrest and apoptosis in chronic myeloid leukemia (CML) cell line K562. *Journal of Medicinal Plants Research*, 7, pp.1561-1567.
- Al-Mustafa, A.H. and Al-Thunibat, O.Y., 2008. Antioxidant activity of some Jordanian medicinal plants used traditionally for treatment of diabetes. *Pakistan Journal of Biological Sciences*, 11, pp.351-358.
- Alsohaili, S., 2018. Seasonal variation in the chemical composition and antimicrobial activity of essential oil extracted from *Achillea fragrantissima* grown in Northern-Eastern Jordanian desert. *Journal of Essential Oil-Bearing Plants*, 21(1), pp.139-145.
- Alsohaili, S.A. and Al-fawwaz, A.T., 2014. Composition and antimicrobial activity of *Achillea fragrantissima* essential oil using food model media. *European Scientific Journal*, 10(30), pp.1857-7881.
- Bakr, R.O., Arafa, R.K., Al-Abd, A.M. and Elshishtawy, H.M., 2014. Phenolics of *Achillea fragrantissima* growing in Egypt and its cytotoxic activity. *Journal of Medicinal Plants Research*, 8(21), pp.763-771.
- Barel, S., Segal, R. and Yashphe, J., 1991. The antimicrobial activity of the essential oil from *Achillea fragrantissima*. *Journal of Ethnopharmacology*, 33, pp.187-191.
- Batanouny, K.H., Aboutabl, E., Shabana, M. and Soliman, F., 1999. *Wild Medicinal Plants in Egypt*. Academy of Scientific Research and Technology, Cairo, pp.1-56.
- Bouaziz, A., Khennouf, S., Zarga, M.A., Abdalla, S., Baghiani, A. and Charef, N., 2015. Phytochemical analysis, hypotensive effect and antioxidant properties of *Myrtus communis* L. growing in Algeria. *Asian Pacific Journal of Tropical Biomedicine*, 5(1), pp.19-28.
- Choucry, M.A., 2017. Chemical composition and anticancer activity of *Achillea fragrantissima* (Forssk.) Sch. Bip. (*Asteraceae*) essential oil from Egypt. *Journal of Pharmacognosy and Phytotherapy*, 9(1), pp.1-5.
- El-Deeb, K., 1985. Chromatographic and Thermal Analysis of Certain Volatile Oil Containing Plants. Ph. D. Thesis: Faculty of Pharmacy, Cairo University.
- Elmann, A., Mordechay, S., Erlank, H., Teerman, A., Rindner, M. and Ofir, R., 2011. Anti-neuroinflammatory effects of the extract of *Achillea fragrantissima*. *BMC Complementary and Alternative Medicine*, 11, p.98.
- El-Shazly, A.M., Hafez, S.S., Wink, M., 2004. Comparative study of the essential oils and extracts of *Achillea fragrantissima* (Forssk.) Sch. Bip. and *Achillea santolina* L. (*Asteraceae*) from Egypt. *Pharmazie*, 59, pp.226-230.
- Farhat, G.N., Affara, N.I. and Gali-Muhtasib, H.U., 2001. Seasonal changes in the composition of the essential oil extract of East Mediterranean sage (*Salvia libanotica*) and its toxicity in mice. *Toxicol*, 39, pp.1601-1605.
- Gohari, A.R., Saeidnia, S., Mokhber-Dezfuli, N., Kiuchi, F.A., 2011. Review on phytochemistry and medicinal properties of the genus *Achillea*. *Daru*, 19, pp.173-186.
- Hammad, H.M., Suzan, A., Simona-Carmen, M., Abuhamdah, S., Al-Jaber, F. and Affi, U., 2014. Biological activities of the hydro-alcoholic and aqueous extracts of *Achillea fragrantissima* (Forssk.) grown in Jordan. *Natural Science*, 6(1), pp.23-30.
- Hazem, A., Al-Charchafchi, F. and Ghazzawi, D., 2012. Biochemical, antibacterial and antifungal activity of extracts from *Achillea fragrantissima* and evaluation of volatile oil composition. *Der Pharmacia Sinica*, 3(3), pp.349-356.
- Hifnawy, M.S., Rashwan, O.A. and Rabeh, M.A., 2001. *Comparative Chemical and Biological Investigations of Certain Essential Oils Belonging to Families Asteraceae, Lamiaceae and Graminae*. Vol. 39. Bulletin Faculty of Pharmacy Cairo University, Egypt, pp.35-53.
- Massada, Y., 1976. *Analysis of Essential Oil by Gas Chromatography and Spectrometry*. John Wiley and Sons, New York.
- Mazandarani, M., Mirdeilami, S.Z. and Pessarakli, M., 2013. Essential oil composition and antibacterial activity of *Achillea millefolium* L. from different regions in North east of Iran. *Journal of Medicinal Plants Research*, 7(16), pp.1063-1069.
- Mottaghi, M., Shanjani, P.S., Jafari, A.A., Mirza, M. and Bihamta, M.R., 2016. Essential oil composition of *Achillea filipendulina*, *A. arabica* and *A. eriophora* cultivated under temperate climate in Iran. *Journal of Medicinal Plants and By Products*, 2, pp.153-158.
- Nemeth, E., 2010. *Achillea* species used medicinally in Hungary. *Israel Journal of Plant Science*, 58, pp.279-289.
- NIST/EPA/NIH., 2005. Mass Spectral Library, Ver. NIST 05.
- Shalaby, A.F. and Richter, G., 1964. Chromatographic investigation of the essential oil of *Achillea fragrantissima*. *Journal of Pharmaceutical Science*, 53, pp.1502-1505.
- Skotti, E., Anastasaki, E., Kanellou, G., Polissiou, M. and Tarantilis, P.A., 2014. Total phenolic content, antioxidant activity and toxicity of aqueous extracts from

- selected Greek medicinal and aromatic plants. *Industrial Crops and Products*, 53, pp.46-54.
- Soltan, M.M. and Zaki, A.K., 2009. Antiviral screening of forty-two Egyptian medicinal plants. *Journal of Ethnopharmacology*, 126, pp.102-107.
- Toker, Z., Ozen, H.C., Clery, R.A., Owen, N.E., 2003. Essential oils of two *Achillea* species from Turkey. *Journal of Essential Oil Research*, 15, pp.100-110.
- Toncer, O., Basbag, S., Karaman, S., Diraz, E. and Basbag, M., 2010. Chemical composition of the essential oils of some *Achillea* species growing wild in Turkey. *International Journal of Agriculture and Biology*, 12, pp.527-530.
- Vandendoo, H. and Kratz, P.D., 1963. A generalization of the retention index system including linear temperature programmed gas-liquid partition chromatography. *Journal of Chromatography*, 11, pp.463-471.
- Vitalini, S., Iriti, M., Puricelli, C., Ciuchi, D., Segale, A. and Fico, G., 2013. Traditional knowledge on medicinal and food plants used in Val San Giacomo (Sondrio, Italy)-an alpine ethnobotanical study. *Journal of Ethnopharmacology*, 145, pp.517-529.
- Zeedan, G.S., Abdalhamed, A.M., Ottai, M.E., Abdelshafy, S. and Abdeen, E., 2014. Antimicrobial, antiviral activity and GC-MS analysis of essential oil extracted from *Achillea fragrantissima* plant growing in Sinai Peninsula, Egypt. *Journal of Microbial and Biochemical Technology*, S8, pp.6-8.

Feasible Time for Extraction of Lead from Spent Paste by Pyrometallurgical Process

Fakhri H. Ibraheem

Department of Chemical Engineering, Faculty of Engineering, Koya University, Kurdistan Region - F.R. Iraq

Abstract—This paper focuses on determining the feasible time for production of lead from spent paste (SP) by pyrometallurgical process through the rotary furnace. The extraction process faces several problems due to difficulties to control reaction media conditions. The experiments had been done on rotary furnace which exists in a secondary lead smelter in Baghdad - Khan Dhary. The SP mainly consists of lead sulfate and lead oxides. The experiments are implemented at high temperatures (1300°C) for reduction and desulfurization. 20 experiments were designed to determine the feasible smelting cycle time. The weight of slag, matte, and lead bullion was determined in each experiment as well as the percent of lead in each phase. These data were analyzed and graphically represented. The reaction's rate profile can be detailed in the following manner: (1) High rate during the first 90 smelting min. Low rate from 90 to 120 min. Very low rate after 120 min. (2) The feasible extraction time is between 120 and 130 min with average lead percent in slag not >8%. (3) The slag with lead percent higher than 5% is returned to the furnace whereas the lower one is extracted by the blast furnace.

Index Terms—Lead, Pyrometallurgical Process, Secondary Lead Smelter, Spent Past.

I. INTRODUCTION

The recycling of lead from lead acid battery scrap (BS) is important for two reasons, the first one is to provide a source for lead metal, and the second is to clean the environment from poisonous materials (Alessandra et al., 2009 and Vest, 2002). The lead in battery consists of alloys for poles and connectors, and pure for positive and negative active materials as shown in Fig. 1 (Vest, 2002 and Wei Zhanga et al., 2016); therefore, the spent paste (SP) is an important source for pure lead (Paul, 2015 and Hota, 2013).

There are three methods to extract lead and as follows:

- Hydrometallurgical process (Habashi, 1997 and Hotea, 2013).
- Electrochemical cell (Cole, 1984).

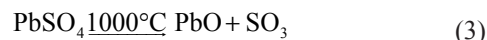
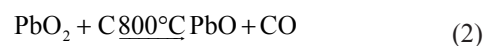
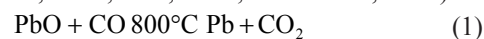
“The objective of the hydrometallurgical methods, or electrolytic methods, is to electrically and selectively reduce all lead compounds to metallic lead” (Vest, 2002).

- Pyrometallurgical process by the blast and/or rotary furnace (EPA, 1986; Habashi, 1997; and Hota, 2013).

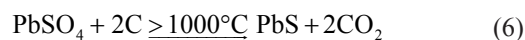
The production technology starts by breaking the BS and separating its components of plastics, polyvinyl chloride, lead metals, and SP (Errington, 2005; Vest, 2002; and Wei Zhanga et al., 2016). The SP represents about 56% weight percent of total battery weight. It consists of about 20% lead oxides PbO_x and 80% of lead sulfate $PbSO_4$ (Paul, 2015; Jaeck, 1989; United Nation, 2002; and Wei Zhanga et al., 2016). The SP is charged into a rotary furnace which is shown in Fig. 2 (Monometer Co., Ltd., manual).

A reduction reaction occurs to lead oxides during the 1st h of smelting by coke (anthracite). A desulfurization reaction occurs to lead sulfates during the 2nd h (Wright et al., 1994; Kateřina et al., 2015). Fluxing agents are mixed with the charge to improve extraction reaction media. They consist of sodium carbonate (Na_2CO_3) to create molten reaction media, coke for reduction reactions of lead oxides, salt NaCl to reduce slag molten temperature, and iron filings for desulfurization reaction of lead sulfate (Habashi, 1997; Iain et al, 2001; Tuffrey, 1989; and Yliaho, 2016).

The chemical reactions inside the furnace during the 1st h are determined as follows (Arnout et al, 2011; Benrontol, 2010; United Nation, 2002; Vest, 2002; and Yliaho, 2016).



Whereas the chemical reactions through the 2nd h are as follows:



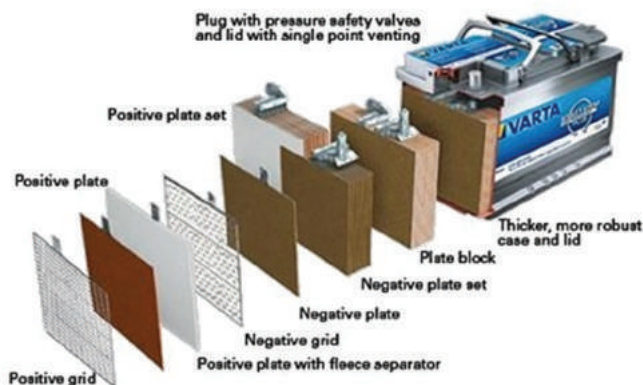


Fig. 1. Lead acid battery components.

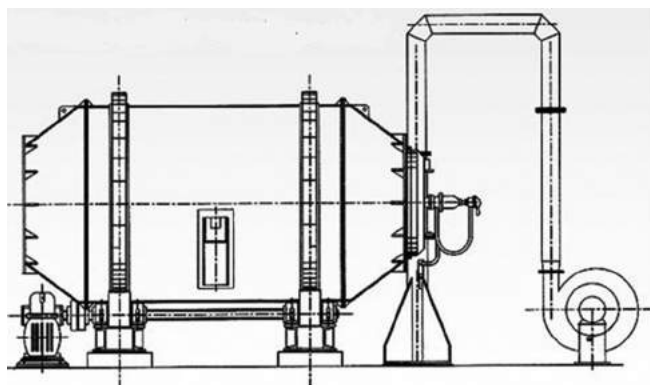
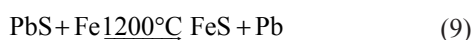
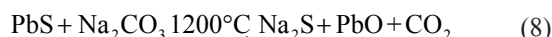
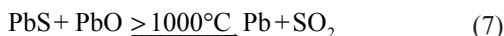


Fig. 2. Rotary furnace with burning system.



It is shown that there are many reactions. The rate of these reactions depends on efficient mixing, heat distribution, and concentration of reactant materials (USAID/Egypt, 1999).

The molten metal, slag, and additives are poured into 500 kg cast iron pots after specified smelting time as shown in Figs. 3-5.

Physically, the molten media are recognized to three layers before pouring. The lower layer is the lead which is of higher density, the matt which is the transition zone between the metal and slag, whereas the slag is the upper layer as shown in Fig. 6 (Calvo, 1985 and Wei Zhanga et al., 2016).

The production is crude lead bullions. The red shiny color for slag is recognized easily; therefore, it is poured in separated pots. The matt is flowing with the lead and forms an upper layer over the crude lead pot. The matt is removed manually and returned to the furnace. Fig. 7 shows two pots one with the matt layer and the other after removing it. The polluted gases are exhausted of the furnace through a cooling and filtration system (Hawkins, 1993 and Jitka, 2016).

A safety precaution was taken in consideration. Monthly monitoring of lead in blood is done by the medical department.



Fig. 3. The actual rotary furnace where the experiments had been done.



Fig. 4. Pouring of molten metals, slag, and additives.

The research experiments were done on rotary furnace in secondary lead smelter factory in Baghdad - Khan Dhary. The aim of this paper is to search for the feasible lead extraction time from SP.

II. EXPERIMENT EQUIPMENT

- Rotary furnace: A 1.5-m diameter, 2 m long rotary furnace is manufactured by Monometer Co., Ltd., UK. Its' capacity is 1 ton charge weight without additives. The furnace is equipped with 70 L/h gasoil burner. A geared motor rotating drive unit is assembled with the furnace; therefore, it rotates at a constant speed of 2 rpm (Vest, 2002).
- Cooling and filtration system for polluted gases (Calvo, 1985).

III. METHODOLOGY

A. Design of Experiments

The efficiency of extraction is affected by many factors in addition to the smelting time such as temperature, mixing rate, and amount of fluxing agent. The weight of the charge is fixed at 1 ton SP. The amount of fluxing agents is determined from the lead smelting knowhow by Chloride Com. Ltd.,



Fig. 5. Cast iron pot, capacity 500 kg.

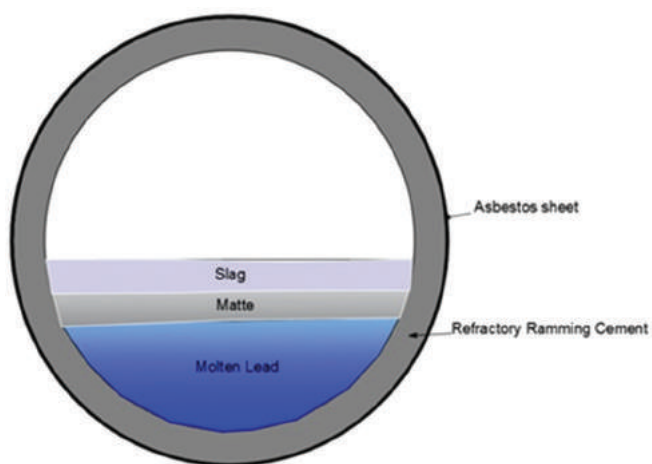


Fig. 6. The molten layers inside the rotary furnace.



Fig. 7. Two metal pouring cases, the right one with matt and the other without.

UK, manual. The charge type of SP is taken in consideration as shown in Table I (Paul, 2015 and Errington et al, 2005 and Eric, 1989).

The smelting time is considered as a variable parameter. The production data after the 1st h is determined each 5–10 min. For this research, 20 experiments have been conducted to cover the range from 60 to 160 min. The weight of lead bullion, matt, and slag was determined for each run. The amount of remaining lead in the slag is determined for each run, and is considered as a guide for efficient extraction.

TABLE I
AMOUNT OF FLUXING AGENTS FOR ONE-TON CHARGE

Material	Amount in kg
Sodium carbonate Na_2CO_3	80
Coke as anthracite	60
Iron filings	50
Commercial salt NaCl	25

B. Chemical Analysis

The amount of the remaining lead in slag is determined by chemical analysis method according to the chemical analysis procedure manual-CHLORIDE technical documents (Dean, 1979). The results were confirmed by additional X-ray fluorescence equipment manufactured by Swiss ARL company, model 1988.

C. Temperature Measurement

A 300 mm portable manual thermometer type k from “Thermo Co., Ltd.,” was used. The temperature of the exhaust gases was measured through the gap between furnace and exhaust duct. It is calibrated by Iraqi Standardization and Quality Control Organization (ISQCO).

D. Weighing Scale

Hanged weighing scale was used with capacity 500 kg and 2 kg accuracy. It is calibrated by ISQCO.

IV. EXPERIMENTAL RESULTS

To determine the feasible production technology time, 20 experiments were done for this research whose details are shown in Table II.

V. DISCUSSION OF RESULTS

1. Increasing the extraction time will increase the amount of produced bullion lead as shown in Fig. 8. The rate of productivity has a uniform increase through 2 h; then, it became slow and approximately constant. The maximum productivity of bullion lead is 400 kg from 1 ton charge.
2. The weight of matte layer reduces by increasing extraction time (Tuffrey, 1989) which means better separation phases. The matte weight decreases over 2 h. A natural cooling leads to mild separation. Fig. 9 shows the profile of reducing matte weight with time.
3. The percent of lead in the matter is reduced by increasing extraction time. The experiments show that the minimum lead weight percent in matte is 15%. The matte materials are recharged to the rotary furnace for efficient extraction. Fig. 10 shows the rate of lead percent decrease in matte material over a time.
4. The weight of slag is reduced by increasing extraction time. The slag constituent of non-extracted lead metal which is still as sulfate and dioxide, and molten fluxing agents. Fig. 11 shows the rate of slag weight decrease over a time.
5. The weight percent of lead in slag is reduced by increasing extraction time. The rate of decrease is high at the first 2 h. The

TABLE II
DETAILS OF EXPERIMENTAL DATA

Experimental No	Extraction time minutes	Weight of slag kg	Percentage lead in slag	Weight matte zone kg	Percentage lead in matte zone	Weight of bullion lead kg
1	60	120	37	28	30	210
2	61	122	35	30	28	200
3	70	120	30	30	28	230
4	70	115	30	35	27	205
5	80	117	24	32	32	250
6	80	112	25	30	30	240
7	90	95	19	29	26	340
8	95	100	21	28	27	320
9	100	93	16	25	21	338
10	100	90	17	27	22	330
11	110	86	12	24	20	364
12	114	80	13	20	20	350
13	120	81	12	24	18	382
14	120	85	12	20	20	370
15	130	79	10	19	16	403
16	133	75	10	17	18	400
17	140	75	8	19	16	410
18	142	65	11	16	18	400
19	150	70	8	18	14	414
20	160	68	10	18	15	405

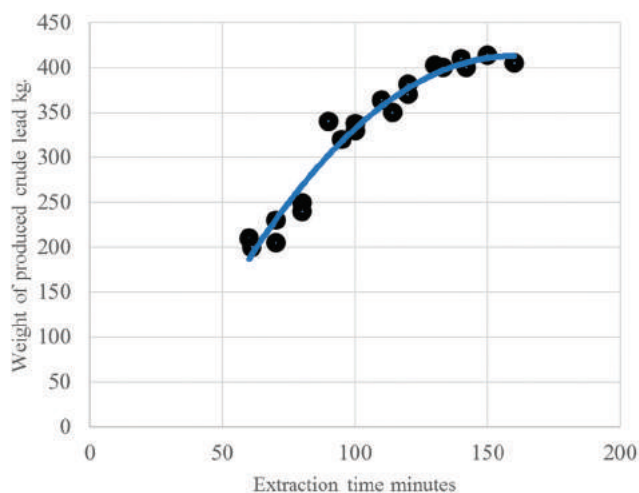


Fig. 8. The effect of extraction time on net lead bullion production efficiency.

lowest lead percent in slag is 8%. The slag that contains lead >5% weight percent is returned to the furnace. The accumulated slag with lead percent <5% is transferred to blast furnace unit for more extraction. The physical properties of slag are effected by its' composition. It is shown obviously that the density of slag is reduced with time while its' viscosity increases. Fig. 12 shows the profile of lead extraction efficiency.

- Fig. 12 shows a decrease in extraction efficiency >2 h smelting. During the period from 120 to 160 min, the saving in the lead is only 2%, that is, 20 kg. The global price of lead in December 2017 is 1140 US\$ for one pure metric ton (Mining Market and Investment sheet). The value of 20 kg lead is 23 US\$. During the 40 min, the amount of consumed diesel oil is 47 L. The local market price of 1-L is 0.4 US\$. The value of fuel is 19 US\$ and when adding the costs of

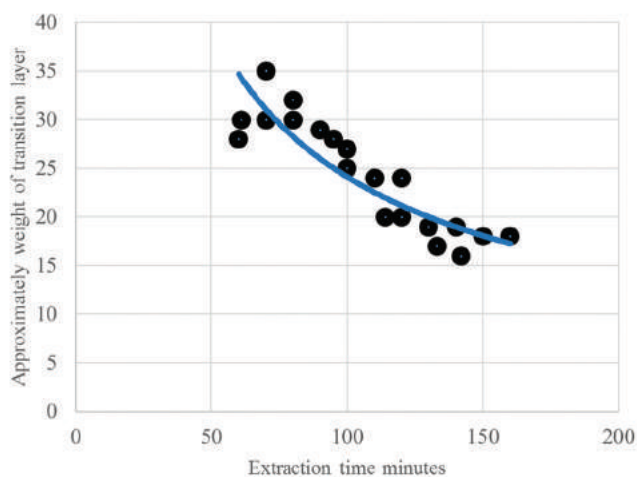


Fig. 9: The effect of extraction time on the matte weight.

operation and services, it looks that the production cost is higher than the saving amount of lead. It is shown obviously that increasing the extraction time >130 min is not feasible.

VI. CONCLUSIONS

- The productivity efficiency of crude lead improved by increasing extraction time.
- The feasible extraction time is between 120 and 130 min.
- The best amount of crude lead produced from 1 ton SP charge is 400 kg.
- The weight percent of lead in slag is about 8% after 2 h smelting.
- The slag with percent lead >5% is returned to the furnace with new charge.

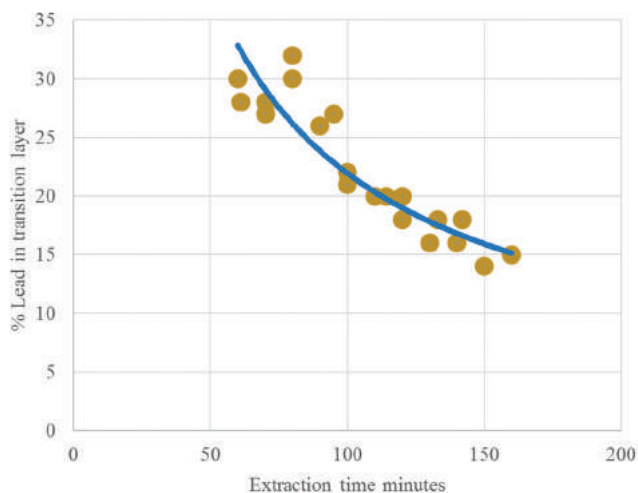


Fig. 10. The effect of extraction time on the matte materials lead percent.

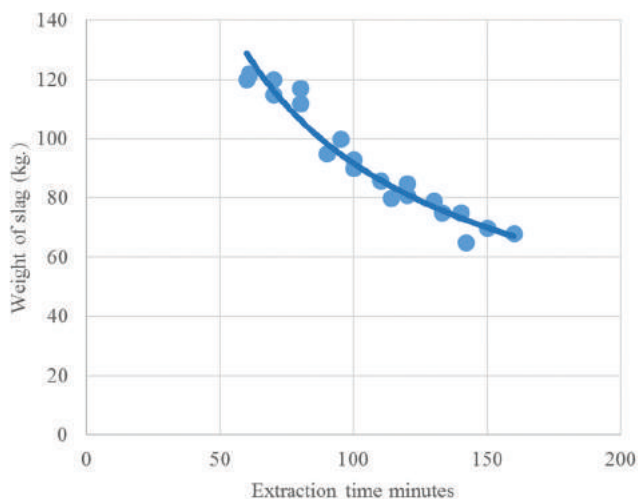


Fig. 11. The effect of extraction time on the amount of produced slag.

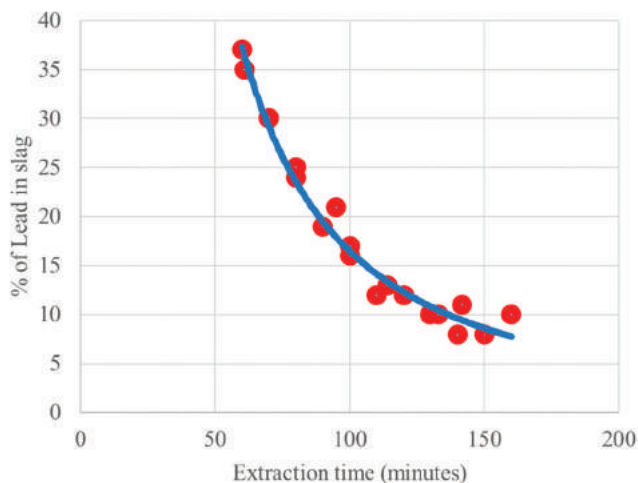


Fig. 12: The effect of extraction time on percent of lead in slag.

VII. RECOMMENDATIONS

The following points are recommended for future work:

1. The mixing efficiency effect on extraction rate.
2. The effect of fluxing agent constituents' amount on the extraction efficiency.
3. The effect of extraction temperature on production efficiency.

REFERENCES

Alessandra, S., Antunes, A., Filho, I.N., Venquiaruto, L.D., de Oliveira, D., Mossi, A., Di Luccio, M., Treichel, H., and Dallago, R., 2009. Qualitative lead extraction from recycled lead-acid batteries slag. *Journal of Hazardous Materials*, 172, pp.1677-1680.

Arnout1, D.S., 2011. *Thermodynamics of Lead Recycling*. Metallurgy Conference, Belgium, p.10.

Benrontol., 2010. *Primary Metal Production No. 20051786*. Available from: <https://www.scribd.com/document/39618162/CM2200-Primary-Metals>.

Bill, E.P., Arthur, P., Wang, J., Dong, Y., 2005. *ISA-YMG Lead Smelting Process*. Proceeding of the International Symposium on Lead and Zinc Processing, Kyoto, Japan.

Brew, R.B.M., Fountain, C., Pritchard, J., 1991. *ISASMELT for secondary lead smelting*. s.l. 10th International Lead Conference, United Kingdom, pp.171-180.

Calvo, F.A., 1985. *Metal losses in lead blast furnace slag: The influence of the charge and the reducing conditions*. Canadian Metallurgical Quarterly, Spain, pp.345-348.

Chemicon International, I., 1999. *Technical and Economic Study for Small- and Medium-Sized Lead Smelters*. Available from: http://www.pdf.usaid.gov/pdf_docs/Pnacy063.pdf.

Cole, E.R., Lee, A.Y., Paulson, D.L., 1984. Electrolytic method for recovery of lead from scrap batteries. United States Department of the Interior, USA.

Dean, J.A., 1979. *Lange's Handbook of Chemistry*. 12th ed. McGraw-Hill, New York.

EPA, 1986. *Secondary Lead Processing*. U.S. Environmental Protection Agency, Research Triangle Park, USA.

Eric, R., 1989. Thermodynamic analysis of the direct converting of lead sulphide. *Journal of the South African Institute of Mining and Metallurgy*, 89, pp.33-39.

Habashi, F., 1997. *Handbook of Extractive Metallurgy*. WILEY-VCH, Canada.

Hawkins, K.R.P., 1993. Lead/acid battery recycling and the new isasmelt process. *Journal of Power Sources*, 42, pp. 299-313.

Hotea, V., 2013. Clean technology of lead recovery. *Applied Economics and Management*, 2, pp.263-269.

Iain, T., Ric, M., Smith, GN., 2001. LEAD the Facts. Surrey KT12 4RG. Ian Allan Printing Ltd., Hershham, London UK.

Jaeck, M.L., 1989. *Primary and Secondary Lead Processing*. Elsevier B.V. All Rights Reserved, Canada, pp.113-118.

Jahahshahi, S., Sun, S., 1992. *Studies on the reduction kinetics of metallurgical lead slags*. 4th International Symposium on Metallurgical Slags and Fluxes, Tokyo.

Jitka, M., 2016. *Recycling of Non-Ferrous Metals*. VŠB Technical University of Ostrava, Czech Republic.

Kateřina, S., Manoko, L.M.K., 2015. *Theory of Production of Non-Ferrous Metals and Alloys*. VŠB Technical University of Ostrava, Moravian-Silesian Region, Czech Republic.

Queneau, P.B., Leiby, R., Robinson, R., 2015. Recycling lead and zinc in the United States. *World of Metallurgy*, 3, pp.149-163.

- Rabah, M.A., Barakat, M., 2001. Energy saving and pollution control for short rotary furnace in secondary lead smelters. *Renewable Energy*, 23, pp.561-577.
- Seetharaman, S., 2005. *Fundamentals of metallurgy*. Woodhead Publishing Limited, England.
- Tuffrey, N.E., 1989. Pyrometry studies of the combustion of lead concentrate particles under controlled conditions. Ph D Theses, University of British Columbia, Canada.
- United Nations, T.W.G., 2002. *Preparation of the Technical Guidelines for the Environmentally Sound Management of Waste Lead-Acid Batteries*. United Nations Environment Programme, Geneva.
- Vest, D.I.H., 2002. *Fundamentals of the Recycling of Lead Acid Batteries*. Available from: https://www.energypedia.info/images/7/78/Fundamentals_of_the_Recycling_of_Lead-Acid_Batteries.pdf.
- Wright, S., Jahanshahi, S., Errington, W.J., 1994. Reduction kinetics of slags produced from recycling of lead batteries; pyrometallurgy for complex materials and wastes. *The Minerals, Metals and Materials Society*, 5, pp.121-132.
- Wright, S., Lim, H., Rand, J., 1994. *An Investigation of the Reduction of Battery Paste (Al₂O₃-As₂O₃-CaO-FeO-Fe₂O₃-PbO-Sb₂O₃-SiO₂) Slags with Graphite*. The Minerals, Metals and Materials Society, Warrendale, PA, pp. 11-22.
- Yliaho, S., 2016. Distribution of Gallium, Germanium, Indium and Tin between Lead Bullion and Slag. School of Chemical Technology Master's Thesis for the Degree of Master of Science in Technology. Aalto University, Espoo.
- Zhang, C., Zahler, R.Z., 2009. *Current Status and Outlook on Chinese Secondary lead Industry*. International Secondary Lead Conference, Macau.
- Zhang, W., Yang, J., Wu, X., Hu, Y., and Yu, W., 2016. A critical review on secondary lead recycling technology and its prospect. *Renewable and Sustainable Energy Reviews*, 61, pp.108-122.
- Zhi, S., Cao, H., Lin, X., Zhang, X., 2017. Spent lead-acid battery recycling in China a review and sustainable analyses on mass flow of lead. *Waste Management*, 64, pp.190-201.

Thermal Stability and Reproducibility Enhancement of Organic Solar Cells by Tris(hydroxyquinoline)gallium Dopant Forming a Dual Acceptor Active Layer

Fahmi F. Muhammad¹, Khaulah Sulaiman²

¹Soft Materials and Devices Lab, Department of Physics, Faculty of Science and Health, Koya University, University Park, Danielle Mitterrand Boulevard, Koya KOY45, Kurdistan Region - F.R. Iraq

²Low Dimensional Materials Research Centre, Department of Physics, Faculty of Science, University of Malaya, 50603 Kuala Lumpur, Malaysia

Abstract—Nowadays, the main barriers facing organic solar cells (OSCs) from being commercialized and widely applied are their weak thermal stability and reproducibility problems. To tackle these problems, researchers usually consider various strategies which include modification in the devices architectural design, utilizing low energy gap materials, functionalizing their active layers, and the use of various optimization procedures. In this research work, we are specifically focused on the utilization of a small molecular organometallic, tris(hydroxyquinoline)gallium (Gaq3), as a secondary acceptor dopant, aiming at improving thermal stability, and reproducibility of OSCs. All-solution processed technique with the help of spin coater was used to deposit the active layer of the devices. Results showed that the addition of 29% molar fraction of Gaq3 into the devices active layer has considerably improved the thermal stability, photo-absorption, and reproducibility of the solar cells thanks to the excellent thermal stability and electron mobility of Gaq3 molecules. Our devices based on DH6T: PCBM:Gaq3 performed highest stable performance at 180°C, implying higher thermal stability compared to that of the reported P3HT: PCBM:F8BT and PTB7:PCBM: F8BT based solar cells. In spite of improved reproducibility, the efficiency of the devices was increased by 5.8 times compared to that of the control ones.

Index Terms—Active layer, dual acceptor, Gaq3 dopant, organic solar cell, reproducibility, Thermal stability.

I. INTRODUCTION

The detrimental effect on the environment and human life due to the long-term use of fossil fuels, oils, and natural

gases demands the involvement of alternative clean and non-harmful resources, such as solar energy, in the production of electricity. Photovoltaic (PV) technology is successfully utilized to convert sunlight energy into electricity by means of solar cells comprising various architectural designs and active materials (Elumalai et al., 2016; Mathew et al., 2014; Muhammad et al., 2018; Schmager et al., 2019; Zhao et al., 2017a). The straightforward installation and low maintenance costs of solar electricity compared to that of other electricity sources make PV technology more convenient and attractive. It has been reported by the United Nations Development Programme in 2000 that the yearly potentiality of solar radiation flux is 1575–49837 exajoules (EJ), while the upper atmosphere of earth encounters 174,000 terawatts of solar energy flux (Johansson et al., 2012). This is much higher than the entire energy utilization around the globe, which was 559.8 EJ in 2012 (Ansari et al., 2018).

At present, the first and second generations of solar cells which are based on inorganic active materials are predominating the PV market, with power conversion efficiencies of up to 25%, but they are expensive enough to be able to compete with the classical energy sources. Alternately, the third generation solar cells, namely organic solar cells (OSCs), dye-sensitized solar cells, and perovskite solar cells (PSCs), have received great attention over the past years due to their solution processability, low cost, flexibility, and their large-scale applications (Elumalai et al., 2016; Marinova et al., 2017; Mathew et al., 2014; Schmager et al., 2019). Third generation solar cells have now achieved a substantial decline in the production price of solar cells by 75% within less than a decade. The power conversion efficiency of OSCs has been significantly increased over the past decades from 1% in 1986 (Tang, 1986) to 5% in 2005 (Xue et al., 2005), and more recently to up to 13% thanks to the molecular optimization and the use of non-fullerene acceptors in their active materials (Zhao et al., 2017a). However, the main problems of these devices are their limited thermal stability and short lifetime which considered to be a real obstacle in front of their commercialization and

ARO-The Scientific Journal of Koya University
Volume VI, No 2(2018), Article ID: ARO.10491, 10 pages
DOI: 10.14500/aro.10491

Received 01 December 2018; Accepted 27 December 2018
Regular research paper: Published 30 December 2018

Corresponding author's e-mail: fahmi.fariq@koyauniversity.org
Copyright © 2018 Fahmi F. Muhammad, Khaulah Sulaiman. This is an open-access article distributed under the Creative Commons Attribution License.



their wide application. To compete OSCs with traditional non-OSCs, efficiencies of >15% and competitive stability are required. The unique features of organic materials making them attractive for OSCs are their optoelectronics tunability, light weight, flexibility, and high absorption coefficient (Liang et al., 2009; Muhammad and Sulaiman, 2011; Kaltenbrunner et al., 2012). The active layer of the device (the component which is responsible for solar energy absorption) is generally composed of two types of semiconducting materials which are n-type (electron acceptor) and p-type (electron donor). There should be a well-aligned energy band levels and viable miscibility between both donor (D) and acceptor (A) components to facilitate efficient charge transfer (CT) between the D-A moieties (Sehati et al., 2010; Treat et al., 2011). When sunlight strikes the donor component, photo-induced excitons (bounded electron-hole) are generated and are moved toward the boundary of D-A, where CT states are accumulated. Consequently, the bounded electrons and holes are dissociated into free charge carriers, whereby electrons are migrated from the lower unoccupied molecular orbital (LUMO) of the donor to that of the acceptor and holes are travelled from the higher occupied molecular orbital (HOMO) of the acceptor to that of the donor in a reverse direction (Sehati et al., 2010) (Fig. 1c). Finally, these free charges are, respectively, collected by the cathode and anode electrodes, thereby realizing a prototype OSC system (Fig. 1a).

It has been found in literature that various approaches and strategies were taken by researchers aiming at improving the overall performance of OSCs (Muhammad, 2014). Among these are bulk heterojunction, tandem and ternary structures which were developed to increase the D-A interfaces and hence improving the CT process compared to that of the bilayer D-A structure (Dennler et al., 2009; Peterson et al., 2011; Mulherin et al., 2011; Ameri et al., 2009; Muhammad

and Sulaiman, 2011b). However, the response of basic electrical parameters governing the performance of these devices has not yet been fully understood (Huajun et al., 2014; Street et al., 2013). Minxia et al. utilized different organic solvents to improve the performance of ternary OSCs (Minxia et al., 2015) and Peterson et al. included inorganic nanoparticle to enhance the performance of these devices (Peterson et al., 2011). Thermal annealing process was also considered for the ternary OSCs based on two-donor incorporated OSCs having active layers of P3HT:PCBM:F8BT (Kim et al., 2009) and PTB7:PCBM:F8BT (Shang et al., 2015). Very recently, the concept of dual acceptor incorporated active layers has been also suggested to enhance the light absorption and CT properties of OSCs (Muhammad et al., 2017b; Zhao et al., 2017b; Liu et al., 2016), whereas the use of non-fullerene based acceptors was found to show a prominent enhancement of efficiency (Zhao et al., 2017a). Besides, various newly synthesized materials and design approaches were reported to better tackle the stability problem and to achieve higher stable devices (Reddy et al., 2016; Cheng and Zhan, 2016; Song et al., 2005; Zhu et al., 2011; Hau et al., 2008).

Ga_q3 is a well-known small molecular organometallic material with interesting optoelectronics properties, photonic response selectivity, and thermal stability (Muhammad et al., 2010; Muhammad and Sulaiman, 2011d; Muhammad et al., 2016; Hernández et al., 2009; Muhammad and Sulaiman, 2011a). The use of Ga_q3 has been widely dedicated for organic light emitting diodes/displays, but its utilization was also extended for solution-processed OSCs (Muhammad et al., 2017b). Incorporation of small molecular materials into the active layer of OSCs is of current research interests (Liu et al., 2015; Ji et al., 2016) due to the distinct optoelectronics features offered by these materials. Benefited by thermal stability and electron mobility of Ga_q3, and

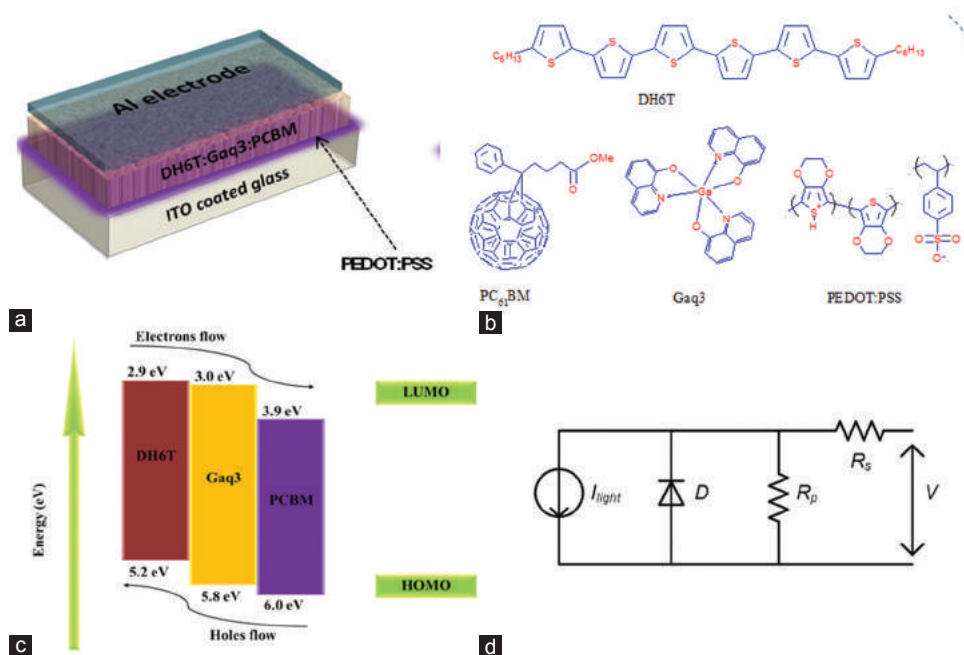


Fig. 1. The studied organic solar cells design (a), materials structure (b), higher occupied molecular orbital-lower unoccupied molecular orbital energy levels (c), and simulated equivalent circuit (d) of DH6T:PCBM:Ga_q3 active layer.

relatively close values of charge carrier mobility for α,ω -dihexyl-sexithiophene (DH6T) donor and methano-fullerene (PC₆₁BM) acceptor (Garnier et al., 1993; von Hauff et al., 2005; Muhammad and Sulaiman, 2011a; Muhammad et al., 2016), it is believed that the dispersion of a specified molar fraction of Gaq3 as a secondary acceptor dopant into the active layer of OSCs can have a great impact on the improvement of stability, reproducibility, and overall performance of these devices. Hence, in the current work, an optimum amount of Gaq3 is used to dope the active layer of OSCs comprising a dual acceptor, PCBM and Gaq3, that is aiming at maximizing the operation stability and reproducibility of the devices. The rest of the paper is organized as follows: In Section 2, the raw materials and methodology of the active layer preparation and characterization along with devices fabrication and assessment are given, whereas in Section 3 the achieved results are analyzed and discussed in detail. Finally, the main conclusions are drawn and presented in Section 4.

II. MATERIALS AND METHODS

The raw organic materials were purchased from Sigma-Aldrich (Malaysia Branch) in powder form and used as received without further purification. The OSC design, the molecular structure of the materials, their HOMO and LUMO energy levels along with an equivalent circuit to represent OSCs are shown in Fig. 1a-d, respectively. Poly(3,4-ethylenedioxythiophene):poly(4-styrenesulfonic) acid (PEDOT: PSS) was coated onto the anode electrode, indium tin oxide (ITO) to facilitate enhanced hole transport and to block the free electrons moving toward ITO. DH6T was utilized as the donor component, whereas the acceptor molecules were PCBM and Gaq3, respectively. To choose an optimum amount of Gaq3 to be doped into the device active layer, optical absorption studies of DH6T: Gaq3 system was initially performed.

The ITO (sheet resistance $\sim 10 \Omega/\text{sq}$) coated glass substrates (H. W. Sands Co., Ltd.) were cut into square shapes and patterned accordingly in a wet etching process using a bath of hydrochloric acid and distilled water (0.4:1) at temperature 60°C for 15 min. The PEDOT: PSS (from H. C. Starck, Baytron P VPAI 4033) was spin-coated onto the ITO at 3000 rpm for 20 s, then baked at 130°C for 5 min to achieve a thickness of $\sim 35 \text{ nm}$. Then, the active layer mixture of DH6T: PCBM:Gaq3, having concentration of 30 mg/ml, was dissolved in chlorobenzene and stirred overnight in the vials. Thin layer of DH6T: PCBM:Gaq3 (about 200 nm) was spin-coated onto the PEDOT: PSS layer followed by thermal deposition of aluminum ($\sim 50 \text{ nm}$ thick) under a vacuum of about 10^{-5} m bar . In this way, four identical devices were fabricated on a single substrate batch. The area of active layers was 14 mm^2 ($2 \text{ mm} \times 7 \text{ mm}$) for each device. To investigate thermal stability, the devices were thermally annealed on a temperature controlled hot plate under air ambient for 20 min in the range from 140 to 220°C with steps of 40°C , whereas the reproducibility strength was assessed based on the electrical records of the

four identical devices of the same batch. To analysis the PV performance of the devices, current density-voltage (J-V) measurement was recorded using Keithley 236 instrument under standard illumination ($100 \text{ mW}/\text{cm}^2$) originated from an Oriel solar simulator-model 67005 with an AM 1.5 G filter. The absorption spectra of the films were recorded using Jasco V-570 UV-visible-NIR spectrophotometer, whereas KLA Tensor P-6 surface profilometer instrument was used to measure the thicknesses of films. Differential Scanning Calorimetry (Q200 thermal analyzer) was utilized to record the thermal profile of Gaq3. Finally, field emission scanning electronic microscopy technique (FESEM, Quanta 200F) and transmission electron microscopy (TEM LEO LIBRA-120) were utilized to capture the morphology and molecular distribution of the films. The light-activated current source (J_{light}) depicts the amount of current generated in the cell when it is exposed to sunlight energy. From the electrical circuit, one can determine the net current as follows (Muhammad et al., 2017a):

$$J = J_{\text{light}} - J_s \left[\exp\left(\frac{V + JR_s}{nK_B T/q}\right) - 1 \right] - \frac{(V + JR_s)}{R_p} \quad (1)$$

Where, J_s is the saturation current of the diode under dark, K_B is the Boltzmann's constant, T is the temperature in Kelvin, q is electron unit charge, R_s and R_p are the series and parallel resistances of the device, respectively.

III. RESULTS AND DISCUSSION

The optimum amount of Gaq3 dopant to be added into the active layer system is selected based on the broadening strength of the absorption spectra of DH6T and its energy gap (E_g) reduction. The measurement of energy gap was carried out using the well-known Tauc's equation as follows (Muhammad and Sulaiman, 2011d):

$$\alpha h\nu = B(h\nu - E_g)^n \quad (2)$$

where, $\alpha = 2.303A/t$, A is the absorbance and t is thickness (optical path) of the film/solution, h is Planck's constant, ν is the frequency of the absorbed photons, B is an energy-independent constant, and E_g is the energy gap. The value of n in Equation 2 determines the type of optical transition during the photo-absorption process, $n = 1/2, 3/2, 2,$ and 3 for direct allowed, direct forbidden, indirect allowed, and indirect forbidden transitions, respectively. Extrapolation of the linear part of curves $(\alpha h\nu)^{2/3}$ versus $h\nu$ at the point where $(\alpha h\nu)^{2/3} = 0$ gives the value of E_g . The calculated energy gap of DH6T incorporated with molar fractions of Gaq3 is shown as inset of Fig. 2, whereas Fig. 2 shows the absorption spectra for DH6T: Gaq3 blends with a molar ratio of 0%, 12.4%, 29.8%, and 41.4% for Gaq3.

One can notice from the figures that the addition of Gaq3 resulted in a clear redshift in the absorption spectrum of DH6T, that is, shifting toward higher wavelength and reducing its energy gap. These are ascribed to a larger π - π stacking overlap between molecules (Muhammad et al., 2016). However, the addition of 41.4% molar fraction of Gaq3 was seen to increase E_g and to produce a blue shift in

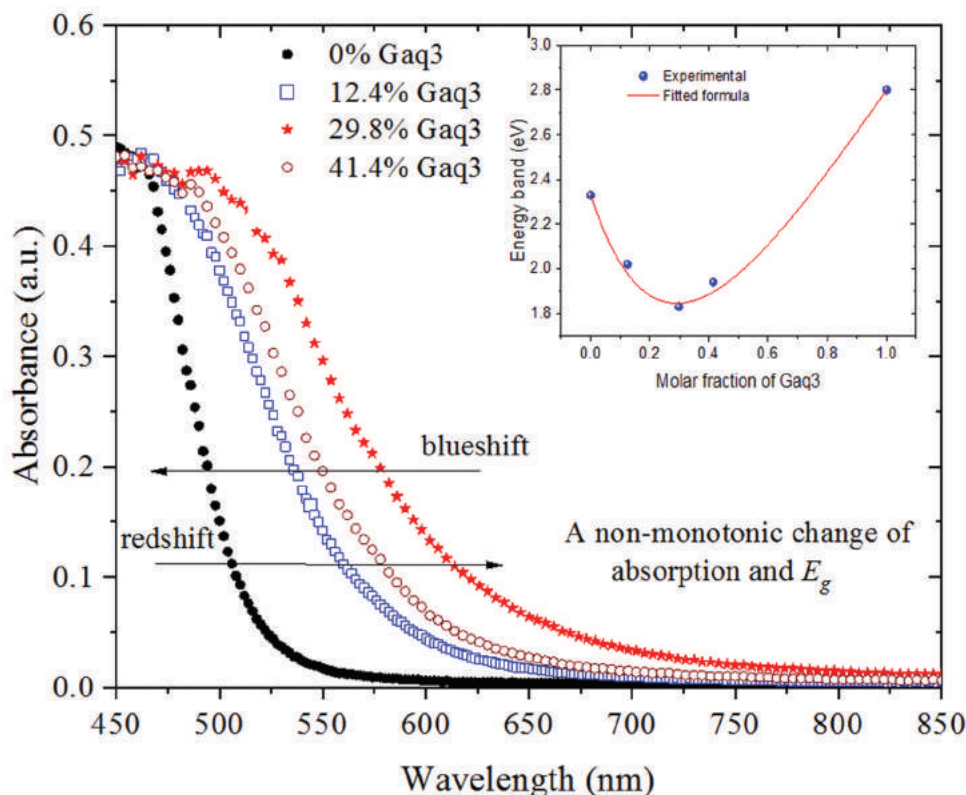


Fig. 2. Variation in the absorption spectra and energy gap of DH6T on the addition of various molar fractions of Gaq3.

the absorption spectrum. At E_g photons are absorbed by the molecules and electrons are jumped from the ground energy state (S_0) to the excited energy state (S_1), thereby transferring photo-energy between the D-A moieties. Therefore, the blue-shifted E_g at higher Gaq3 content is counted for the reduced π - π stacking. This can be understood as the increased spatial geometry due to Gaq3 content acts on increasing the tail-tail rotational defect (Sotgiu et al., 2002), which, in turn, leads to a reduced intermolecular interaction and decreased π - π orbital overlapping. To exactly identify the optimum amount of Gaq3 to be added in the next experimental steps during DH6T: PCBM:Gaq3 preparations, an empirical formula was derived, see Equation 3, by which the optimum molar fraction of Gaq3 was found to be 29% (Fig. 2).

$$E_g = E_{g1} \left(\frac{1-x}{1+Cx} \right) + E_{g2} \left(\frac{x+Cx}{1+Cx} \right)^2 \quad (3)$$

Where, C is a numerical factor that was deduced to be 0.74. The terms E_{g1} , E_{g2} , and x define the energy gap of DH6T (2.33 eV), Gaq3 (2.80 eV), and the molar percentage of Gaq3, respectively.

Fig. 3 shows the normalized absorption spectra of DH6T, PCBM, Gaq3, and their mixture with 29% molar fraction of Gaq3 in the DH6T: PCBM:Gaq3 active layer. Two characteristic absorption peaks at low and high wavelengths were detected for Gaq3 that is due to the orbital electronic transitions from p - π^* and π - π^* , respectively (Muhammad and Sulaiman, 2011d). The two peaks at 370 and 340 nm were assigned to DH6T and PCBM characteristic absorptions, respectively. These were found to be close

enough to those reported in literature (Cook et al., 2007; Kwon and Seo, 2007). It is worth to notice that the absorption spectra of DH6T: PCBM were broadened compared to that of DH6T, implying an improved photo-induced CT from DH6T to PCBM (Koeppel and Sariciftci, 2006). Interestingly, the addition of 29% Gaq3 into the DH6T: PCBM active layer has led to a useful broadening in the absorption spectrum tailoring to about 720 nm, where a vibronic shoulder was appeared. This vibronic peak can be directly correlated to the crystalline nature of the films as a result of the enhanced conjugation stacking and interchain interaction (Jo et al., 2009).

Fig. 4 shows the current density-voltage (J-V) characteristics of the OSCs based on DH6T: PCBM active layer with and without the addition of 29% molar fraction of Gaq3 that were tested in dark and under illumination conditions. Noticeably, the addition of Gaq3 molecules has increased the potential barrier (V_{D}) of the device in dark situation, meaning that a larger D-A boundary has been generated, that is, an increased p-n junction barrier. Consequently, a higher open circuit voltage (V_{oc}) is expected under light condition (see the solid blue triangle data points). The results showed a pronounced enhancement in the photocurrent and output voltage of the devices when Gaq3 is included. The short current density (J_{sc}) was increased from 0.63 mA to 1.26 mA and the V_{oc} improved from 0.30 V to 0.74 V. As such, the J_{sc} and V_{oc} were increased by an order of about 2 and 2.5, respectively. These increments are thought to be originated from a complementary enhancement of the photo-absorption ranging from 300 nm to about

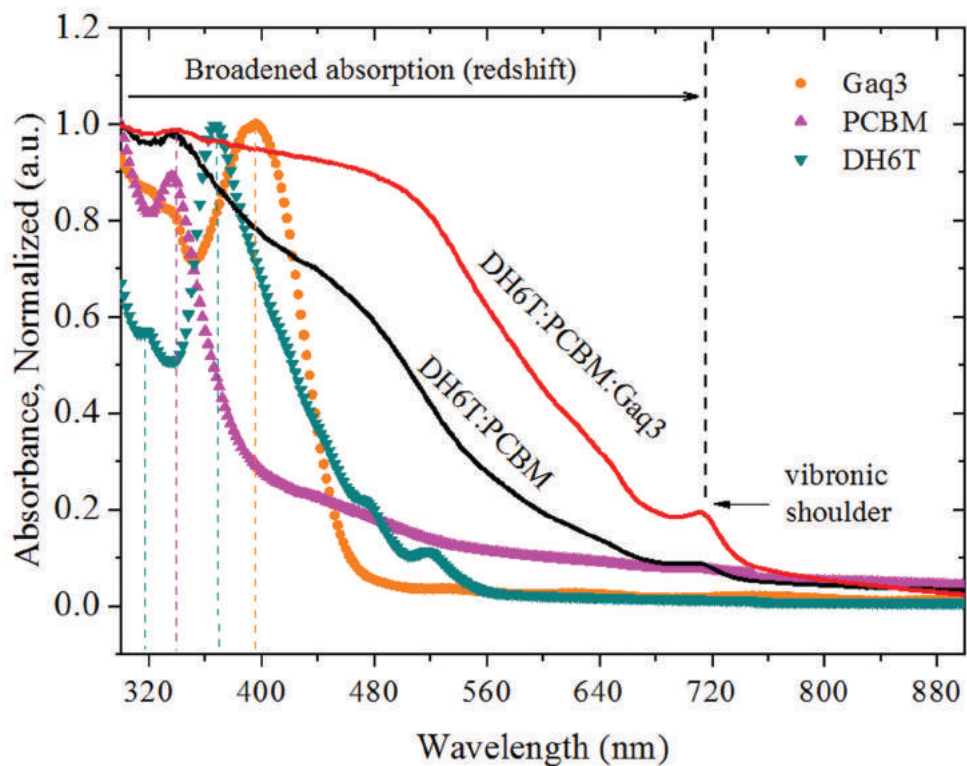


Fig. 3. Normalized absorbance of DH6T, PCBM, Gaq3, and their mixture with 29% molar fraction of Gaq3 in the DH6T: PCBM:Gaq3 active layer.

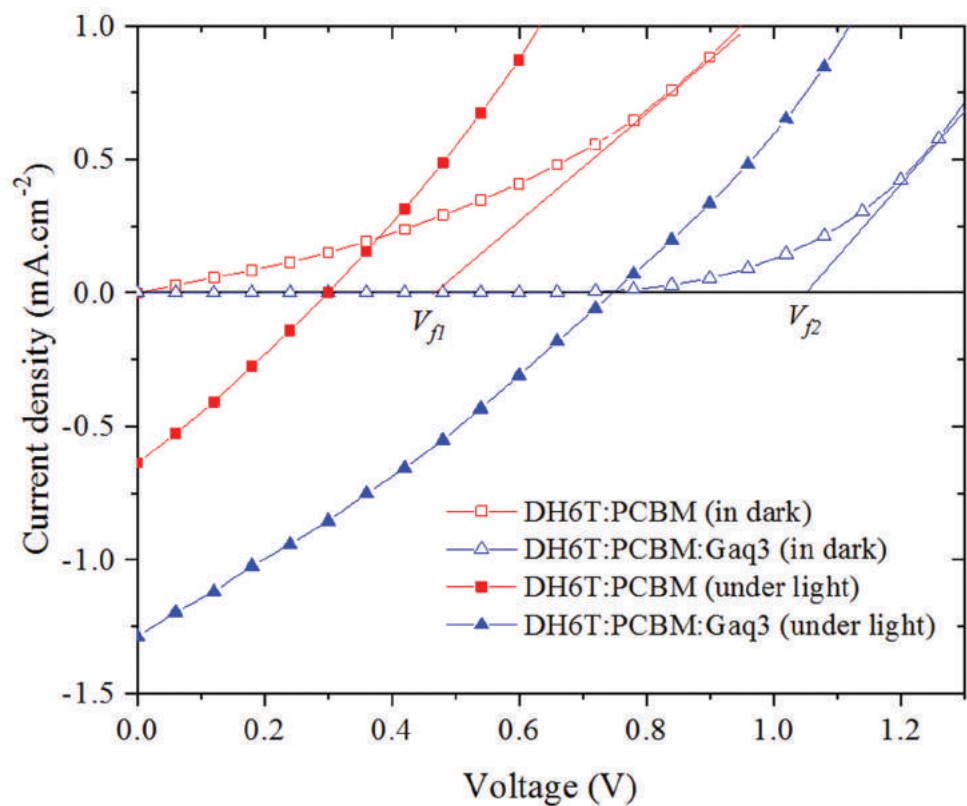


Fig. 4. The J-V characteristics of DH6T: PCBM:Gaq3 based organic solar cells incorporating 29% of Gaq3.

750 nm, which was brought about by the inclusion of Gaq3 (Fig. 3). Referring to Fig. 1c, one can see that the HOMO and LUMO levels of the DH6T: Gaq3:PCBM system are

well aligned to facilitate a smooth migration of free electrons and holes, thereby reducing the probability of electron-hole recombination at the D-A boundaries.

Information on thermal stability of the OSCs was investigated through subjecting the devices to different annealing temperatures, ranging from room temperature 25°C to 220°C. The performance of solar cells was assessed at each thermal condition, and their parameters were determined accordingly. It is seen from Fig. 5 that the J_{sc} of the two-acceptor based solar cells was continuously increased by annealing temperatures up to 180°C but decreased by annealing at 220°C. On the contrary, the V_{oc} was found to be decreased with the rise of temperature to 140°C, and then a subsequent increase in V_{oc} was observed until the temperature has reached 220°C. The same variation trend of the J_{sc} and V_{oc} on thermal annealing was also observed for the ternary OSCs comprising two-donor components such as P3HT:PCBM:F8BT (Kim et al., 2009) and PTB7:PCBM:F8BT (Shang et al., 2015), except that the point of inversion in the monotonic change of J_{sc} for our devices was appeared at higher temperature of 180°C compared to that of the reported devices which were occurred at 120°C. This indicated a higher thermal stability for our devices compared to that of the P3HT:PCBM:F8BT and PTB7:PCBM:F8BT based ones, which can be due to the effect of Gaq3 inclusion. We have previously reported that glass transition temperature (T_g) for Gaq3 is about 182°C

(Muhammad and Sulaiman, 2011a), which is close enough to the point of inversion in the J_{sc} variation versus temperature, pointing out to the reasonable contribution of Gaq3 in the improvement of thermal stability of our devices.

Table I presents the PV and intrinsic parameters of the studied OSCs, which were extracted by fitting Equation 1 to the experimental J-V data. One can see that the series resistance (R_s) of the OSCs was decreased with the increase of temperature to up to 180°C, whereas it was slightly increased at 220°C. Comparably, it can be concluded that both R_s and J_{sc} are inversely proportioned each with other, which is in agreement with the theoretical reported results (Muhammad et al., 2017a). The decrease in R_s is thought to be the consequence of increased crystallinity in the DH6T molecules on annealing, thereby improving photo-generated charge transport and percolation pathways in the devices active layer (Hwang et al., 2014). On the other hand, the decrease in R_p with annealing temperature to about 180°C is evidenced to the relative increase in charge carriers' recombination. Noteworthy, the best performance for the OSCs based on DH6T:PCBM:Gaq3, that is, the dual acceptor based OSCs, was obtained at temperature of 180°C, which is at higher temperature compared to those reported for the dual donor based devices (Sariciftci, 2004; Shang

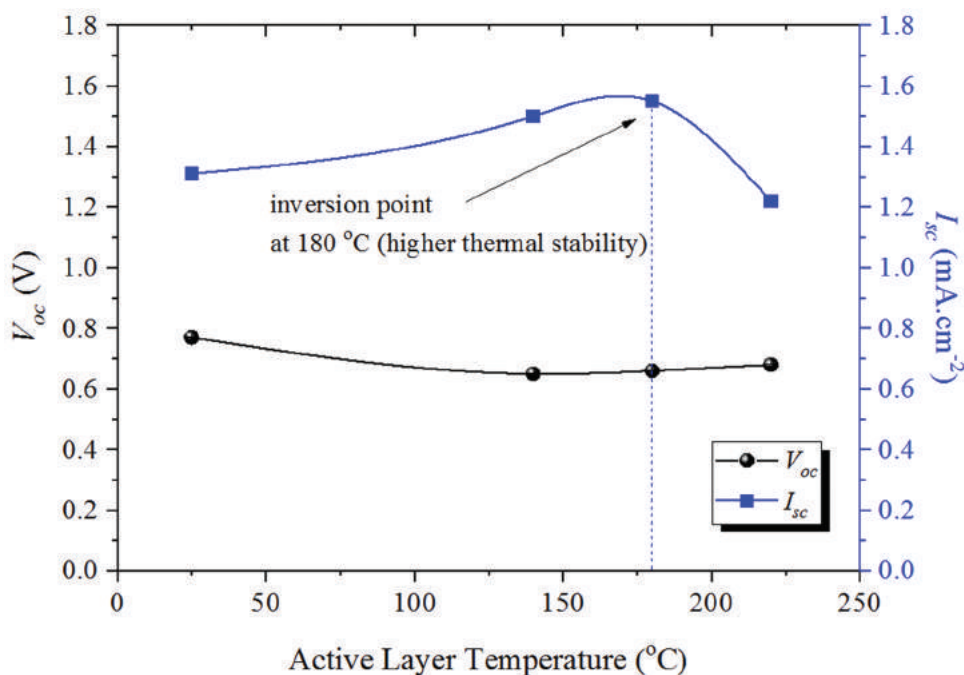


Fig. 5. Plot of J_{sc} and V_{oc} versus temperature for the organic solar cells based on DH6T:PCBM:Gaq3 active layer.

TABLE I
THE PHOTOVOLTAIC AND DEVICE PARAMETERS OF ORGANIC SOLAR CELLS BASED ON DH6T:PCBM:GAQ3 DUAL ACCEPTORS EXTRACTED FROM EXPERIMENTAL AND MODELING RESULTS

Devices	Annealing T (°C)	J_{sc} (mA/cm ²)	V_{oc} (V)	n	R_s (Ω)	R_p (Ω)	FF %	η %
DH6T:PCBM	25	0.63	0.30	3.81	887	5502	26.2	0.06
DH6T:PCBM:Gaq3	25	1.31	0.77	3.76	573	6775	26.7	0.27
DH6T:PCBM:Gaq3	140	1.50	0.65	2.23	367	4730	28.7	0.28
DH6T:PCBM:Gaq3	180	1.55	0.66	1.94	310	4836	29.3	0.30
DH6T:PCBM:Gaq3	220	1.22	0.68	1.96	337	5814	26.5	0.22

et al., 2015). This is another confirmation of high thermal stability for our devices thanks to the inclusion of small molecular Gaq3 acceptor. It is worth noting that the value of ideality factor (n) for the pristine devices is high and it gets reduced from 3.76 to 1.94 with the increase of annealing temperature to 180°C. The close values of ideality factor to

about two indicate that the charge carriers' recombination in these devices is governed by both of minority and majority carriers. It was generally observed that the efficiency of these devices was increased by order of 5.8 on the addition of Gaq3. Further enhancement in the efficiency, performance and stability of the OSCs can be achieved by taking the

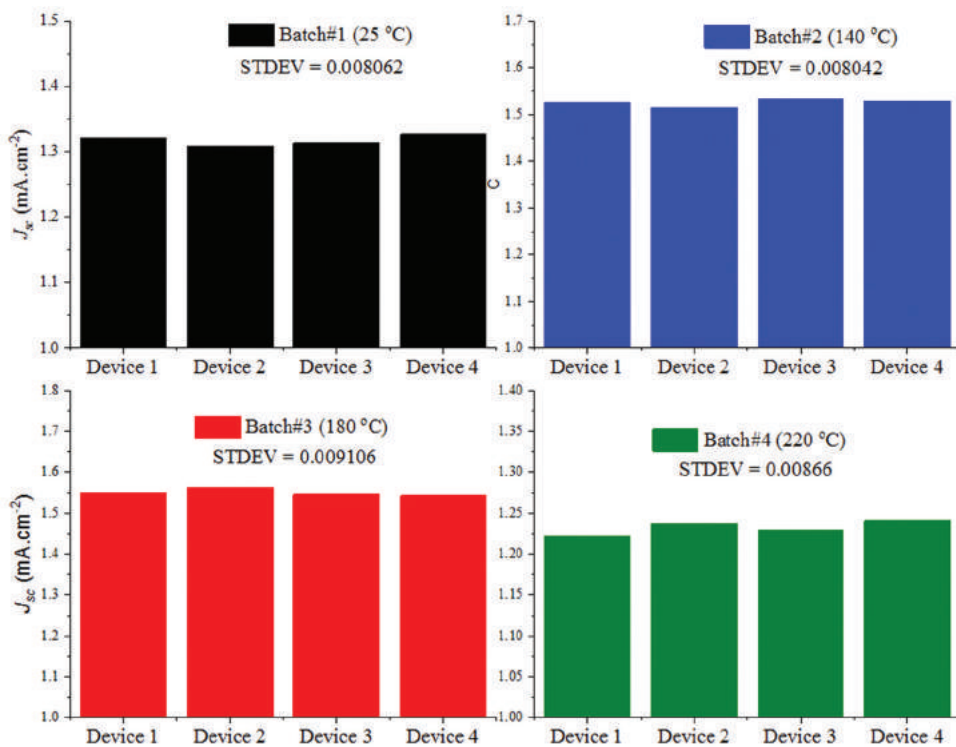


Fig. 6. Reproducibility comparison of the organic solar cells considering J_{sc} variation among four different batches annealed at different temperatures.

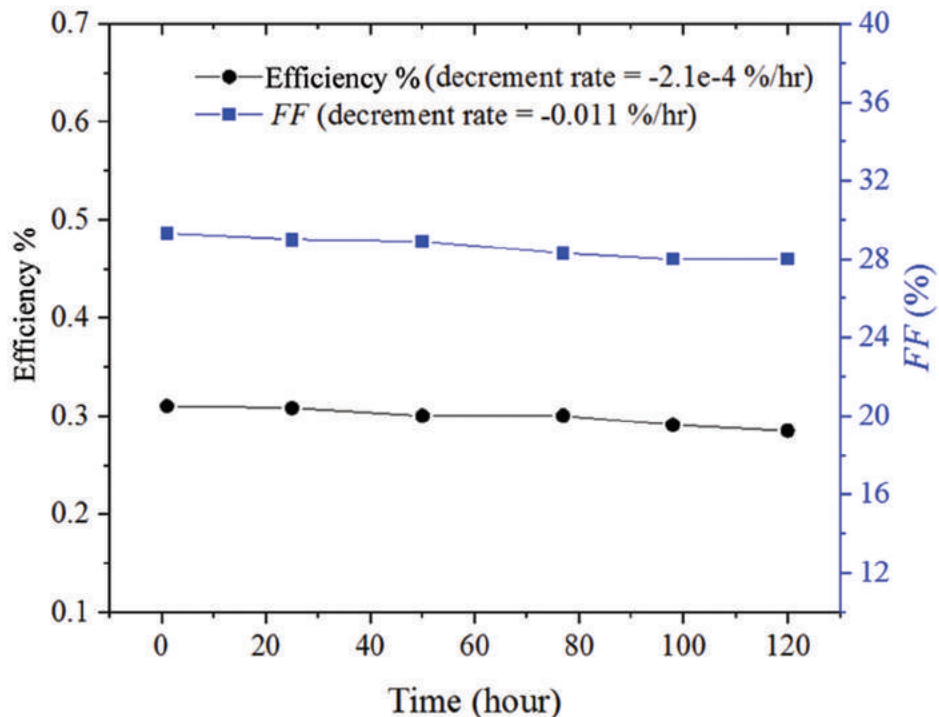


Fig. 7. The change in efficiency and fill factor for the studied organic solar cells in 120 h recorded within 6 consecutive days.

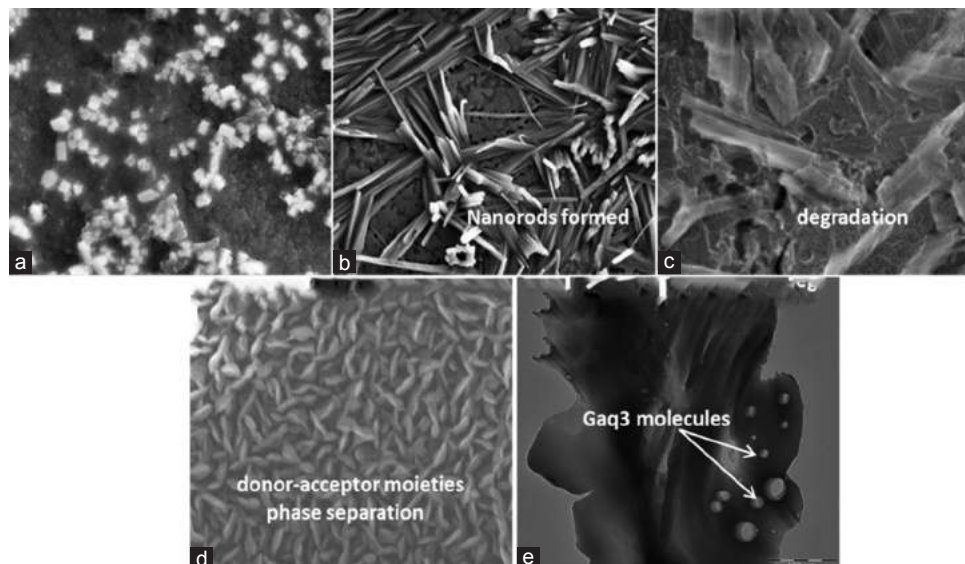


Fig. 8: Field emission scanning electronic microscopy images of Gaq3 film at room temperature 25°C (a), 180°C (b), 255°C (c), images of DH6T: Gaq3 at room temperature 25°C (d and e) and TEM image of the active layer based on DH6T: PCBM:Gaq3.

fabricating process inside glove box followed by the device's encapsulation. The current approach of using Gaq3 as the secondary acceptor can be generalized to the organic and PSCs aiming at improving their thermal stability and overall performance.

To reveal the impact of Gaq3 acceptor dopant on the reproducibility of the OSCs, the change in J_{sc} was considered among four devices that were fabricated on the same substrate (a single batch). The fabrication process of each device was analogous and was carried out for similar materials and under similar environmental conditions. Four different batches (comprising four devices each) annealed at various temperatures were tested for their J_{sc} parameter, as shown in Fig. 6. Results showed that the change in the J_{sc} is trivial among four devices of each batch with standard deviations (STDEV) ranging from 0.008 to about 0.009. This small deviation is a good indication of high reproducibility of the OSCs which was brought about by the high thermal stability of Gaq3 when it was used as a second acceptor in the OSCs.

To further elucidate the operational stability of the Gaq3 incorporated OSCs, the J-V characteristics of the devices were recorded at different times within 6 consecutive days. Interestingly, it was noticed that the decrement in efficiency and fill factor of the devices over the studied time span are relatively small and almost similar performance was achieved for the devices, as shown in Fig. 7. The decrement rate was found to be $-2.1E-4\%$ and $-0.011\%/h$ for the efficiency and fill factor, respectively.

Fig. 8a-e shows the surface and interface morphologies capture by FESEM and TEM for the Gaq3, DH6T: Gaq3 and DH6T: PCBM:Gaq3 films within 1 μ (1000 nm) resolution. It was seen that the surface morphology of Gaq3 start growing nanorods at temperature 180°C (Fig. 8-b). This temperature is close enough to the T_g (182°C) of Gaq3, at which the material presents a rubbery state. We have seen previously that the OSCs showed the highest performance

at this temperature, which might be due to the effect of Gaq3 distribution among DH6T: PCBM molecules. At a higher temperature of 255°C, the nanostructures were degraded and no longer fortified (Fig. 8-c), suggesting good thermal stability of Gaq3 to be used in OSCs. One can see from Fig. 8-d and 8-e that the donor-acceptor components present a clear spatial distribution of the DH6T, Gaq3 and PCBM moieties, whereas the inclusion of Gaq3 molecules, positioned themselves in nanoballs stacking the active layer matrix at room temperature.

IV. CONCLUSIONS

In this study, 29% molar fraction of Gaq3 dopant was dispersed into the active layer of DH6T: PCBM to produce a solution-processed system having a dual acceptor to be used as the active layer of OSCs. It was concluded that the addition of Gaq3 resulted in a pronounced broadening in the absorption spectra of DH6T and DH6T: PCBM films. The results showed a pronounced enhancement in the photocurrent and output voltage of the devices when Gaq3 is included. The short current density (J_{sc}) was increased from 0.63 mA to 1.26 mA, and the V_{oc} improved from 0.30 V to 0.74 V. As such, the J_{sc} and V_{oc} were increased by order of about 2 and 2.5, respectively. An inflection temperature of 180°C was noticed for J_{sc} which was higher than that of the P3HT: PCBM:F8BT and PTB7:PCBM: F8BT based solar cells at 140°C. This indicated higher thermal stability for our devices thanks to the effect of Gaq3 inclusion. It was generally observed that the efficiency of these devices was increased by an order of 5.8 on the addition of Gaq3. Four different batches (comprising four devices each) annealed at various temperatures were tested for their J_{sc} parameter. Results showed that the change in the J_{sc} is trivial among four devices of each batch with STDEV ranging from 0.008 to about 0.009. This small deviation is a good indication of high reproducibility of the OSCs. The decrement rate of

efficiency and fill factor of the devices over 120 h was found to be $-2.1\text{E-}4\%$ and $-0.011\%/h$, respectively, which are small enough to conclude a stable operation of the devices. The surface morphology of Gaq3 start growing nanorods at temperature 180°C . This temperature is close enough to the T_g (182°C) of Gaq3, at which the material presents a rubbery state. The use of Gaq3 due to its good thermal stability can be potentially generalized to the other OSCs.

ACKNOWLEDGMENTS

The authors would like to thank University of Malaya to support this work under the project UMRG grant RP007A/13AFR.

REFERENCES

- Ameri, T., Dennler, G., Lungenschmied, C. and Brabec, C.J., 2009. Organic tandem solar cells: A review. *Energy and Environmental Science*, 2, pp.347-363.
- Ansari, M.I.H., Qurashi, A. and Nazeeruddin, M.K., 2018. Frontiers, opportunities, and challenges in perovskite solar cells: A critical review. *Journal of Photochemistry and Photobiology C: Photochemistry Reviews*, 35, pp.1-24.
- Cheng, P. and Zhan, X., 2016. Stability of organic solar cells: Challenges and strategies. *Chemical Society Reviews*, 45, pp.2544-2582.
- Cook, S., Ohkita, H., Kim, Y., Benson-Smith, J.J., Bradley, D.D.C. and Durrant, J.R., 2007. A photophysical study of PCBM thin films. *Chemical Physics Letters*, 445, pp.276-280.
- Dennler, G., Scharber, M.C. and Brabec, C.J., 2009. Polymer-fullerene bulk-heterojunction solar cells. *Advanced materials*, 21, pp.1323-1338.
- Elumalai, N., Mahmud, M., Wang, D. and Uddin, A., 2016. Perovskite solar cells: Progress and advancements. *Energies*, 9, pp.861.
- Garnier, F., Yassar, A., Hajlaoui, R., Horowitz, G., Deloffre, F., Servet, B., Ries, S. and Alnot, P., 1993. Molecular engineering of organic semiconductors: Design of self-assembly properties in conjugated thiophene oligomers. *Journal of the American Chemical Society*, 115, pp.8716-8721.
- Hau, S.K., Yip, H.L., Baek, N.S., Zou, J., O'malley, K. and Jen, A.K.Y., 2008. Air-stable inverted flexible polymer solar cells using zinc oxide nanoparticles as an electron selective layer. *Applied Physics Letters*, 92, pp.225.
- Hernández, I., Gillin, W. and Somerton, M., 2009. Spectroscopic study of Mq3 (M= Al, Ga, In, q= 8-hydroxyquinolate) at high pressure. *Journal of Luminescence*, 129, pp.1835-1839.
- Huajun, X., Hideo, O., Hiroaki, B. and Shinzaburo, I., 2014. Open-circuit voltage of ternary blend polymer solar cells. *Japanese Journal of Applied Physics*, 53, pp.01AB10.
- Hwang, I., Mcneill, C.R. and Greenham, N.C., 2014. Evolution of phase separation upon annealing and the influence on photocurrent generation in ternary blend organic solar cells. *Synthetic Metals*, 189, pp.63-68.
- Ji, J., Ma, S., Shan, F., Wang, F. and Song, Y., 2016. Improving the performance of ternary bulk heterojunction polymer cell by regioregular poly (3-hexylthiophene)-grafted oxide graphene on in situ doping of CdS. *Journal of Materials Science*, 51, pp.7395-7406.
- Jo, J., Kim, S.S., Na, S.I., Yu, B.K. and Kim, D.Y., 2009. Time-dependent morphology evolution by annealing processes on polymer: Fullerene blend solar cells. *Advanced Functional Materials*, 19, pp.866-874.
- Johansson, T.B., Patwardhan, A.P., Nakićenović, N. and GOMEZ-Echeverri, L. 2012. *Global Energy Assessment: Toward a Sustainable Future*. Cambridge University Press, Cambridge.
- Kaltenbrunner, M., White, M.S., Głowacki, E.D., Sekitani, T., Someya, T., Sariciftci, N.S. and Bauer, S., 2012. Ultrathin and lightweight organic solar cells with high flexibility. *Nature Communications*, 3, pp.770.
- Kim, H., Shin, M. and Kim, Y., 2009. Distinct annealing temperature in polymer: Fullerene: Polymer ternary blend solar cells. *The Journal of Physical Chemistry C*, 113, pp.1620-1623.
- Koeppel, R. and Sariciftci, N.S., 2006. Photoinduced charge and energy transfer involving fullerene derivatives. *Photochemical and Photobiological Sciences*, 5, pp.1122-1131.
- Kwon, J.H. and Seo, J.H., 2007. P-type semiconducting a,w-dihexylsexithiophene for an organic thin film transistor. *Journal of Applied Physics*, 101, pp.064502.
- Liang, Y., Feng, D., Wu, Y., Tsai, S.T., Li, G., Ray, C. and Yu, L., 2009. Highly efficient solar cell polymers developed via fine-tuning of structural and electronic properties. *Journal of the American Chemical Society*, 131, pp.7792-7799.
- Liu, L., Li, H., Yao, S., Wei, Y. and Tian, W., 2015. Synthesis, characterization, and photovoltaic properties of a solution-processable two-dimensional-conjugated organic small molecule containing a triphenylamine core. *Journal of Materials Science*, 50, pp.57-65.
- Liu, T., Guo, Y., Yi, Y., Huo, L., Xue, X., Sun, X., Fu, H., Xiong, W., Meng, D. and Wang, Z., 2016. Ternary organic solar cells based on two compatible nonfullerene acceptors with power conversion efficiency > 10%. *Advanced Materials*, 28, pp.10008-10015.
- Marinova, N., Valero, S. and Delgado, J.L., 2017. Organic and perovskite solar cells: Working principles, materials and interfaces. *Journal of Colloid and Interface Science*, 488, pp.373-389.
- Mathew, S., Yella, A., Gao, P., Humphry-Baker, R., Curchod, B.F., Ashari-Astani, N., Tavernelli, I., Rothlisberger, U., Nazeeruddin, M.K. and Grätzel, M., 2014. Dye-sensitized solar cells with 13% efficiency achieved through the molecular engineering of porphyrin sensitizers. *Nature Chemistry*, 6, pp.242.
- Minxia, S., Xinge, Y., Xu, Y., Hanyu, W., Lei, Z., Quan, J. and Hui, L., 2015. Effect of different solvents on the performance of ternary polymer solar cells based on PTB7: PC71BM: F8BT. *Journal of Physics D: Applied Physics*, 48, pp.295105.
- Muhammad, F.F. and Sulaiman, K., 2011a. Effects of thermal annealing on the optical, spectroscopic, and structural properties of tris (8-hydroxyquinolate) gallium films grown on quartz substrates. *Materials Chemistry and Physics*, 129, pp.1152-1158.
- Muhammad, F.F. and Sulaiman, K., 2011b. Photovoltaic performance of organic solar cells based on DH6T/PCBM thin film active layers. *Thin Solid Films*, 519, pp.5230-5233.
- Muhammad, F.F. and Sulaiman, K., 2011c. Tuning the optical band gap of DH6T by Alq3 dopant. *Sains Malaysiana*, 40, pp.17-20.
- Muhammad, F.F. and Sulaiman, K., 2011d. Utilizing a simple and reliable method to investigate the optical functions of small molecular organic films—Alq3 and Gaq3 as examples. *Measurement*, 44, pp.1468-1474.
- Muhammad, F.F., 2014. Design approaches to improve organic solar cells. *Journal of Technology Innovations in Renewable Energy*, 3, pp.63.
- Muhammad, F.F., Hapip, A.I.A. and Sulaiman, K., 2010. Study of optoelectronic energy bands and molecular energy levels of tris (8-hydroxyquinolate) gallium and aluminum organometallic materials from their spectroscopic and electrochemical analysis. *Journal of Organometallic Chemistry*, 695, pp.2526-2531.
- Muhammad, F.F., Ketuly, K.A. and Yahya, M.Y., 2018. Effect of thermal annealing on a ternary organic solar cell incorporating Gaq3 organometallic as a boosting acceptor. *Journal of Inorganic and Organometallic Polymers and Materials*, 28, pp.102-109.
- Muhammad, F.F., Yahya, M.Y. and Sulaiman, K., 2017b. Improving the performance of solution-processed organic solar cells by incorporating small molecule acceptors into a ternary bulk heterojunction based on DH6T: Mq3:

PCBM (M= Ga, Al). *Materials Chemistry and Physics*, 188, pp.86-94.

Muhammad, F.F., Yahya, M.Y., Hameed, S.S., Aziz, F., Sulaiman, K., Rasheed, M.A. and Ahmad, Z., 2017a. Employment of single-diode model to elucidate the variations in photovoltaic parameters under different electrical and thermal conditions. *PLoS One*, 12, pp.e0182925.

Muhammad, F.F., Yahya, M.Y., Ketuly, K.A., Muhammad, A.J. and Sulaiman, K., 2016. A study on the spectroscopic, energy band, and optoelectronic properties of α , ω -dihexylsexithiophene/tris (8-hydroxyquinolate) gallium blends; DH6T/Gaq3 composite system. *Spectrochimica Acta Part A: Molecular and Biomolecular Spectroscopy*, 169, pp.144-151.

Mulherin, R.C., Jung, S., Huettner, S., Johnson, K., Kohn, P., Sommer, M., Allard, S., Scherf, U. and Greenham, N.C., 2011. Ternary photovoltaic blends incorporating an all-conjugated donor-acceptor diblock copolymer. *Nano Letters*, 11, pp.4846-4851.

Peterson, E.D., Smith, G.M., Fu, M., Adams, R.D., Coffin, R.C. and Carroll, D.L., 2011. Charge balance and photon collection in polymer based ternary bulk heterojunction photovoltaic devices containing cadmium selenide nanoparticles. *Applied Physics Letters*, 99, p.073304.

Reddy, S.S., Gunasekar, K., Heo, J.H., Im, S.H., Kim, C.S., Kim, D.H., Moon, J.H., Lee, J.Y., Song, M. and Jin, S.H., 2016. Highly efficient organic hole transporting materials for perovskite and organic solar cells with long-term stability. *Advanced Materials*, 28, pp.686-693.

Sariciftci, N.S., 2004. Plastic photovoltaic devices. *Materials Today*, 7, pp.36-40.

Schmager, R., Gomard, G., Richards, B.S. and Paetzold, U.W., 2019. Nanophotonic perovskite layers for enhanced current generation and mitigation of lead in perovskite solar cells. *Solar Energy Materials and Solar Cells*, 192, pp.65-71.

Sehati, P., Braun, S., Lindell, L., Xianjie, L., Andersson, L.M. and Fahlman, M., 2010. Energy-level alignment at metal-organic and organic-organic interfaces in bulk-heterojunction solar cells. *IEEE Journal of Selected Topics in Quantum Electronics*, 16, pp.1718-1724.

Shang, M., Yu, X., Ye, X., Zhang, L., Jiang, Q. and Lin, H., 2015. Effect of

thermal annealing on the performance of ternary organic photovoltaics based on PTB7: PC71BM: F8BT. *Journal of Materials Science: Materials in Electronics*, 26, pp.5708-5714.

Song, Q., Li, F., Yang, H., Wu, H., Wang, X., Zhou, W., Zhao, J., Ding, X., Huang, C. and Hou, X., 2005. Small-molecule organic solar cells with improved stability. *Chemical Physics Letters*, 416, pp.42-46.

Sotgiu, G., Zambianchi, M., Barbarella, G. and Botta, C., 2002. Synthesis and optical properties of soluble sexithiophenes with one central head-to-head junction. *Tetrahedron*, 58, pp.2245-2251.

Street, R.A., Davies, D., Khlyabich, P.P., Burkhart, B. and Thompson, B.C., 2013. Origin of the tunable open-circuit voltage in ternary blend bulk heterojunction organic solar cells. *Journal of the American Chemical Society*, 135, pp.986-989.

Tang, C.W., 1986. Two-layer organic photovoltaic cell. *Applied Physics Letters*, 48, pp.183-185.

Treat, N.D., Brady, M.A., Smith, G., Toney, M.F., Kramer, E.J., Hawker, C.J. and Chabinyc, M.L., 2011. Interdiffusion of PCBM and P3HT reveals miscibility in a photovoltaically active blend. *Advanced Energy Materials*, 1, pp.82-89.

Von Hauff, E., Dyakonov, V. and Parisi, J., 2005. Study of field effect mobility in PCBM films and P3HT: PCBM blends. *Solar Energy Materials and Solar Cells*, 87, pp.149-156.

Xue, J., Rand, B.P., Uchida, S. and Forrest, S.R., 2005. Mixed donor-acceptor molecular heterojunctions for photovoltaic applications. II. Device performance. *Journal of Applied Physics*, 98, pp.124903.

Zhao, W., Li, S., Yao, H., Zhang, S., Zhang, Y., Yang, B. and Hou, J., 2017a. Molecular optimization enables over 13% efficiency in organic solar cells. *Journal of the American Chemical Society*, 139, pp.7148-7151.

Zhao, W., Li, S., Zhang, S., Liu, X. and Hou, J., 2017b. Ternary polymer solar cells based on two acceptors and one donor for achieving 12.2% efficiency. *Advanced Materials*, 29, pp.1604059.

Zhu, W., Wu, Y., Wang, S., Li, W., Li, X., Chen, J., Wang, Z.S. and Tian, H., 2011. Organic D-A- π -A solar cell sensitizers with improved stability and spectral response. *Advanced Functional Materials*, 21, pp.756-763.

General Information

ARO's Mission: ARO seeks to publish those papers that are most influential in their fields or across fields and that will significantly advance scientific understanding. Selected papers should present novel and broadly important data, syntheses, or concepts. They should merit the recognition by the scientific community and general public provided by publication in ARO, beyond that provided by specialty journals.

We welcome submissions from all fields of natural science and technology, and from any source. We are committed to the prompt evaluation and publication of submitted papers. ARO is published biannually; selected papers are published online ahead of print.

Submission

Manuscripts should be submitted by the correspondent authors of the manuscript via the on-line submission page. Regardless of the source of the word-processing tool, only electronic Word (.doc, .docx, .rtf) files can be submitted on-line. There is no page limit. Only online submissions are accepted to facilitate rapid publication and minimize administrative costs. Submissions by any other one but the authors will not be accepted. The submitting author takes responsibility for the paper during submission and peer review. If for some technical reason submission through the email is not possible, the author can contact ARO.journal@koyauniversity.org for support. Before submitting please check ARO's guide to authors thoroughly to avoid any delay in the review and publication process.

Authors are explicitly responsible for the language of their texts. Paper should be submitted in a well written in understandable English. Authors should not expect the editor or editorial board to rewrite their paper. Prior to submission, authors should have their paper proofread by a possible academic native speaker of English.

- Submit the Article with contact Information
- File name should be your article title
- Don't submit your article in multiple journal, we are taking only minimum time for review process. please don't waste our time
- Once the paper is accepted, it can't be withdrawn
- Please follow publication ethics and regulation
- Avoid plagiarism and copied material
- Strictly Follow ARO's Template

Terms of Submission

Papers must be submitted on the understanding that they have not been published elsewhere and are not currently under consideration by another journal or any other publisher. ARO accepts original articles with novel impacts only. Post conference papers are not accepted "as is", however, regular papers on the same topic but with a different title can be submitted. The new paper should contain significant improvements in terms of extended content, analysis, comparisons with popular methods, results, figures, comments, etc. Please do not forget that the publication of the same or similar material in ARO constitutes the grounds for filing of an (auto) plagiarism case.

The submitting author is responsible for ensuring that the article's publication has been approved by all the other co-authors. It is also the authors' responsibility to ensure that the articles emanating from a particular institution are submitted with the approval of the necessary institution. Only an acknowledgement from the editorial office officially establishes the date of receipt. Further correspondence and proofs will be sent to the author(s) before publication unless otherwise indicated. It is a condition of submission of a paper that the authors permit editing of the

paper for readability. All enquiries concerning the publication of accepted papers should be addressed to aro.journal@koyauniversity.org.

Peer Review

All manuscripts are subject to peer review and are expected to meet standards of academic excellence. Submissions will be considered by an editor and “if not rejected right away” by peer-reviewers, whose identities will remain anonymous to the authors.

Guide to Author

We welcome submissions from all fields of science and from any source. We are committed to the prompt evaluation and publication of submitted papers. Selected papers are published online ahead of print. Authors are encouraged to read the instructions below before submitting their manuscripts. This section arranged into an overview speedy guidelines below and more detailed at the bottom section of this page

Manuscript Preparation

Submitting your manuscript will be in two stages namely before final acceptance and after.

Stage one:

At the first stage manuscript needs to be prepared electronically and submitted online via the online submission page in a Word (.doc, .docx, .rtf) format of one column double-spaced page, Times New Roman font type, and 12 p font size. A pdf version of the submitted manuscript should be submitted too. All authors' names, affiliations, e-mail addresses, and mobile phone numbers should be typed on a cover page, indicating the correspondent author.

Stage two:

- File type: MS-Word version 2003 or later.
- Format: The preferred format of the manuscript two-column template with figures and captions included in the text. This template can be downloaded via the following link. Please follow instructions given in the template; <http://aro.koyauniversity.org/about/submissions#onlineSubmissions>
- Text: All text is in Times New Roman font. The main text is 10-point, abstract is 9-point font and tables, references and captions are 8-point font.
- Figures: Figures should be easily viewed on a computer screen.

Units of Measurement

Units of measurement should be presented simply and concisely using System International (SI) units.

Title and Authorship Information

The following information should be included;

- Paper title.
- Full author names.
- Affiliation.
- Email addresses.

Abstract

The manuscript should contain an abstract. The abstract should be self-contained and citation-free and should not exceed 200 words.

Introduction

This section should be succinct, with no subheadings.

Materials and Methods

This part should contain sufficient detail so that all procedures can be repeated. It can be divided into subsections if several methods are described.

Results and Discussion

This section may each be divided by subheadings or may be combined.

Conclusions

This should clearly explain the main conclusions of the work highlighting its importance and relevance.

Acknowledgements

All acknowledgements (if any) should be included at the very end of the paper before the references and may include supporting grants, presentations, and so forth.

References

References must be included in the manuscript and authors are responsible for the accuracy of references. Manuscripts without them will be returned. ARO is following Harvard System of Referencing. (Learn how to import and use Harvard Styling in your Microsoft Office by following this link:

<http://bibword.codeplex.com/releases/view/15852>)

Preparation of Figures

Upon submission of an article, authors are supposed to include all figures and tables in the PDF file of the manuscript. Figures and tables should be embedded in the manuscript. Figures should be supplied in either vector art formats (Illustrator, EPS, WMF, FreeHand, CorelDraw, PowerPoint, Excel, etc.) or bitmap formats (Photoshop, TIFF, GIF, JPEG, etc.). Bitmap images should be of 300 dpi resolution at least unless the resolution is intentionally set to a lower level for scientific reasons. If a bitmap image has labels, the image and labels should be embedded in separate layers.

Preparation of Tables

Tables should be cited consecutively in the text. Every table must have a descriptive title and if numerical measurements are given, the units should be included in the column heading. Vertical rules should not be used.

Copyright

Open Access authors retain the copyrights of their papers, and all open access articles are distributed under the terms of the Creative Commons Attribution License, which permits unrestricted use, distribution and reproduction in any medium, provided that the original work is properly cited.

The use of general descriptive names, trade names, trademarks, and so forth in this publication, even if not specifically identified, does not imply that these names are not protected by the relevant laws and regulations.

While the advice and information in this journal are believed to be true and accurate on the date of its going to press, neither the authors, the editors, nor the publisher can accept any legal responsibility for any errors or omissions that may be made. The publisher makes no warranty, express or implied, with respect to the material contained herein.

ARO Reviewer/Associate Editor Application Form

ARO is a scientific journal of Koya University (p-ISSN: 2410-9355, e-ISSN: 2307-549X) which aims to offer a novel contribution to the study of Science. The purpose of ARO is twofold: first, it will aim to become an ongoing forum for debate and discussion across the sciences and Engineering. We hope to advance our problem solving capacity and deepen our knowledge regarding a comprehensive range of collective actions. Second, ARO accepts the challenges brought about by multidisciplinary scientific areas and aspires to expand the community of academics who are able to learn from and help to produce advances in a variety of different disciplines.

The Journal is seeking reviewers who can provide constructive analysis of papers thus enhancing overall reputation of the Journal. If any expert is interested in participating of the review process, we highly encourage you to sign up as a reviewer for our Journal and help us improve our presence in domain of your expertise. Appropriate selection of reviewers who have expertise and interest in the domain relevant to each manuscript are essential elements that ensure a timely, productive peer review process. We require proficiency in English.

How to apply

To apply for becoming a reviewer of ARO, please submit the application form by following the link:

<http://aro.koyauniversity.org/user/register>

To apply for becoming a member of the Editorial Board of ARO, please submit the application form by following the link: <http://aro.koyauniversity.org/pages/view/AEB>

Both Associate Editor and Reviewers should specify their areas of research and expertise. Applicants must have a doctorate (or an equivalent degree), and if Master degree they need to have significant publishing experience. Please note that;

- You will need to write your full official name.
- Please provide an email which reflects your official name, such as nameOne.NameTwo@... , or your institute's official email.
- All data need to be written in English.

Note: For more information, kindly visit the following websites:

1. aro.koyauniversity.org.
2. <http://libweb.anglia.ac.uk/referencing/harvard.htm>.
3. <http://bibword.codeplex.com/releases/view/15852>.

INDEXING



Koya University (KOU) is a young University established in 2003 and it is located in the city of Koya (Koysinjaq), short distance to the East of the regional capital city of Erbil (Arbil, Hewlêr) in Kurdistan Region of Iraq. It is on the foothills of beautiful High Mountain. Its campus has been carefully laid out to embrace the beautiful mountainous nature. The Koya University has a Faculty system which enhances the interactions between similar academic fields. Today, Koya University has four Faculties: Engineering, Science and Health, Humanities and Social Sciences and Education in addition to the School of Medicine, which all consist of twenty-five scientific departments in different fields, such as Petroleum Engineering, Geotechnical Engineering, Software Engineering, Physics, Chemistry, Clinical Psychology, Social Science, Medical Microbiology and Sport Education.

ARO-The Scientific Journal of Koya University is a biannual journal of original scientific research, global news, and commentary in the areas of Science and Technology. ARO is a Peer-reviewed Open Access journal with CC BY-NC-SA 4.0 license. It provides immediate, worldwide and barrier-free access to the full text of research articles without requiring a subscription to the journal, and has no article processing charge (APC). ARO Journal seeks to publish those papers that are most influential in their fields or across fields and that will significantly advance scientific understanding. ARO Journal is a member of ROAD and Crossref agencies and has got ESCI, DOAJ seal, SHERPA/RoMEO deposit policy, and LOCKSS archiving policy.

Aro the Scientific Journal Office

Koya University (KOU)
University Park
Danielle Mitterrand Boulevard
Koya KOY45, Kurdistan Region - Iraq

aro.koyauniversity.org

ISSN: 2410-9355 (printed version) ISSN: 2307-549X (electronic version)
ARO - DOI: 10.14500/2307-549X